



University of Bergamo
&
University of Naples Federico II

PhD Program in Technology, Innovation and Management

XXXV Cycle

PhD Thesis

**EXPERIMENTAL AND MODELLING ANALYSIS OF TECHNOLOGIES
INNOVATIONS AT COMPONENT AND SYSTEM LEVEL IN THE
REFRIGERATION FIELD: THERMO-ECONOMIC OPTIMIZATION,
PERFORMANCE ASSESSMENT AND ECONOMIC FEASIBILITY**

PhD Program Coordinator

Prof. Ing. Renato Redondi

Tutor

Prof. Arch. Fabrizio Ascione

Supervisor

Prof. Ing. Luca Viscito

PhD Candidate

Ing. Giovanni Napoli

List of contents

List of contents	1
Introduction	6
Layout of the thesis	9
1. Context: refrigeration and air conditioning systems	11
1.1 Energetic consumption	11
1.2 Environmental impact.....	14
1.3 Measures to limit the environmental impact.....	16
1.3.1 <i>Policies to reduce the indirect environmental impact</i>	16
1.3.2 <i>Policies to reduce the direct environmental impact</i>	18
2. Thermo-economical sensitivity analysis of a linear compressor for domestic refrigeration	22
2.1 Linear compressor state of the art.....	22
2.2 Objective of the study	26
2.3 Linear compressor model.....	27
2.3.1 <i>Energy and mass conservation equations</i>	27
2.3.2 <i>Piston dynamics</i>	28
2.3.3 <i>Friction losses</i>	30
2.3.4 <i>Leakages</i>	30
2.3.5 <i>Valve dynamics</i>	31
2.3.6 <i>Heat transfer model</i>	32
2.3.7 <i>Linear compressor global and volumetric efficiency</i>	33
2.3.8 <i>Computational procedure</i>	34
2.3.9 <i>Model validation</i>	35
2.4 Sensitivity analysis and thermo-economic comparison.....	36

2.4.1	<i>Sensitivity analysis on compressor efficiencies and cost</i>	38
2.4.2	<i>Thermo-economic analysis</i>	42
2.5	Conclusion of the chapter	44
3.	Flow boiling heat transfer and pressure drop data of low GWP mixtures R455A and R454C	48
3.1	State of the art	48
3.2	Objective of the research	52
3.3	Experimental facility.....	53
3.3.1	<i>Test section</i>	54
3.3.2	<i>Measurement instrumentation</i>	55
3.4	Experimental method.....	57
3.4.1	<i>Experimental procedure</i>	57
3.4.2	<i>Data reduction</i>	57
3.4.3	<i>Uncertainty analysis</i>	59
3.4.4	<i>Thermocouples calibration</i>	61
3.4.5	<i>Test rig validation and preliminary tests</i>	62
3.5	Effect of the operating parameters on the heat transfer coefficient.....	63
3.5.1	<i>Operating conditions</i>	63
3.5.2	<i>Effect of the imposed heat flux</i>	63
3.5.3	<i>Effect of mass flux</i>	65
3.5.4	<i>Effect of bubble saturation temperature</i>	67
3.6	Effect of the operating parameters on the frictional pressure drop.....	69
3.6.1	<i>Effect of mass flux</i>	69
3.6.2	<i>Effect of bubble saturation temperature</i>	70
3.7	Assessment of correlations	71

3.7.1	<i>Heat transfer coefficient</i>	71
3.7.2	<i>Pressure drop</i>	76
3.8	Conclusions of the chapter.....	79
4.	State of the art on heat driven system	83
4.1	Absorption systems.....	83
4.2	Combined ORC/VCC systems.....	89
4.3	Heat driven ejector systems	94
5.	Waste heat driven ejector cycle modelling	105
5.1	Objective of the research	105
5.2	System modelling	105
5.2.1	<i>Ejector model</i>	105
5.2.2	<i>Thermal power in the vapor generator</i>	113
5.2.3	<i>Heat exchanger modelling</i>	114
5.2.4	<i>Compressor model</i>	117
5.2.5	<i>Refrigerant pumps, condenser fans and water pumps</i>	118
5.2.6	<i>Tank model</i>	119
5.2.7	<i>Cost functions</i>	120
5.3	Resolution algorithms	121
5.3.1	<i>Resolution algorithms and control strategy for the waste heat driven multi-ejector cooling system</i>	121
5.3.2	<i>Resolution algorithms and control strategy for the solar driven compressor assisted ejector cooling system</i>	128
5.3.3	<i>Resolution algorithms and control strategy for the waste heat drive multi-ejector compressor assisted chiller for cruise ships air conditioning</i>	133
6.	Optimization of design at partial load, seasonal performance and costs evaluation of a waste heat driven multi-ejector cooling system	142

6.1	Objective of the study	142
6.2	Operating conditions and climatic data	142
6.3	Sizing results.....	144
6.4	Multi-ejector optimization	147
6.5	Seasonal comparison.....	148
6.6	Economic comparison.....	150
6.7	Conclusions of the chapter.....	154
7.	Thermo-economic analysis and optimization strategy of a solar driven ejector cooling system employing natural refrigerants.....	156
7.1	Objective of the study	156
7.2	Operating conditions and climatic data	156
7.3	Sizing results.....	158
7.4	Seasonal comparison.....	159
7.5	Economic comparison.....	160
7.6	Conclusions of the chapter.....	162
8.	Thermo-economic analysis and optimization strategy of a waste heat driven cooling system employed for cruise ships air conditioning.....	164
8.1	Objective of the study	164
8.2	Case study description	164
8.3	Sensitivity analysis and system optimization	165
8.3.1	<i>Sensitivity analysis</i>	166
8.3.2	<i>System optimization</i>	167
8.4	Seasonal analysis results	171
8.5	Environmental comparison	173
8.6	Economic comparison.....	174
8.7	Conclusions of the chapter.....	177

9. Conclusions	179
9.1 Summary of the numerical analysis on the linear compressor for domestic refrigeration	179
9.2 Summary of the flow boiling experimental campaign on low-GWP mixtures R455A and R454C	180
9.3 Summary of the hybrid ejector cycle investigation	181
Nomenclature	184
List of Figures	190
List of Tables.....	196
Bibliography.....	199

Introduction

Greenhouse gases emissions related to anthropic activities are leading to an increase of the Earth surface temperature, that following the present trend in 2100 could be 4°C higher compared the preindustrial levels [1, 2]. Moreover, the forecasted 35% global population augment and a 3.5 times larger economy in the 2070, compared to the current level, will lead to a rise of nearly 40% in global energy demand, according to the International Energy Agency [3], constituting a dramatic issue since the 80% of the total energy supply is still provided by means fossil fuels [4]. For these reasons, with the Paris Agreement in 2015 [5], and the COP26 held in Glasgow in 2021, several countries have pledged to take concrete actions to pursue the common objective of limiting the global warming up to 1.5°C by 2100. The increased energy demand in the next decades will be led by developing countries. As a matter of fact, advanced economies accounted for 38% of global primary energy demand in 2019 compared with 63% in 1971. Emerging economies in Asia today account for 36% of global energy demand compared with less than 15% at the beginning of the 1970s [3]. In fact, while since 2000 in developed countries CO₂ emissions increase has slowed, an increasing contribution is given by all the emerging economies. Between 2000 and 2019 emissions tripled in China and more than doubled in other emerging economies, where, however, per capita emissions still remain at a lower level compared to the advanced economies, but this trend is expected to change due to the improvement of the life conditions in Asia and in Sub-Saharan Africa.

Among the several sectors contributing to the energy consumption and pollutant emissions, refrigeration and air conditioning are crucial, accounting for 17% of the total electricity consumption around the world [6]. Refrigeration is the set of all processes constituting the cold chain, namely the supply chain that ensures the temperature chilling, transport and storage of food, medical supply and all the sensitive goods that need to be stored at low temperature. Air conditioning includes all the processes allowing to provide the thermal comfort to the people occupying a confined environment. Given the remarkable importance of these sectors, their energy consumption is forecasted to increase in the next years, with three times the current installation in the following decades [6]. According to IEA [7] the air conditioning stock should increase four times

by 2050. Moreover, the energy transition is leading to a wider use of the electricity as energy carrier, also because it is expected an enhancement of its production by means of renewable sources in the following years. Consequently, electric heat pumps are more and more developed not only for heat and cooling, but also for hot sanitary water production. In fact, they give the opportunity to use electric energy instead of fossil fuels, are suitable for the integration with renewable sources and the heat removed from the environment is recognized as equivalent to the adoption of renewable energy. For these reasons, the heat pump number installed globally is expected to increase between the 2020 and 2030 from 180 million to approximately 600 million [8].

Almost the totality of the technologies employed in the previous sectors adopt conventional vapor compression cycles (VCC), driven by electric energy. Despite the not negligible energy consumption, the vapor compression cycle contributes to the environmental impact both, in direct and indirect ways. Specifically, the direct environmental impact is related to the accidental leakages of refrigerants having high-GWP (global warming potential), while the second is connected to the pollutant emissions to produce the electric energy employed to drive VCCs. To overcome these issues, some regulations require the adoption of low-GWP refrigerant, and the increase of the efficiency of the equipment employed. Particularly, the Kigali Amendment to the Montreal Protocol [9] aims to reduce the hydrofluorocarbons production and to achieve over 80% reduction in HFC consumption by 2049. On this regard, the European Union has approved the EU Regulation No 517/2014 (F-gas regulation) [10], setting the GWP threshold value of refrigerant employed in each specific application in the refrigeration, air conditioning and heat pumps sectors. Moreover, also the performance of the systems must comply with requirements more and more stringent. Minimum Energy Performance Standards (MEPS) have been introduced in order to set the minimum performance of refrigeration and air conditioning equipment. A clear example is the European regulation Eco-design [11]. Another need in the aforementioned sectors is to directly drive a vapor compression cycle by means of renewable sources, such as solar power or waste heat from industrial processes.

The objective of this thesis is to deepen the aforesaid issues related to vapor compressions cycles, following a double approach, both modelling and experimental, with the objective to analyse the performance of low-GWP refrigerants and to investigate the innovations

both at components and at system level, to define the performance, the economic feasibility and the competitiveness on the market.

Particularly, the thesis has been divided into three parts, with the first two focused on the analysis of different component constituting the vapor compression cycle, while in the third part an investigation at system level is carried out, analysing a novel vapor compression cycle, driven by means of low-grade thermal sources, aiming to assess this brand-new technology, still not commercially developed, from a thermo-economic point of view.

As regards the innovation at component level a numerical study of a linear compressor is proposed, with the purpose to perform a thermo-economic analysis and to investigate which are the design parameters having the higher influence on the compressor performance and costs, optimizing its design from the thermodynamic and the economic point of view. Concerning the heat exchangers, an experimental investigation on the flow boiling heat transfer coefficient and pressure drop measurement of low-GWP refrigerants (the mixtures R454C and R455A) is carried out. The experimental data collected allow to carry out a critical assessment of several predictive methods available in the scientific literature, in order to provide useful information to the heat exchangers designers regarding the more reliable correlations to evaluate the heat transfer coefficient of these refrigerants. As a matter of fact, most of the prediction methods available were calibrated with experimental data obtained for traditional high-GWP fluids, having different thermodynamic properties and operating conditions compared to the new low-GWP mixtures.

As regards the innovations in vapor compression cycles, a thermodynamic model of a novel hybrid ejector cycle is developed. The novel cycle is made up of a direct/indirect system. The ejector allows to compress the refrigerant without the use of an electrically driven compressor. The proposed thermodynamic cycle provides the cool production by means of solar energy or waste heat from industrial processes, allowing a reduction of the electricity consumption. The system under investigation has been optimized for different applications, concerning the domestic air conditioning by using the solar energy and the air conditioning of a cruise ship, exploiting the residual heat of the exhaust gas released from the engines employed for the ship propulsion. The purpose of this investigation is

to compare the performance of this new-brand technology with respect to the traditional electric chiller and to evaluate its economic feasibility.

Layout of the thesis

- In Chapter 1 is given the background of the study, analyzing the energy consumption and environmental impact related with refrigeration and air conditioning systems and describing the normative framework that industries and research have to deal with.
- Chapter 2 deals with the numerical simulation of the novel linear compressor, in order to carry out a thermo-economic analysis. After the state of the art related to this technology, the equations constituting the model are shown. Then, a sensitivity analysis is carried out to find and optimize the major geometrical parameters affecting the compressor efficiency and cost, to provide a guideline for compressors manufacturers looking for an optimized design. Finally, a thermo-economic assessment is proposed, comparing performance and cost of the solutions analyzed with those currently on the market.
- Chapter 3 presents an experimental activity to collect data of flow boiling heat transfer coefficient and pressure drop of low-GWP mixtures, R454C and R455A, employed as drop-in solutions for the high-GWP refrigerant R404A in commercial refrigeration, refrigerated transports and condensing units. After a critical review about drop-in replacements of R404A, the experimental apparatus, the calibration procedure, the uncertainty analysis and the data reduction are shown. Subsequently, the effect of mass flux, saturation temperature, imposed heat flux and vapor quality on the heat transfer coefficient and pressure drop of the two refrigerants is presented. Finally, the assessment of several predictive methods is carried out, also proposing a correction to some correlations to take into account the temperature glide.
- In Chapter 4 a thorough state of the art of heat driven technologies is carried out, analyzing conventional heat driven technologies, such as absorption cycle and combined ORC/VCC systems and the novel waste heat driven hybrid ejector cycle.

- In Chapter 5 the thermodynamic model of each component constituting the hybrid ejector cycle is presented and the resolution algorithms for the several case studies analyzed in the present thesis are also shown.
- Chapter 6 deals with a seasonal performance analysis of a waste heat driven multi-ejector cooling system, having a nominal cooling power of 20 kW, for domestic air conditioning. In the first part of the chapter the system is optimized to find the best configuration and optimal ejector numbers. In the second part seasonal simulations are performed, considering different climate scenarios. Finally, a comparison between the seasonal performance and the total costs of the investigated solutions and the reference technologies, namely absorption and electric chiller, is carried out considering different electricity costs.
- In Chapter 7 a solar driven hybrid multi-ejector compressor assisted chiller, having a nominal power of 10 kW and employing natural refrigerants (ammonia and propane), for domestic air conditioning, is simulated. After the system sizing, considering different size of the solar collectors and different climate scenarios, to account the differences in ambient temperatures and solar radiation, the system is simulated during the whole cooling season to evaluate the seasonal energy efficiency ratio. Finally, a thermo-economic comparison between the proposed technology and the electric chiller is carried out.
- Chapter 8 presents a case study of a waste heat driven hybrid multi-ejector compressor assisted chiller for a cruise ship air conditioning. In this case the system is driven by means the waste heat from the engines exhaust gas. Particularly, the cruise ship under investigation operates during the whole year in the Baltic Sea and has a nominal cooling load of 1350 kW. Firstly, a sensitivity analysis is carried out to quantify the influence of several design parameters on the system performance and costs. Then, the system design has been optimized by means of a genetic algorithm. Some notable points have been selected afterwards and simulated during the cooling season and the results are compared with those of a vapor compression chiller, in terms of performance, pollutant emissions and total cost (considering different price scenarios for the fuel).
- In chapter 9 the main outcomes of the thesis are summarized.

1. Context: refrigeration and air conditioning systems

In this chapter the context in which the thesis takes place is addressed, focusing the attention on actual energetic and environmental impact of refrigeration and air conditioning systems, together with the normative framework. Initially, the current status in terms of energetic consumption and environmental impact of refrigeration and air conditioning applications is provided. Then, the perspective of growth in terms of installation will be analysed and the projections in terms of energy consumption and environmental impact, altogether with the measures proposed to contain them. Finally, the major agreements and regulations to reduce the consumption and pollutant emissions related to these technologies, both worldwide and at European level, will be shown.

1.1 Energetic consumption

Cooling appliances are fundamental for many purposes, from one side, they ensure the correct functioning of the cold chain, allowing the food safety, vaccines storage and transportation and on the other side provide the thermal comfort and productivity in homes, working and public spaces. According to [6] in 2018 3.6 billion of cooling appliances were employed around the world. However, the rise of the Earth surface temperature together with a concomitant increasing request of cooling from developing countries where 1.1 billion people still do not have access to a developed cold chain, lacking in fundamentals goods, such as fresh food and vaccines [12], will result in a huge increase of the cooling appliances, reaching almost 10 billion by 2050, as shown in Figure 1.

The Growth of the Cooling Sector

If air conditioning adoption continues at projected rates, there could be more than 9.5 billion units by 2050.

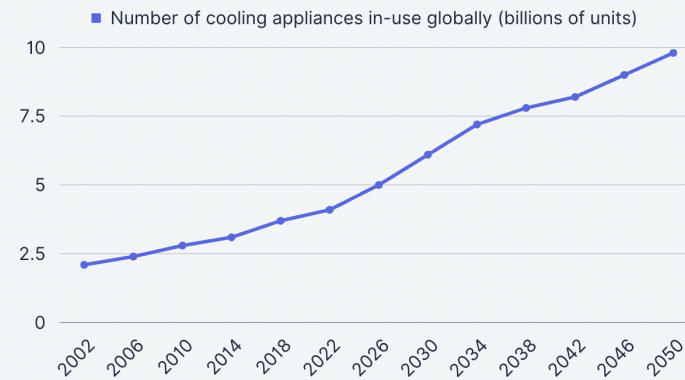


Figure 1 Predicted growth of the cooling sector [6].

The cold chain includes a wide range of appliances, such as 1.5 billion of domestic refrigerators, 90 million of commercial refrigerated equipment, 4 million of refrigerator road vehicles, 1.2 million of refrigerated containers and almost 500000 supermarkets [13]. A substantial growth is forecasted especially due to the emerging economies. The development and improving of the cold chain are fundamental to make available food all over the world (in 2018 821.6 million of people worldwide were undernourished [14]) and to reduce food losses and waste, that according to FAO account up to 8% of total greenhouse gas emissions, having a cost of 2.6 trillion USD per year [15]. An inadequate cold chain is responsible for about 9% of loss of perishable foods in developed countries and 23% in developing countries [16]. According to the Project Drawdown [17], an improved cold chain could allow to avoid up to 21 GtCO₂ emission between 2020 and 2050.

Also air conditioning demand is expected to increase enormously. In Figure 2 is reported the predicted increase of air conditioning appliances around the world, passing from 2 billion units in the 2020 up to almost 6 billion in the 2050 [18], with an exponential increase in the units sold especially in the developing countries. According to the Commission's European Heating and Cooling Strategy [19] the EU's cooling energy consumption is expected to augment by 74.5% by 2050, increasing the already huge energy demand. As a matter of fact, space heating and air conditioning in the EU accounts

for 60% and the 80%, respectively, the energy demand and the direct CO₂ emissions in the building sector according to the World Energy Outlook 2021 [20].

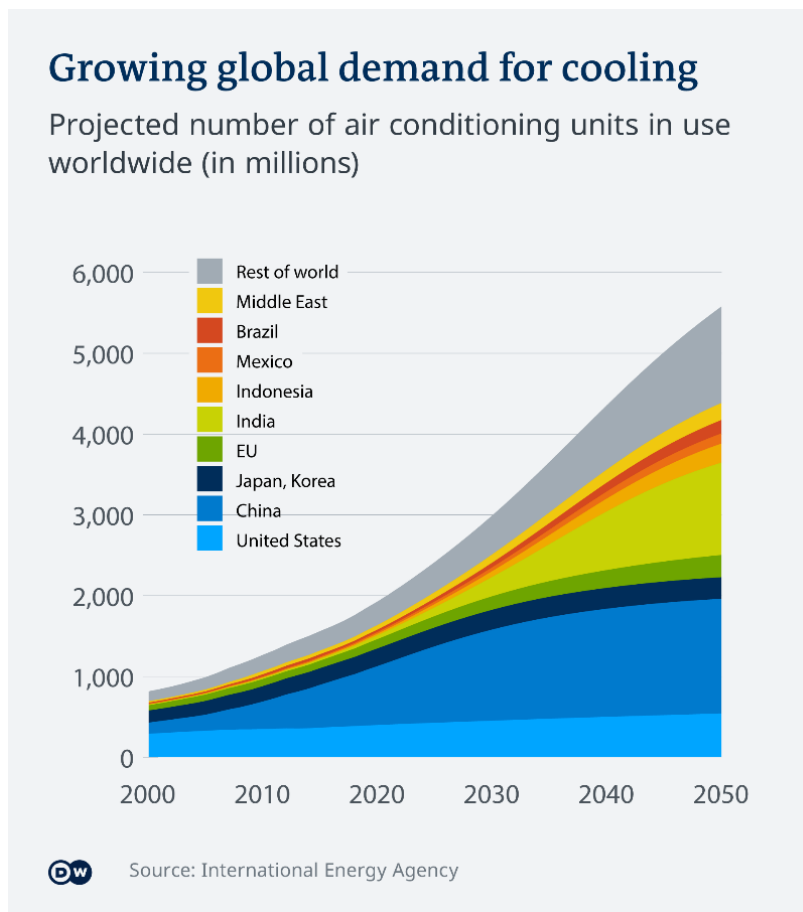


Figure 2 Forecasted air conditioning stock increase [21].

Most of the cooling technologies employ vapor compression cycles, which are now spreading also for different applications, such as heating and hot sanitary water production, due to different concurrent reasons: firstly, the heat removed from the environment is recognized as equivalent to the adoption of renewable energy sources. Secondly, because of the energy transition, electricity will be the main energy carrier and electrical heat pumps allow the production of both heating and cooling with a higher efficiency compared to traditional fossil fuel boilers. For these reasons, the number of heat pumps installed around the world is predicted to increase from 180 million in 2020 to 600 million in 2030.

It was estimated [6] that these sectors accounted for 3.900 TWh/year of global electricity consumption, 17% of the total electricity demand and the 3.4% of the world's total energy demand.

1.2 Environmental impact

The increasing number of equipment using cooling appliances and heat pumps and the consequent energy demands causes a huge environmental impact.

Firstly, since most of the electricity productions still comes from non-renewable fossil fuels [21], as shown in Figure 3, vapor compression cycles are responsible for an indirect environmental impact related to the pollutant emissions caused by the electricity production. However, despite renewables sources are expected to cover the 85% of the global electricity production by 2050, the share of renewables in the energy mix will only reach approximately the 50% [21].

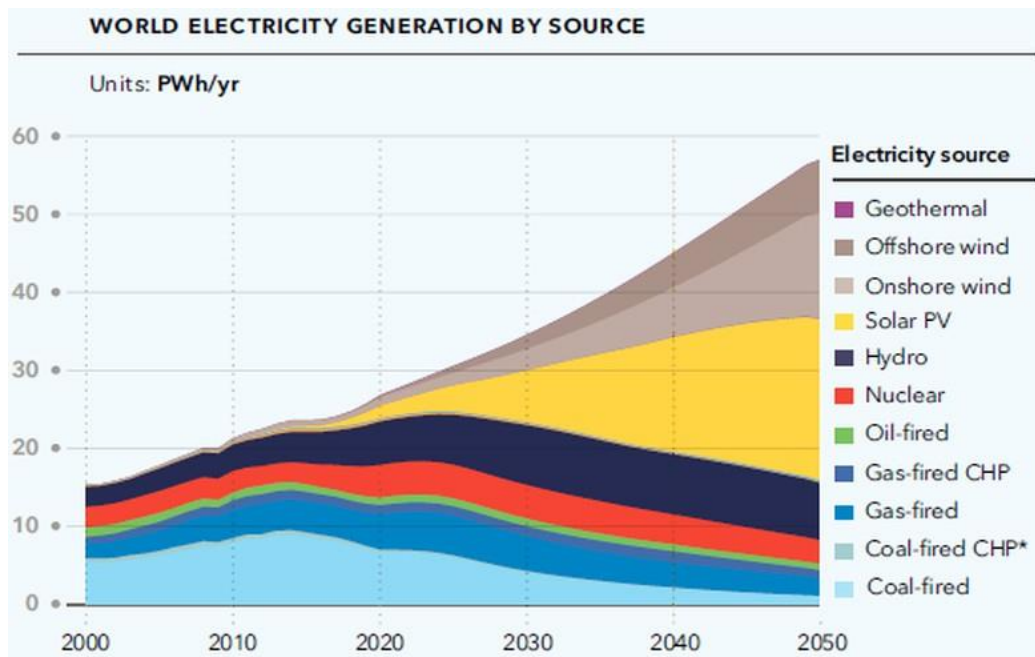


Figure 3 Expected electricity production distribution up to 2050 [21].

The direct environmental impact, instead, is related to the release into the environment of fluorinated gases typically used as working fluids in vapor compression cycles. As a matter of fact, the majority of the refrigerants employed are hydrofluorocarbons (HFCs), extremely harmful with respect to the global warming, having a GWP (Global Warming

Potential) significantly higher than CO₂. The GWP value of some of the most widespread refrigerants is reported in Figure 4, as provided by [22].

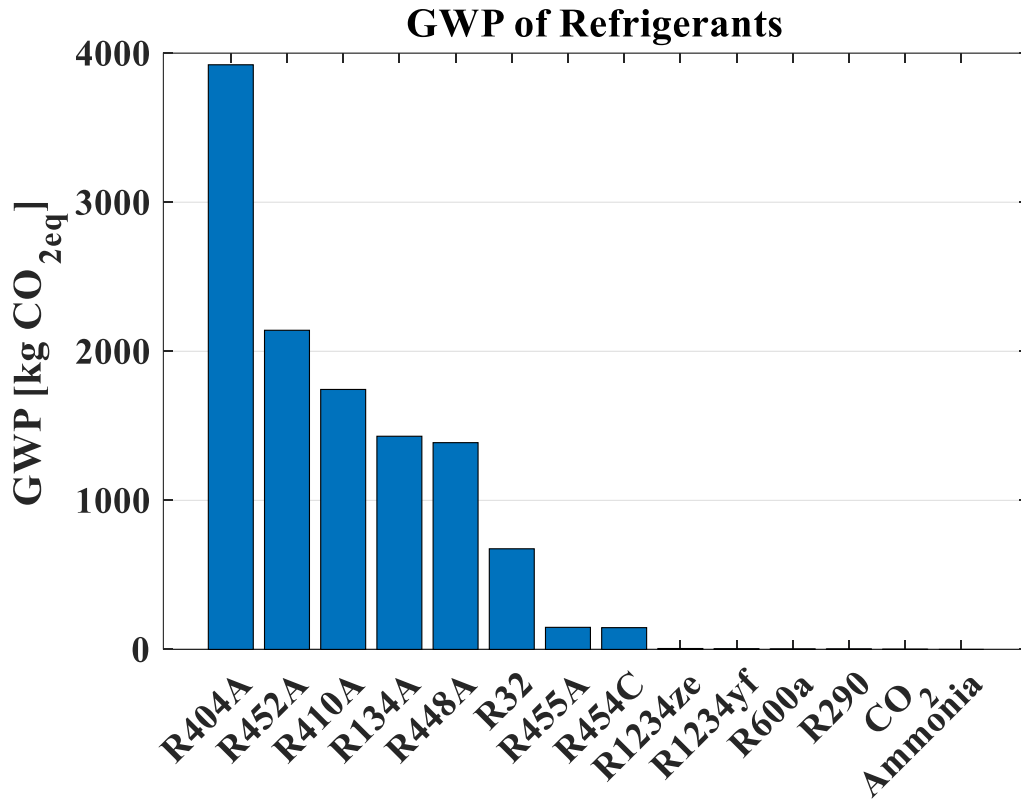


Figure 4 GWP values of several refrigerants [22].

According to [23], over the last 20 years, HFC emissions are responsible for 2% of the total GHG emissions. Without any interventions HFC emissions are predicted to increase dramatically by 2050 [24], as shown in Figure 5, accounting for a share between the 10 and the 19% of the total GHG emissions. Following the business-as-usual scenarios only the emissions of HFC would contribute to raise the global surface temperature up 0.5°C by 2100, whereas policies aimed to reduce the use of high GWP refrigerants could contain the HFC contribution to global temperature rise to 0.06°C, avoiding 53 GtCO₂ emissions by 2060 [25].

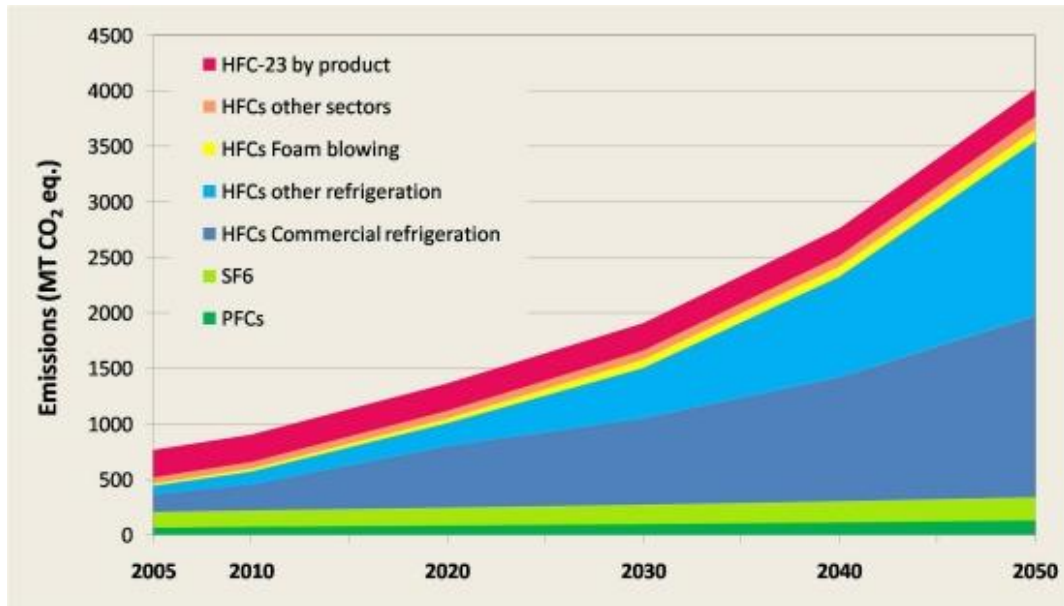


Figure 5 HFC emissions between 2005 and 2050 according to the business-as-usual scenario [24].

1.3 Measures to limit the environmental impact

1.3.1 Policies to reduce the indirect environmental impact

In the previous paragraph, it has been clarified that the indirect environmental impact of vapor compression cycles is related to GHG emissions caused by the electricity production. Consequently, the first countermeasure to pursue its reduction should be the increase of electricity production by means renewable sources. However, this aspect does not relate to vapor compression cycles, thus is not the object of this thesis. Therefore, in this work only the measures acting directly on VCC to reduce their indirect environmental impact are analysed.

The first solution is to increase the efficiency of the components and of the whole system to reduce the energy consumption. For these reasons Minimum Energy Performance Standards (MEPS) have been introduced by several regulations to set the minimum allowed performance of refrigeration and air conditioning equipment. In this regard, the European Union introduced the regulation Eco-Design [11], establishing a framework for the setting of ecodesign requirements for energy-related products, such as heating and cooling products, high temperature process chiller and fan coil units. Particularly, for each product released on the market by 1 January 2018 is provided the minimum seasonal energy efficiency threshold allowed.

These policies are coupled with labelling programmes aiming to promote the sale of energy-efficient technologies, having the purpose to inform the customer about the energy class of the product. In this regard, the EU introduced the Regulation (EU) 2017/1369 [26], then updated with the Regulation EU 2021/340 [27], aiming to classify the energy efficiency of several products. An example of energy label for refrigerating appliances is given in Figure 6.

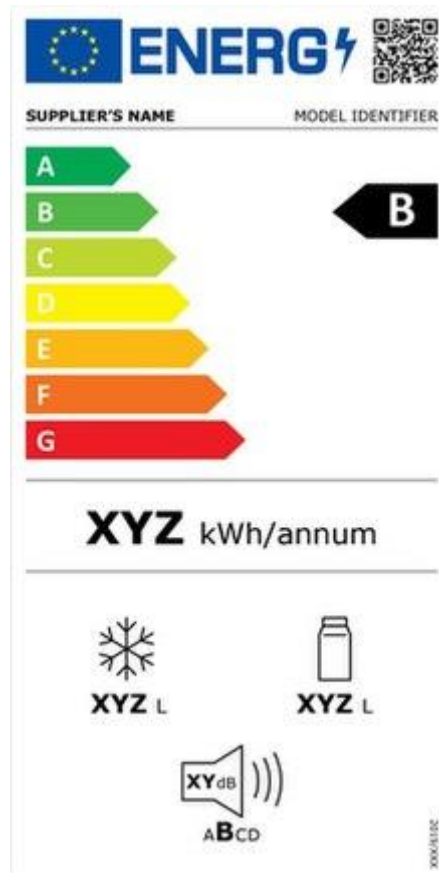


Figure 6 Label for refrigerating appliances according to [27].

A further possibility is to develop innovative systems that allows the cold production in an eco-friendly way. For these reasons are more and more widespread heating and cooling systems driven by means renewable sources, such as thermally driven cooling technologies employing solar energy, geothermal energy or waste heat.

However, the aforementioned countermeasures, both at component and at system level, need a careful assessment in order to evaluate their thermodynamic performance and the effectiveness from the economic point of view compared with more widespread and already mature technologies and plant schemes.

1.3.2 Policies to reduce the direct environmental impact

The Montreal Protocol [28] ratified by 197 nations in 1987 planned the gradual phase-out of CFC and HCFC refrigerants due to their contribution to the destruction of the ozone layer. Consequently, HFC refrigerants were introduced, but their huge GWP contributes to the Earth surface temperature rise. For these reasons, in 2019 became effective the Kigali Amendment to the Montreal Protocol [9], with the aim to achieve over an 80% reduction in projected HFC production and consumption by 2047, as reported in Figure 7.

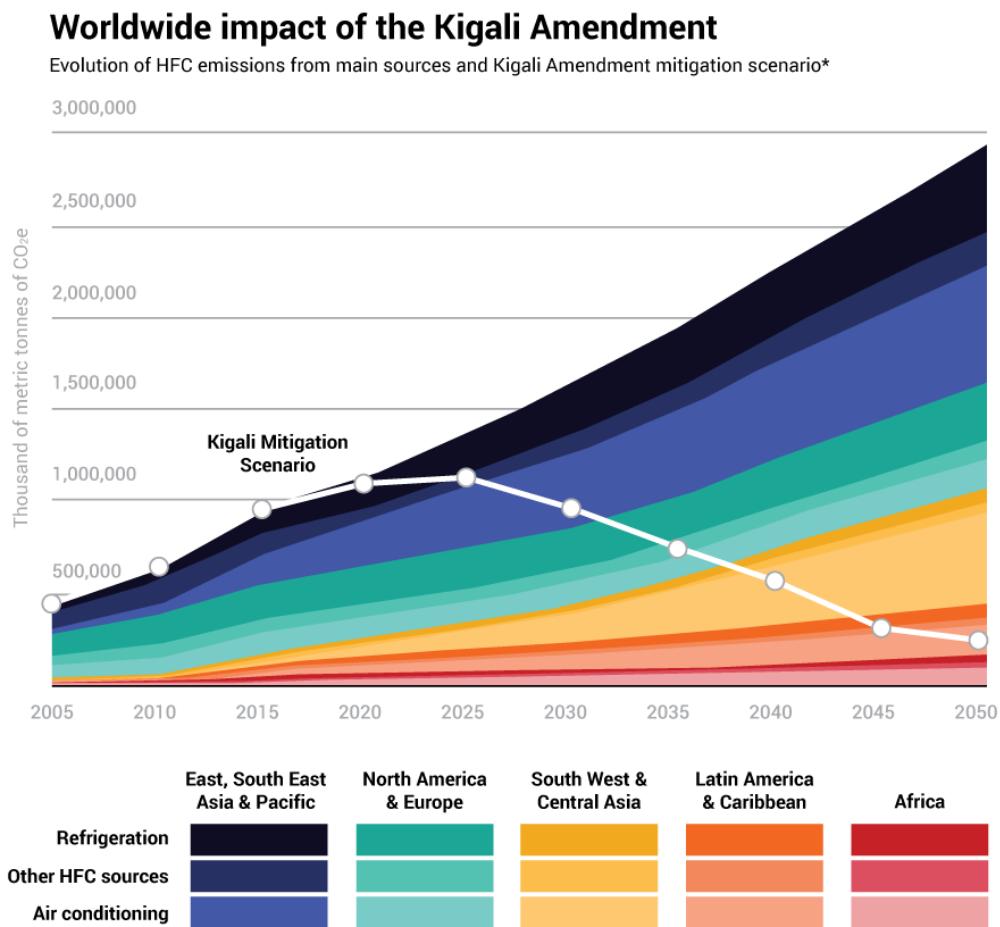


Figure 7 Comparison of HFC emissions trends with the Kigali Amendment and following the business-as-usual scenario [24].

According to the Kigali Amendment the most developed countries began to reduce the HFC consumption in 2019, while for the majority of the developing countries the phase down will begin in 2024. Other developing countries, especially those susceptible to high

ambient temperatures will freeze the HFC production and consumption in 2028, whereas will be allowed to begin the phase down in 2032. In Figure 8 the roadmap established by the Kigali Amendment is shown.

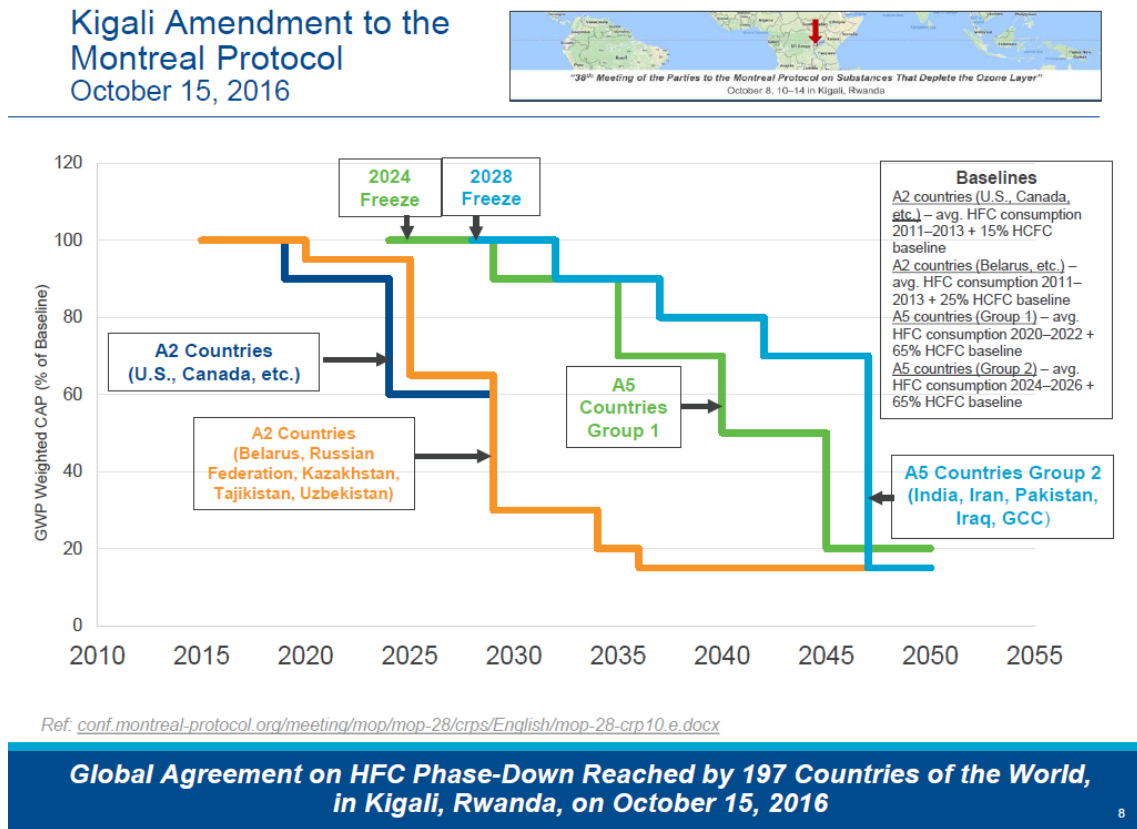


Figure 8 HFCs phase-down schedule according to Kigali Amendment [9].

In this framework, the European Union enacted the regulation 517/2014 [10], the F-gas regulation, with the purpose to limit the production and consumption of HFC substances at European level, aiming to achieve within 2030, a reduction of 79% of HFCs manufactured, imported and commercialized compared to the level between 2009 and 2012 in all the European countries. To pursue this goal the F-gas regulation sets limits on the GWP value for the fluids that are approved depending on the application.

To meet the Kigali Amendment and F-gas requirements the adoption of low-GWP mixtures and natural refrigerants, such as hydrocarbons and Ammonia, will be more and more widespread. However, refrigerants blends have different thermodynamic characteristics (such as a not negligible temperature glide in several cases), while hydrocarbons are highly flammable (A3 refrigerants according to ASHRAE Standard 34

[29]) and ammonia is toxic (B2L in the AHSRAE classification), leading to security issues that limits the refrigerants charge and them room of use in several applications. Consequently, in some cases, a redesign of the whole plant is needed, being not feasible the use of drop-in solutions. In Figure 9 is reported the GWP versus density of several refrigerants, showing the possible low-GWP alternatives for each category, highlighting also the ASHRAE security class [29].

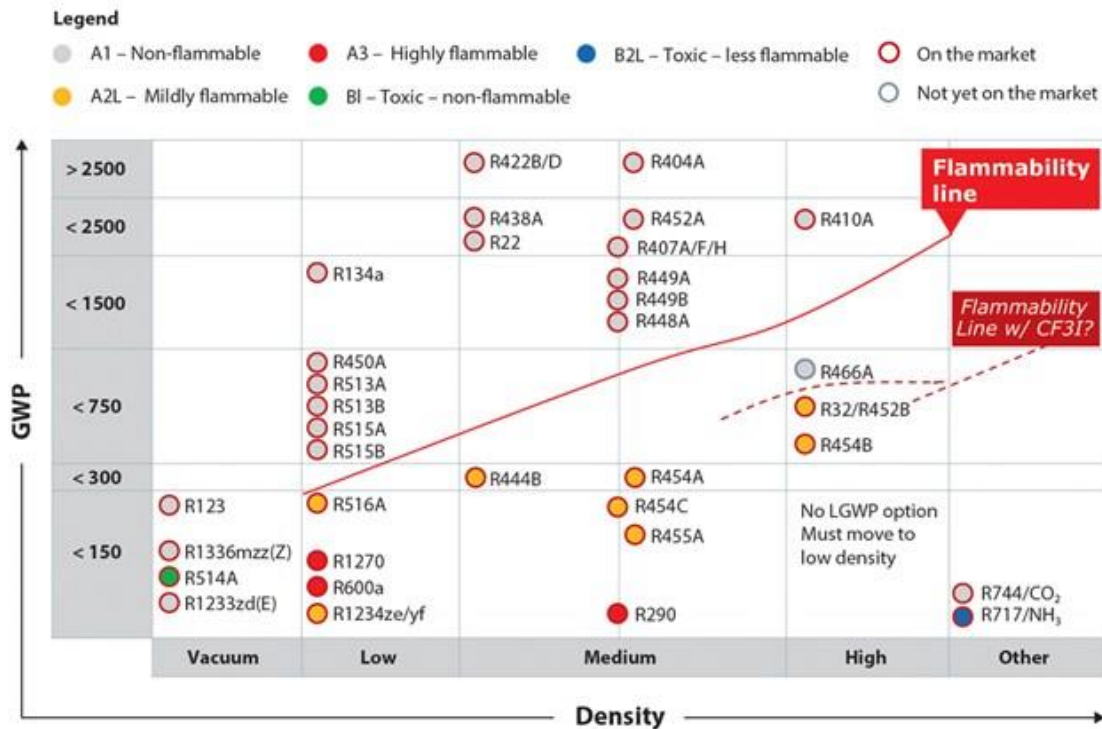


Figure 9 GWP of several refrigerants as a function of the density.

PART 1

INNOVATIONS REALATED TO COMPONENTS: LINEAR COMPRESSORS FOR DOMESTIC REFRIGERATION

2. Thermo-economical sensitivity analysis of a linear compressor for domestic refrigeration

This chapter focuses on the innovations at component levels, analysing a novel kind of compressor for household refrigeration, namely the linear compressor. As a matter of fact, to reduce the energetic consumption in this sector is fundamental to improve the compressor efficiency, which is a critical component in the domestic refrigerator, whose consumption accounts for almost the 6% of the total electricity consumption around the world [30, 31], and could contribute to a better regulation of the temperature inside the cabinet allowing to reduce food waste occurring at domestic levels, that nowadays contributes to the 25% of the total food waste [32]. Since the room for improvement of the traditional reciprocating compressor is limited, the research is currently focusing on linear compressors. Firstly, a detailed model of the compressor is developed, with the aim to design a compressor for a domestic refrigerator having a cooling capacity of 200 W. The main geometrical and design parameters have been identified and their influence on the global and volumetric efficiency and costs is evaluated by means of a sensitivity analysis, comparing the solutions investigated to the traditional reciprocating technology currently available on the market. The same outcomes have been published in [33].

2.1 Linear compressor state of the art

The linear compressor is a new typology of reciprocating compressor in which the crank mechanism is replaced by a linear motor, which provides the reciprocating motion to the piston by means of an alternating magnetic field, which causes a reciprocating force that acts on a moving magnet directly connected to the piston, finally generating the reciprocating motion. With only one point of friction, between the piston and the cylinder, the friction losses are remarkably reduced with respect to the conventional reciprocating compressor, having four friction points. Consequently, oil-free operations and a continuous regulation of the cooling capacity via the stroke variation (depending on the force balance acting on the piston) are possible with this compressor, which is shown in Figure 10.



Figure 10 LG linear compressor.

The linear compressor, whose schematic representation is shown in Figure 11, is a reciprocating compressor differing from the traditional one in the way the motion is provided to the piston. As a matter of fact, it is driven by a linear motor, that replaces the crank mechanism, creating an alternating magnetic field and thus a reciprocating force acting on a moving magnet connected directly to the piston. For this reason, there is only one friction point (between the piston and the cylinder), that allows to oil-free operation, eliminating all the issues related to the discharge temperature, the compatibility between refrigerant and lubricant, widening the choice of the working fluid, and avoiding the need for oil separation and return. The balance of the several forces acting on the piston directly influences the linear compressor stroke, that is therefore variable with the operating conditions. Consequently, by changing the excitation voltage, the stroke will be accordingly adjusted. The suction valve is sited on the piston, reducing the required dead volume. The non-linear force relating to the gas in the compression chamber could cause the piston to oscillate unsteadily, making it challenging to regulate the compressor operation. In order to ensure little variation in the resonant frequency, which must be near to the operating frequency, it is necessary to use a mechanical spring whose stiffness is significantly higher than the gas equivalent one.

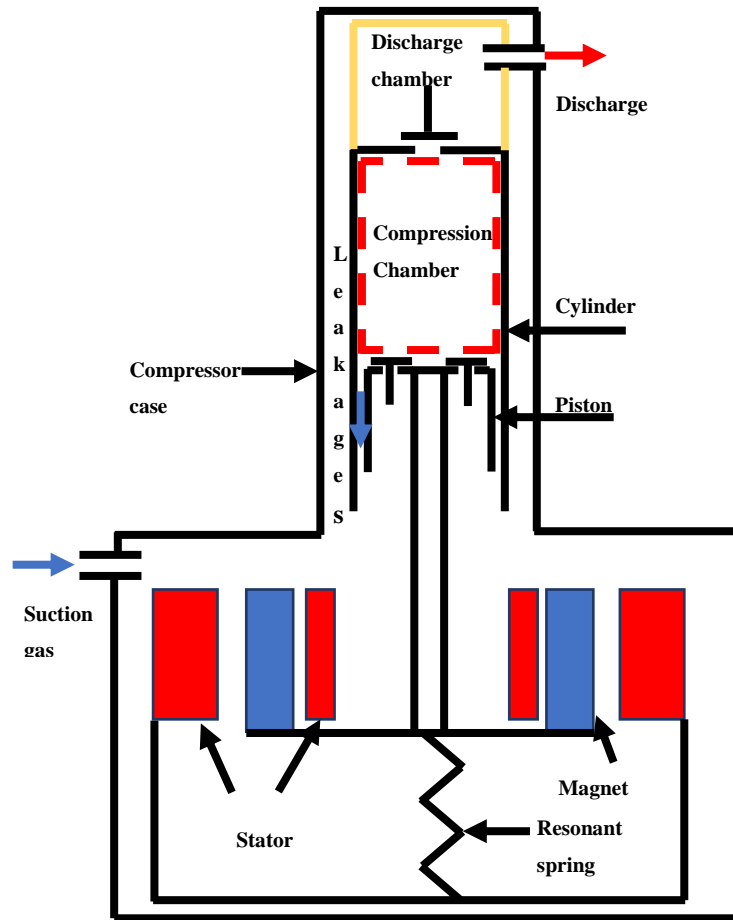


Figure 11 Schematic diagram of the linear compressor.

Liang [34] conducted a review of the scientific literature about linear compressor, pointing out that the possibility of oil-free operation makes it not necessary the presence of components for the lubricant separation and improves the performance of the whole system since the absence of oil increases the heat transfer performances enabling the use of smaller heat exchangers. Consequently, the possibility to reduce the plant size and thus a reduced refrigerant charge, facilitating the adoption of flammable fluids with lower GWP, as required by the F-Gas Regulation [10]. However, the author highlighted also that the main issue related to this emerging technology are the higher costs compared to the conventional reciprocating compressor and their limited potential for usage in larger applications, including air conditioning.

Several works in the scientific literature have presented and studied the linear compressor technology with both numerical and experimental approaches.

In the work of Park et al. [35] the losses of a linear motor and those of a rotary induction motor are experimentally compared, pointing out that the linear compressor achieved a 20-30% higher efficiency than the conventional reciprocating compressor driven by a rotary induction motor. Bijanzad et al. [36] measured a very high electrical efficiency, equal to 87%. Comparable findings were obtained by Lamantia et al. [37], who attributed the better performance of the linear compressor to the lower friction losses.

Chen et al. [38] built a prototype of a linear compressor having a mechanical efficiency 11.4% higher than the traditional reciprocating technology.

Jomde et al. [39] presented a numerical model for the linear compressor, validated with experimental data using a R134a prototype. The experimental data pointed out that the power consumption and cooling capacity of the linear compressor were respectively 33% and 8.9% lower than those of the system with reciprocating compressor, resulting in a COP increase of 18.6%. Also, Bradshaw et al. [40] developed and validated a comprehensive model for a miniature linear compressor. Subsequently, they compared the linear and the reciprocating compressor [41], underlining the possibility of the new technology to operate with higher efficiencies in a wider range of dead volume.

Since the linear compressor is a technology recently introduced, it is still open to improvement and optimization, as underlined by Walt and Under [42], which performed a numerical work aiming to analyse the possibility to reduce the friction losses between piston and cylinder.

Liang et al. [43] designed and tested a new kind of oil-free moving magnet linear compressor having clearance seals and flexure springs. The compressor was embedded in a vapor compression refrigeration system using R134a as refrigerant, resulting in a COP of 3.2, giving a cooling capacity of 384 W for a pressure ratio of about 2.5. Moreover, they emphasized the importance to operate in resonant conditions, since a 5% change of drive frequency respect to the resonance value caused a decrease of COP of 12%. Also in Zhu et al. [44] is highlighted the influence of the operating frequency on linear compressor performance, since they experimented lower consumption during resonant operation. Furthermore, they focused on one of the key aspects of the linear compressor, being the capacity modulation by varying the stroke. Particularly, they

noticed that by increasing the stroke by 1 mm, the cooling capacity was enhanced from 130 W up to 210 W, for a pressure ratio of 3.

A similar outcome was reached with numerical models [45], pointing out also a COP enhancement from 2.2 up to 2.7 with increasing the available stroke from 10 to 14 mm. The same research group [46] carried out a thermo-economic-environmental analysis of a domestic refrigerator using a linear compressor. The results show that the power consumption can be reduced thanks to the possibility given by the linear compressor to regulate the stroke at partial load. Particularly, the desired value of the stroke can be set by means stroke controllers, which change the required load according to the ambient temperature variation, and thus to the required cooling load. Also Kim et al. [47, 48] focused the attention on the stroke tuning, and developed a linear compressor able to modulate its capacity from 55 to 90% without requiring stroke controllers, over an ambient temperature range between 5 and 43 °C.

Another critical aspect that influences the performance of the linear compressor is the coupling between the mechanical and the electrical part. This issue was investigated by Zhang et al. [49], that developed a comprehensive model able to predict both the steady-state and the transient operation of the compressor. You et al. [50] focused on the reduction of the input power by looking for an expression of the stroke amplitude based on different parameters. Li et al. [51] studied the possibility to employ a linear compressor using low GWP refrigerants, focusing the attention on the development of an optimization method to improve the capacity-modulation performance. In particular, they found out that the piston diameter has a great effect on the capacity modulation, and the optimal value ranges from 28 to 32 mm. Subsequently, taking into account the optimization analysis, a prototype was developed, obtaining variations of the cooling capacity between 583.8 W and 1628.6 W, with a maximum COP value of 4.25.

2.2 Objective of the study

From the scientific literature analysis, it is evident that, despite a large number of works, both numerical and experimental, dealing with linear compressor in small-size refrigeration units for domestic refrigerator, lacks a detailed analysis aiming to find and to optimize the major geometrical parameters affecting the compressor cost and efficiency. Consequently, in the present chapter of the thesis a thermo-economic analysis

of a linear compressor is performed. Particularly, a detailed compressor model has been implemented aiming to design a compressor for household refrigerators, using R600a as working fluid and having a cooling capacity of 200 W. The main geometrical and design parameters have been identified to quantify those with the highest impact on compressor performance and cost. Afterward, the model is run to carry out a sensitivity analysis to provide a guideline for compressor manufactures and looking for the optimal design. Finally, a thermo-economic comparison, in terms of performance and set-up cost, between all the configurations designed and those available on the market is proposed.

2.3 Linear compressor model

The compressor is modelled following the approach of Bradshaw et al. [40]. The refrigerant thermodynamic state is evaluated by means of energy and mass conservation equations applied over a control volume that contains the compression chamber. Then, the compressor is solved coupling different sub-models, involving the description of the piston dynamics, the flow through the valves, the leakage across the gap between the piston and the cylinder and the heat transfer through the cylinder. The modelling of the linear motor is not considered in the present work since it is outside the scope of the research. All the equations that will be shown are solved in MATLAB [52] environment, and the refrigerant thermodynamic properties are evaluated using the software Refprop 9.1 [53], developed by NIST.

2.4.1 Energy and mass conservation equations

The energy and mass conservation laws are given in Eqs. (1)-(2) under the hypothesis of isentropic process and by neglecting the kinetic and potential terms. They allow the determination of the refrigerant thermodynamic conditions once solved for temperature and density.

$$\frac{dT}{dt} = \frac{\left[T \cdot \frac{\partial P}{\partial T} \cdot \left(\frac{1}{\rho} \cdot \frac{dm}{dt} - \frac{dV}{dt} \right) - \left(\frac{dm}{dt} \cdot i_{cv} \right) - \left(\frac{dm_{dis}}{dt} \cdot i_{cv} \right) + \left(\frac{dm_{suc}}{dt} \cdot i_{in} \right) + \dot{Q} \right]}{m \cdot c_v} \quad (2.1)$$

$$\frac{dm}{dt} = \frac{dm_{in}}{dt} - \frac{dm_{out}}{dt} - \frac{dm_{leak}}{dt} \quad (2.2)$$

$$\frac{dm_{cv}}{dt} = \frac{d(\rho \cdot V)}{dt} = \rho \cdot \frac{dV}{dt} + V \cdot \frac{d\rho}{dt} \quad (2.3)$$

2.3.2 Piston dynamics

To solve the main equations, is required the determination of $dV \cdot dt$ related to the piston dynamics. The piston is modelled as a two-degree of freedom vibration system, as shown in Figure 12, by considering the unwanted piston rotation due to the eccentricity of the application point of the elastic force, depending on the eccentricity of the spring assembling.

$$m_p \cdot \ddot{x}_p + c_{fric} \cdot \dot{x}_p + K_{mech} \cdot x_p + F_{gas} = K_{mech} \cdot \theta_p \cdot \epsilon + I \cdot \alpha \quad (2.4)$$

$$J_p \cdot \ddot{\theta}_p + K_{mech} \cdot \theta_p \cdot \epsilon^2 = K_{mech} \cdot x_p \cdot \epsilon \quad (2.5)$$

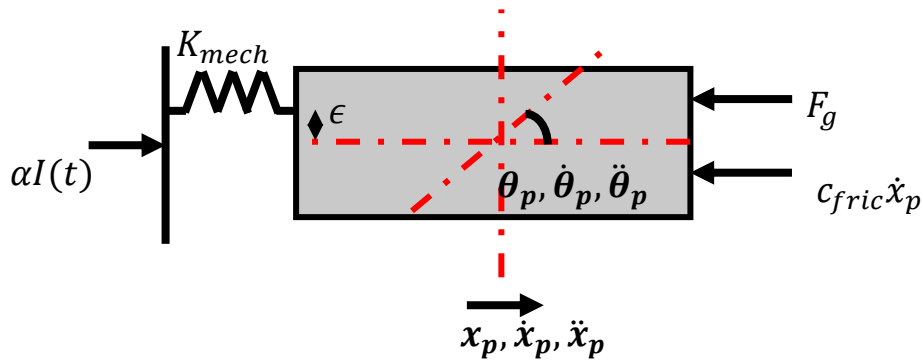


Figure 12 Schematic representation of the piston as a two-degree of freedom vibration system.

In the previous equations, the terms \ddot{x}_p , \dot{x}_p , x_p and $\ddot{\theta}_p$, θ_p are related, respectively, to the reciprocating motion and the piston rotation; m_p is the piston mass; c_{fric} is the damping coefficient associated with the frictional forces due to the accidental contact between the piston and the cylinder; k_{mech} is the mechanical spring stiffness; F_{gas} is the total force applied to the piston by the gas in the compression chamber; ϵ is the spring eccentricity; $I\alpha$ is the driving force, resulting in the product between the current intensity I and the linear motor factor, α ; J_p is the piston rotational moment of inertia. The total gas force is given in Eq. (2.6):

$$F_{gas} = k_{gas} \cdot x_p + c_{gas} \cdot \dot{x}_p \quad (2.6)$$

k_{gas} and c_{gas} are, respectively, the equivalent stiffness and damping coefficient, and their formulation is the following:

$$k_{gas} = \frac{(P_{dis} - P_{suc}) \cdot A_p}{S} \quad (2.7)$$

$$c_{gas} = \frac{W_{gas}}{\pi \cdot \omega_{res} \cdot x_p^2} \quad (2.8)$$

where P_{dis} and P_{suc} are the discharge and the suction pressure; A_p is the piston surface and S is the stroke; ω_{res} is the resonant pulsation of the system (considering an operating frequency of 50 Hz). W_{gas} is the work on the gas evaluated by assuming a polytropic compression and expansion.

$$W_{gas} = \gamma \cdot P_{suc} \cdot \frac{V}{\gamma - 1} \cdot \left(\frac{P_{dis}}{P_{suc}} - 1 \right) \quad (2.9)$$

The damping coefficient generated by the friction force is evaluated as reported in the next equation:

$$c_{fric} = \frac{4 \cdot f \cdot N}{\omega_n \cdot x_p^2 \cdot \pi} \quad (2.10)$$

N is the normal force caused by the contact between piston and cylinder, determined by:

$$N = \frac{1}{S} \cdot [K_{mech} \cdot (x_p(t_i) - \epsilon \cdot \theta(t_i)) \cdot \epsilon] \quad (2.11)$$

and t_i is the time instant when the contact piston-cylinder occurs.

Finally, the following vibration parameters are derived:

$$\omega_{res} = \omega_n \cdot \sqrt{1 - \xi^2} \quad (2.12)$$

$$\xi = \frac{c_{fric} + c_{gas}}{2 \cdot m_p \cdot \omega_n} \quad (2.13)$$

$$\omega_n = \sqrt{\frac{K_{tot}}{m_p}} \quad (2.14)$$

$$K_{tot} = K_{mech} + K_{gas} \quad (2.15)$$

where ξ is the system damping ratio.

2.3.3 Friction losses

As described by Zhang et al. in [49], the friction between the piston and the cylinder is due to two different issues: the eccentricity in the spring assembly and the piston rod elasticity. In this study, only the first term is accounted. It is related with the spring geometry and arrangement. As a matter of fact, employing a single spring can result in an eccentricity of the elastic force respect to the piston center of mass, bringing to an undesired rotation around its axis, as described in equation (2.5). Particularly, rotations higher than the clearance gap determine a contact between the piston and the cylinder with a huge increase in frictional losses and the possibility to cause irreversible damages to the compressor. The piston rotation and the normal contact force are obtained in the previous sections, by means of Equations (2.5) and (2.11). The power loss for friction is calculated by Equation (2.16):

$$\dot{W}_{fric} = f \cdot N \cdot \dot{x}_p \quad (2.16)$$

being f the dry friction coefficient, which is related to the material constituting the piston and the cylinder and the coating eventually adopted on the piston. This issue may be avoided by means of a multiple springs system, by splitting the total stiffness on more springs to have a resultant force applied to the piston center of mass. However, the adoption of this solution is not always possible or affordable due to the small dimension of the system.

2.3.4 Leakages

A gap between piston and cylinder is needed to avoid friction, causing refrigerant leakages from the compression chamber. According to the approach of Zhang et al. [54] the leakage flow has been modelled as a 1-D lubrication film, that allows the computation

of pressure distribution inside the gas film along the piston length, and thus the leakage mass flow rate as follows:

$$\dot{m}_{leak} = \int_0^{Time} \frac{\rho \cdot g^3}{12 \cdot \zeta} \cdot \left(\frac{\delta P}{\delta L_p} \right) + \frac{\rho \cdot g \cdot \dot{x}_p}{2} dt \quad (2.17)$$

where *Time* is the period of piston displacement, ρ and ζ are respectively gas density and viscosity, g is the clearance gap; $\delta P \cdot \delta L_p^{-1}$ is the pressure gradient in the clearance gap along the piston length, L_p , and \dot{x}_p is the piston velocity.

2.3.5 Valve dynamics

The gas flow through the valves is assumed to be isentropic and compressible, thus the mass flow rate can be evaluated as follows:

$$\dot{m}_{valve} = A_{flow} \sqrt{2 \cdot \rho_{high} \cdot P_{high} \cdot \left(\frac{\gamma}{\gamma - 1} \right) \cdot \left(\frac{P_{low}}{P_{high}} \right)^{\frac{2}{\gamma}} - \left(\frac{P_{low}}{P_{high}} \right)^{\frac{\gamma+1}{\gamma}}} \quad (2.18)$$

The subscripts high and low are related, respectively, to the high and low side pressures of the valve. A_{flow} is the area available for the gas passage through the valves, depending on the valves motion, since they do not open instantaneously. In this study the plate valves are considered, and there are modeled as a mass-spring system with one degree of freedom. Particularly, two alternative valves behavior can be identified: first, in the pressure force dominant region, the main driving force that leads to the valve motion is the pressure difference; then, in the mass flux dominant region, the mass flux force is dominant and the valve motion is controlled by the movement of the fluid and the pressures on the two sides of the valve reach the same value. The equations describing the two regimes are, respectively, Eq. (2.19) and Eq. (2.20):

$$m_{valve} \cdot \ddot{x}_{valve}(t) + K_{valve} \cdot x_{valve} = (P_{high} - P_{low}) \cdot A_{valve} + C_d \cdot \frac{1}{2} \cdot \rho_{gas} \cdot V_{gas}^2 \cdot A_{valve} \quad (2.19)$$

$$\begin{aligned}
m_{valve} \cdot \ddot{x}_{valve}(t) + K_{valve} \cdot x_{valve} \\
= \rho_{gas} \cdot (V_{gas} - \dot{x}_{valve}(t))^2 \cdot A_{port} + C_d \cdot \frac{1}{2} \cdot \rho_{gas} \cdot V_{gas}^2 \cdot A_{valve}
\end{aligned} \tag{2.20}$$

where m_{valve} is the valve mass, \ddot{x}_{valve} , \dot{x}_{valve} and x_{valve} are valve acceleration, velocity and position, k_{valve} is the equivalent stiffness, A_{valve} and A_{port} are the valve area and the valve opening area, C_d is the drag coefficient. The transition between the two regimes occurs when the valve lift reaches the subsequent value:

$$x_{tr} = \frac{1}{4} \cdot \frac{D_{port}^2}{D_{valve}} \tag{2.21}$$

2.3.6 Heat transfer model

The heat transfer through the cylinder is modeled following the same approach of Zhang et al. [49]

$$\dot{Q} = \frac{(T_{ref} - T_{amb})}{R_{conv}} \tag{2.22}$$

where R_{conv} is the convective resistance associated with the gas inside the compression chamber and T_{ref} and T_{amb} are respectively the refrigerant and ambient temperatures.

$$R_{conv} = \frac{1}{h \cdot A_{cyl}} \tag{2.23}$$

The heat transfer coefficient h is calculated by means the Adair et al. [55] correlation as follows:

$$Nu = \frac{h \cdot D_p}{\lambda} = 0.053 \cdot \frac{\lambda}{D_h} \cdot Re^{0.8} \cdot Pr^{0.6} \tag{2.24}$$

The other thermal resistances, namely the convective resistance of the ambient air and the conductive resistance, are neglected in the present work.

2.3.7 Linear compressor global and volumetric efficiency

The compressor global efficiency is defined as the ratio between the ideal isentropic power required by the compressor and the effective electric power needed, which is higher due to all the losses analyzed in the previous paragraph. Regarding the electric motor, it has been considered a constant efficiency equal to 0.9.

$$\eta_g = \frac{\dot{W}_{is}}{\dot{W}_{tot}} \cdot \eta_{el} \quad (2.25)$$

where the isentropic power is given by:

$$\dot{W}_{is} = \oint P_{is} dV \quad (2.26)$$

The total power required by the compressors is:

$$\dot{W}_{tot} = \dot{W}_{ind} + \dot{W}_{leak} + \dot{W}_{fric} \quad (2.27)$$

The indicated power is the given integrated pressure along the volume:

$$\dot{W}_{ind} = \oint P_{ind} dV \quad (2.28)$$

This term differs from the isentropic power due to the pressure peaks during the suction and the discharge phases.

Then the power loss due to the leakages is:

$$\dot{W}_{leak} = \dot{m}_{leak} \cdot (i_{cc} - i_{suc}) \quad (2.29)$$

Being i_{cc} and i_{suc} the specific enthalpies in the compression chamber and in the suction section. The power related to the friction loss is given by Equation (2.16).

The compressor volumetric efficiency is the ratio between the actual discharge mass flux and the theoretical mass flux elaborated by the compressor. The differences between the two values depend on the leakages between the piston and the cylinder, and the re-expansion of the gas due to the presence of the dead volume.

$$\eta_v = \frac{\dot{m}_{calc}}{\dot{m}_{theor}} \quad (2.30)$$

$$\dot{m}_{theor} = \rho_{suc} \cdot V_{tot} \cdot f_{res} \quad (2.31)$$

2.3.8 Computational procedure

All the equations previously described need to be solved simultaneously. Particularly, the compression process is divided into small time-steps and each differential equation is solved with an Eulerian method.

The main steps constituting the resolution algorithm are the subsequent:

1. The input parameters, in terms of compressor geometrical features, and the boundary conditions, namely the suction temperature and pressure, the discharge pressure and the ambient temperature are given.
2. A first attempt natural frequency of the compressor is guessed, corresponding to the value calculated with Eqs. (2.10)-(2.15) assuming no rotation of the piston.
3. Eqs. (2.4)-(2.5) allow to solve the piston motion for each time step.
4. The gas thermodynamic state inside the chamber is solved by means of the remaining equations of the model.
5. When the entire compression cycle is solved, the natural frequency of the system is calculated again and compared to the guessed value, which is updated, by considering also the corresponding rotation. Steps 3-5 are repeated until convergence.
6. After convergence, the global and the volumetric efficiencies are evaluated by means of Eqs. (2.25)-(2.31).

Figure 13 shows the Pressure-Volume diagram obtained by solving the complete set of equations. Particularly, the refrigerant employed is R600a, the suction temperature and pressure are, respectively, 8°C and 1.5 bar and the discharge pressure is set at 5.6 bar.

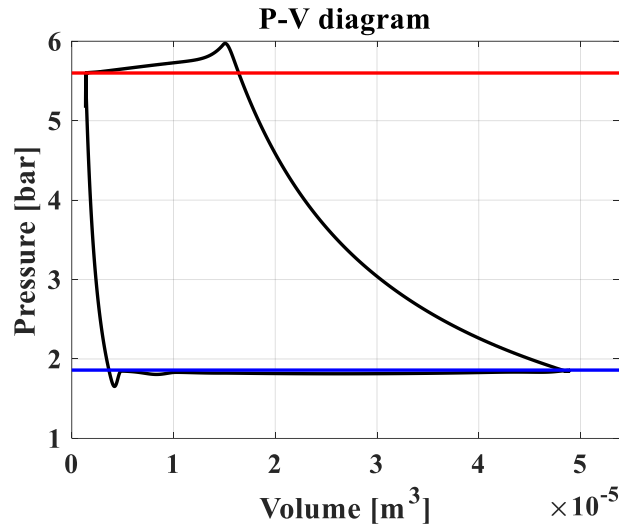


Figure 13 Example of the simulated p-V diagram, for refrigerant R600a, suction temperature and pressure respectively equal to 8°C and 1.5 bar, and the discharge pressure set to 5.6 bar.

2.3.9 Model validation

Despite in the original reference [40] the model was already validated with satisfactory results, due to the introduction of new terms, such as the evaluation of the leakages and the heat transfer, a new validation is here carried out by collecting independent experimental data from the literature [56]. The comparison between the experimental and the calculated global efficiency and mass flow rate is shown in Figure 14, where the *MAPE*, calculated as follows, is reported:

$$ER_i = \frac{\eta_{cal} - \eta_{exp,i}}{\eta_{exp,i}} \cdot 100 \quad (2.32)$$

$$MAPE = \frac{1}{n} \sum_{i=1}^n |ER|_i \quad (2.33)$$

The calculated Mean Absolute Percentage Error (*MAPE*) is equal to 9.10% as concerns the global efficiency and 10.57 % for the mass flow rate. Consequently, the agreement between the model and the experimental data can be considered acceptable.

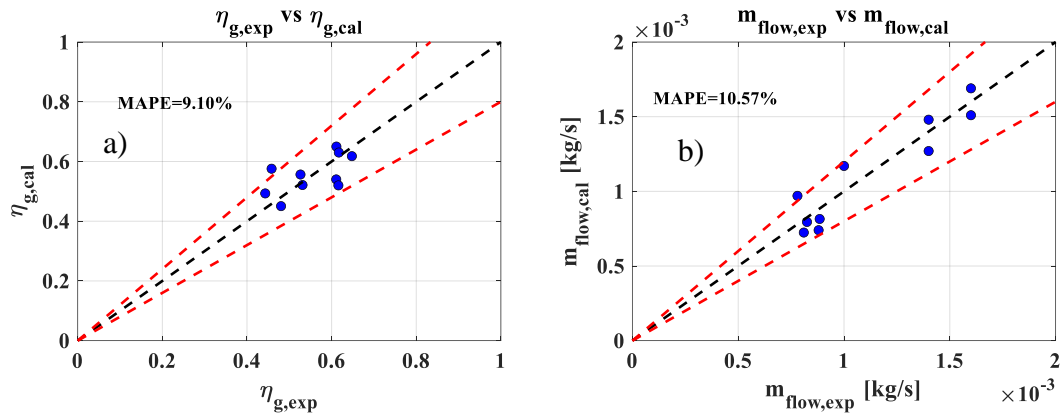


Figure 14 Model validation. a) Calculated vs. experimental overall efficiency. b) Calculated vs. experimental mass flow rate.

2.4 Sensitivity analysis and thermo-economic comparison

The model is employed to carry out a multivariate sensitivity analysis on the linear compressor main design parameters, with the scope to investigate and to quantify the influence of each of them on the compressor cost and efficiencies, both global and volumetric. The intervals considered for each independent variable examined in the sensitivity analysis are shown in Table 1. Each of them is varied in a wide range compared to the typical values reported in scientific literature, resulting in over 20000 combinations.

Table 1 Independent variables analysed and their variation range.

Independent variable	Range	Independent variable	Range
Piston stroke [m]	0.01 – 0.055	$\frac{D_{suction, valve}}{D_{piston}}$	0.5 - 0.9
Piston diameter [m]	0.02 – 0.06	$\frac{D_{discharge, valve}}{D_{piston}}$	0.5 – 0.9
Stroke length occupied by the dead volume	$0.1 \cdot 10^{-3}$ – $0.1 \cdot 10^{-5}$	Gap [m]	$1 \cdot 10^{-6}$ – $2 \cdot 10^{-5}$
Dry friction coefficient	0.1 – 0.6	Eccentricity [m]	$1 \cdot 10^{-4}$ – $5 \cdot 10^{-3}$

Table 2 shows the boundary conditions, selected according to what prescribed by the normative ASHRAE 23 [57] for household refrigerator test, along with the values chosen for the design parameters that are not the object of the sensitivity analysis. The cooling power is set to 200 W for all the simulations performed, and all solutions not complying with the required cooling load are automatically discarded.

Table 2 Boundary conditions and input parameter adopted in the simulations.

Parameter	Value	Parameter	Value
T _{ev} [°C]	-23.3	T _{amb} [°C]	25
T _{co} [°C]	54.4	Working fluid	R600a
T _{sh} [°C]	32.2	Valve drag coefficient	1.17
T _{sub} [°C]	32.2	Valve thickness [mm]	0.15
Frequency [Hz]	50	Valve Length [mm]	18

In the present work the influence of each independent variable on the compressor design is quantified by means of two statistic parameters, namely the Spearman rank correlation coefficient and the Mann-Kendall correlation coefficient, both widely used when the correlation between the independent and dependent variables are monotone but not linear. The first is defined as follows:

$$\varphi = \frac{cov(RX_i, RY_i)}{\sigma_{RX_i} \sigma_{RY_i}} \quad (2.34)$$

Being RX_i and RY_i the ranked variables, while σ_{RX_i} and σ_{RY_i} are the standard deviations of the ranked variable. X and Y, denote, respectively, the independent and the dependent variable. The Mann-Kendall coefficient, instead, represents the ratio between the difference of concordant and discordant pairs and the total number of pairs:

$$\tau = \frac{\sum_{i < j} sgn(x_i - x_j) \cdot sgn(y_i - y_j)}{\frac{(n-1) \cdot n}{2}} \quad (2.35)$$

These parameters vary between 1, when the independent variable has a monotone positive influence on the dependent variable, and -1 in the opposite case. If there is a negligible dependence their value is close to zero.

2.4.1 Sensitivity analysis on compressor efficiencies and cost

The two correlation coefficients previously defined have been calculated for each independent variable with respect to the global and volumetric efficiencies and on the set-up costs of the linear compressor. The influence of each independent variable on efficiency is shown in *Figure 15 (a)* for the global efficiency and *Figure 15 (b)* for the volumetric efficiency. By increasing the piston diameter, the compressor global efficiency augments since a larger diameter allows to use greater valves, bringing to a decrease of the fluid dynamic losses during the suction and the discharge phases. On the contrary, the volumetric efficiency is negatively affected by an increase of the piston diameter. As a matter of fact, with both cooling power and displacement fixed, a larger piston diameter leads to a rise in the ratio between the dead volume and the displacement, causing a greater percentage of not exhausted gas.

The increase in the suction valve diameter positively affects the compressor global efficiency. Indeed, a larger area of the suction valve involves a lower velocity of the gas for a fixed mass flow rate and thus lower pressure drops across the valve. Due to the increased space for the suction gas, also the volumetric efficiency is improved, even if this effect is not significant. Analogous considerations can be drawn for the discharge valve diameter, even if its influence on both efficiencies is almost negligible in the range of discharge valve considered. In fact, due to the gas higher density, a lower diameter is needed in the discharge phase compared to the suction phase. The clearance gap is not filled by lubricant oil or piston rings, and it is essential to avoid the contact between the piston and cylinder. Greater clearance gap leads to two opposite effects: from one side, it increases the leakage losses; on the other side, it enhances the maximum rotation value that the piston could suffer before its contact with the cylinder. These two conflicting aspects result in values of the Spearman and Mann-Kendall coefficients slightly lower than zero. As regards the effect on the volumetric efficiency, the higher leakages with an increased gap significantly affect the discharge mass flow rate. For this reason, the Spearman and Mann-Kendall coefficients reach values of almost -0.5 and -0.4,

respectively. The dead volume is defined as the space between the top dead center and the head of the cylinder. This parameter particularly affects the compressor performance at partial load, because the change in the compressor stroke leads to change in the dead volume. Although a slight negative effect on the global efficiency is observed in *Figure 15(a)* (due to a proportional decrease of the required electrical power), the correlation coefficients for the volumetric efficiency reach -0.7 and -0.5. As a matter of fact, an increased dead volume leads to higher quantity of not ejected vapor from the compression chamber at the end of the discharge phase. Those gases will expand during the movement of the piston from the top to the bottom dead center, occupying a higher space that causes a lower availability for suction gas and thus lower mass flow rate evolving in the compressor. Regarding the dry friction coefficient, it directly influences the mechanical friction losses due to the contact between piston and cylinder caused by the spring eccentricity and therefore piston rotation. Although in this work it is treated as an independent variable, the dry friction coefficient is dependent on the material for the compressor or on the coating used on the piston. The increase of this parameter, bringing to an increase of the normal force between the piston and the cylinder, and thus higher friction losses, obviously brings to lower compressor global efficiency. On the other hand, it has a negligible influence on the volumetric efficiency. To decrease the dry friction coefficient, polymeric coating can be adopted to cover the piston, as reported in Yeo et Polycarpou [58] where PFTE and PEEK based coatings were tested on oil-free reciprocating compressors, reaching dry friction coefficients between 0.08 and 0.2. However, the durability of the polymeric layer is still a critical aspect. The compressor stroke increase causes a rise in the friction losses due to the contact between the piston and the cylinder, resulting in a negative impact on the global efficiency. Furthermore, with a fixed displacement, higher strokes imply smaller piston diameter, causing lower space for the valves, and consequently higher fluid dynamic losses during the suction and discharge phases. On the contrary, a higher stroke leads to a lower dead volume and thus higher volumetric efficiency. The independent variable having the higher influence on the compressor performance is the eccentricity of the resonant spring. The Spearman and the Mann-Kendall coefficients are respectively -0.7 and -0.5. In fact, the eccentricity of the elastic force causes an axial rotation of the piston, leading to a contact with the cylinder and causing a dramatic increase of friction losses and a decrease of the global

efficiency. Despite the eccentricity causes a piston shift from the original position, the gap between the two sides of the piston and the cylinder changes, resulting in a different gap distribution compared to the original one and thus different leakage losses at the two sides of the piston. However, this effect is not included in the model, assuming that the total gap is constant. Consequently, the leakage losses and thus the volumetric efficiency are not affected by the eccentricity parameter.

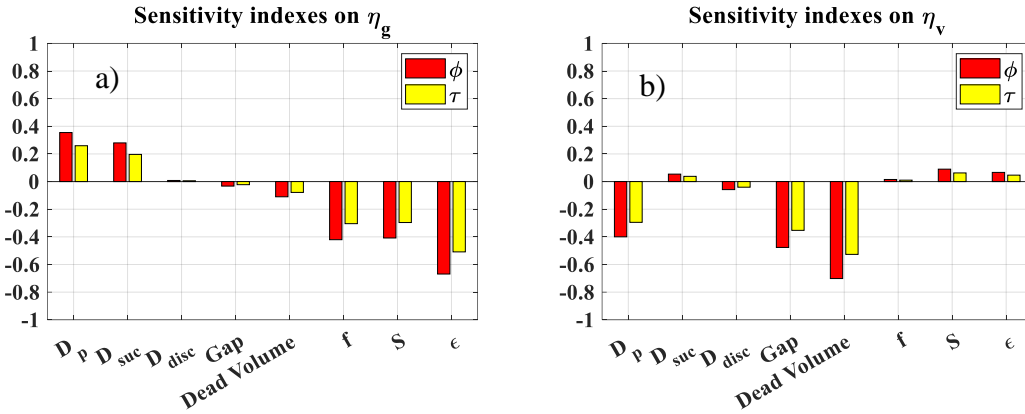


Figure 15 Sensitivity indices of the linear compressor efficiencies with respect to the independent design variables. a) Sensitivity indices of the linear compressor global efficiency. b) Sensitivity indices of the linear compressor volumetric efficiency.

The effect of each independent variables analysed on compressor set up cost is reported in Figure 16. The compressor cost is evaluated as reported in Eq. (2.36):

$$C_{comp} = (C_{steel} \cdot m_{tot} + C_{springs} \cdot N_{springs} + C_{motor}) \cdot 1.5 \quad (2.36)$$

where c_{steel} is the stainless steel cost, assumed to be 4 €/kg after a market analysis; m_{tot} is the total mass of the compressor, involving the piston, the cylinder and the external frame; $c_{springs}$ and $N_{springs}$ are, respectively, the cost of a single spring, assumed to be 4 € according to [59], and the total number of springs employed. Finally, c_{motor} is the cost of a linear motor, which is about 80 € for the power considered according to a market analysis. All manufacturing costs are included in the chosen cost functions, whereas, to consider the final market price for this analysis, a profit margin equal to the 50% of the sum of each component cost is assumed. Other extra costs are not considered, since the chosen variation ranges of the decision variables fall within standard manufacturing techniques [60].

As shown in Figure 16, among all the independent variables analyzed in the sensitivity analysis, only the piston diameter and the stroke has a significant influence on compressor costs. In particular, for a fixed displacement, an increased piston diameter leads to higher compressor weight and consequently a rise in material cost. On the contrary, increasing the piston stroke allows to reduce the piston diameter leading to lower costs.

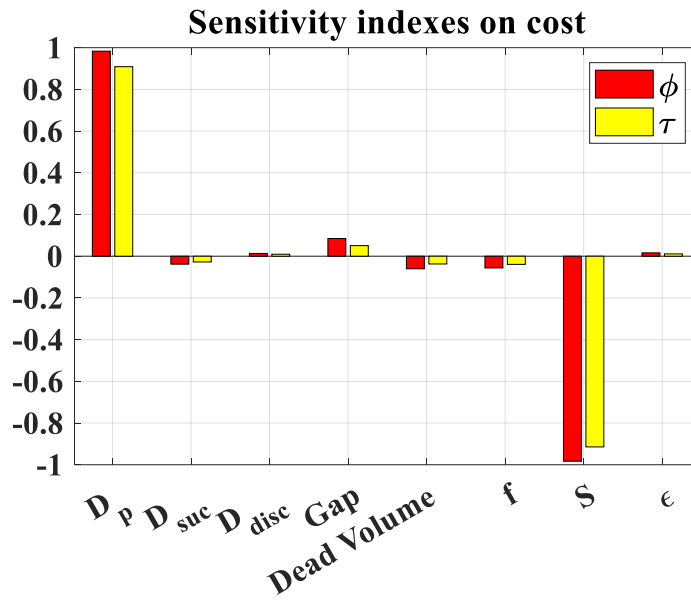


Figure 16 Sensitivity indexes of the linear compressor cost with respect to the independent design variables.

Table 3 summarizes the Spearman and the Mann-Kendall coefficients for the three objective functions of interest.

Table 3 Spearman and Mann-Kendall coefficients for the three objective functions of interest.

	η_g		η_v		Cost	
	ϕ	τ	ϕ	τ	ϕ	τ
D_p	0.35	0.26	-0.40	-0.29	0.98	0.91
D_{suc}	0.28	0.20	0.05	0.04	-0.04	-0.03
D_{dis}	0.01	0.01	-0.06	-0.04	0.01	0.01
Gap	-0.03	-0.02	-0.48	-0.35	0.08	0.05
Dead Volume	-0.11	-0.08	-0.70	-0.53	-0.06	-0.04
f	-0.42	-0.30	0.02	0.01	-0.06	-0.04
S	-0.41	-0.30	0.09	0.05	-0.98	-0.91
ε	-0.67	-0.51	0.07	0.05	0.02	0.01

2.4.2 Thermo-economic analysis

The compressor cost versus the compressor global efficiency of all the solutions analyzed is shown in Figure 17, highlighting A and B points as non-dominated solutions. Particularly, solution A is the one with lower costs, while B is the configuration with the highest efficiency. It is worth pointing out that only points with a global efficiency higher than 0.3 have been considered, since all the remaining solutions, for a fixed cooling capacity, would require a significantly higher electricity consumption and a possible re-design of the linear motor. The price [46, 61] and efficiencies [54] ranges of the solutions currently available on the market, namely traditional reciprocating compressors and the linear compressors now on sale, are also displayed. The compressor design parameters can be chosen from the displayed solutions by looking for a trade-off between higher efficiencies and lower cost, according to the specific manufacturer needs. Table 4 shows the two non-dominated simulated configurations A and B, together with the corresponding values of the decision variables.

Table 4 Objective functions and input parameters values for the non-dominated points on the Pareto front. A: lower cost configuration. B higher efficiency configuration.

	A	B
D_p [m]	0.02	0.04
D_{suc} [m]	0.018	0.034
D_{dis} [m]	0.15	0.034
Gap [m]	$1.00 \cdot 10^{-6}$	$5.75 \cdot 10^{-6}$
Dead Volume [m³]	$1.58 \cdot 10^{-7}$	$3.27 \cdot 10^{-7}$
f [-]	0.10	0.10
S [m]	0.03	0.10
ε [m]	$1.00 \cdot 10^{-4}$	$1.00 \cdot 10^{-4}$
η_g [-]	0.62	0.74
η_v [-]	0.78	0.68
Cost [€]	130.22	246.64

The market analysis also points out that the traditional reciprocating compressors have a lower global efficiency, but also minor costs compared to both, the simulated and the currently available linear compressors on the market. It is also evident that the linear compressor has room for improvement regarding its efficiency, without much economic effort with respect to the solutions already offered on the market.

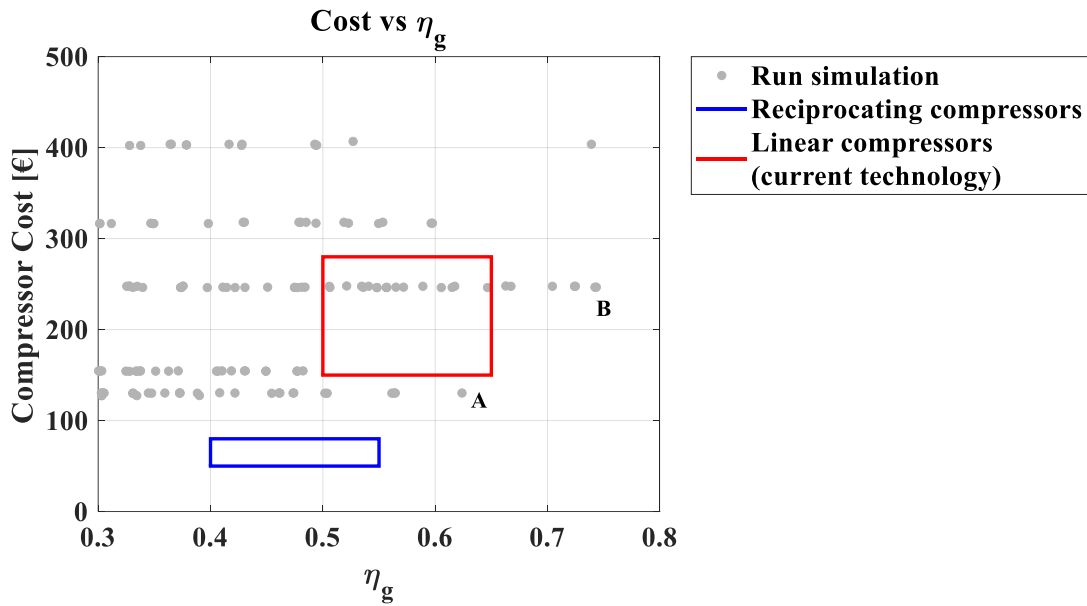


Figure 17 Diagram of the compressor cost and overall efficiency of the sized solutions compared with the prices and efficiencies ranges of the reciprocating and linear compressors now available on the market.

2.5 Conclusion of the chapter

In this chapter a linear compressor model is developed to perform a sensitivity analysis of the main geometrical and design parameters on compressor cost and efficiency (both global and volumetric), and to carry out a thermo-economic comparison between this technology and the conventional reciprocating compressor for domestic refrigerators. Two statistic indexes have been taken into account, namely the Spearman and the Mann-Kendall coefficient, and the influence of eight independent variables is analysed. The working fluid is R600a and the cooling power is set to 200 W. The main results are summarized as follows:

- The increase of piston diameter and suction valve diameter lead to an increase in global efficiency. Particularly, Spearman and Kendall indexes assume values of 0.38 and 0.27 for the first independent variable and 0.3 and 0.2 for the second one. Larger piston diameter allows to greater room for the valves, leading to a reduction of the fluid-dynamic losses during the suction and discharge phases. On the other side, the global efficiency decreases with increasing dry friction coefficient, stroke and spring eccentricity. For these variables, the Spearman and Kendall coefficient are, respectively, -0.41 and -0.31, -0.4 and -0.3, and -0.7 and

-0.5. Particularly, the negative influence of these three factors on the global efficiency is mainly related to an increase in friction losses.

- The volumetric efficiency decreases with the increase of the piston diameters, the dead volume and the clearance gap between piston and cylinder. For a fixed power, a higher piston diameter leads to a lower stroke and a higher dead volume percentage, with a decrease in the volumetric efficiency. Similarly, the increase of the dead volume leads to a reduction of the volumetric efficiency. The gap between piston and cylinder, being directly responsible for the refrigerant leakages and a loss of the discharge flow rate causes a huge volumetric efficiency decrease. The Spearman and Kendall coefficients for the piston diameter, the dead volume and the clearance gap are, respectively, -0.4 and -0.3 for the first, -0.7 and -0.5 for the second and -0.45 and -0.37 for the last one. The influence of the other parameters on the volumetric efficiency is negligible.
- The piston diameter and the stroke are the parameters that mainly affect the compressor cost. Indeed, by increasing the first the compressor weight increases, whereas a higher stroke allows lower diameters and thus a lighter compressor, requiring a lower amount of material. Consequently, these two parameters have an adverse effect on the compressor cost, and thus an opposite value of the sensitivity indexes. Particularly, the first has a Spearman coefficient of 0.98 and a Kendall coefficient of 0.9, while for the second the two coefficients have values of, respectively, -0.98 and -0.9.
- The thermo-economic comparison between the solutions proposed and the reference compressors for domestic refrigerators has shown that the currently available reciprocating compressors have lower costs and performances compared to both off-the-shelf linear compressors and the new solutions sized. Particularly, it is pointed out that there is a great room of improvement for linear compressors, both in terms of higher performance and lower costs compared to the available linear compressors on the market. As a matter of fact, an efficiency of 0.74 can be reached with a purchase cost of approximately 250 €.

The analysis carried out in this chapter points out that linear compressor is an interesting technology for domestic refrigerator, having a wide room for improvement in terms of

costs and efficiency. However, further analyses, including the coupling between the piston and the linear motor, are suggested verifying its applicability to a large-scale level. Moreover, it is worth noting that the results obtained in the economic analysis refer to the specific cost functions employed. Since the costs of materials, components and manufacturing strongly depend on the geographic area and on the market conditions, different results may be achieved using different cost functions.

PART 2

INNOVATIONS RELATED TO COMPONENTS:

HEAT EXCHANGERS - FLOW BOILING OF

REFRIGERANTS

3. Flow boiling heat transfer and pressure drop data of low GWP mixtures R455A and R454C

The present chapter deals with an analysis at component level, focusing on the heat exchangers. In particular, an experimental campaign is carried out to measure the flow boiling heat transfer coefficient and pressure drop for the low-GWP refrigerants R455A and R454C in a stainless-steel tube having an internal diameter of 6.0 mm. A wide range of operating conditions is explored to investigate the effect of the saturation temperature, mass flux and imposed heat flux, in the whole range of vapor quality, from 0 up to the occurrence of the dry-out. The experimental data collected are then used for a critical assessment of several predictive methods available in the scientific literature, to provide useful information to the engineers involved in the heat exchangers design process. As a matter of fact, the need to replace high-GWP refrigerants with low-GWP alternatives implies remarkable differences in the heat exchanger design, since the traditional predictive methods to estimate the heat transfer coefficient are not always reliable with new low-GWP refrigerants. The results regarding the flow boiling of R455A and R454C are, respectively, published in [62] and [63].

3.1 State of the art

In the framework presented in the first chapter of the thesis, several regulations were introduced in the last decades in order to contain the greenhouse gas emissions and thus to limit the global warming to avoid an excessive increase of the Earth surface temperature. As underlined, a great contribution to the global warming is given by vapor compression cycles, which employ HFC with high-GWP, contributing directly to the Earth temperature increase. Consequently, the Kigali Amendment to the Montreal Protocol [9], acting at global level, and the and the European F-gas Regulation [10] set the roadmap to phase-out HFC refrigerants to achieve over 80% reduction in their consumption. Particularly, among the different sectors constituting the cold chain and employing a vapor compression cycle, refrigerated transport units, commercial refrigeration systems at low and medium temperature and multipack refrigeration systems are crucial. Indeed, these applications share a considerable amount of refrigerant charge and high rate of accidental leakages.

For these reasons, the new GWP threshold in these fields, according to the aforementioned regulation, was set to 2500 up to 2020 and to 150 by 2022, as reported in Figure 18. The severe limit imposes to replace not only the quasi-azeotropic mixtures R404A, having a GWP equal to 3922, that has been the most used refrigerant in commercial applications for many years, but also the two middle-term replacements, namely R452A and R448A, having a GWP significantly higher than 150. In addition, the cost of the refrigerant R404A is increasing dramatically, concurring to the environmental motivations for its prompt replacement. In this regard, R455A and R454C have been identified as suitable long-term substitutes [64], thanks to the similar thermophysical characteristic as R404A and very low GWP indexes. Both fluids are non-azeotropic mixtures characterized by a low flammability (classified as A2L refrigerants according to ASHRAE standards), caused by the presence of R32, being an A2 class refrigerant. The first is a 3-component mixture, made up with CO₂/R32/R1234yf (3%/21.5%/75.5% composition in mass), having a temperature glide of 10.52 at 20°C. R454C is made up of R32 and R1234yf (21.5% and 78.5% as mass composition).

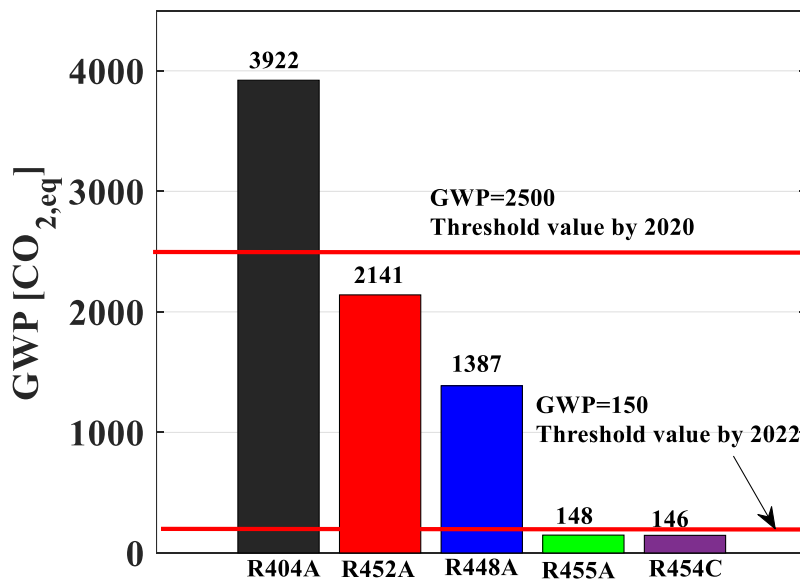


Figure 18 GWP threshold value for refrigerated transports, commercial refrigeration and condensing units according to [10].

Table 5 shows the main thermodynamical and transports properties of the two low-GWP refrigerants in comparison with the reference R404A fluid.

Table 5 Properties comparison between mixtures R454C, R455A and R404A, at a bubble saturation temperature of 20°C.

Fluid @20°C	GWP	Temperature glide [°C]	ρ_v/ρ_l	ρ_v [kg · m ⁻³]	ζ_v/ζ_l	ζ_l [10 ⁻⁶ Pa · s]	λ_l [W · m ⁻¹ · K ⁻¹]	ASHRAE class
R454C	148	4.2	0.035	37.40	0.078	148.2	0.0798	A2L
R455A	145	10.52	0.043	45.97	0.085	143.80	0.0813	A2L
R404A	3922	0.43	0.053	57.03	0.086	137.48	0.0655	A1

Different studies in scientific literature deal with the comparison between thermo-physical properties of different mixtures or experimental and/or numerical drop-in analysis in specific case studies. Makhnatch et al. [65] investigated R454C and R455A as R404A alternatives and have compared some characteristics such as components and composition, global warming potential, energetic performances, material and lubricant compatibility. Zgiczynski and Sedliak [66] performed an experimental analysis for a hermetic reciprocating compressor when using an A2L refrigerant, looking at three different mixtures: R455A, R454C and R457A. The compressor using R454C showed a greater efficiency, but higher operating cost. Furthermore, R455A exhibits an increase in the overall compressor internal and discharge temperature and, to compensate for such growth, return gas temperature or condensing temperature shall be reduced to avoid compressor lifetime reduction. Mota Babiloni et al. [67] presented a drop-in analysis of R454C and R455A for an experimental set-up of a vapor compression refrigeration system originally designed for R404A. The results indicated that the COP of R455A and R454C was 10% higher compared to R404A, without the adoption of an internal heat exchanger (IHX), and 4% higher by using an IHX. Sethi et al. [68] carried out a drop-in analysis of fluids R448A and R455A for a commercially available low-temperature R404A self-contained freezer. Tests showed a similar capacity for R455A with respect R404A, with about a 6% lower compressor energy consumption. Oruc and Devecioglu [69] experimentally compared R404A with R454A and R454C in a refrigeration system, finding that the COP was 10% higher employing R454C, thanks to a 15% reduction of the compressor power consumption, but on the other side a lower cooling capacity was achieved. Lee and Kim [70] tested the R454C as a drop-in in an ice maker originally designed to work with R404A. They found an increased time (14%) for the ice formation and a decreased amount of ice produced in a day (8%). No information are reported about the performance and the energy consumption. Llopis et al. [71] evaluated R454C and other blends as substitutes in a stand-alone commercial refrigeration system for fresh products, concluding that the new mixtures managed to provide a higher evaporating temperature, with similar discharge temperatures and pressures to those of R404A. Minor et al. [72] experimentally evaluated a self-contained freezer originally designed for R404A using R454C as refrigerant, finding a higher efficiency.

As regards the heat transfer coefficient, very few works analyse the heat transfer performance and pressure drops of R455A and R454C. Regarding the first, Azzolin et al. [73] studied the condensation heat transfer and pressure drop inside a minichannel and a conventional tube, and in [74] the same research group studied the flow boiling of the aforesaid fluid in the same geometries, founding out a reduced heat transfer performance due to a high temperature glide. Regarding the latter mixture, Jacob and Fronk [75] and Lee et al. [76] carried out an experimental campaign of R454C condensation inside tubes, finding similar heat transfer coefficient values as those of R404A. In case of microfin tubes [77], for low mass fluxes the heat transfer coefficient of R454C was found to be 25-31% lower than that of R404A, with higher pressure drops. Jige et al. [78] experimentally studied the flow boiling heat transfer and frictional pressure drop of mixtures made up of R1234yf and R32, with different compositions in mass, inside a horizontal multiport tube with rectangular minichannels. They observed that by increasing the R1234yf percentage, there was a decrease of the heat transfer coefficient. In fact, the mixture with 47% of R1234yf and 53% of R32 gave higher heat transfer coefficients with respect to a 79/21% mixture (very close to the composition of R454C). The degradation of the heat transfer performance was more severe in conditions promoting nucleate boiling contribution.

Only two studies, carried out by the same research group, deal with the flow boiling of R454C, respectively in a 5.6 mm tube [79] and in a microfin tube [80].

3.2 Objective of the research

As shown in the state of the art, most of the works deal with the possibility to employ R454C and R455A as drop-in substitutes of R404A. However, the amount of data on flow boiling heat transfer and pressure drop of the two non-azeotropic mixtures is very limited. The availability of such experimental data is of great importance to properly design heat exchangers working with these new mixtures, to avoid undesired under/over sizing. Reliable predictive methods are also needed, since the existing correlations are usually calibrated for pure refrigerants, at different operating conditions than those used for the new low-GWP mixtures. As a matter of fact, both fluids are characterized by the presence of a not negligible glide temperature, causing a penalization of the nucleate boiling contribution, due to the increased mass transfer resistance that inhibits the bubble formation. This phenomenon might, therefore, lead to considerable errors when

predicting the boiling two-phase heat transfer coefficient with conventional prediction methods, which are calibrated for pure fluid or quasi-azeotropic mixtures. Moreover, the flammability of the alternative fluids leads to the necessity to reduce the refrigerant charge in the plant, encouraging the design of compact heat exchangers where the operating conditions are quite peculiar with respect to traditional systems.

For these reasons, in this chapter experimental data of flow boiling heat transfer and pressure drop for the mixtures R454C and R455A are presented inside a single horizontal smooth 6.0 mm stainless steel (AISI SS316) tube, to assess the predictive methods currently available in the literature, to evaluate those performing better with the experimental data collected and to provide careful information to the heat exchangers designers. Tests are performed within a wide range of operating conditions, namely imposed heat flux from 4 to 40 kW·m⁻², mass flux from 150 to 600 kg·m⁻²s⁻¹ and a bubble saturation temperature from 10°C to 55°C, from the boiling incipience up to the dry-out condition.

3.3 Experimental facility

The test rig employed to carry out the experimental campaign, and shown in Figure 19, along with its schematic representation, is made up by two different loops, one for the refrigerant under investigation and the other for the cooling media, which is demineralized water, represented, respectively, in black and blue in Figure 19.

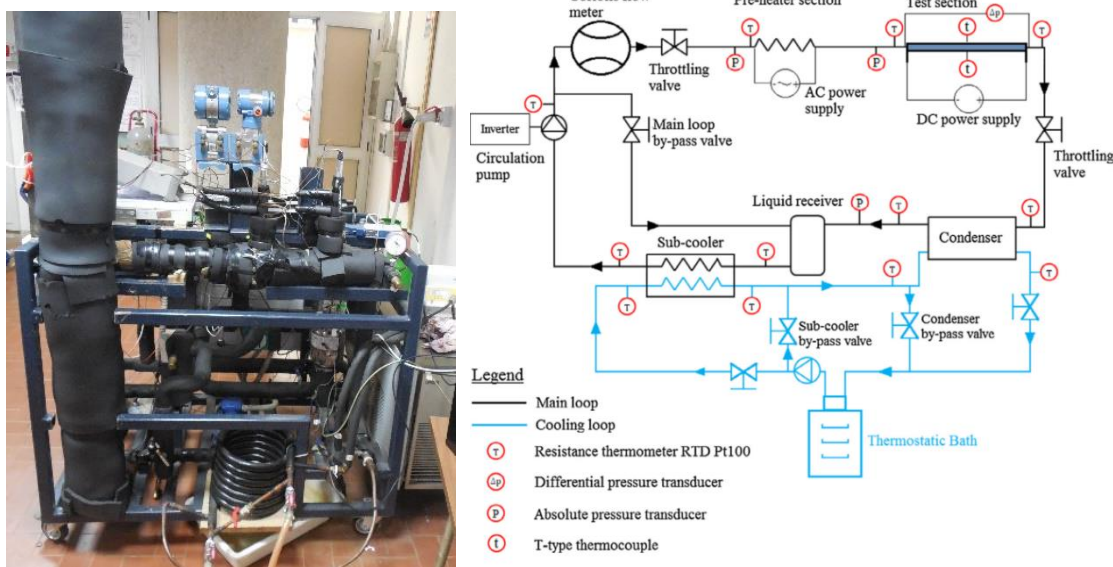


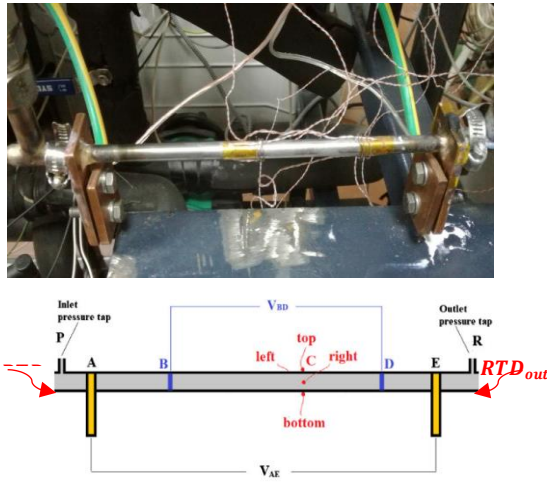
Figure 19 Photography and piping layout of the test facility.

The refrigerant is pumped by means of a gear circulation pump, whose rotation speed is controlled by an inverter to regulate the refrigerant mass flow rate, which can be also adjusted by manipulating a throttling valve or by activating the by-pass circuit, allowing to recirculate parts of the subcooled refrigerant in a liquid receiver, avoiding the completion of the refrigerant loop. After the pump, the refrigerant goes through a Coriolis mass flow meter for the evaluation of the mass flow rate. Subsequently, the sub-cooled refrigerant flows into a preheating section in AC made of copper and having a heating capacity of 3.0 kW, where it evaporates reaching the desired vapor quality. The heat load necessary to reach the vapor quality required during the experiment is provided by four fiberglass heating tapes wrapped on the copper tube external surface, ensuring the evaporation of the fluid until the desired vapor quality. The preheater is followed by the test section tube, where the measurement of the heat transfer coefficient and pressure drop is performed. Then, the saturated flow is condensed in a plate heat exchanger, that is followed by the aforementioned liquid receiver. Finally, a sub-cooler (tube-in-tube heat exchanger) closes the loop. The refrigerant saturation temperature is indirectly controlled by means of a thermostatic bath, which set the demineralized water temperature used as cooling media in the sub-cooler and the condenser, fed by a circulation pump. The whole test bench is covered by several layers of synthetic foam to minimize the heat transfer to/from the environment.

More details about all the components and equipment of the test facility can be found in several previous works of the research group [81] [82] [83].

3.3.1 Test section

The test section, where the heat transfer coefficient and the pressure drop measurements occur, is a horizontal smooth stainless-steel tube (AISI SS316) having an internal diameter d of 6.0 ± 0.05 mm and an outer diameter D of 8.0 ± 0.05 mm. In Figure 20 the test section is shown with its schematic representation and the main geometrical parameters.



Geometrical features	
A, E	copper electrodes
B, D	voltage measurement points
C	temperature measurement point
AE	193.7 ± 0.79 mm
BD	101.6 ± 0.41 mm
AC	146.7 ± 0.64 mm
d	6.00 ± 0.05 mm (internal diameter)
D	8.00 ± 0.05 mm (outer diameter)
PR	237.5 ± 0.91 mm (pressure taps distance)
PC	166.9 ± 0.91 mm

Figure 20 Representation of the test section and its geometrical features.

A DC power generator (up to 8.0 V and 300 A) connected to the test section with two copper electrodes welded to the tube surface at a distance of 193.7 ± 0.79 mm provide the heat flux for the two-phase refrigerant flowing inside the tube. The imposed voltage is measured between points B and D, over a length of 101.6 ± 0.41 mm. The local two-phase heat transfer coefficient is measured at a distance of 146.7 ± 0.64 mm from the first copper electrode by using 4 T-type thermocouples placed on the top, bottom and the two sides of the tube external surface. A thin layer of epoxy resin at high thermal conductivity guarantees the contact between the four sensors and the tube, with the latter being previously covered with an adhesive Kapton layer for electrical insulation purposes. Two 4-wire calibrated resistance thermometer Pt100 are installed at the inlet and outlet of the test section. To evaluate the pressure drop across the test section the absolute pressure at the inlet and at the outlet is measured by two pressure taps, located right outside the heated length (P and R in Figure 20, at a distance of 237.5 ± 0.91 mm).

3.3.2 Measurement instrumentation

In Table 6 the list of all the measurement instruments with their range and accuracy is provided. For the temperature measurements of the fluids different RTDs, with an overall uncertainty of ± 0.180 °C, are placed throughout the refrigerant and the cooling loop. The external wall temperature in the heat transfer coefficient measurement point is measured by means four T-type thermocouples, calibrated in situ with a procedure that will be

shown in the following paragraphs. The absolute pressure at the test section inlet is measured with an absolute pressure transducer with a measuring range of 0-35 bar, characterized by overall uncertainty of $\pm 0.5\%$ of the read value. The pressure drop is evaluated with a differential pressure transducer, calibrated with a water liquid column and a yardstick. The instrumental uncertainty is estimated to be ± 0.06 kPa. A Coriolis mass flow meter allows the evaluation of the mass flow rate. It is calibrated up to 2% of the full scale, with a maximum uncertainty of $\pm 1\%$ of the measurement. A digital wattmeter provides the heat applied to the preheater section, by separately measuring the voltage (100 mV-500 V) and current (1 mA-16 A). Its uncertainty is $\pm 1.0\%$ of the reading, as provided by the manufacturer. The heat flux applied to the test section requires the measurement of the DC voltage (electrical voltage transducer within 0-5 V and an uncertainty of $\pm 0.03\%$ of the reading) and the DC current (directly measured by the DC power unit within 0-300 A and an uncertainty of $\pm 1.0\%$).

Table 6 Range and accuracy of the measurement instruments employed in the test rig.

Measurement	Range	Instrument Accuracy
Temperature (4-wire Pt100 RTDs)	-80/250 °C	± 0.180 °C
Wall temperature (T-type thermocouples)	10/90 °C	± 0.10 °C
Inlet absolute pressure transducer (test section)	0/35 bar	$\pm 0.1\%$ reading
Other absolute pressure transducers (test rig)	0/50 bar	$\pm 0.3\%$ reading
Differential pressure transducer	0/14.51 kPa	± 0.06 kPa
Coriolis flow meter	2.3/115.7 g·s ⁻¹	$\pm 1\%$ reading
Pre-heater electrical power	0/3.6 kW	$\pm 1\%$ reading
Voltage (test section)	0/5 V	$\pm 0.03\%$ reading
Current (test section)	0/300 A	$\pm 1\%$ reading

3.4 Experimental method

3.4.1 Experimental procedure

Each experimental point collected during the experimental campaign is recorded only when the steady state conditions are ensured. The desired operating conditions, in terms of mass flux, saturation temperature, and heat flux are fixed by means of the several instruments previously shown. The software Labview allows to monitor and to control the variation of each parameter. Each experiment starts from the onset of the boiling, ending with the occurrence of the dry-out, increasing gradually the vapor quality. The experiment is stopped when the dry-out heat transfer is recorded (namely when the heat transfer coefficient drops more than 25% from its previous value) and the huge wall temperature fluctuations does not guarantee steady state conditions and thus high-quality experimental data.

Since the two mixtures under investigation have a considerable temperature glide, each test is performed with a fixed bubble temperature and thus a fixed saturation pressure. In particular, its desired value is obtained by adjusting the set point temperature of the thermostatic bath, or by varying the efficiency of the condenser and the sub-cooler using the water by-pass circuit. The heat flux applied in the test section is provided by varying the voltage from the DC power supply. The mass flux is controlled by a magnetic gear pump coupled with the electrical inverter. Thin adjustments are made by manipulating the micrometric valve on the liquid line and the by-pass circuit. Finally, the desired quality in the test section is obtained by adjusting the heat rate in the preheater section.

Each point is recorded with a frequency of 1 Hz and a recording time of 90 s. The value of each parameter corresponds to the arithmetical average of the sample. Furthermore, to ensure a better quality of the experimental results, the data acquisition is allowed only if the uncertainty of all the parameters is below a chosen threshold value ($\pm 3\%$ for the mass velocity, ± 0.5 °C for the saturation temperature), except for the dry-out points, for which the operating parameters are no longer under control and the uncertainties become larger.

3.4.2 Data reduction

The mean local heat transfer coefficient is evaluated, for each experimental point, by using the Newton equation, assuming a uniform heat flux and an average wall temperature

from the measurement of the four thermocouples placed on the top, bottom, left and right side of the tube:

$$h_{mean} = \frac{q}{T_{wall,mean} - T_{sat,c}} \quad (3.1)$$

where $T_{wall,mean}$ is calculated as:

$$T_{wall,mean} = \frac{T_{wall,top} + T_{wall,bot} + T_{wall,left} + T_{wall,right}}{4} \quad (3.2)$$

The inner $T_{wall,i}$ is obtained by the measured outer wall temperature T_{th} , and considering the analytical solution to the heat transfer problem, assuming a one-dimensional heat flux in the radial direction, steady-state conditions, uniform heat generations inside the tube and homogeneous and isotropic material.

$$T_{wall,i} = T_{th,i,out} + \frac{V \cdot I}{4 \cdot \pi \cdot \lambda_{tube} \cdot L_h} \cdot \frac{\left(\frac{D}{d}\right)^2 \cdot \left(1 - \log\left(\left(\frac{D}{d}\right)^2\right)\right) - 1}{\left(\frac{D}{d}\right)^2 - 1} \quad (3.3)$$

The thermal conductivity λ_{tube} of the stainless-steel tube is assumed to be constant and equal to $16.23 \text{ W}\cdot\text{m}^{-1}\text{K}^{-1}$, according to the information provided by several data sheets. D and d are, respectively, the outer and the inner diameters of the tube. The outer wall temperature is evaluated through a thermocouple calibration laws, obtained with the procedure described in the following paragraphs. The saturation temperature is the average between two temperatures measured by means of as many RTDs, one at the inlet and one at the outlet of the test section. The local vapor quality is then a function of temperature and specific enthalpy in the measurement point:

$$\chi_c = f(T_{sat,c}, i_c) \quad (3.4)$$

where the specific enthalpy is obtained from the energy balance performed on a control volume involving the preheater and the test section (see Figure 20):

$$i_c = i_{in,preh} + \frac{\dot{Q}_{preh}}{\dot{m}} + \frac{\dot{Q}_{TS} \cdot \left(\frac{AC}{AE}\right)}{\dot{m}} \quad (3.5)$$

The preheater inlet specific enthalpy is evaluated as a function of temperature and quality, in the hypothesis of saturated liquid ($\chi=0$).

The frictional pressure drop, obtained in dedicated adiabatic tests, is measured by subtracting the momentum contribution, due to the ongoing evaporation, from the total pressure drop measured in the test section.

$$\left. \frac{\Delta P}{\Delta z} \right|_{fr} = \frac{\Delta P - \Delta P_{mom}}{\overline{PR}} \quad (3.6)$$

where the momentum term could be expressed as Equation (41) in which the void fraction v is evaluated by the Rouhani-Axelsson [84] correlation, modified with the Steiner model [85].

$$\Delta P_{mom} = G^2 \cdot \left\{ \left[\frac{(1-\chi)^2}{\rho_l \cdot (1-v)} + \frac{\chi^2}{\rho_v \cdot v} \right]_{out} - \left[\frac{(1-\chi)^2}{\rho_l \cdot (1-v)} + \frac{\chi^2}{\rho_v \cdot v} \right]_{in} \right\} \quad (3.7)$$

All the thermodynamic and transport properties of two mixtures under investigation, namely R454C and R455A, are calculated with the software Refprop 9.1 [53], developed by NIST, while the data reduction has been implemented with a MATLAB [52] code.

3.4.3 Uncertainty analysis

For all the measured parameters the combined uncertainty is evaluated by composing the instrumental uncertainty and the bias during the experiments. Accordingly to the law of propagation of error [86] the combined uncertainty for all the derived parameters is estimated. The equations employed for the main values of interest are shown in Table 7.

Table 7 Uncertainty equations for the derived parameters of interest.

Parameter	Equations for the uncertainty evaluation
Mass flux	$u_c(G) = \sqrt{\left(\frac{4 \cdot u_c(\dot{m})}{\pi \cdot d^2}\right)^2 + \left(\frac{8 \cdot \dot{m}}{\pi \cdot d^3} \cdot u_c(d)\right)^2}$
Heat flux	$u_c(q) = \sqrt{\left(\frac{V_{BD} \cdot u_c(l)}{\pi \cdot d \cdot \overline{BD}}\right)^2 + \left(\frac{l \cdot u_c(V_{BD})}{\pi \cdot d \cdot \overline{BD}}\right)^2 + \left(\frac{V_{BD} \cdot l}{\pi \cdot d^2 \cdot \overline{BD}} \cdot u_c(d)\right)^2 + \left(\frac{V_{BD} \cdot l}{\pi \cdot d \cdot \overline{BD}^2} \cdot u_c(\overline{BD})\right)^2}$
Saturation temperature	$u_c(T_{sat,C}) = \frac{\partial T}{\partial P} \cdot dP = \frac{\partial T}{\partial P} \cdot u_c(P_C)$ $u_c(P_C) = \sqrt{u_c(P_{in})^2 + \left(\frac{\overline{PC} \cdot u_c(\Delta P)}{\overline{PR}}\right)^2 + \left(\frac{\Delta P \cdot u_c(\overline{PC})}{\overline{PR}}\right)^2 + \left(\frac{\overline{PC} \cdot \Delta P \cdot u_c(\overline{PR})}{\overline{PR}^2}\right)^2}$
Local vapor quality	$u_c(x_c) = \sqrt{\left(\frac{1}{i_{v,c} - i_{L,c}} \cdot u_c(i_c)\right)^2 + \left(\frac{i_c - i_{v,c}}{(i_{v,c} - i_{L,c})^2} \cdot u_c(i_{L,c})\right)^2 + \left(\frac{i_{L,c} - i_c}{(i_{v,c} - i_{L,c})^2} \cdot u_c(i_{v,c})\right)^2}$
Local heat transfer coefficient	$u_c(h) = \sqrt{\left(\frac{u_c(q)}{T_{wall} - T_{sat,C}}\right)^2 + \left(\frac{q \cdot u_c(T_{wall})}{(T_{wall} - T_{sat,C})^2}\right)^2 + \left(\frac{q \cdot u_c(T_{sat,C})}{(T_{wall} - T_{sat,C})^2}\right)^2}$
Pressure gradient	$u_c\left(\frac{\Delta P}{\Delta z}\right) = \sqrt{\left(\frac{u_c(\Delta P)}{\overline{PR}}\right)^2 + \left(\frac{\Delta P \cdot u_c(\overline{PR})}{\overline{PR}^2}\right)^2}$

A coverage factor equal to 2 is applied to guarantee a confidence level higher than 95%. A summary of the uncertainty analysis for the mean heat transfer coefficient and the main parameters, for the experimental campaign of each fluid, is provided in Table 8. Particularly, for most of the entire database (points recorded in stable conditions before the occurrence of dry-out), the system is stable and the variation of parameters during the experiments occurs in a restricted range. On the other side, for dry-out and post dry-out conditions (approximately 10% of the entire database), the uncertainty becomes meaningfully higher.

Table 8 Maximum uncertainty recorded for all the parameters of interest, both in stable boiling and for post-dryout conditions.

Parameter	Maximum uncertainty for points in stable conditions R454C	Maximum uncertainty for the whole database (including dry-out conditions) R454C	Maximum uncertainty for points in stable conditions R455A	Maximum uncertainty for the whole database (including dry-out conditions) R455A
<i>Bubble temperature T_B</i>	$\pm 0.2^\circ\text{C}$	$\pm 1.8^\circ\text{C}$	$\pm 0.04\%$	$\pm 1.61\%$
<i>Mass flux G</i>	$\pm 1.82\%$	$\pm 2.15\%$	$\pm 2.95\%$	$\pm 8.03\%$
<i>Heat flux q</i>	$\pm 0.81\%$	$\pm 4.52\%$	$\pm 0.87\%$	$\pm 1.83\%$
<i>Vapor quality χ</i>	± 0.024	± 0.126	± 0.034	± 0.092
<i>Mean heat transfer coefficient h_{mean}</i>	$\pm 16.48\%$	$\pm 25.03\%$	$\pm 18.91\%$	$\pm 62.6\%$
<i>Pressure gradient $\Delta P/\Delta z$</i>	$\pm 10.57\%$	$\pm 15.57\%$	19.16%	22.3%

3.4.4 Thermocouples calibration

Since the heat transfer coefficient is strongly influenced by the wall temperature measurement, to ensure the best quality of the collected data, the four thermocouples placed in the measurement point have been calibrated in situ with the aid of two RTDs, performing over than 100 calibration tests for each fluid under investigation. Particularly, the calibration tests are carried out in adiabatic conditions, for several bubble saturation pressure and vapor quality. Given the negligible pressure gradient in adiabatic conditions, the saturation temperature is assumed to be the arithmetic average among the measurement of the two RTDs. Since the cold junction temperature is unknown, an additional calibrated thermocouple is located in the environment, together with another calibrated RTD. For each location (top, bottom, left and right size) a function $\Delta T_i = f(\Delta V_i)$ has been provided, being ΔT_i the temperature difference among the saturation temperature and the ambient temperature given by the corresponding RTD, while ΔV_i is the difference between the voltage read by the thermocouple on the tube surface and the

voltage recorded by the thermocouple installed in the room. The residuals of the calibrated functions were lower than 0.1°C. However, for precautionary purposes, this value was selected, being the instrumental uncertainty, as reported in Table 6.

3.4.5 Test rig validation and preliminary tests

Before the experimental campaign for the heat transfer evaluation, some preliminary tests were performed in liquid single phase with refrigerant R134a, in order to verify the correct insulation of the test section and the preheater section and to ensure the proper functioning of the whole experimental facility. Regarding the heat losses in the preheater section, the imposed electrical power by the fiberglass heating tapes has been compared to the heat absorbed by the sub-cooled refrigerant, showing discrepancies of approximately 8%. As pointed out in a previous study with the same test section [87], the heat losses at the preheater were fitted with a linear equation depending on the temperature difference between the heating tapes and the environment. The correct insulation of the test section was verified by comparing the calculated liquid single-phase heat transfer coefficient with the predicted values by the Dittus-Boelter [88] method, showing a very good agreement ($\pm 10\%$). In Figure 21 the results of the energy balance on the test section and the comparison between the experimental and expected liquid phase heat transfer coefficient are shown.

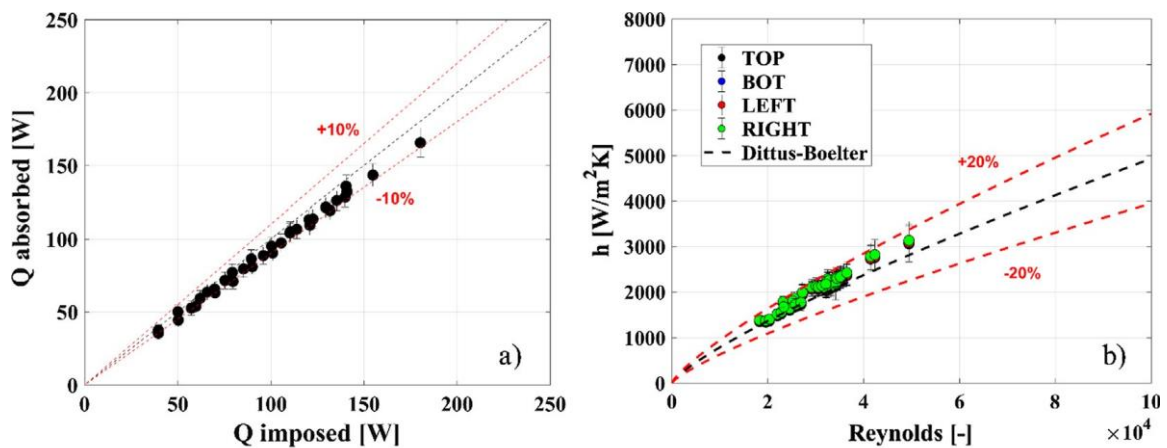


Figure 21 a) Adiabacity tests performed for the test section. b) Experimental and predicted single-phase heat transfer coefficient against Reynolds number.

3.5 Effect of the operating parameters on the heat transfer coefficient

3.5.1 Operating conditions

The trend presented herein is referred to the local heat transfer coefficient calculated as previously shown in the data reduction. The results are reported as a function of the vapor quality, by investigating the effect of the operating parameters in terms of imposed heat flux, mass flux and bubble saturation temperature. Since for both mixtures under investigation the glide temperature is not negligible, the experiments have been performed with a constant saturation pressure, to reproduce the conditions of a real heat exchanger, where the pressure remains approximately the same during the whole process. The error bands of each point are related to the composed uncertainties discussed previously. In Table 9 the operating conditions investigated are provided for each fluid.

Table 9 Operating condition investigated in the experimental campaign for the heat transfer coefficient measurement.

Parameter	Range/value	Range/value
<i>Fluid</i>	R454C	R455A
<i>Saturation pressure [bar]</i>	10.9-19.9	7.8-16.7
<i>Bubble saturation temperature [°C]</i>	30.0-55.0	8.3-38.7
<i>Mass flux G [kg·m⁻²·s⁻¹]</i>	150.0-600.0	299.0-512.4
<i>Heat flux q [kW·m⁻²]</i>	9.9-40.1	4.7-40.8
<i>Vapor quality χ [-]</i>	0.09- 0.96	0.09- 0.96
<i>Tube diameter d [mm]</i>	6.0	6.0

3.5.2 Effect of the imposed heat flux

The effect of the imposed heat flux on the heat transfer coefficient of the mixture R454C is shown in Figure 22 for a bubble saturation temperature of 35°C and two different mass

fluxes, $597.0 \text{ kg}\cdot\text{m}^{-2}\cdot\text{s}^{-1}$ (Figure 22(a)) and $151.2 \text{ kg}\cdot\text{m}^{-2}\cdot\text{s}^{-1}$ (Figure 22.(b)). As expected, the convective heat transfer coefficient is significant for high mass flux, as shown by the positive slopes of the curves at both 9.9 and $40.1 \text{ kW}\cdot\text{m}^{-2}$. However, the nucleate boiling contribution also plays an important role, since an increase of the heat flux, from 10.0 to $40.1 \text{ kW}\cdot\text{m}^{-2}$ causes a heat transfer coefficient enhancement (by 133% at the onset of boiling and about 80% for a vapor quality of 0.50). Moreover, a higher heat flux brings to an anticipated dry-out, that occurs at a vapor quality of 0.55 . In Figure 22(b) the almost constant trend of the heat transfer coefficient for vapor qualities higher than 0.3 suggests that the operating conditions do not promote the convective contribution. In these conditions, the stratification of the two-phases, due to a low mass flux, brings to an anticipated dry-out and thus the heat flux does not affect the heat transfer coefficient, except for vapor qualities lower than 0.20 , where an imposed heat flux of $39.5 \text{ kW}\cdot\text{m}^{-2}$ leads to an increase of the heat transfer coefficient of more than the 70% .

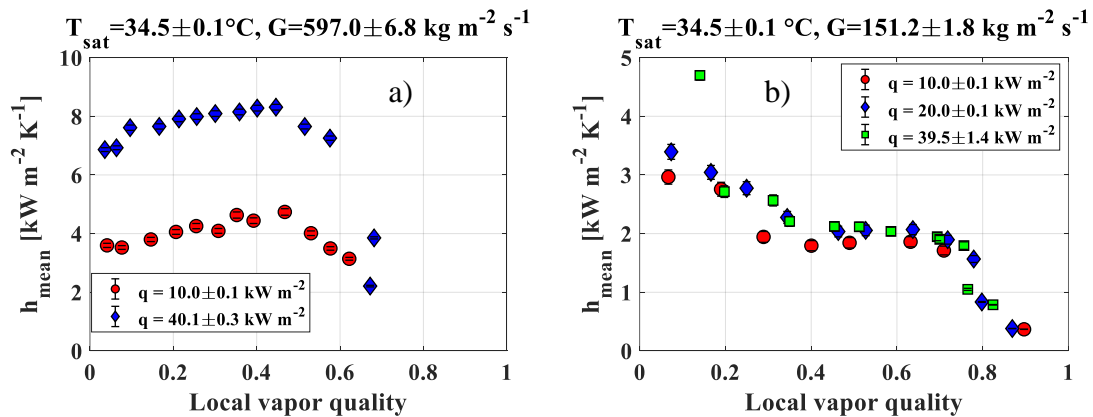


Figure 22 Effect of the imposed heat flux on the R454C heat transfer coefficient for a bubble saturation temperature of 34.49°C . (a) Mass flux of $597.0 \text{ kg}\cdot\text{m}^{-2}\cdot\text{s}^{-1}$. (b) Mass flux of $151.2 \text{ kg}\cdot\text{m}^{-2}\cdot\text{s}^{-1}$.

The effect of the imposed heat flux on the R455A heat transfer coefficient is shown for a bubble saturation temperature of 19°C and two different mass fluxes of $498.4 \text{ kg}\cdot\text{m}^{-2}\cdot\text{s}^{-1}$ (Figure 23 (a)) and $300.1 \text{ kg}\cdot\text{m}^{-2}\cdot\text{s}^{-1}$ (Figure 23 (b)). Also in this case, it appears evident that an increased heat flux leads to a strong enhancement of the nucleate boiling contribution with a remarkable augmentation of the heat transfer coefficient. However, as for R454C, being the mass flux considerably high Figure 22 (a) it can be noticed a predominance of the convective contribution, hypothesis corroborated by the growing trend with vapor quality. For a vapor quality of 0.3 , the increase in the heat transfer coefficient is close to 60% when the heat flux goes up from 9.98 to $40 \text{ kW}\cdot\text{m}^{-2}$, whereas

the difference is lower (about 25%) for a vapor quality of 0.8. The differences are included within the uncertainty bands when the heat flux is lower (i.e. 9.98 and 19.9 kW·m⁻²), showing that the nucleate boiling is still weak at low imposed heat flux. Moreover, the lower the mass flux is, the lower the convective contribution is, confirmed by the Figure 23 (b), where the slope of the heat transfer coefficient trend with the ongoing evaporation is limited compared to the one in Figure 23 (a). Finally, also in this case, the dry-out occurs at progressively lower vapor qualities when a higher heat flux is applied.

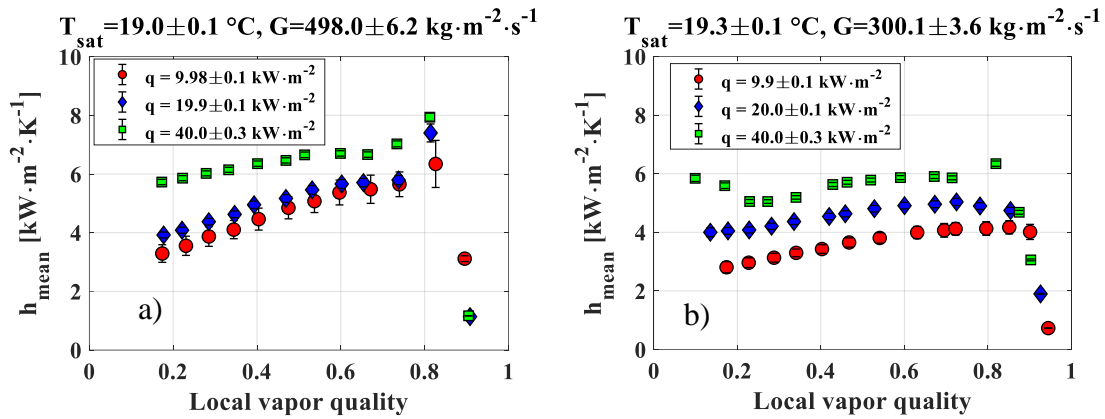


Figure 23 Effect of the imposed heat flux on the R455A heat transfer coefficient, for a bubble saturation temperature of 19.0°C. (a) Mass flux of 498.4 kg·m⁻²·s⁻¹. (b) Mass flux of 300.1 kg·m⁻²·s⁻¹.

3.5.3 Effect of mass flux

The effect of the mass flux on the R454C heat transfer coefficient is shown in Figure 24 for a bubble saturation temperature of 45.0°C and a heat flux of 9.9 kW·m⁻². For medium (298.0 kg·m⁻²·s⁻¹) and high (495.0 kg·m⁻²·s⁻¹) mass fluxes, only a slightly increasing trend of the heat transfer coefficient with vapor quality is observed. This is attributable to the medium-high saturation pressure (corresponding to a reduced pressure of 0.38) that promotes nucleation and inhibits convective heat transfer. For a mass flux of 150.0 kg·m⁻²·s⁻¹, instead, the negative slope indicates a possible flow stratification due to the low inertia. This hypothesis is corroborated by analyzing the local heat transfer on the top and bottom sides of the tube, depicted in Figure 24 (b) and (c), respectively. Indeed, starting from a vapor quality of 0.10, the two-phases seem completely stratified, since the liquid can wet only the bottom side of the tube (with small differences in the heat transfer coefficient with respect to higher mass velocities), while the vapor at the top causes a reduction of the heat transfer coefficient.

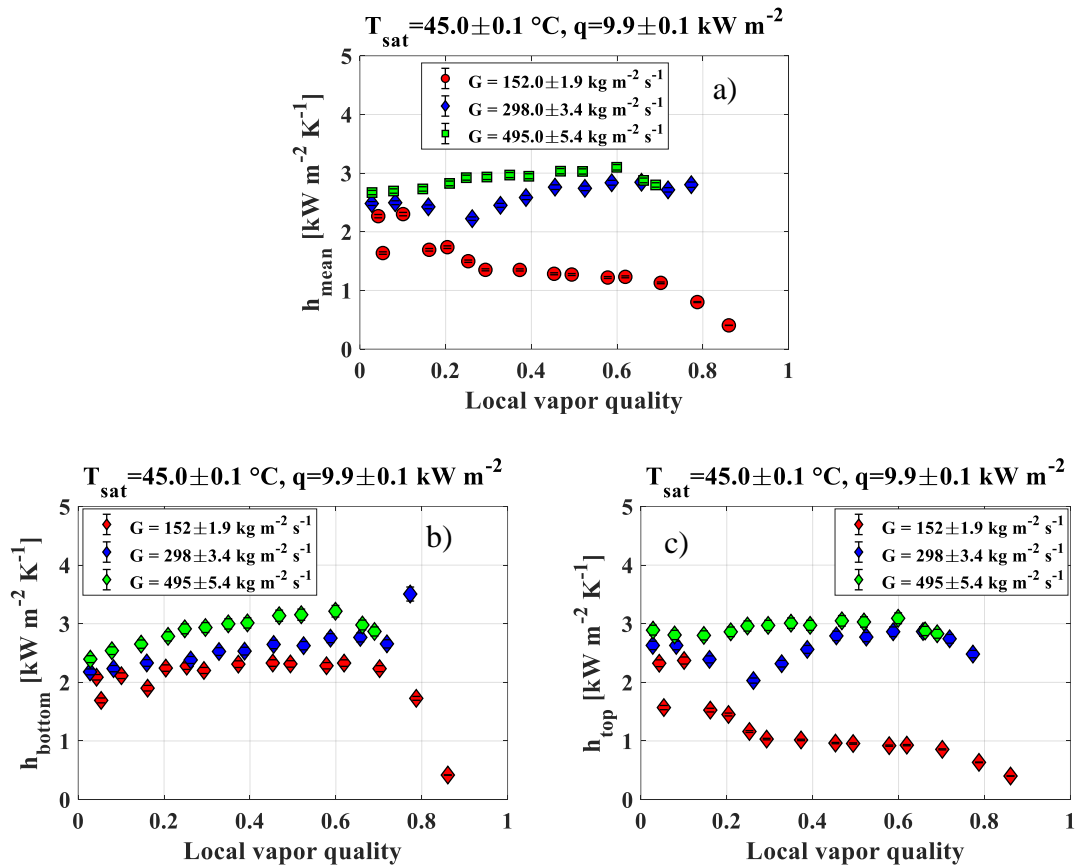


Figure 24 Effect of the mass flux on the R454C heat transfer coefficient at a bubble saturation temperature of 45.0°C and for an imposed heat flux of 9.9 kW·m⁻². (a) Average cross sectional heat transfer coefficient. (b) Heat transfer coefficient on the bottom side of tube.

The effect of the mass flux on the mean heat transfer coefficient of R455A is depicted in Figure 25. For a bubble temperature of 19°C and a heat flux of 9.9 kW·m⁻² (Figure 25 (a)) a predominant convective behavior is observed. Since the imposed heat flux is low, an increasing heat transfer coefficient with ongoing evaporation can be noticed, with enhanced value for higher mass fluxes, especially when the vapor quality is greater than 0.2. As a matter of fact, the average heat transfer coefficient at $G=496.0 \text{ kg}\cdot\text{m}^{-2}\cdot\text{s}^{-1}$ is 14.6% higher than that at $G=299.0 \text{ kg}\cdot\text{m}^{-2}\cdot\text{s}^{-1}$ for a vapor quality of 0.2, whereas its enhancement at the incipience of the dry-out is close to 53% with an increasing mass flux. The steady linear trend starting from $\chi= 0.2$, suggests the presence of a completely developed annular flow. This is ascribable to a high slip factor, due to the lower vapor-to-liquid density ratio occurring at low reduced pressures (equal to 0.23 in these conditions).

The influence of the mass flux on the R455A heat transfer coefficient for a higher heat flux ($20.0 \text{ kW}\cdot\text{m}^{-2}$) and the same bubble temperature is shown in Figure 25(b). In this case, the increased heat flux leads to an augmentation of the nucleate boiling contribution, likewise for R454C, causing a lower difference in the heat transfer coefficient at different mass fluxes. Up to a vapor quality of approximately 0.3, the effect of the mass flux is irrelevant, considering that the nucleate boiling contribution is predominant. By increasing the vapor quality ($\chi > 0.4$), the inhibition of the nucleate contribution with respect to the convective heat transfer leads to a stronger dependence of the heat transfer coefficient on the mass flux.

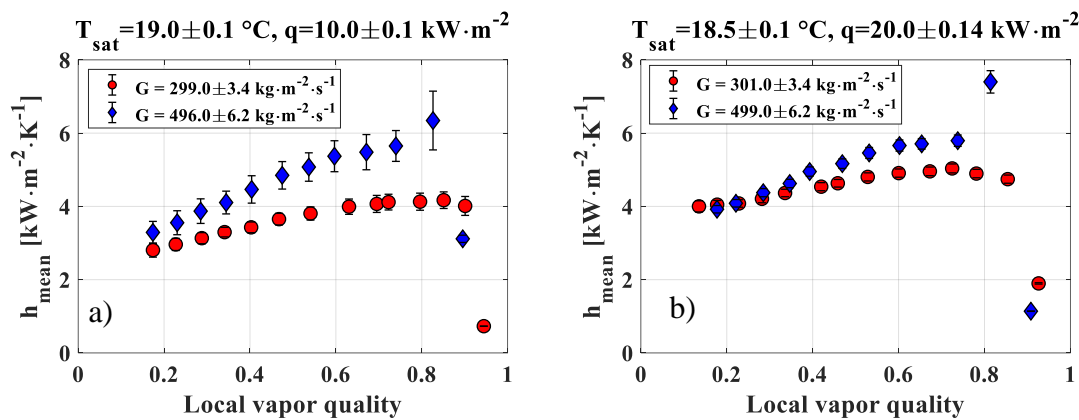


Figure 25 Effect of the mass flux on the R455A heat transfer coefficient, for a saturation bubble temperature of 19.0°C . (a) Imposed heat flux of $9.9 \text{ kW}\cdot\text{m}^{-2}$. (b) Imposed heat flux of $20.0 \text{ kW}\cdot\text{m}^{-2}$.

3.5.4 Effect of bubble saturation temperature

The effect of the bubble saturation temperature on the heat transfer coefficient of R454C is shown in Figure 26 for a mass flux of $496.0 \text{ kg}\cdot\text{m}^{-2}\cdot\text{s}^{-1}$ and a heat flux of $20.0 \text{ kW}\cdot\text{m}^{-2}$. It is evident that the increase of the bubble saturation temperature negatively affects the heat transfer coefficient. Particularly, passing from 44.9°C to 55.0°C , the heat transfer coefficient drops by 20% at the incipience of the evaporation and is almost 42% lower at a vapor quality of 0.60. The possible reason could be ascribed to the fact that an enhancement in the bubble temperature (i.e. the reduced pressure) brings to the increase of vapor density, causing a lower slip factor, lower mean velocity and therefore a depletion of the convective contribution. On the contrary, the drop of the surface tension caused by the rise in the bubble temperature facilitates the nucleate boiling heat transfer, enhancing its contribution.

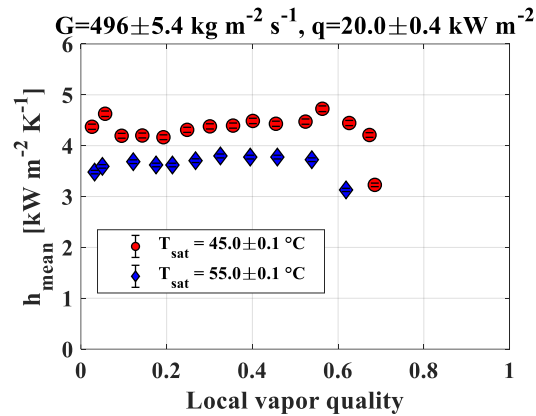


Figure 26 Effect of the saturation pressure on the R454C heat transfer coefficient for a mass flux of $496.0 \text{ kg}\cdot\text{m}^{-2}\cdot\text{s}^{-1}$ and an imposed heat flux of $20.0 \text{ kW}\cdot\text{m}^{-2}$.

Similar findings are shown in Figure 27 for the heat transfer coefficient of R455A. For a mass flux of $495.0 \text{ kg}\cdot\text{m}^{-2}\cdot\text{s}^{-1}$ and a heat flux of $10.1 \text{ kW}\cdot\text{m}^{-2}$, Figure 27 (a), it is evident that the bubble temperature negatively affects the heat transfer coefficient. In fact, up to a quality of 0.3, the decrease is limited and included in the uncertainty range, while increasing the vapor quality up to 0.8 the difference reaches 21%.

For low vapor qualities the two effects seem to be equivalent, while with ongoing evaporation the dominance of the first effect, due to a gradual depletion of the boiling contribution, can explain the heat transfer coefficient decreasing trend with saturation temperature. Moreover, the higher the bubble saturation temperature the lower the incipient dry-out vapor quality is. This is probably due to a weaker liquid film caused by the reduction of the surface tension. For lower mass flux, $301.0 \text{ kg}\cdot\text{m}^{-2}\cdot\text{s}^{-1}$, and higher heat flux, $20.0 \text{ kW}\cdot\text{m}^{-2}$, Figure 27 (b), a huge decrease (up to 40%) of the heat transfer coefficient with the increase of the bubble saturation temperature is observed. Furthermore, also its trend changes, being unaffected by the vapor quality variation, since the convective contribution seems to be suppressed, showing a behavior similar to the one seen for R454C.

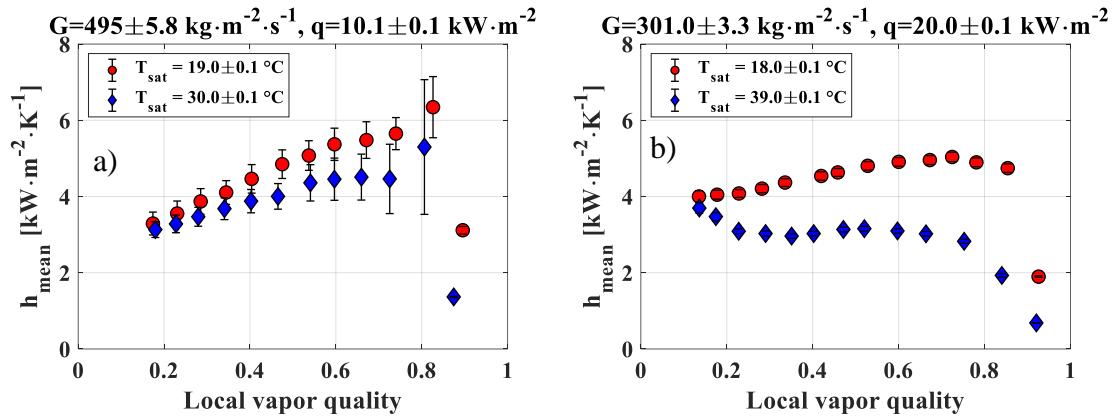


Figure 27 Effect of the bubble saturation temperature on the R455A heat transfer coefficient. (a) Mass flux of $49.05 \text{ kg}\cdot\text{m}^{-2}\cdot\text{s}^{-1}$, heat flux of $10.1 \text{ kW}\cdot\text{m}^{-2}$. (b) Mass flux of $301.0 \text{ kg}\cdot\text{m}^{-2}\cdot\text{s}^{-1}$, heat flux of $20.0 \text{ kW}\cdot\text{m}^{-2}$.

3.6 Effect of the operating parameters on the frictional pressure drop

3.6.1 Effect of mass flux

All the tests carried out for the evaluation of the frictional pressure drops along the test section are performed with the same operating conditions of the heat transfer coefficient tests, in terms of vapor quality, mass flux, and bubble saturation pressure, but in adiabatic conditions. In Figure 28 (a) is shown the effect of the mass flux on the R454C frictional pressure drop for a bubble saturation temperature of 35.0°C , while in Figure 28 (b) the same effect is depicted for R455A with a bubble saturation temperature of 19°C . For both refrigerants the frictional pressure gradient has a remarkable growth with the ongoing evaporation, caused by the increase of the mean velocity of the fluid, until a peak is reached. Subsequently, a further increase of the vapor quality leads to a decrease of the frictional pressure drop.

As can be noticed, the increase of the mass flux, and therefore of the refrigerant velocity, leads to an augmentation of the pressure drop. With the R454C these differences become higher with the ongoing evaporation, being 50% higher for a vapor quality of 0.6 passing from $300.0 \text{ kg}\cdot\text{m}^{-2}\cdot\text{s}^{-1}$ to $402.0 \text{ kg}\cdot\text{m}^{-2}\cdot\text{s}^{-1}$, while for R455A, passing from a mass flux of 299.0 and $496.0 \text{ kg}\cdot\text{m}^{-2}\cdot\text{s}^{-1}$, the pressure drop augment with the mass flux increase is almost constant increasing the vapor quality, passing from 1.8 to $4.0 \text{ kPa}\cdot\text{m}^{-1}$ (+122%) when the vapor quality is fixed to 0.3 and from 3.7 to $7.9 \text{ kPa}\cdot\text{m}^{-1}$ (+114%) for a vapor quality equal to 0.7. The difference in the behaviour of the two refrigerants can be

attributed to the fact that the experiments for R454C are carried out to a higher reduced pressure (0.3) with respect to the data collected for R455A (reduced pressure of 0.23). As a matter of fact, for R454C a higher reduced pressure leads to lower differences between the densities of the two phases and thus a slip ratio (ratio between vapor and liquid velocities) close to 1 at low vapor quality. While, increasing the vapor quality the slip ratio rises also, proportionally to the mass flux (however, this is not true for the test with a mass flux of $594.0 \text{ kg}\cdot\text{m}^{-2}\cdot\text{s}^{-1}$, when the pressure drop is higher already in saturated liquid conditions, due to a significantly higher mass flux). On the contrary, for R455A the lower reduced pressure causes a higher difference in the two phases density, the slip ratio higher than 1 (meaning a separated flow model) for both testes, already for a vapor quality of 0.2, determines a greater impact of the mass flux on the frictional pressure drop. This effect remains constant during all the ongoing evaporation.

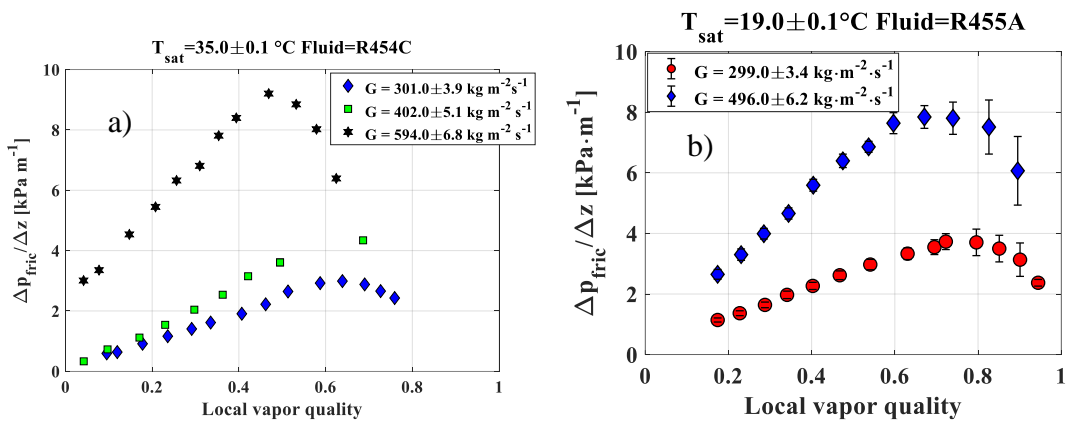


Figure 28 Effect of the mass flux on the adiabatic frictional pressure gradient against local vapor quality. (a) Effect of the mass flux on pressure drop of R454C for a bubble saturation temperature of 35.0°C . (b) Effect of the mass flux on pressure drop of R455A for a bubble saturation temperature of 19.0°C .

3.6.2 Effect of bubble saturation temperature

In Figure 29 the effect on the bubble saturation pressure on the frictional pressure drop of R454C, Figure 29(a), and R455A, Figure 29 (b), is shown for a mass flux of, respectively, $301.0 \text{ kg}\cdot\text{m}^{-2}\cdot\text{s}^{-1}$ and $495.0 \text{ kg}\cdot\text{m}^{-2}\cdot\text{s}^{-1}$. The same increasing trend with the ongoing evaporation seen before can be noticed in this case, until reaching the peak. The increase of the bubble saturation temperature leads to a decrease of the frictional pressure drop for both mixtures. As a matter of fact, by increasing the reduced pressure the vapor-to-liquid

density ratio augments as well, therefore the vapor density rises bringing to lower flow velocity and consequently lower frictional pressure drops.

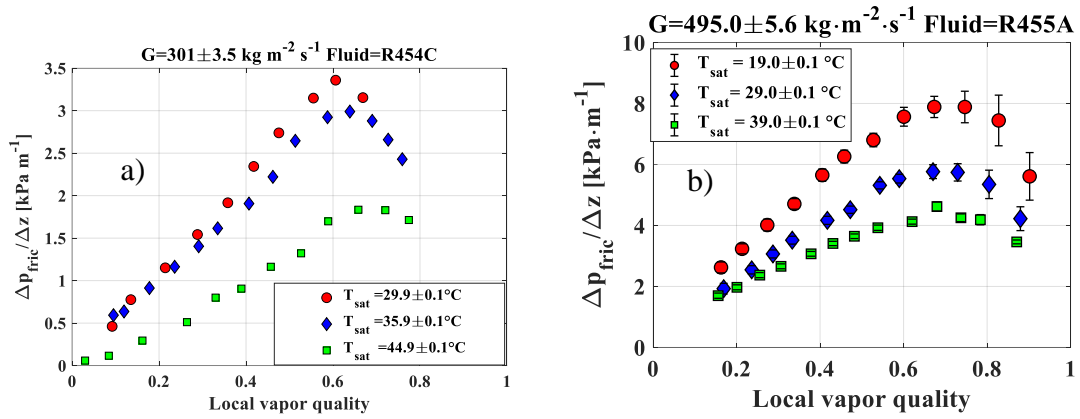


Figure 29 Effect of the bubble saturation temperature on the adiabatic frictional pressure gradient against the local vapor quality. (a) Effect of the bubble saturation temperature on pressure drop of R454C for a mass flux of $301.0 \text{ kg m}^{-2} \text{ s}^{-1}$. (b) Effect of the bubble saturation temperature on pressure drop of R455A for a mass flux of $495.0 \text{ kg m}^{-2} \text{ s}^{-1}$.

3.7 Assessment of correlations

3.7.1 Heat transfer coefficient

In the statistical analysis carried out the percentage error between the predicted and the experimental data is defined as (by considering the heat transfer coefficient):

$$ER_i = \frac{h_{\text{pred},i} - h_{\text{exp},i}}{h_{\text{exp},i}} \cdot 100 \quad (3.9)$$

Therefore, statistical parameters used for the comparison are defined as follows:

$$MRPE = \frac{1}{n} \sum_{i=1}^n ER_i \quad (3.10)$$

$$MAPE = \frac{1}{n} \sum_{i=1}^n |ER|_i \quad (3.11)$$

$$\sigma = \sqrt{\frac{1}{n} \sum_{i=1}^n (ER_i - MRPE)^2} \quad (3.12)$$

Moreover, the percentage of experimental point falling into an error range of $\pm 30\%$ is expressed as $\delta_{\pm 30\%}$.

The assessment of the heat transfer correlation for both refrigerants is carried out by excluding stratified flow, dry-out and post dry-out points.

Concerning R454C, a good agreement is obtained with the Liu-Winterton's [89] method (Figure 30), that is an asymptotic correlation ($\alpha=2$) developed with water and other refrigerants in both horizontal and vertical channels. Specifically, this correlation underestimated the experimental results, with a *MRPE* of -19.25% and a *MAPE* of 30.04%.

Due to the negative effect of the temperature glide on the nucleate boiling contribution, the Kim-Mudawar [90] correlation and the superposition model of Gungor-Winterton [91] provide huge discrepancies with the collected data, despite their proven reliability with traditional pure refrigerants. For this reason, these correlations are modified by adjusting the nucleate boiling contribution with the Thome and Shakir correction [92], as already tested for other refrigerant mixture (such as R452A) in a previous work [93].

$$h_{NB,mod} = h_{NB} \cdot \left(1 + \frac{h_{id} \Delta T_{glide}}{q} \cdot \left(1 - e^{-\left(\frac{B}{\beta_l}\right) \cdot \left(\frac{q}{\Delta i_{LV} \cdot \rho_l}\right)} \right) \right)^{-1} \quad (3.13)$$

The term h_{NB} is the nucleative boiling factor obtained for a specific correlation, h_{id} is the ideal heat transfer coefficient evaluated with the Cooper equation [94], ΔT_{glide} is the glide temperature, B is a scaling factor representing the ratio between the heat flux converted to latent heat and the total heat flux, generally assumed equal to 1.0, β_l is the liquid mass transfer coefficient, set to $0.0003 \text{ m}\cdot\text{s}^{-1}$ (typically varying among 0.0001 and $0.0005 \text{ m}\cdot\text{s}^{-1}$).

The assessment with the original and modified form of the Kim-Mudawar [90] and Gungor-Winterton [91] correlations is shown in Figure 30 (b) and (c). Cioncolini-Thome [95] developed a turbulence model for symmetric annular flow. In the present analysis

the database was filtered by considering only points with a Froude vapor number higher than 4, for which the inertia force overcomes the gravity effect. In fact, as confirmed by the present data, the condition $Fr_v > 4$ occurs for similar top and bottom heat transfer coefficients, therefore implying a symmetric liquid film. With this operation, 44 out of 262 data points were therefore used for comparison, Figure 30 (d). This correlation provides a *MAPE* of 36.14%, with the 48.98% of the points into the range $\pm 30\%$. The general assessment of several heat transfer coefficient predictive methods is provided in Table 10.

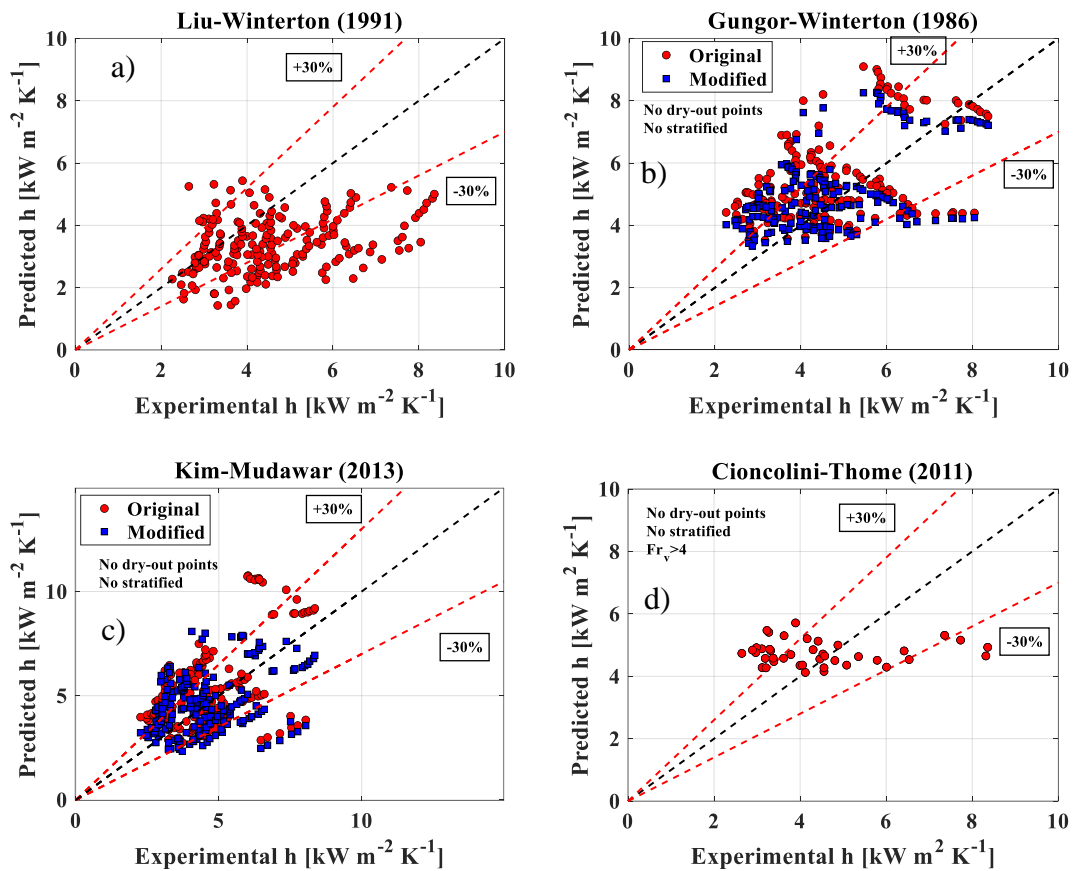


Figure 30 Experimental vs. predicted heat transfer coefficients of R454C, by excluding stratified conditions and post-dryout heat transfer. a) Liu-Winterton [89]; b) original and modified version of Gungor-Winterton [91]; c) original and modified version of Kim-Mudawar [90]; d) Cioncolini-Thome [95], filtered for only symmetric annular flow (vapor Froude numbers higher than 4.0).

Table 10 Assessment of all the chosen two-phase heat transfer coefficient predictive methods for the refrigerant R454C.

Correlation	MAPE [%]	MRPE [%]	STD [%]	$\delta_{\pm 30\%}$ [%]	Number of data points used for comparison (% of the entire database)
<i>Cioncolini-Thome</i> [95]	36.14	23.11	40.97	48.98	44 (17%)
<i>Liu-Winterton</i> [89]	30.04	-19.25	30.80	51.27	199 (76%)
<i>Gungor-Winterton</i> [91]	34.59	25.58	35.46	53.33	
<i>Gungor-Winterton</i> [91] <i>modified</i>	29.32	17.78	32.26	61.03	
<i>Kim-Mudawar</i> [90]	44.69	31.99	47.33	46.81	
<i>Kim-Mudawar</i> [90] <i>modified</i>	31.70	9.12	38.58	56.19	

Also for R455A a good agreement is provided by the Liu-Winterton [89] asymptotic model, with a *MAPE* of 19.5 % and a *MRPE* of 1.6 %. No improvement has been found applying the glide correction to this model. The experimental results show a good agreement also with the heat transfer coefficient predicted by means the Cioncolini-Thome [95] correlation, that provides a *MAPE* of 26.5 % and *MRPE* of 4.1%. The Wojtan method [96] [97], based on a flow pattern map identification, underestimates the heat transfer coefficient. For this reason, as done for R454C, also in this case some correlation, such as the Wojtan [96] [97], the Kim-Mudawar [90] and Gungor-Winterton [91] methods have been modified to take into account the nucleate boiling depletion due to the glide temperature. For all the modified correlations the assessment improves with a significant reduction of the mean errors. The best improvement was obtained by the modified Kim and Mudawar [90] model, with a new *MAPE* of 23.5% and 78.0 % of the data points falling into an error range of $\pm 30\%$. The comparison between the R455A experimental and the predicted heat transfer coefficient is shown in Figure 31 for all the aforementioned correlations, both in the original and in the modified version.

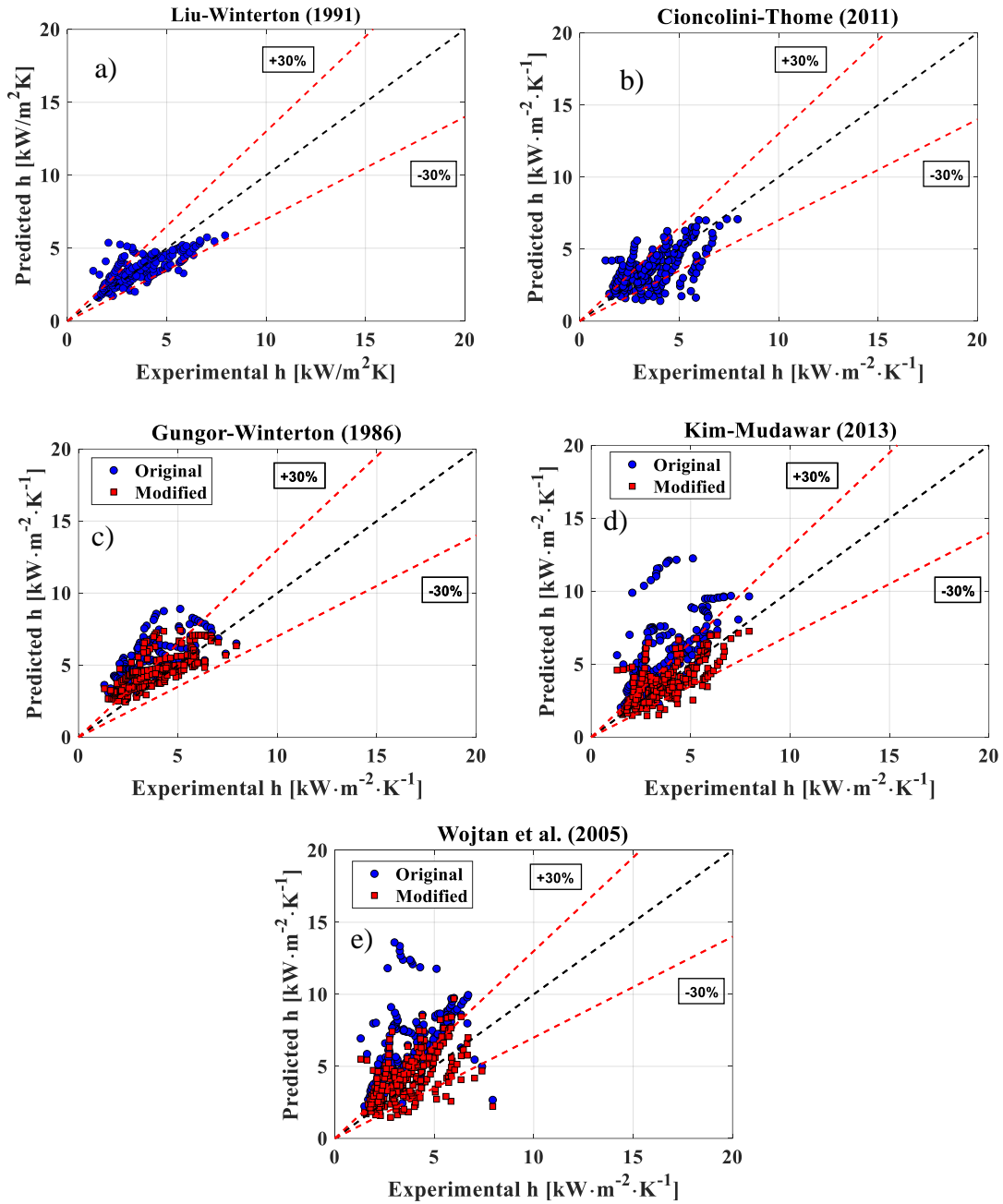


Figure 31 Experimental vs. predicted heat transfer coefficients of R455A, by excluding stratified conditions and post-dryout heat transfer. a) Liu-Winterton [89]; b) Cioncolini-Thome [95] filtered for only symmetric annular flow (vapor Froude numbers higher than 4.0); c) original and modified version of Gungor-Winterton [91]; d) original and modified version of Kim-Mudawar [90]; e) Wojtan [96] [97].

The complete assessment with the evaluation of the statistical parameters for the refrigerant R455A is provided in Table 11.

Table 11 Assessment of all the chosen two-phase heat transfer coefficient predictive methods for the refrigerant R455A.

Correlation	MAPE [%]	MRPE [%]	STD [%]	$\delta_{\pm 30\%}$ [%]
<i>Liu-Winterton [89]</i>	19.5	1.6	25.7	82.8
<i>Cioncolini-Thome (2011) [95]</i>	26.5	4.1	34.2	63.6
<i>Gungor-Winterton (1986) [91]</i>	51.1	49.2	42.0	39.0
<i>Gungor-Winterton (1986) [91] Modified</i>	32.5	29.0	30.4	56.2
<i>Kim-Mudawar (2013) [90]</i>	50.5	48.9	38.6	34.4
<i>Kim-Mudawar (2013) [90] Modified</i>	23.5	3.67	32.7	78.0
<i>Wojtan (2005) [96]</i>	53.3	51.7	33.7	10.4
<i>Wojtan (2005) [96] Modified</i>	32.6	17.9	38.0	52.6

3.7.2 Pressure drop

For both refrigerants under investigation, the experimental frictional pressure drop values have been compared with the outcomes of four correlations widely used. The methods developed by Müller Steinhagen and Heck [98] considers the two-phase pressure drop as a sort of geometrical average on the vapor quality of the all-liquid and all-vapor frictional pressure drop. Friedel [99] and Cioncolini-Thome [100] models are based on separated flow approach, where the two phases are assumed to be separated. Finally, Cicchitti [101] developed a two-phase viscosity expression useful for a homogeneous flow approach. This approximation usually leads to considerable errors when adopted for saturated vapor-liquid flows, especially for high saturation temperatures, but it could be suitable for refrigerants like R454C and R455A, that work at very low reduced pressure in the range investigated in the present chapter, in which the liquid-to-vapor density ratio is very high and reaches similar values to a gas-liquid mixture.

The comparison between the predicted and the experimental values is given in Figure 32 for R454C.

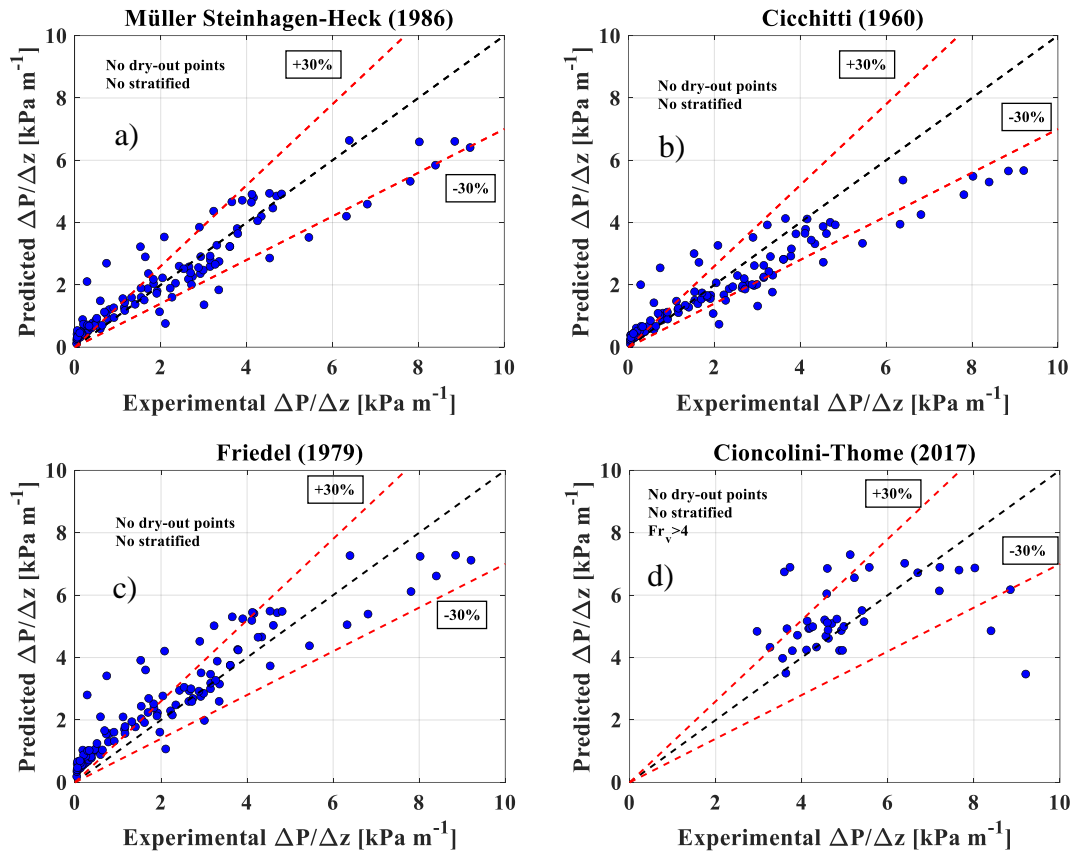


Figure 32 Experimental vs. predicted frictional pressure drop of R454C, by excluding stratified conditions and post-dryout heat transfer. (a) Müller Steinhagen and Heck [98], (b) Cicchitti [101], (c) Friedel [99], (d) Cioncolini-Thome [100], filtered for only symmetric annular flow (vapor Froude numbers higher than 4.0).

In Figure 33 the comparison between the experimental and the predicted frictional pressure drop is shown for the mixture R455A.

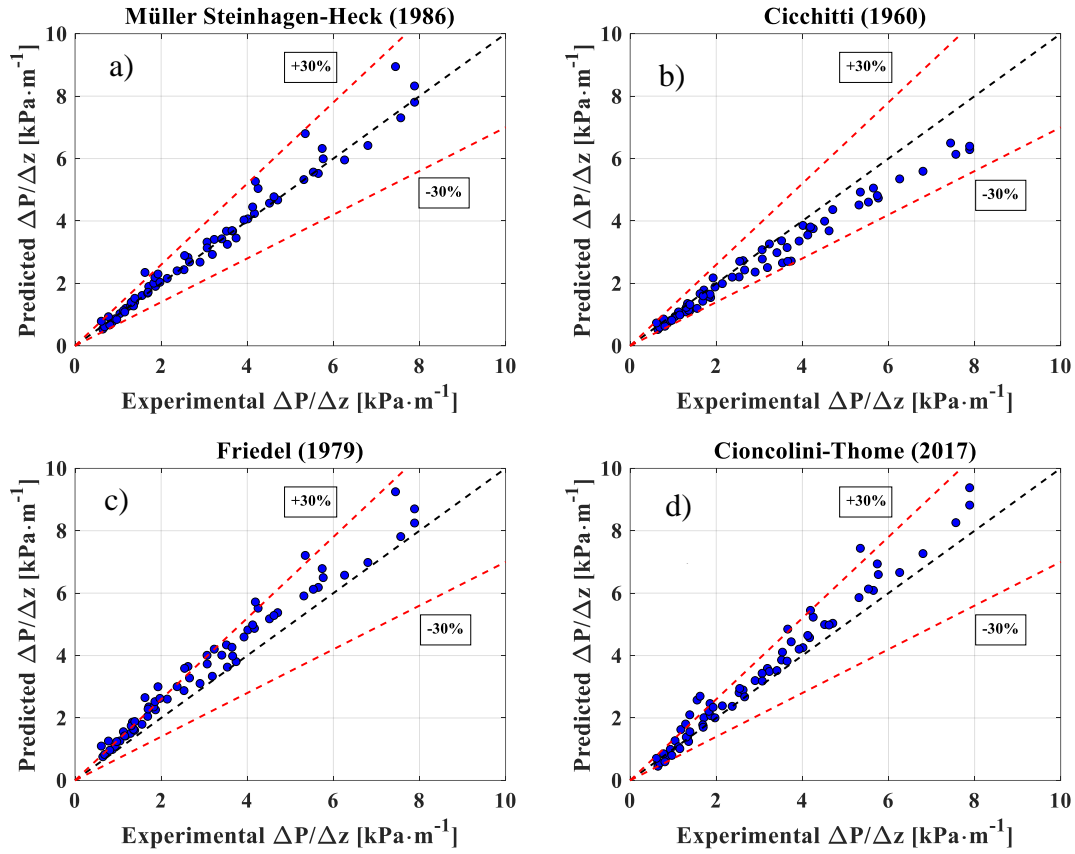


Figure 33 Experimental vs. predicted frictional pressure drop of R455A, by excluding stratified conditions and post-dryout heat transfer. (a) Müller Steinhausen and Heck [98], (b) Cicchitti [101], (c) Friedel [99], (d) Cioncolini-Thome [100], filtered for only symmetric annular flow (vapor Froude numbers higher than 4.0).

Finally, the summary of the assessment for both the mixtures and for all the tested methods is provided in Table 12.

Table 12 Assessment summary of all the chosen two-phase frictional pressure drop predictive methods.

Correlation	MAPE [%] R454C	MRPE [%] R454C	STD [%] R454C	$\delta_{\pm 30\%}$ [%] R454C	MAPE [%] R455A	MRPE [%] R455A	STD [%] R455A	$\delta_{\pm 30\%}$ [%] R455A
<i>Müller Steinhagen and Heck [98]</i>	32.56	15.27	44.47	60.87	12.8	8.78	22.1	91.7
<i>Cioncolini-Thome [100]</i>	29.62	12.25	36.29	56.98	23.4	19.9	32.0	77.7
<i>Friedel [99]</i>	39.42	31.67	45.87	55.29	28.1	28.1	23.1	66.7
<i>Cicchitti [101]</i>	34.65	6.14	46.04	55.21	13.3	-8.50	12.6	98.6

3.8 Conclusions of the chapter

This chapter deals with an experimental investigation for the two-phase heat transfer coefficient and frictional pressure drop of the low GWP mixtures R454C and R4554A, both employed as drop-in replacement for R404A. The effect of the imposed heat flux, mass flux and bubble saturation temperature from the onset evaporation up to the incipience dry-out is analysed in a smooth circular horizontal stainless-steel tube having an inner diameter of 6.0 mm. Subsequently, the collected data have been compared with several well-known predictive methods taken from the scientific literature. The main outcomes are the following:

- The increase of the mass and heat flux positively affects the heat transfer coefficient. Particularly, the greater the heat flux the higher is the influence on the heat transfer coefficient, due to the augmentation of the nucleate boiling contribution caused by the rise of the heat flux. This influence is negligible when the heat flux passes from 10 to 20 kW·m⁻², but becomes significant when the heat flux passes from 20 to 40 kW·m⁻², especially for low vapor qualities (up to 0.30), with a 60% increase of the heat transfer coefficient of R455A. For R454C at a mass flux of 298 and 495 kg·m⁻²·s⁻¹ the slight increase of the heat transfer coefficient with the vapor quality suggests the presence of a not negligible convective contribution. However, for a mass flux of 151.2 kg·m⁻²·s⁻¹, the decreasing trend of the heat transfer coefficient indicates an anticipated dry-out,

that is confirmed analyzing the heat transfer coefficient on the top and bottom sides of the channel. In case of stratified flow, the effect of the heat flux can be neglected for vapor qualities higher than 0.30, when the top side of the channel is no more wet by the liquid phase. On the other side, when the imposed heat flux increases (starting from $20 \text{ kW}\cdot\text{m}^{-2}$), the nucleate boiling contribution augmentation implies lower differences with mass flux variation, especially when the quality vapor is lower than 0.3.

- The bubble saturation temperature negatively affects the heat transfer coefficient, particularly when the mass flux is low. As a matter of fact, a higher saturation temperature brings to higher vapor density and thus lower flow velocity, causing a decrease in the convective contribution. In these conditions, an anticipated dry-out occurs at the top side of the tube, penalizing the average heat transfer coefficient.
- The assessment of the collected data with the predictive methods is performed by excluding stratified flow, dry-out and post dry-out data from the database. Moreover, some correlations have been modified [93] to take into account the not-negligible temperature glide, by using the Thome and Shakir [92] correction factor on nucleate boiling contribution. Specifically, for R454C the best accuracy is provided by the modified version of the Kim-Mudawar [90] and Gungor-Winterton [91] correlations, providing, respectively a *MAPE* of 31.70 and 29.32%. Also regarding R455A the modified version of Kim-Mudawar [90] correlation provides a good agreement, with a *MAPE* and a *MRPE* of, respectively 23.5% and 3.67%. Finally, the Liu-Winterton [89] method gives good results for both refrigerants, having a *MAPE* of 30.04 % with respect to the experimental data collected for R454C, and a *MAPE* of 19.50 % with respect to the database of the mixture R455A.
- For both refrigerants the frictional pressure drops increase with the rise of the mass flux, while it decreases with the bubble saturation temperature. Furthermore, higher mass velocities lead also to an anticipated peak of the frictional pressure drops as a function of the vapor quality.

- Comparing the experimental frictional pressure drop with those predicted by four well known correlations, it has been found that the correlation of Müller-Steinhagen and Heck [98] provides the best agreement with the experimental data collected for both refrigerants. Particularly, for R454C it provides a *MAPE* of 32.56% with the 60.87% of the data points falling into an error range of $\pm 30\%$, while for R455A, the *MAPE* is 12.8% and the 91.7% of the experimental points are within the range $\pm 30\%$. With the latest fluid, also the Cicchitti [101] correlation provides a very good agreement, with a *MAPE* of 13.3% and the 98.6% of the points included in the interval $\pm 30\%$.

PART 3

INNOVATIONS RELATED TO THE SYSTEM: HEAT DRIVEN VAPOR COMPRESSION CYCLES

4. State of the art on heat driven system

In this chapter a state of the art of the cooling technologies powered by means of low-grade thermal sources is carried out, considering the solar source or waste heat available from industrial processes or from the exhaust gas of internal combustion engines. The aim is to investigate different solutions that allow to integrate renewable sources for the cool production to pursue a reduction in energy consumption and indirect environmental impact. Firstly, a review about experimental and theoretical works dealing with already developed and mature technologies, such as absorption system and Organic Rankine cycle plus vapor compression cycle (ORC/VCC cycle) is carried out. Subsequently, the analysis of the scientific literature about a novel technology, namely the waste heat driven ejector cycle, is conducted.

4.1 Absorption systems

Among the different technologies allowing the cold production by means of low-grade thermal source, the absorption systems, especially single effect chillers using LiBr/Water as working pair, are the most developed and commercially widespread. In an overview of solar assisted system for building air conditioning, Henning [102] pointed out that in Europe the 59% of the cooling systems employing solar collectors are absorption technologies, and according to Balaras et al. [103], the 70% of the solar air-conditioning projects in Europe employ absorption technology based on the LiBr/Water working pair. As reported by Baniyounes et al. [104] absorption technologies available on the market span from 50 to 200 kW, with a thermal COP ranging between 0.3 and 1.2. Regarding single effect systems the maximum COP achievable is 0.8, for a heat source temperature varying between 80°C and 120°C. COP values up to 1.3 are obtainable with double effect systems and higher heat source temperature (up to 180°C). Similar results were reported by Guido et al. [105], that analysed the on-field operation of several small and medium scale absorption systems, with a cooling load ranging from 30 to 160 kW. The COP obtained was between 0.7 and 0.8 for most of the conditions investigated. Also in [106] is highlighted that after a careful optimization of the system single effect absorption plants can reach a COP of 0.6-0.8, while with a double effect system a higher COP, up to 1.3, can be achieved.

Several works deal with the investigation of the climate condition on the absorption chiller performance. Rosiek and Batlles [107] analysed a single effect absorption system, working with LiBr/Water, used as air conditioning system in a building located in south Spain, comparing the performance with those of conventional systems. Their results pointed out that the absorption system can lead to more than 17000 kWh saved in electricity consumption and a significant reduction in CO₂ emissions (about 13 t). Desideri et al. [108] analysed the technical and economic feasibility to use solar absorption cooling systems for two different applications: industrial refrigeration and hotel air conditioning. In the first case the adoption of solar driven absorption system can lead to a reduction in CO₂ emissions by 58%, compared to the conventional vapor compression chiller, with a discounted payback period of the investment evaluated to be approximately 10 years, considering tax allowance, and 13 years without it. Regarding the second case, a hotel located in centre Italy, absorption system brings to a 40% reduction in CO₂ emissions for air conditioning, with a payback period of the investment equal to 12 years. Bellos et al. [109] assessed the energetic, exergetic and economic performance of a 100 kW solar single-effect absorption chiller in Athens, Greece. A parametric study of the system was carried out to achieve the highest system exergetic efficiency. A cost analysis of the optimal case was performed to determine the system payback time. The results indicated that these systems would be economically attractive only when the environmental factors are considered. The results also suggested that with a decrease in the system capital costs and an increase in the electricity price, this technology can become economically viable soon, especially in countries with high solar energy potential. An energetic, economic and environmental assessment of a solar assisted heating and cooling absorption system, using LiBr/water as working pairs, for a hotel building located in Sydney, Australia, is carried out by Shirazi et al. [110]. They modelled different configurations, comparing the solutions with a gas-fired heater and a conventional electric chiller as backup solution, and different size of the absorption chiller. The results pointed out that a gas-fired backup system is extremely inefficient due to a very low primary energy savings compared to a reference vapor compression chiller. The configuration with the absorption system sized to meet the maximum cooling load required by the hotel allows to achieve a 54.51% decrease in primary energy consumption compared to the conventional system and saving almost 146 ton/year of CO₂ emissions.

However, the extremely high cost of this configuration brings to an unacceptable payback period of 94.5 years. A more economical design of the system, with the absorption system and the solar field sized to meet only the 20% of the maximum cooling demand, with a 50% of the capital costs financed by government subsidies, brings to a payback period of 4.1 years, solar fraction of about 43% and a 27.16% of primary energy consumption compared to the reference system. The same research group carried out a review about solar powered absorption chiller [111], highlighting that single effect and double effect absorption chiller can reach, respectively a cooling COP of 0.8 and 1.4, with generator temperature between 80 and 100°C in the first case and of around 180°C in the latter one. A higher efficiency can be reached with a triple-effect absorption chiller, able to achieve a cooling COP of around 1.8, but requiring a generator temperature of 240°C, that is hardly reachable with solar collectors, and consequently makes this solution scarcely analysed in scientific literature and not developed on the market. Moreover, regarding the integration systems in case of lack of solar power, the use of a gas-fired backup is inefficient for a single-effect absorption system, while it can be convenient only for double or triple-effect chillers. Finally, regarding the economic assessment of the technology, the authors pointed out that both, the high cost of the solar collectors and the absorption chiller itself dramatically affect the convenience of the system. For these reasons a policy of public funding is needed to achieve a satisfactory economic performance of these systems.

Al-Alili et al. [112] presented a thermal and economic analysis of solar driven absorption chiller situated in Abu Dhabi. The results showed that the proposed solar cooling plant reduced the electricity consumption by 47% compared to conventional cooling systems and the collector area was found to be the key parameter influencing payback period of the initial investment, being longer than 10 years also in this case. The authors did not consider the cost associated with equipment installation, integration, and piping (which can be even higher than the purchased cost of equipment) while performing the economic analysis of the system. Similar findings were found by Eicker et al. [113], who carried out a primary energy analysis and economic evaluation of solar thermal and photovoltaic cooling systems for an office building in three locations in Europe. The annual results revealed that the primary energy consumption of such systems can be up to 50% less than a reference conventional cooling system. The energetic and economic convenience of

solar assisted absorption chiller, working with LiBr/water, is evaluated also by Calise [114], for different types of school buildings and Italian climates (Milan, Naples and Trapani). The analysis is carried out by means of a zero-dimensional model, also including the dynamic behaviour of the building. It is underlined that with scarce solar radiation an auxiliary system is needed. However, most of the scientific literature considers a gas-fired auxiliary heater, that is a low energy efficiency solution. For this reason, a reversible electric driven heat pump is considered as auxiliary system. The results highlight that the proposed system allows a significant Primary Energy savings (64,7%) considering both winter and summer operations. However, despite the remarkable annual cost savings, the dramatic increase in the investment causes a scarce economic convenience of the proposed system without any public contribution to the investment. In particular, among the three locations considered, the higher payback occurs considering the case of Milan, where the drawback of the lower solar irradiation brings to worsen the thermo-economic performance of the system. On the other side, the author suggests that such a system may be profitable of new insulated buildings in Mediterranean temperate climates.

The need of an integration in case of lack of the power input in the generator is underlined also by Pongtornkulpanich et al. [115], who experimentally investigated a solar absorption cooling system having a nominal power of 35 kW, fed by 72 m² solar collectors and installed in Thailand. They pointed out that the solar collectors delivered a yearly average of 81% of the thermal energy required by the chiller with the remaining 19% generated by an LPG-fired backup heating unit. The authors also did a primary investment and operating costs investigation related to the year 2006 and expected that large-scale solar absorption cooling components production and increasing electricity costs would enable solar driven cooling technology to be more competitive.

Ghafoor and Munir [116] reviewed several works dealing with solar thermal driven cooling technologies, founding similar results of the previous works. As a matter of fact, in case of modelling work the COP of absorption systems lies between 0.6 and 0.8, and 0.45 and 0.85 for experimental system, with a generating temperature ranging between 70 and 100°C. Moreover, they underlined that they high cost of these systems requires a considerable amount of public incentives to make them economically convenient. Particularly, in case of LiBr/water as working pair the cost of the chiller is between 300

and $350 \text{ €}\cdot\text{kW}^{-1}$, that becomes significantly higher in case of Ammonia/water systems, being between 500 and $600 \text{ €}\cdot\text{kW}^{-1}$. Concerning the economic analysis, high payback time and the need for public incentives are also pointed out.

Besides solar driven absorption chillers, there are also several works dealing with cooling systems driven by waste heat from internal combustion engines. Wang and Wu [117] simulated through a black box model the thermodynamic characteristics and the off-design performance of a double effect absorption chiller having the high-pressure generator directly driven by the exhaust gas, while the low-pressure generator is driven by the jacket water waste heat. For an engine having a nominal power of 16 kW the cooling output can reach 34.4 kW, with a COP of 0.96 and an exergy efficiency of 0.186.

Tao et al. [118] simulated a waste heat powered absorption cooling system for a cargo ship application under Miami weather conditions. The cooling system reaches a cooling COP of 0.6, but if the thermal energy is considered as “freely available” the COP could be up to 9.4, significantly higher than the baseline VCC cycle, having a COP of 3.6. The proposed system can achieve a 62% reduction in CO_2 emissions. The analysis is carried out also by considering different climates, pointing out that the emissions reduction increases in hotter conditions (up to 68% in Abu Dhabi), while decreases to 38% in a colder climate (decreasing to 38% in Baltimore).

Ezgi [119] developed a thermodynamics model of an absorption heat pump driven by the exhaust gas of a ship diesel engine. The results showed that this system can guarantee up to 75477 litres and 81961 litres of fuel savings respectively, for cooling and heating, considering an operating time of 1000 hours per year. Moreover, it is also reported that the increase of the generator temperature from 90 to 100°C leads to a COP enhancement from 0.7 to 0.8, while a further increase of the generator temperature does not provide COP improvements. Shi and Li [120] modelled an ammonia/water absorption cycle driven by the waste heat of a fishing boat for ice-making applications. According to the results, being the heat source free, the system can reach a good economic convenience, having a payback of 2.5 years with an exergy efficiency of 37.85%. Udomsri et al. [121] analysed the potential of waste heat driven absorption technology in tropical locations, finding out that such systems can reduce the fuel consumption by 1 MW of fuel for each

MW of refrigeration. Moreover, the CO₂ emission can be reduced by 60% and the payback period of the proposed system is estimated to be less than 5 years.

Hsu et al. [122] carried out an optimization of a waste heat recovery district cooling system on a remote island, by means an absorption chiller sized to satisfy the peak cooling demand of 756 kW. The results showed that a 510 kW absorption chiller and a storage tank with a capacity of 1978 kWh allow to optimize the district cooling system. The averaged energy conservation rate was about 75.7% and a reduction of the electricity consumption and CO₂ emission of, respectively, 955.8 MWh and 675 tons per year was achieved. Based on these results, the investment is expected to have a four-year payback period.

However, these cooling systems have some drawbacks: LiBr/water chillers have low performance when the generation temperature is under 90°C. Furthermore, they cannot operate at generation temperatures lower than 80°C due to the vanishing of the concentration difference between strong and weak solutions. Moreover, as reported by Hassan and Mohamad [123] for temperatures higher than 200°C serious problems of corrosion occur. In addition, single-effect and double effect LiBr/Water cooling system cannot operate at condensation temperature of 50°C due to the crystallization limit at lower concentrations [124].

The problems related to water freezing and crystallization, as well as issues related to vacuum conditions, can be solved by means ammonia-based absorption system. Wu et al. [125] carried out a review of the scientific literature dealing with ammonia absorption systems, also giving the possibility to reach very low evaporating temperatures (up to -70°C). Furthermore, they pointed out also that solar drive absorption applications are very common, whereas geothermal and biomass energy systems are less studied and developed on the market.

Finally, absorption cycle is a mature technology for cold production when the heat source temperature is above 90°C, bringing to substantial energy savings compared to traditional electric chillers. However, there are some drawbacks: the payback time is extremely high without any government funding; LiBr/water working pairs cannot work at negative temperature and shows crystallization issues; ammonia/water working pair brings to security issues because the presence of ammonia, being toxic and flammable; lack of

availability of the heat source make it necessary the use of a backup system, such as a gas heated boiler, penalizing dramatically the energy saving potential of the system.

4.2 Combined ORC/VCC systems

Another interesting solution is the possibility to convert low grade waste heat into mechanical power by means of an Organic Rankine Cycle (ORC) allowing to produce electric energy to drive a VCC for cooling purposes. Aphornratana and Sriveerakul [126] theoretically analysed a heat-powered combined ORC coupled with a VCC for refrigeration purposes. The combined system is able to work with a thermal energy input at 60°C, producing a cooling temperature of -10°C. Then, after a parametric analysis varying the generator temperature between 60 and 90°C, the condenser temperature between 30 and 50°C and the evaporator temperature between -10 and 10°C, a COP ranging from 0.1 and 0.6 was found.

Several works focused the attention on the effect of the working fluid on the system performance. Bu et al. [127] developed a thermodynamic model of a solar driven ORC/VCC ice maker to investigate the influence of four different working fluids (R123, R245fa, R600 and R600a) on the system overall efficiency, also analysing the influence of generation and condenser temperature. The authors found out that the two hydrocarbons considered are more appropriate for VCC due to a higher coefficient of performance and reasonable pressure ratio. Regarding the ORC cycle, the hydrocarbons allow to higher power efficiency and smaller expander, for a heat source temperature range of 60-160°C, compared to the other fluids considered. Considering, instead, the overall efficiency and the ice production per square meter, R123 is the most suitable refrigerant for the combined ORC/VCC plant. Furthermore, the generation temperature has a great influence on the overall system efficiency, thus an optimal value, different for each working fluid, can be found. The influence of the working fluid, analysing eight different pure fluids and five zeotropic mixtures, on the overall efficiency of a solar driven ORC/VCC cycle is studied by Zheng et al. [128]. Also, the influence of the generating temperature, refrigerating temperature, superheating and internal heat exchanger is analysed. Among the pure fluids, considering an operating temperature between -5 and 80°C, the dry fluid R600a shows the better efficiency (0.22). Regarding the binary mixtures, the authors found out that there exists a composition range to achieve a higher

efficiency than that of the single component constituting the mixture. The highest system efficiency of 0.31 was found to be with the mixture R161/R600a (0.25/0.75 in mass fraction), increased by 39.6% and 54.7% compared to the efficiency of the system operating, respectively, with R161 and R600a. The inclusion of the internal heat exchanger brings to efficiency enhancement, especially for dry fluids and mixtures. Wet fluids are applicable in ORC/VCC system only with a refrigerant superheating, but it does not allow to performance improvement without the internal heat exchanger. The increase in the vapor generator outlet temperature, from 60 to 120°C brings to a huge overall efficiency increase by 199.1%.

Nasir and Kim [129] investigated the influence of different working fluids employed in a VCC powered by an ORC for domestic air conditioning. The results showed that isobutane gave the best performance in the standalone VCC, while R134a was found to be the best candidate for the ORC, considering the system thermal efficiency, pressure ratios, mass flow rate and expander outlet volumetric flow rate as evaluation criteria. Consequently, the combination of R134a for the power cycle and isobutane for the refrigeration cycle was found to be the best solution. After an optimization of the system parameters the authors found a maximum COP of 0.22. Kim and Blanco [130] found out that among eight refrigerants isobutane has the best efficiency.

The use of the same refrigerants for the ORC and VCC loops was analysed by Wang et al. [131], who developed a system that uses waste heat from engines to provide air conditioning, considering different applications, such as building and vehicles air conditioning. The considered power system is a standard ORC cycle having an internal heat exchanger and using R245fa as working fluid in the ORC loop and having a waste heat temperature of approximately 200°C. Regarding the cooling side, it operates with a standard vapor compression cycle having a cooling capacity of 5 kW, with the compressor and the expander of the ORC directly coupled and using R134a as refrigerant. The system was tested in off-design conditions, and it was demonstrated to be capable to satisfy a cooling load of 4.4 kW achieving a COP of 0.48. The same research group, [132] analysed different cycle configurations of the combined ORC/VCC system in order to investigate their effects on the overall COP. In the solution with both, subcooling and cooling recovery in the VCC, the COP reached 0.66 with outdoor temperature of 48.9°C. Subsequently, a parametric trade-off analysis was performed to find out the most critical

design parameters on the system performance. Particularly, five design parameters were selected, namely expander isentropic efficiency, condensing and evaporating temperatures, pump/boiling pressure and internal heat exchanger effectiveness. Among these variables, the increase of the expander isentropic efficiency was found to be the most beneficial on the overall COP.

Li et al. [133] studied the adoption of natural refrigerants (hydrocarbons) instead of HFC in a vapor compression cycle powered by an ORC. The results indicated that butane is the best refrigerant in case of a boiler exit temperature between 60 and 90°C, for a condensation temperature between 30 and 55°C and the evaporation temperature ranging from -15 to 15°C, with a maximum COP of 0.47, achieved when the heat source temperature reaches 90°C. Molés et al. [134] theoretically investigated a combined ORC/VCC cycle driven by low grade heat sources. The authors considered two low GWP refrigerants as working fluid in the VCC and as many fluids in the ORC side. By means of a thermodynamic model the influence of several operating conditions was studied. The performance of the system was evaluated by considering all the possible combinations in terms of working fluid in the ORC and VCC side. The results point out that the thermal COP of the system varies between 0.30 and 1.10 over the range of operating conditions considered. Particularly, an increase in the COP was found with the rise of the evaporator temperature and the ORC/VCC internal heat exchanger effectiveness, while it decreases with higher condenser temperature. Considering the electric COP, being the ratio between the cooling load and the ORC pump consumption, as performance indicator, the COP ranges between 15 and 110. Among the refrigerant investigated, their influence on the VCC efficiency was limited, with R1234ze(E) having slightly higher performance than R1234yf. Regarding the ORC cycle, the use of R1336mzz(Z) allows to slightly better thermal efficiencies and a considerable increase of the electric efficiency with respect to R1233zd(E) as working fluid.

Karellas and Braimakis [135] presented a thermo-economic model of a micro-scale trigeneration system able to combine heat, power and cool production by means an ORC coupled with a VCC. The ORC expander, the VCC compressor and the electricity generator are connected on the same shaft. The system configuration includes a single condenser in which the condensation of both cycles takes place. The heat to the ORC is provided by means of a biomass boiler and parabolic solar collectors. The effect of

various operating parameters, such as condensation and evaporation temperatures on the system performance is evaluated, also considering the impact of superheating and the installation of a recuperator. In case of evaporation temperature at 90°C without superheating, and using R245fa as working fluid, assuming an overall heat input of 50 kW and a cooling load of 5 kW, the system reaches an electric efficiency of 2.38% and an exergy efficiency of the ORC approximately of 7%. The superheating and the recuperator do not lead to a remarkable increase of the efficiency, in turn having the need for greater heat exchangers and larger solar collectors. An economic assessment of the system was carried out for a case study of a typical apartment block on a Greek Island. The reduction in fuel and electricity consumption leads to remarkable savings, giving to the whole system an acceptable payback period of 7 years.

Bao et al. [136] developed a thermodynamic model to investigate different configuration of a combined ORC/VCC plants driven by geothermal water at 140°C as heat source, in order to analyse the differences between the single-fluid and the dual-fluid configurations. The results pointed out that the optimum working fluid in the single-fluid configuration is R1234yf, achieving a COP, a cooling capacity and a second law efficiency of, respectively, 0.47, 2177.52 kW and 0.29. Since the single fluid configuration is not able to achieve high power and cooling output, the dual-fluid system is also analysed. Particularly, the greatest cooling output is reached using R1234yf and R290 as working pair, while the couple R290-R152a gives better performance. However, by changing the heat source temperature between 100 and 150°C, a change of the optimal working pair is observed. Particularly, at 100°C the optimum working fluid combination is R1270-R152a, whereas for a heat source temperature of 150°C the optimum is reached with R1234yf-R152a. In general, higher the heat source temperature better the system cooling capacity, COP and second low efficiency are. Meng et al. [137] analysed a cascade ORC/VCC system from the energetic, economic and environmental point of view. Particularly, they highlighted that the best performance of the proposed system can be reached increasing the heat source temperature. As a matter of fact, with its rise from 80 to 190°C the system payback time drops from 20.46 to 3.25 years, with a variable trend that becomes lower and lower with the increase of the heat source temperature. This is attributable to the increase of the system thermal efficiency, from 30% to 50% with the heat source temperature increase. Also, the reduction in CO₂ emissions follows a similar

trend, passing from 700.3 kg per year when the heat source temperature is 80°C to 13376.4 kg per year for a heat source temperature of 190°C.

The influence of the working pairs in a double-fluid ORC/VCC system for air conditioning purposes is analysed also by Nasir et al. [138]. They found out that for a condenser temperature of 30°C, the optimal working pair is R245fa-R600a, while increasing the condenser temperature at 35 and 40°C, the best solution is the one using R600a in the ORC loop and R245fa in the VCC.

A thermodynamic model of an ORC/VCC system driven for recovering the waste heat of bottom slag in coal-fired plant is proposed by Liao et al. [139]. R1234ze(E) and the working pair heptane/R601a are selected as the optimal working fluids for the single-fluid and dual-fluid configurations, respectively. A parametric analysis is performed to quantify the effect of several working parameters, such as the superheat degree at the turbine inlet, the chilled water mass flow rate and condenser temperature on the coefficient of performance, thermal efficiency, heat exergy, cooling exergy, total exergy production and exergy production rate. They found out that the increase of the superheat degree at the turbine inlet benefits the exergy efficiency of the system. Enhancing the chilled water mass flow rate leads to an increase of the refrigerating capacity and COP, whereas causes a reduction in cooling exergy, total exergy production and exergy production rate. The rise of condenser temperature leads to a huge decrease in terms of all the performance parameters considered.

Bounefour et al. [140] conducted an exergy analysis of different ORC/VCC layouts for waste heat recovery onboard ships. Three different layouts of the ORC are investigated, namely a simple ORC, an ORC with internal heat exchanger and a serial cascade ORC, considering R134a, R600 and R600a as possible working fluids. For all the configurations the increase of the heat source temperature leads to an overall COP increase due to a higher power production in the ORC sub-cycle, which results to be more efficient, while the COP of the VCC is not affected by this change. The analysis of the rate of exergy destruction in each component constituting the system points out that the higher loss belongs to the ORC condenser, followed by the other heat exchangers (VCC evaporator, ORC boiler, VCC condenser), then the VCC compressor, the ORC expander and finally the VCC throttling valve and ORC pump. Among the three fluids analysed, butane is the

one resulting in lower exergy loss. The solution with the internal heat exchanger and the serial cascade allows to, respectively, a 0.52% and 2.41% higher overall COP compared to the solution with the baseline ORC. Among the different fluid combinations in the dual-fluid configuration, the higher COP is achieved by using R600 in the ORC subsystem and R600a in the VCC.

Liang et al. [141] designed a prototype of a waste heat driven ORC/VCC system to recover exhaust heat from internal combustion engine. R245fa and R134a are selected, respectively, as working fluid of the ORC and VCC. The system achieves an overall efficiency of 0.18 (being the ratio between the cooling capacity to the heat input) with a hot water temperature of 95°C, a cool production of 1.8 kW and providing a refrigeration effect at -4°C.

4.3 Heat driven ejector systems

Instead of running an Organic Rankine cycle to produce mechanical power needed for a vapor compressor cycle, an interesting solution is represented by the heat driven ejector cooling cycle, that allows to use the heat to directly drive a novel vapor compression cycle. This system is made up by a direct/indirect system by means of a single-phase ejector. As a matter of fact, superheated vapor is generated in the power loop, constituting the ejector primary flow. Subsequently, going through the ejector nozzle, it allows the entrainment of the low-pressure vapor from the evaporator, that provides the cooling effect. In this way the refrigerant compression in the low-pressure loop (where the cooling effect is provided) happens by means of a static element, namely the single-phase ejector, whereas to compress the working fluid in the high-pressure side of the plant there is a liquid pump, which power absorption is significantly lower than the compressor.

Bellos and Tzivanidis [142] simulated, in steady-state conditions, a solar ejector refrigeration system for different evaporator temperatures and different condenser temperatures, from -10 to 10°C and from 30 to 50°C, respectively, investigating the effect of different refrigerants. The results pointed out that R141b is the best fluid in all the operating conditions simulated, finding the maximum COP of 0.23 for a cold production at 10°C and a condenser temperature of 30°C. The optimum generator temperature was found to be between 114 and 157°C, providing a cooling capacity ranging from 1.85 and 23.39 kW. Elakhdar et al. [143] presented a 1D thermodynamic model for a constant area

mixing ejector employed in an ejector enhanced vapor compression refrigeration cycle, using a zeotropic mixture of R290/R600a in a domestic refrigerator. The COP and the cooling capacity are evaluated for the novel cycle under optimal operating conditions and then compared with those of the conventional cycle using R134a and the mixture R290/R600a. Firstly, the optimal mass fraction of R290 is found to be the 60%. Then, the results pointed out that the proposed mixture brings to COP and cooling capacity enhancement by, respectively, 23% and 62.71%. Moreover, the proposed cycle has 70% higher COP and cooling capacity than the conventional vapor compression cycle. Zegenhagen and Ziegler [144] experimentally investigated an ejector cooling cycle employing R134a and operating in double choking conditions. The ejector performance is characterized by its entrainment ratio. Particularly, similar values of the ejector entrainment ratio and system thermal COP are found, while the cooling capacity increases with the motive pressure.

Butrymowicz et al. [145] tested a heat driven ejector refrigeration cycle driven by waste heat from small size maritime combustion engines which nominal load is between 100 and 250 kW. The system can provide 30 kW of cold production from 75 kW of heat recovered from the exhaust gas. Moreover, the authors pointed out that also the heat from the water jacket cooling can be recovered to provide hot sanitary water and to satisfy the thermal load, covering almost all the mid-sized vessels thermal demand. The same research group [146] performed also another experimental study dealing with an ejector cycle for air conditioning, using R1234ze as refrigerant and activated by waste heat. A maximum thermal COP of 0.3 is achieved, demonstrating the feasibility to employ waste heat from a marine piston engine to drive the system in a wide range of heat source temperatures.

Hasan et al. [147] compared different heat driven technologies for cold production, pointing out that direct cooling system, such as absorption system and ejector system are characterized by a lower exergy destruction and payback period (between 5 and 7 years) compared to the indirect cooling system (ORC coupled with VCC), that has a greater exergy destruction and higher payback period (between 5 and 7 years more than the previous solutions). A comparison between these technologies was performed also by Lillo et al. [148] Firstly, after an investigation between several refrigerants, the higher COP for the ejector cycle is achieved employing ammonia as working fluid. Afterword,

the performance of the ejector cycle is found to be slightly worse than those of the single-effect absorption plant, with similar investment costs, whereas a higher COP and lower set-up costs are found in comparison with an ORC/VCC plant. Consequently, the authors pointed out that ejector cycle can be considered an interesting solution, especially for low size applications, for which the other technologies are not commercially developed. Moreover, they highlighted that an optimization of the ejector cycle design could bring to a huge performance improvement.

Several studies focus on the analysis of different working fluid to find the most suitable in the ejector cycle. Sun [149] developed a thermodynamic model to investigate the effect of the working fluid on the ejector cycle performance. The higher performance was obtained with R152a (COP of 0.5) and R500 (COP of 0.47). A correlation between the COP variation range and the entrainment variation range for several working fluids was found. Cizungu et al. [150], compared the performance of R123, R134a, R152a and ammonia. They found out that the COP and the entrainment ratio are strongly dependent on the ejector geometry and compression ratio at different values of generator temperature. Furthermore, they observed that R134a and R152a are more suitable for heat sources at 70-80°C, while ammonia is more appropriate for temperatures higher than 90°C. The highest COP, equal to 0.45, was achieved using R134a. Similar results were presented by Selvaraju and Mani [151], who also found a maximum COP of 0.4 using R134a as working fluid. Kasperki and Gil [152] carried out a theoretical analysis based on the 1D model developed by Huang et al. [153] to investigate the performance of different hydrocarbons and the optimal temperature of the vapor generation. The optimum generator temperature and entrainment ratio were found to increase with the hydrocarbon heaviness, whereas the COP does not follow the same trend. Particularly, the highest COP, equal to 0.32, was found for R600a at a generation temperature of 102°C, while for R601 the maximum COP, of 0.28, was achieved at a generation temperature of 165°C. Later, the same research group [154] investigated different working fluids for a wide range of heat source temperatures (from 70 to 200°C). None of the refrigerant analysed was able to accommodate the entire operating range, and each fluid allowed to achieve the maximum ejector entrainment ratio and system COP for a certain optimal generator temperature. Consequently, the optimal working fluid depends on the generation temperature achievable. Moreover, among all the tested configurations, the higher COP

of about 0.35 was obtained using cyclopentane with a generator temperature higher than 190°C. On the other side, the lower performance was obtained for toluene, with a COP lower than 0.2 in the whole range of generator temperature. Chen et al. [155], by means of a numerical model, investigated several working fluids, considering wet, dry and isentropic fluid in an ejector refrigeration system. To avoid droplet formation, that is highly unwanted in a single-phase ejector, when working with wet fluid the primary flow should have a sufficient degree of superheating before entering the primary nozzle. They also developed a numerical procedure to find the minimum superheat needed to avoid droplet formation. It is crucial to provide the optimal superheating, that guarantees the elimination of the droplet formation and allows the primary flow to leave the nozzle at vapor saturated conditions. An over-superheating has a limited effect on the ejector entrainment ratio and no effect on the COP, while it causes a decrease in the system ideal efficiency. For dry and isentropic fluids, the superheat can be avoided as long as the refrigerant does not operate at temperature levels close to the critical temperature. R600 was found to be a good option considering both system performance and environmental aspects. The same research group, in [156], focused the attention on the analysis of the ejector operating characteristic, analysing the effects of external parameters (generator, condenser and evaporator saturation temperature, primary and secondary flow superheating) and internal parameters (efficiency of ejector components). They found that the COP and the entrainment ratio increased with generator and evaporator temperatures, while decreased with the rise in the condenser saturation temperature. However, after a certain value of the vapor generator temperature the ideal efficiency may decrease. For this reason, an optimal vapor generator temperature is required for each fluid to achieve the maximum ideal efficiency, while the increase of the evaporator temperature and the decrease of the condensation temperature always allow to reduce the ejector irreversibility. The influence of the primary and secondary fluid superheating was found to have a significant influence on the system performance when wet fluids are employed. The higher COP is reached using R141b as refrigerant. Shestopalov et al. [157, 158] studied both, numerically and experimentally, the design and off-design functioning of an ejector cooling system. After a preliminary screening of several working fluids R145fa was found to be the best solution. Then, the experimental results were validated on an

experimental prototype, built also to investigate the NXP and the shape of the mixing chamber on the overall system efficiency.

Several works deal with the analysis of the ejector geometry and operating conditions on the system performance. Sun [159] presented an experimental and theoretical analysis underlining that the use of a fixed-geometry ejector in the refrigeration cycle limits the system COP (approximately to 0.2-0.3) making it difficult to run the system maintaining acceptable performance under a wide range of operating conditions. Consequently, it is highlighted the necessity to adopt an ejector with a variable geometry, allowing to increase the performance and to operate the ejector in a wider range of operating conditions. The ejector geometry can be changed having a movable spindle that varies the motive nozzle throat section, as experimentally demonstrated by Pereira et al. [160] in a 1.6 kW cooling system. The change in the spindle position, causing a primary flow variation up to the 80%, implied COP variation between 0.45 and 0.88. Consequently, COP improvement up to 85% were obtained and the existence of an optimal spindle position, depending on the operating conditions, was demonstrated. Mazzelli and Milazzo [161] tested a supersonic ejector chiller for industrial refrigeration and for air conditioning purposes. The system has a nominal cooling power of 40 kW, employs R245fa as working fluid, and is driven by a low temperature heat source (from 90 up to 100°C). The ejector has a movable primary nozzle. A numerical analysis, considering the real gas behaviour of the refrigerant, was carried out to analyse the internal dynamics of the ejector. Comparing the numerical results with the experimental data, a close agreement was found. After an ejector redesign and optimization, the system reached quite high levels of COP, close to those obtained with single effect absorption systems. The critical condenser pressure was found to be a crucial parameter in the ejector functioning, due to its low value. The authors underlined the importance to limit the friction losses to increase the critical pressure. The effect of the primary nozzle throat diameter was experimentally analysed also by Meyer et al. [162], keeping constant the secondary ejector throat diameter and using water as working fluid. They found out that the minimum generator temperature decreased with the nozzle diameter rise. A maximum COP of 0.253 was found for the maximum nozzle diameter tested. Aphornratana and Eames [163] investigated the effect of the nozzle shape and position on the ejector cycle performance. Particularly, they found a cooling capacity and COP increase when retracting the nozzle

into the mixing chamber. Moreover, also in this case is underlined that exists an optimum nozzle position, related to all the operating conditions.

Other authors focused the attention on the ejector area ratio beyond the nozzle position. Varga et al. [164], by means a CFD analysis, found that by increasing the ejector area ratio the entrainment ratio increases, but the critical back pressure decreases. These results were confirmed by Dong et al. [165], that investigated the effect of the area ratio and the nozzle position in a prototype using water as working fluid. Three ejectors having the same nozzle, but different area ratio, were built to investigate the effect of the nozzle exit position (NXP), area ratio and the operating temperatures. The generator temperature is ranged between 40 and 70°C, with a fixed evaporating temperature of 15°C. They stated that the increase in the generator temperature led to a decrease of the system COP but allows the system to operate in a wider range of operating conditions (i.e., condenser temperature), due to an increase of the critical back pressure. They also found that there is an optimum NXP related with the area ratio, and for fixed operating conditions the COP decreases for lower area ratio, until the ejector is no longer operating. Selvaraju and Mani [166] studied 6 different geometric configurations of the ejector varying the evaporator, generator and condenser temperature. Fixed the evaporator and condenser saturation temperature, there exists an optimum generator temperature that maximizes the ejector entrainment ratio and the overall COP. Moreover, having set the primary flow conditions, an increase in the area ratio caused an entrainment ratio increase, while the pressure recovery decreased. Yapici et al. [167], using R123, theoretically and experimentally demonstrated that exists an optimum value of the vapor generator temperature to maximize the COP as a function of the ejector area ratio for fixed evaporator and condenser temperatures.

Del Valle et al. [168] tested a R134a ejector investigating the effect of the mixing chamber, by means of three different geometries. They found that the shape of the mixing chamber has a large influence on the ejector performance. Jia and Wenjian [169] examined the optimal area ratio for an ejector employed in a cooling cycle utilizing R134a and having a cooling capacity of 2 kW. The ejector was designed with a 1D approach and then six different ejector areas were investigated experimentally, under various operating conditions, by using an ejector with a movable spindle. They found a linear relationship between the optimum area ratio and the increase of the primary flow pressure. They also

found that the cooling capacity is affected by the area ratio and the nozzle diameter, while the COP is only influenced by the area ratio. Ma et al. [170] inserted a spindle into an ejector designed for a 5 kW ejector cooling cycle in order to modify its primary flow. The cycle uses water as working fluid with a generation temperature of 90°C. They experimentally investigated the effect of the spindle position, the generator temperature and the evaporator temperature on the ejector performance. The spindle position movement towards the nozzle causes a primary flow decrease and thus a lower cooling capacity. They demonstrated the existence of an optimum area ratio leading to an optimum entrainment ratio and overall COP. The rise in the evaporator temperature allows to increase the entrainment ratio, the cooling capacity and the COP, whereas the increase of the generator temperature does not necessarily lead to performance enhancement, even though the primary flow increases.

Van Nguyen et al. [171] investigated a solar driven ejector air conditioning system. Also in this case the advantage to use a variable geometry ejector was underlined, with COP improvement up to 24%, reaching a maximum thermal COP of 0.29. Aidoun and Ouzzane [172] simulated an ejector refrigeration system considering different ejector operating characteristics. The mixing chamber geometry, the fluid properties, the inlet and the outlet conditions can affect the fluid mixing conditions and consequently cause a decrease of the ejector performance in off-design conditions. Moreover, due to the inefficient mixing and normal shock waves, the internal superheat generation in off-design conditions becomes relevant on ejector performance. To prevent droplet formation inside the ejector, a primary flow superheating of 5°C is needed. A larger superheat causes a decrease in the condenser efficiency. Varga et al. [173] performed an experimental campaign on a small scale solar driven ejector cooling system installed in Porto, Portugal. The system has a nominal cooling capacity of a 1.5 kW, uses R600a as refrigerant and has a variable geometry ejector. The experimental data were collected during the summer, and they found a cooling capacity ranging from 1 to 2 kW, depending on the operating conditions, with a thermal COP varying between 0.15 and 0.4 and an electrical COP of about 4.6. The results pointed out the good system stability during the sunny days or during overcast days with a short interruption of the solar radiation. Moreover, concerning the operating conditions, the system was found to work properly with a generator temperature above 70°C and a condenser temperature up to 34°. For higher condenser temperatures a higher

generator temperature is needed. They also demonstrated the benefits to use a variable geometry ejector and the existence of an optimal spindle position, allowing a COP enhancement up to 35%.

Since the ejector performance is very sensitive to the boundary conditions, namely the evaporator, condenser and generator saturation temperatures, different studies investigate specifically the effect of the operating conditions on the ejector performance. Boumaraf and Lallemand [174] investigated the performance and the operating characteristics of the ejector cycle using R142b and R600a. For a fixed ejector geometry and evaporator temperature for an ejector working in critical mode, the COP decreases if the generator temperature exceeds the design point. Consequently, the authors suggest designing the ejector at the highest possible generator temperature, guaranteeing a better performance at lower heat source temperature. Chunnanod and Aphornratana [175] studied the static pressure trends through the ejector with variable operating temperature and different degrees of superheating of the primary flow considering different heat input, ejector geometry and nozzle positions. An increase of the vapor generator pressure as well as the increase of evaporator temperature (losing the desired cooling temperature) leads to a COP enhancement. The influence of the superheating of the primary flow on the system performance was found to be negligible. Li et al. [176] tested an ejector refrigeration cycle working with R134a, to investigate the effect of the operating parameters and area ratio. They found that the ejector performance is directly affected by the condenser pressure, that should be lower than the critical value to guarantee the proper functioning. By having fixed the evaporation and condensing temperatures, the entrainment ratio, COP and cooling capacity firstly increase and then decrease with a rise in the generator temperature, since the operating mode changes from subcritical to critical. Consequently, there is an optimum generating temperature. The increase in the ejector area ratio results in a higher critical entrainment ratio, while it decreases the critical condensing temperature.

As reported in the previous works, ejector performance is very sensitive to the boundary conditions, thus, different research groups have been focused on the analysis of solution to enhance the system performance, such as a compressor and an ejector in series, to increase the entrainment ratio. According to this plant scheme, the secondary flow is compressed by the compressor before entering the ejector. Boumaraf and Khadraoui

[177], developed a simulation model for a hybrid compression/ejector cycle driven by solar energy at low or medium temperature. Specifically, an air conditioning system with a cooling capacity of 10 kW is simulated, having water in the ejector loop and R1234yf for the VCC, with the two cycles separated by an intercooler. A 50% COP improvement is achieved with the proposed system in comparison to the stand-alone VCC cycle. Suresh and Datta [178] proposed a hybrid ejector cycle integrated in a traditional vapor compression cycle for automotive air conditioning. The proposed system switches between three operation modes, namely compressor, ejector and hybrid. A theoretical model based on the refrigerant real gas property is developed, exploiting both critical and sub-critical operation modes using a variable area ejector. Several environmentally friendly refrigerants are analysed, investigating the system performance over a wide range of operating conditions in terms of evaporator, condenser and generator temperatures. Due to the presence of the compressor and the ejector in series, the compression ratio is reduced by 54% in the hybrid mode, increasing the cooling capacity by 22% compared to the traditional VCC. Moreover, this configuration allows to a COP four times higher than the standalone ejector mode. Wang et al. [179] developed a hybrid ejector prototype combining a vapor compression cycle and an ejector refrigeration cycle. Two ejectors with different mixing chamber diameters were tested and the system was operated under various working modes, to investigate the effect of the operating conditions. The authors verified that the COP of the hybrid cycle was around 34% higher compared to the conventional VCC. Dorantes et al. [180] numerically compared the performance of the combined compression ejector cycle and the simple ejector refrigeration cycle, founding a COP more than double for the first solution, but underlining that the coupling between booster compressor and ejector in series may cause control issues. Takleh and Zare [181] optimized the exergy efficiency of a booster compressor assisted ejector cycle for six environmentally friendly refrigerants and with an evaporating temperature between -5 and 5°C. They found that an exergy efficiency improvement by 5.5% and 11% was obtained with respect to the simple ejector cycle. Moreover, an optimum booster pressure ratio was found, depending on the operating conditions. Zhu and Jiang [182] simulated a combined ejector cycle using R152a and R22 founding a COP increase of 5.5% and 8.8%, respectively, compared to the basic system. Mansour et al. [183] numerically compared a hybrid ejector-compressor booster and two cascade compressor-ejector cycles with

respect to a traditional VCC. After an optimization of the proposed solutions, substantial improvements with respect to the conventional VCC were found. Particularly, the COP, that is equal to 3.71 in the conventional cycle, increases up 4.49 in the hybrid cycle and, respectively, 5.21 and 4.12 in the two cascade systems analysed. Sanaye et al. [184] proposed a novel combined ejector refrigeration cycle, constituted by a simple vapor-vapor ejector refrigeration cycle and a simple liquid-vapor ejector refrigeration cycle, carrying out an energy, exergy, environmental and economic analysis. The results underlined that a 18% higher COP, a 25% higher exergy efficiency and a reduction up to 31% and 8%, respectively in electricity consumption and annual cost for a fixed cooling capacity can be achieved in comparison with another combined (hybrid) ejector compressor refrigeration cycle (namely a simple vapor-vapor ejector refrigeration cycle plus a traditional vapor compression cycle).

In some cases, the availability and the discontinuity of the heat source at disposal does not allow to satisfy the cooling demand, requiring a mechanical integration by means a compressor working in parallel with the compressor, able to provide the cooling load when the ejector is not activated by the waste heat. Evely and Alkendi [185] simulated a solar driven compressor assisted multi-ejector chiller for a 36 kW air conditioning system. Firstly, the advantages to use a multi-ejector pack instead of a fixed geometry ejector is underlined, since it contributes to widen the condenser temperature of the system, allowing the ejector cycle to have acceptable performance also in off-design conditions. Furthermore, the proposed solution, using R245fa as working fluid, enables to reduce of 24 MWh_e the electricity consumption compared with split air conditioning, saving 15.7 tons of CO₂-equivalent emissions. Also Xu et al. [186] proposed a numerical evaluation of a solar powered hybrid ejection-compression cycle, with the ejector and the compressor working in parallel, for air conditioning or refrigeration purposes. The system performance was evaluated with five different refrigerants, finding that R152a constitutes the best solution due to its characteristics. The proposed cycle has a higher electrical and thermal COP compared to the conventional one and for a generator temperature of 90°C the novel cycle consumes only 66.6 kW of heat to increase the electric COP from 3.01 to 3.76, whereas the conventional hybrid ejector cycle (working with compressor and ejector in series) requires a three times higher power input in the vapor generator to achieve the same COP. Moreover, the novel cycle has also a higher cold production per m² of solar

collector. The same research group [187] analysed a solar-heat-driven ejector assisted combined compression cycle designed for a multistore building located in Shanghai, founding that the proposed system can reduce the electricity consumption up to 11.8% resulting in a 203.17 MJ savings per day.

From the literature analysis about ejector hybrid cycles, it emerges that most of the works focus on the following topics: the research of the optimal working fluid; the effect of the operating conditions on the ejector performance and the optimization of its geometry in order to widen the ejector operating conditions without performance deterioration; the development of ejector/compressor hybrid cycle to increase the ejector entrainment ratio, to enlarge its operating conditions and to improve the system performance. However, there are very few works dealing with a thermo-economic comparison of the novel cycle with respect to more widespread chiller technologies, such as the electric chiller.

5. Waste heat driven ejector cycle modelling

This chapter deals with the analysis of a technology innovations at system level, by numerically investigating a novel hybrid ejector cycle, made up by a direct/indirect system, with the presence of an ejector that allows to compress the refrigerant without using a compressor. Particularly, the proposed plant scheme allows to employ renewable energies, being potentially more efficient than the traditional electric driven VCC and resulting in lower power consumption and indirect environmental impact. All the equations to model each component constituting the system are shown, altogether with the resolution algorithm for the system sizing and simulation for each of the different system layouts under investigation. The thermo-economic analysis will be then carried out in the subsequent chapters of the thesis, to assess the performance and the economic feasibility of this system with regards to different applications, and to carry out a comparison with the reference electric chiller technology.

5.1 Objective of the research

The aim of the present chapter is to develop a thermodynamic model simulating hybrid ejector cycle, in order to carry out, in the subsequent sections, a thermo-economic analysis of the proposed systems, with different layouts and different applications, either using waste heat or the solar source for domestic applications, or by using waste heat from engine for a cruise ship air conditioning system. For each application, the model will be used to size the system and then to carry out seasonal simulations to compare the proposed technology with absorption systems and traditional VCC.

Particularly, in Chapter 6 is investigated an ejector cooling system for domestic air conditioning considering a free thermal source continuously available. Then, in Chapter 7 a hybrid multi-ejector compressor assisted chiller driven by solar energy for a domestic chiller is analysed. Finally, in Chapter 8 a waste heat driven multi-ejector compressor assisted for air conditioning of a cruise ship operating in the Baltic Sea is studied.

5.2 System modelling

5.2.1 Ejector model

The ejector under investigation, being a single-phase ejector, work with both, the primary and the secondary flows in superheated or saturated vapor conditions, as well as the

mixing flow at the diffuser exit. A schematic representation of the ejector is shown in Figure 34(a), while the refrigerant processes, both for the primary and the secondary flows, are reported in Figure 34(b).

The operating principles of the ejector are here summarized:

- **Nozzle section:** A high-pressure superheated steam, constituting the ejector primary flow, reaches sonic conditions in the nozzle throat and then increases its velocity reaching supersonic conditions at the nozzle exit (section 3). Here, the primary flow, reaching a pressure lower than the evaporator one, allows the entrainment of the low-pressure secondary flow from the evaporator.
- **Mixing section:** the contact and the mixing between the two flows in the mixing chamber determines a deceleration of the primary flow, while the secondary one continues accelerating. The two flows are completely mixed at a certain section of the mixing chamber and their development continues until the end of this section, where the compression shock occurs.
- **Diffuser section:** the normal shock that is induced at the end of the constant area section leads to a compression effect, with the velocity that suddenly decreases from supersonic to sonic. A further pressure recovery is achieved in the diffuser, from which the total flow is discharged at the condenser pressure.

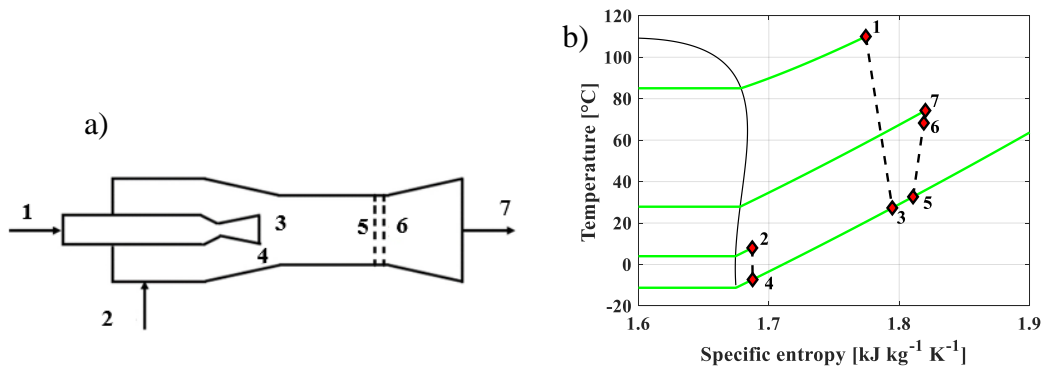


Figure 34 (a) Schematic representation of the single-phase ejector. (b) Ejector internal transformation on T-s diagram.

The ejector performance is highly affected by the boundary conditions, as underlined in the state of the art carried out in Chapter 4. The typical ejector performance curve is shown in Figure 35, where the trend of the ejector entrainment ratio μ (defined as the ratio

between the ejector secondary and primary flow) is reported as a function of the discharge pressure. Particularly, three different operating modes can be identified: the critical region, the subcritical region and the backflow region.

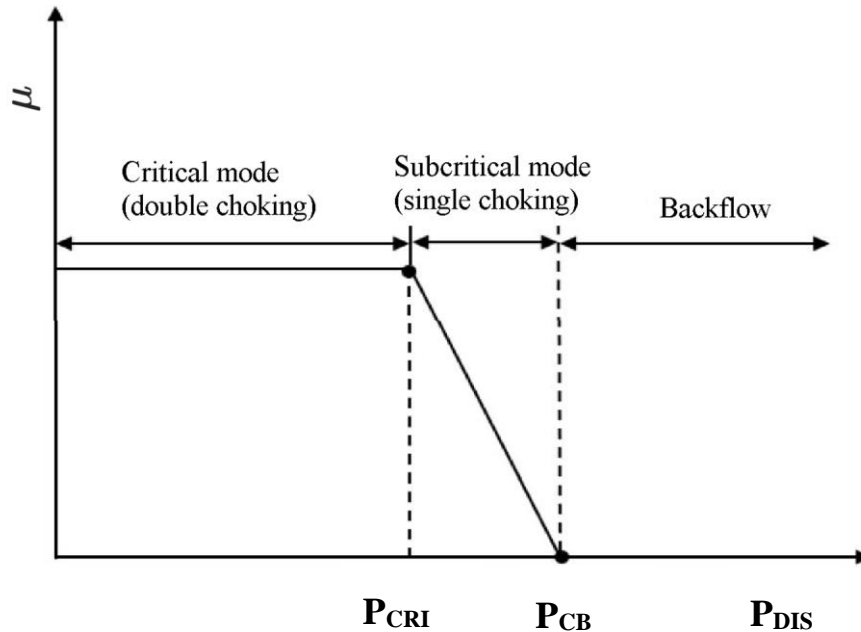


Figure 35 Ejector entrainment ratio as a function of the condenser pressure.

When the ejector works in critical mode the discharge pressure is lower than the critical one and the entrainment ratio remains constant throughout this region. The ejector processes the same amount of the secondary flow despite the change in the discharge pressure. The primary flow appears to be always choked at the nozzle exit. The secondary flow is also choked under this condition. The shock position of the mixed flow in this case is at the mixing chamber throat or at the inlet of the diffuser, not affecting the secondary flow entrainment. In the subcritical region the discharge pressure is higher than the critical value and the entrainment ratio decreases dramatically, having a linear trend with the increase of the discharge pressure. In this case the secondary stream is no longer choked. According to Ruangtrakoon et al. [188] and Sriveerakul [189] the shock position of the mixed fluid moves back, going closer and closer to the entrance of the mixing chamber, constituting a disturbance to the mixing process of the two steams. Consequently, the secondary flow is no longer choked, and the entrainment ratio decreases. When the discharge pressure reaches and overcome the breakdown value, the

ejector operates in the reversed flow region, where the secondary fluid is no longer entrained. This condition represents an ejector malfunctioning since the shock position of the mixed fluid moves very close to the primary nozzle, disturbing the formation of the expansion wave within the mixing chamber. Moreover, almost the entire primary flow is forced back, resulting in a backflow from the mixing chamber.

To simulate the ejector the approach developed by Chen et al. [190], has been followed. All the assumptions are summarized below:

- The system is assumed to be in steady state conditions and the flow inside the ejector is one-dimensional. The ejector walls are adiabatic and consequently it is neglected the heat transfer with the surrounding.
- The kinetic energies at the primary and secondary inlets are neglected. Also the velocity of the mixed flow at the diffuser exit is not considered
- The losses in the different ejector sections are accounted by means of defining three efficiencies, namely the nozzle (η_N), the mixing chamber (η_M) and the diffuser (η_D) efficiency.

All the equations employed in the model are here reported.

From the conservation of energy equation the velocity of the primary flow at the nozzle exit can be evaluated as follows:

$$\vec{u}_2 = \sqrt{2 \cdot \eta_N \cdot (i_1 - i_{3s})} \quad (5.1)$$

Where i_{3s} is the specific enthalpy at the nozzle exit assuming an isentropic process, evaluated as a function of the mixing pressure. The actual specific enthalpy at the nozzle exit is calculated by the definition of the nozzle efficiency:

$$\eta_N = \frac{i_1 - i_3}{i_1 - i_{3s}} \quad (5.2)$$

Given that the primary flow reaches sonic conditions in the nozzle throat, the expansion process can be written also in terms of Mach number, assuming ideal gas behaviour, as shown by El-Dessouky et al. [191] and by Sun and Eames [192].

$$M_{p,4} = \sqrt{2 \cdot \frac{\eta_N}{\gamma - 1} \cdot \left[\left(\frac{P_1}{P_{mix}} \right)^{\frac{\gamma-1}{\gamma}} - 1 \right]} \quad (5.3)$$

Since the difference between the primary flow pressure at the nozzle outlet (P_3) and the secondary flow (P_2) causes the entrainment of the low-pressure flow, the velocity of the latter is evaluated by means of the energy conservation equation and assuming an isentropic process, since the low velocity of the flow determines very limited losses.

$$\vec{u}_4 = \sqrt{2 \cdot (i_2 - i_4)} \quad (5.4)$$

Where i_4 is the specific enthalpy of the secondary flow at the beginning of the mixing chamber. As for to the primary flow, the Mach number of the secondary flow at the beginning of the mixing section is given by:

$$M_{s,4} = \sqrt{\frac{2}{\gamma - 1} \cdot \left[\left(\frac{P_2}{P_{mix}} \right)^{\frac{\gamma-1}{\gamma}} - 1 \right]} \quad (5.5)$$

The mixing process happening in the mixing chambers determines a completely mixed flow, between the primary and the secondary one, before the occurrence of the shock wave. The balance of the momentum of the ideal mixing process is expressed as follows:

$$\vec{u}_{5s} = \frac{\vec{u}_3 + \mu \cdot \vec{u}_4}{1 + \mu} \quad (5.6)$$

The real mixing process is obtained using the mixing chamber efficiency as defined in Yu et al. [193]:

$$\eta_M = \frac{\vec{u}_5^2}{\vec{u}_{5s}^2} \quad (5.7)$$

Consequently, the real velocity and specific enthalpy after the mixing process are:

$$\vec{u}_5 = \vec{u}_{5s} \cdot \sqrt{\eta_M} \quad (5.8)$$

$$i_5 = \frac{i_3 + \mu \cdot i_4}{1 + \mu} - \frac{\vec{u}_5^2}{2} \quad (5.9)$$

Considering the mixing efficiency, the Mach number at the state 5 in terms of the critical Mach number of the primary flow and the secondary flow at the state 3 is:

$$M_5^* = \sqrt{\eta_M} \cdot \frac{M_{p4}^* + \mu \cdot M_{s4}^* \cdot \sqrt{\frac{T_2}{T_1}}}{\sqrt{(1 + \mu) \cdot \left(1 + \mu \cdot \frac{T_2}{T_1}\right)}} \quad (5.10)$$

At any point inside the ejector the equation describing the relationship between the Mach number M and the critical Mach number M^* is expressed as follows:

$$M^* = \sqrt{\frac{M^2 \cdot (\gamma + 1)}{M^2 \cdot (\gamma - 1) + 2}} \quad (5.11)$$

Consequently, the Mach number at point 5 is:

$$M_5 = \sqrt{\frac{2 \cdot M_5^{*2}}{(\gamma + 1) - M_5^{*2} \cdot (\gamma - 1)}} \quad (5.12)$$

According to the aforementioned assumptions, the velocity of the mixed flow at the ejector outlet (condition 7) is neglected, thus the specific enthalpy i_7 is obtained by means of the energy conservation:

$$i_7 = i_5 + \frac{\vec{u}_5^2}{2} \quad (5.13)$$

$$i_7 = i_5 + \frac{i_{7s} - i_5}{\eta_D} \quad (5.14)$$

$$i_5 = f(P_7, s_5) \quad (5.15)$$

Where the diffuser efficiency is given by:

$$\eta_D = \frac{i_{7s} - i_5}{i_7 - i_5} \quad (5.16)$$

Combining Eqs. (5.8), (5.1), (5.4), (5.13) and (5.16), the ejector entrainment ratio is expressed by Eq. (5.17):

$$\mu = \frac{\dot{m}_{sf}}{\dot{m}_{pf}} = \frac{\sqrt{2 \cdot \eta_N \cdot (i_1 - i_{3s})} - \sqrt{2 \frac{i_{7s} - i_5}{\eta_D \cdot \eta_M}}}{\sqrt{2 \frac{i_{7s} - i_5}{\eta_D \cdot \eta_M}} - \sqrt{2 \cdot (i_2 - i_4)}} \quad (5.17)$$

At the end of the mixing process a shock wave occurs (5→6) causing a pressure increase and thus a drop in the mixing flow velocity. Also in this case, by following the assumption of real gas behaviour, the Mach number of the mixed flow after the shock point is:

$$M_6 = \sqrt{\frac{M_5^2 + \frac{2}{\gamma + 1}}{2 \cdot \gamma \cdot \frac{M_5^2}{\gamma - 1} - 1}} \quad (5.18)$$

The ratio between the pressure after and before the shock wave is:

$$\frac{P_6}{P_5} = \frac{1 + \gamma \cdot M_5^2}{1 + \gamma \cdot M_6^2} \quad (5.19)$$

After the shock wave the flow reaches subsonic conditions, and consequently a further pressure recovery occurs in the diffuser. It is expressed by the following relationship:

$$\frac{P_7}{P_6} = \left(\frac{\gamma - 1}{2} \cdot M_6^2 + 1 \right)^{\frac{\gamma}{\gamma - 1}} \quad (5.20)$$

In Eq. (5.20) P_7 is the calculated pressure at the ejector outlet, which should be the same as the defined ejector outlet pressure, namely the condenser pressure. For this reason, two iterative processes are needed to solve the ejector model and allows the calculation of the outlet pressure P_7 and the entertainment ratio μ .

Using this set of equations, it is possible to define the ejector area ratio, being the ratio between the area of the mixing chamber and the area of the nozzle throat:

$$A_r = \frac{A_m}{A_t} = \frac{p_1 \cdot (1 + \mu)^{0.5} \cdot (1 + \frac{\mu T_2}{T_1})^{0.5} \cdot [\frac{2}{\gamma + 1}]^{\frac{1}{\gamma-1}} \cdot [1 - \frac{2}{\gamma + 1}]^{0.5}}{p_7 \cdot (\frac{p_5}{p_7})^{1/\gamma} \cdot [1 - (\frac{p_5}{p_7})^{\frac{\gamma-1}{\gamma}}]^{0.5}} \quad (5.21)$$

Regarding the mass flow rate of the primary flow, it is determined according to [194], considering choked conditions at the nozzle throat:

$$\dot{m}_{pf} = P_1 \cdot \frac{A_{th}}{\sqrt{T_1}} \cdot \sqrt{\frac{\gamma}{R} \cdot \left(\frac{2}{\gamma + 1}\right)^{\frac{\gamma+1}{\gamma-1}} \cdot \sqrt{\eta_N}} \quad (5.22)$$

Where A_{th} is the nozzle throat cross section, P_1 and T_1 are, respectively, the pressure and the temperature of the primary flow at the nozzle inlet, γ is the gas heat capacity ratio, R is the specific gas constant and η_N represent the nozzle efficiency, previously described.

The steps followed to solve the ejector model, implemented in Matlab [52] and using Refprop 9.1 [53] for refrigerant properties, are summarized below:

1. The working fluid and the ejector boundary conditions (T_1 , P_1 , T_2 , P_2 , P_7) are selected. The isentropic ejector efficiencies (η_N , η_M , η_D) and the heat capacity ratio (γ) are assumed as constant.
2. An initial value for the pressure at the nozzle exit (P_{mix}) is guessed. Eqs. (5.1)-(5.2) are solved to obtain \bar{u}_3 , while Eqs. (5.4) is used to calculate \bar{u}_4 .
3. A guess value of μ is set initially. Eqs. (5.6)-(5.9) and (5.13)-(5.16) are used to calculate h_5 , \bar{u}_5 , and h_7 respectively. Then, the new value of entrainment ratio μ can be obtained from the Eq. (5.17).
4. The calculated μ is compared to the guessed value. If the difference between those two values is lower than the fixed tolerance (10^{-3} in the present work), a new μ value will be assumed and the previous step is repeated.
5. The pressure at the ejector outlet P_7 is calculated by Eq. (5.20). Subsequently, this value is compared to the input condenser pressure. If the difference between these two values overcome a prefixed tolerance, a new value for the mixing pressure (P_{mix}) is chosen and the previous steps are repeated until the desired value is reached.

6. The parameters μ and P_{mix} are stored as the converged solution. Finally, the area ratio A_r is calculated by Eq. (5.21).

5.2.2 Thermal power in the vapor generator

As will be shown in the following chapters of the thesis, different thermal sources are considered in the systems analysed. In the first case study, no considerations are done regarding the way the waste heat is generated, and the work is carried out under the hypothesis of full availability of the heat required to produce the cooling capacity needed by the user. In the second work, the thermal power in the vapor generator is provided by means of solar collectors. Finally, in the last case study regarding a cruise ship, the thermal power is a function of the exhaust gas of the several engines of the ships.

Consequently, in this section the models employed for the solar collectors and the exhaust gas are shown.

The solar collector efficiency is evaluated according to Clausse et al. [195]:

$$\eta = \eta_0 - \frac{a_1 \Delta T}{\dot{Q}_{sol}} - \frac{a_2 \Delta T^2}{\dot{Q}_{sol}^2} \quad (5.23)$$

Where ΔT is the difference between the refrigerant average temperature and the ambient temperature. The coefficients η_0 , a_1 and a_2 are, respectively, 0.75, $2.57 \text{ W}\cdot\text{m}^{-2}\cdot\text{k}^{-1}$ and $4,67 \text{ W}^2\cdot\text{m}^{-4}\cdot\text{K}^{-2}$. \dot{Q}_{sol} is the total solar radiation on the panel. Then, the heating power absorbed by the refrigerant is evaluated by means of an energy balance on the solar collector.

Regarding the exhaust gas, according to Zhu et al. [196], a standard marine two-stroke Diesel engine has a mechanical efficiency of 49.3%, and the 25.5% of the thermal power is wasted through the exhaust gas. Thus, assuming that the gases enter the WHR at 350 °C and that can be cooled until 130°C to avoid sulfuric acid formation, the recoverable heat provided to the hot water is given by Eq. (5.24):

$$\dot{Q}_{ex} = \dot{m}_{fuel} \cdot H_{Diesel} \cdot 0.255 \cdot \frac{\Delta T}{\Delta T_{av}} \quad (5.24)$$

Where \dot{m}_f and H_{Diesel} are, respectively, the mass flow rate and the lower calorific value of the fuel, $\Delta T/\Delta T_{av}$ is the ratio between the actual temperature difference of the gases in

the WHR, and the maximum temperature difference at disposal, considering a hypothetical outlet at ambient temperature.

5.2.3 Heat exchanger modelling

For each heat exchanger constituting the system, dedicated heat transfer correlations have been considered to evaluate the heat transfer surface. According to the characteristic of the refrigerants chosen in the different applications, and according to the pressure levels occurring in the system, the high-pressure evaporator and the regenerative heat exchanger (if present) are suitable for a plate heat exchanger, due to its compactness and cost-effectiveness. Regarding the condenser, its choice changes with the kind of system under investigation. As a matter of fact, for domestic air conditioning a fin and tube heat exchanger is selected, while in the case of the chiller for cruise ships the condenser is a titanium shell and tube one, having the refrigerant inside the tubes and seawater outside. Finally, the evaporator is a shell and tube heat exchanger. However, due to the low refrigerant pressure, it boils outside the tube bundle to avoid large pressure drops, while the chilled water flows inside the tubes.

In the heat exchangers the refrigerant phase transition occurs, thus the overall heat transfer coefficient cannot be considered constant during the whole heat transfer process. Consequently, each heat exchanger has been divided into different sub-sections for single-phase and two-phase flows, for which dedicated heat transfer equations were adopted, taking into account the geometry of the heat exchanger considered, as summarized in Table 13.

Table 13 Single-phase and two-phase heat transfer correlations for each heat exchanger considered.

Single phase	Two-phase
Plate heat exchanger	
Correlation of Martin: [197] $Nu = 0.205 \cdot Pr^{\frac{1}{3}} \cdot \left(\frac{\zeta_m}{\zeta_{wall}} \right)^{\frac{1}{6}} \cdot (f \cdot Re^2 \cdot \sin 2\beta)^{0.374}$	Boiling heat transfer correlation of Park and Kim [198]: $Nu = 12.74 \cdot Re_{eq}^{0.33} \cdot Pr_l^{\frac{1}{3}}$
Shell and tube evaporator- shell side	
Correlation of McAdams [199]: $Nu = 0.36 \cdot \left(\frac{D_e \cdot G_s}{\zeta} \right)^{0.55} \left(\frac{c_p \cdot \zeta}{\gamma} \right)^{\frac{1}{3}} \cdot \left(\frac{\zeta}{\zeta_w} \right)^{0.14}$	Pool boiling correlation of Cooper [200]: $h_{NB} = 55 \cdot pr^{0.12} (-0.4343 \cdot \log(pr))^{-0.55} \cdot M^{-0.5} \cdot q^{0.67}$
Shell and tube evaporator- tube side	
Correlation of Dittus-Boelter [201]: $Nu = 0.023 \cdot Re^{0.8} \cdot Pr^{0.4}$	
Shell and tube condenser- shell side	
Bell-Delaware method [202]	
Shell and tube condenser- tube side	
	Condensation inside tubes, correlation of Shah [203]: $Nu = 0.023 \cdot Re^{0.8} \cdot Pr^{0.4} \cdot \left[(1 - \chi)^{0.8} + \frac{3.8\chi^{0.76} \cdot (1 - \chi)^{0.04}}{pr^{0.38}} \right]$
Fin and tube heat exchanger-air side	
Wang et al. [204] $X = 0.096 \cdot Re_{air}^{P3} \cdot N_R^{P4} \cdot \left(\frac{P_{fin}}{D_c} \right)^{P5} \cdot \left(\frac{P_{fin}}{D_h} \right)^{P6} \cdot \left(\frac{P_{fin}}{P_t} \right)^{-0.93}$ $h_{air} = X \cdot \rho_{air} \cdot \vec{u}_{air,max} \cdot c_{p,air} \cdot Pr_{air}^{-2/3}$	

The overall heat transfer equation is applied to each elementary area dA , corresponding to an elementary length dz equal to 5 mm, on which the heat exchangers are divided:

$$\delta\dot{Q}(z) = U(z)dA \cdot [T_{hot}(z) - T_{cold}(z)] \quad (5.25)$$

Using the refrigerant pressure and specific enthalpy, by means of the software Refprop 9.1 [53] its temperature is evaluated. The water properties are also evaluated with the same software, while air is assumed as ideal gas. For each elementary length dz the local properties of both fluids in the heat exchangers are evaluated from the inlet, by means of the energy balance equation for each side, as reported below:

$$i_{ref}(z + 1) = i_{ref}(z) - \frac{d\dot{Q}}{\dot{m}_{ref}} \quad (5.26)$$

$$i_{sf}(z + 1) = i_{sf}(z) - \frac{d\dot{Q}}{\dot{m}_{sf}} \quad (5.27)$$

Where the subscripts *ref* and *sf* refer, respectively, to the refrigerant and the secondary fluid. The overall heat transfer coefficient U considers both conductive and convective thermal resistance, with the latest resulting of the contributes of both fluids, the hot and the cold one:

$$U = \frac{1}{\frac{1}{h_{ref}} + \frac{\delta}{\lambda_{mat}} + \frac{1}{h_{sf}}} \quad (5.28)$$

Where δ and λ_{mat} are, respectively, the thickness and the thermal conductivity of the tube or the plate (depending on whether the heat exchanger is a shell and tube, a fin and tube or a plate one), while h is the convective heat transfer coefficient computed as follows:

$$h = \frac{Nu \cdot \lambda_{fluid}}{D_h} \quad (5.29)$$

Where λ_{fluid} is the fluid thermal conductivity and D_h is the hydraulic diameter. For each fluid, phase and geometry, the correlations reported in Table 13 have been used. To calculate the heat exchanger surfaces an algorithm developed in Matlab [52] environment was employed. The following steps are followed:

1. The thermodynamic and geometric parameters are selected as input of the model.
2. In the first elementary section of each heat exchanger the local temperature of the working fluid is set equal to the selected temperature of the generator, the condenser and the evaporator, depending on the heat exchanger considered.
3. The overall heat transfer coefficient U for each elementary volume is evaluated by Eqs. (5.28) and (5.29) using the heat transfer correlation reported in Table 13.
4. The elementary heat power is then evaluated by using Eq. (5.25).
5. By means Eqs. (5.26) and (5.27) the specific enthalpies and temperatures for the next integration steps ($z+1$) are calculated.
6. The steps from 3 to 5 are repeated until the heat exchanger surface balances the required heat power.
7. Finally, the total heat transfer surface A is obtained for each investigated geometric configuration and boundary conditions.

When used, the waste heat recovery heat exchanger and the regenerative heat exchanger are modelled by means the well-known ε -NTU method:

$$\varepsilon = \frac{\dot{Q}}{\dot{Q}_{max}} \quad (5.30)$$

Where, ε is the efficiency of the heat exchanger, defines as the ratio between \dot{Q} , the actual thermal power transferred, and \dot{Q}_{max} , the maximum thermal power that could be exchanged between the two fluids.

5.2.4 Compressor model

In the system considered, when the waste heat or the solar power are not sufficient to provide the whole cooling effect, the aid of a booster compressor is required to satisfy the user demand. A lumped parameter model is adopted to model this component, where the electrical power required by the compressor is expressed as follows:

$$\dot{W}_{comp} = \frac{\dot{m} \cdot (i_{out,id} - i_{in})}{\eta_{comp}} \quad (5.31)$$

\dot{m} is the mass flow rate in the compressor, $i_{out,id}$ and i_{in} are respectively the ideal outlet (considering and isentropic compression) and inlet compressor specific enthalpies. η_{comp} is the compressor global efficiency, for which a polynomial relation is calibrated on manufacturer data as a function of the compressor pressure ratio. The overall compressor efficiency is shown in Figure 36 as a function of the compression ratio.

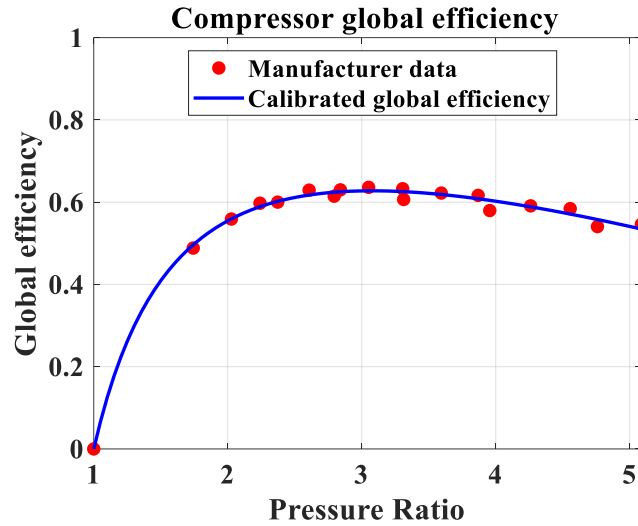


Figure 36 Compressor global efficiency as a function of compression ratio.

5.2.5 Refrigerant pumps, condenser fans and water pumps.

The refrigerant pump has a global efficiency evaluated as function of the differential pressure, as reported in Figure 37.

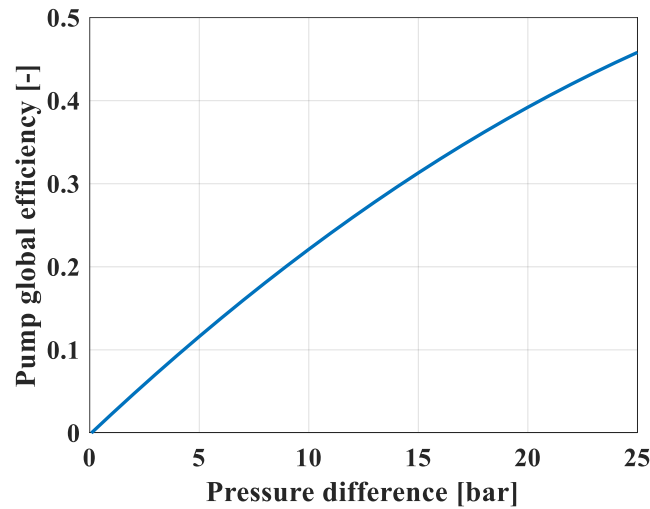


Figure 37 Pump global efficiency as function of pressure difference [205].

Eq. (5.32) is used to estimate the pump efficiency according to the experimental results given by Declay [205]. This function was calibrated for compression ratio typical of ORC cycles, that are a bit higher than those exploited for the present analysis.

$$\eta_{gl} = -2.6 \cdot 10^{-4} \cdot \Delta P^2 + 2.5 \cdot 10^{-2} \cdot \Delta P + 2 \cdot 10^{-3} \quad (5.32)$$

The electric power required by the fans of the condenser is calculated with Eq. (5.33), where the fan efficiency η_{fan} is evaluated with fans map performance collected by a market analysis.

$$\dot{W}_{fan} = \frac{\Delta P_{air} \cdot \dot{V}_{air}}{\eta_{fan}} \quad (5.33)$$

Finally, regarding the water pumps, an efficiency of 0.7 is assumed.

5.2.6 Tank model

The cold water tank is modelled with the same approach followed in Tammaro et al. [206] assumed to be a completely stratified tank having a height-over-diameter ratio equal to five. It is modelled as a one-dimensional item with water entering from the top and the bottom fully mixed, with several nodes having an equal volume. For each i -th node of the tank mass and energy balances are applied as follows:

$$M_i \cdot c_p \cdot \frac{dT}{dt} = \alpha_i \cdot \dot{m}_H \cdot c_p \cdot (T_H - T_i) + \beta_i \cdot \dot{m}_L \cdot c_p \cdot (T_L - T_i) + UA_i \cdot (T_{AMB} - T_i) + F \quad (5.34)$$

Where α is 1 if the i -th node is the top of the tank, while is 0 otherwise; β is 1 if the considered node is at the bottom of the tank, 0 for the other nodes; T_H and T_L are, respectively, the temperatures of hot water entering from the top and cold water entering from the bottom. The factor F is described in the next equations:

$$F = \gamma_i \cdot c_p \cdot (t_{i-1} - t_i) \quad \text{if } \gamma_i > 0 \quad (5.35)$$

$$F = \gamma_i \cdot c_p \cdot (t_i - t_{i-1}) \quad \text{if } \gamma_i < 0 \quad (5.36)$$

Considering a tank having N nodes, the factor γ is:

$$\gamma_l = \dot{m}_H \cdot \sum_{j=1}^{l-1} \alpha_j - \dot{m}_L \cdot \sum_{j=l+1}^N \beta_j \quad (5.37)$$

The time step for the tank integration is 1 minute.

5.2.7 Cost functions

The investment cost of the different configurations analyzed are evaluated by considering the sum of the costs of each component constituting the system, for which the cost correlations summarized in Table 14 are employed.

Table 14 Cost functions for each component of the system.

Component	Dependent variable	Cost [€]
Pumps. Declay [205]	Electrical power [kW]	$900 \cdot \left(\frac{W_{pump}}{300}\right)^{0.5}$
High pressure evaporator [207]	Heat exchanger surface [m ²]	$190 + 310 \cdot A_{gv}$
Low pressure Evaporator. Wildi-Tremblay et Gosselin [208]	Heat exchanger surface [m ²]	$3.28 \cdot 10^4 \cdot \left(\frac{A_{ev}}{80}\right)^{0.68}$
Titanium shell and tube condenser. [209]	Heat exchanger surface [m ²]	$15811 + 632 \cdot A_{co}^{0.93}$
Compressor. Botticella et al. [210]	Volumetric flow rate [m ³ ·h ⁻¹]	$52.63 \cdot \dot{V}_{comp}$
Cold storage tank. Ferreira et al. [211]	Tank volume [m ³]	$3647.5 \cdot 0.32 \cdot \left(\frac{Vol}{0.32}\right)^{0.3} \cdot 0.985$
Waste heat recovery heat exchanger. Sakalis [212]	Thermal power [kW]	$65 \cdot \dot{Q}_{ex} + 120000$
Regenerative heat exchanger [207]	Heat exchanger surface [m ²]	$190 + 310 \cdot A_{Reg}$
Solar collectors. Ferreira et al. [211]	Solar panel surface [m ²]	$C_{refe} \cdot A_{refe} \cdot \left(\frac{A_{solar}}{A_{refe}}\right)^{0.5} \cdot \eta_0^{1.2} \cdot a_1^{-0.04}$

5.3 Resolution algorithms

5.3.1 Resolution algorithms and control strategy for the waste heat driven multi-ejector cooling system.

For each thermodynamic system under investigation, both, the resolution algorithm for the system sizing and the system simulation are solved in Matlab [52] environment.

In the case of the waste heat driven multi-ejector cooling system a free thermal source continuously available is considered and thus the ejector system is always able to satisfy the whole cooling load required by the user. A schematic layout of the cycle is shown in Figure 38 (a), altogether with the thermodynamic cycle on the T-s diagram, Figure 38 (b). For simplicity purposes, in this thermodynamic cycle, and in the subsequent, the transformations inside the ejectors (given as an example in Figure 34(b)) are not shown.

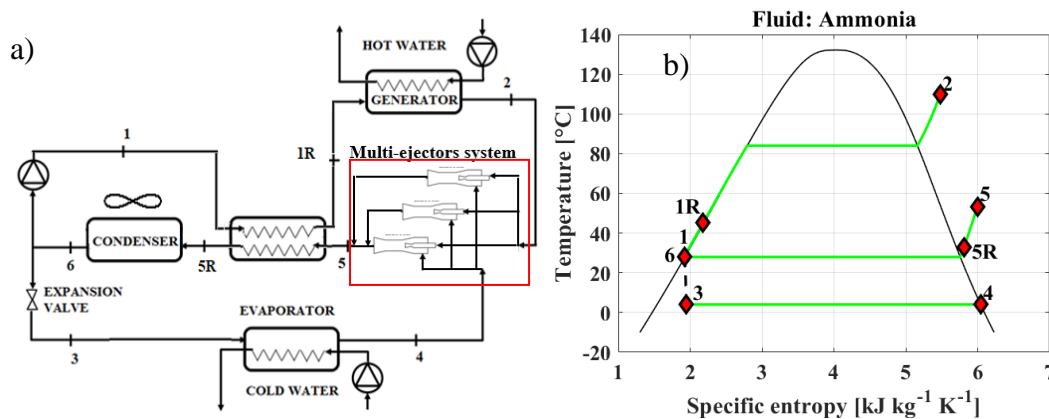


Figure 38 (a) Schematic lay-out of the hybrid ejector cycle proposed in this analysis. (b) Thermodynamic cycle of Ammonia on the Temperature-specific entropy diagram.

In the system analysed, hot water produced from an unlimited source of waste heat is employed to produce superheated vapor (point 2) in the steam generator. The high-pressure vapor, being the ejector primary flow, expands into the motive nozzle, from which it exits with a pressure lower than the evaporator one, allowing the entrainment of the low-pressure vapor from the evaporator, that constitutes the ejector secondary flow. Then, the two flows are mixed into the ejector mixing chamber, and then compressed into the ejector diffuser, reaching the condenser pressure (point 5). After the condenser, the total mass flow rate is cooled into the regenerative heat exchanger (point 5R) and then condenses into the condenser, from which exits in point 6. Here the total flow is divided into two parts. The first goes in the high-pressure side of the plant, where a pump sends

the refrigerant into the regenerator, where it reaches point 1R, and then in the vapor generator, as shown before. The second part goes through the expansion device (reaching point 3) and then it evaporates in the evaporator, from which it exits as a saturated vapor, satisfying the user cooling demand.

With the knowledge of the evaporator pinch-point temperature and the cold water temperature, the evaporator temperature is directly evaluated, while the high-pressure vapor generator and the condenser saturated conditions are calculated by means of an iterative process in order to meet the desired pinch-point values. As first step, the condensation and high temperature evaporator pressures are guessed, allowing to obtain the whole thermodynamic cycle. Subsequently, the pinch point values for the two heat exchangers (occurring at saturated vapor for the condenser and in liquid conditions for the vapor generator) are evaluated according to the chosen saturation temperatures. Then, the saturation temperatures chosen are adjusted up to the convergence in the design temperature difference. For instance, if the pinch point value is higher than the design one, the condenser/evaporator pressure is accordingly decreased/increased. Once the thermodynamic properties are defined, the heat exchanger models are applied to evaluate the heat transfer surfaces. Finally, the system COP is evaluated as follows:

$$COP = \frac{\dot{Q}_{ev}}{\dot{W}_{pump,ref} + \dot{W}_{fan}} \quad (5.38)$$

Where \dot{Q}_{ev} is the nominal cooling power, while $\dot{W}_{pump,ref}$ and \dot{W}_{fan} are, respectively, the power required by the refrigerant pump and the condenser fans. The same algorithm is schematically shown in *Figure 39*.

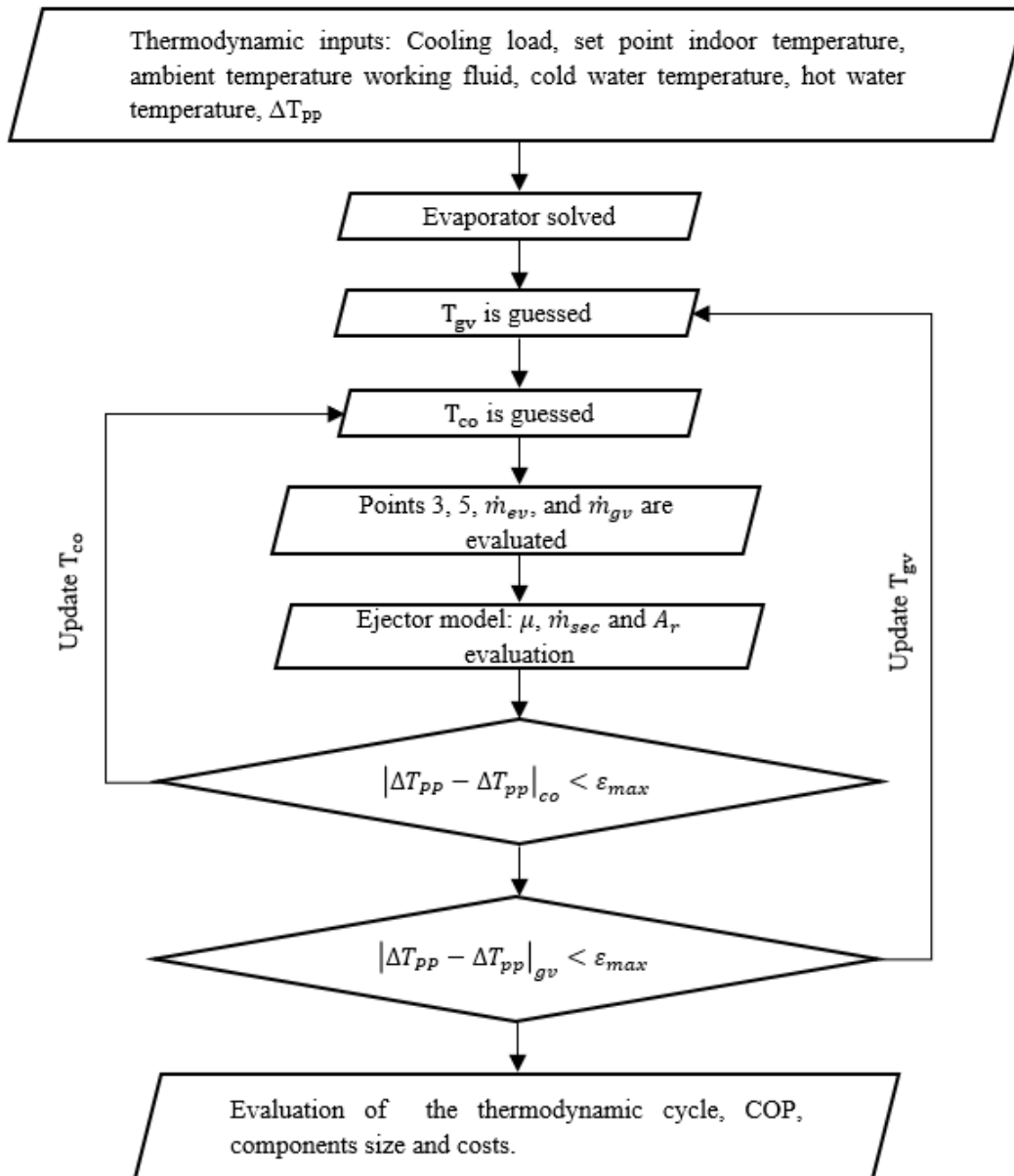


Figure 39 Sizing algorithm for an ejector cycle for domestic air conditioning.

For dynamic simulations several configurations are considered with a variable number of ejectors, from 1 to 9, to obtain the optimal multi-ejector configuration. Differently from the case with one ejector, various configurations of the multi-ejector system can satisfy the cooling load required by the user. Such condition occurs when the secondary mass flow rate of the multi-ejector is higher than the evaporator mass flow rate ($\dot{m}_{sf} > \dot{m}_{ev}$). The employed multi-ejector control strategy is reported in Figure 40, showing the trend of the secondary mass flow rate as a function of the condensing temperature or different

values of the vapor generator temperature. The dotted line represents the required evaporator mass flow rate needed to satisfy the user cooling demand.

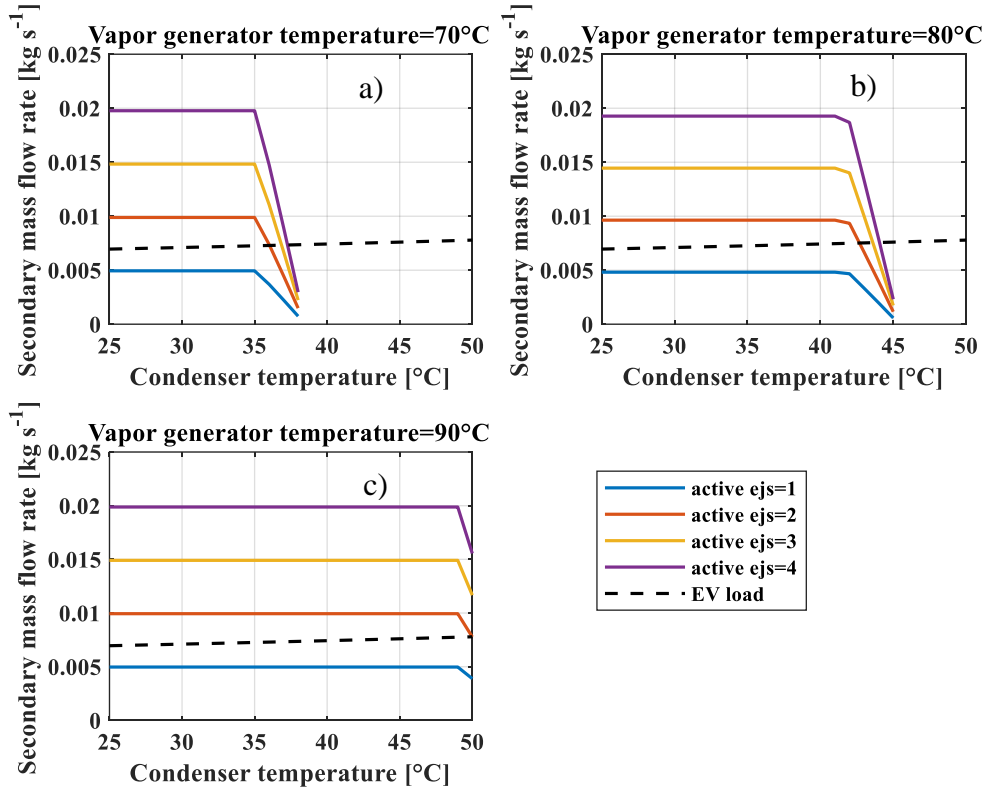


Figure 40 Example of multi-ejector control strategy by assuming four ejectors with the same size at (a) $T_{gv}=70^{\circ}\text{C}$, (b) $T_{gv}=80^{\circ}\text{C}$, (c) $T_{gv}=90^{\circ}\text{C}$.

As shown in Figure 40, there is a minimum number of ejectors able to satisfy the cooling demand, namely two active ejectors. This represents an oversized configuration of the system, because the secondary mass flow rate of the multi-ejector pack is higher than the evaporator mass flow rate. It is worth mentioning that among all the possible solutions in terms of vapor generator and condenser saturation pressure it is considered the one bringing to the highest ejector entrainment ratio according to the heat transfer matching in the heat exchangers. To balance the required cooling load, the multi-ejector system will work both, with the oversized configuration ($\dot{m}_{sf} > \dot{m}_{ev}$) and the condition that immediately precedes it, being an under-sized configuration ($\dot{m}_{sf} < \dot{m}_{ev}$). The operating time τ of the oversized configuration is evaluated by Eq. (5.39).

$$\tau = \frac{\dot{Q}_{user} - \dot{Q}_{ev}^{ej,under}}{\dot{Q}_{ev}^{ej,over} - \dot{Q}_{ev}^{ej,under}} \quad (5.39)$$

After the evaluation of the operating time in each configuration, the total electric load E_{el} can be evaluated as follows:

$$E_{el} = \dot{W}_{el}^{ej,over} \cdot \tau + \dot{W}_{el}^{ej,under} \cdot (1 - \tau) \quad (5.40)$$

Despite different multi-ejector control strategies could be considered, the approach followed in the present work guarantees a continuous operation of the system, avoiding frequent on/off operations that inevitably lead to a degradation of the system performance. With this control strategy on/off regimes occur only when the oversized multi-ejector configuration consists of 1 active ejector.

By having chosen the multi-ejector configuration, together with the components geometry and the working fluid the system seasonal performance is evaluated considering the variation of the external ambient temperature and thus the cooling load required by the final user at each operating hour of the cooling season. The hot water temperature at the vapor generator and its variation across the heat exchanger are input parameters as well as the external air temperature variation across the condenser and the chilled water temperature. The algorithm for the dynamic simulations is shown in Figure 41, whereas all the steps are here summarized:

1. The multi-ejector configuration, the working fluid, secondary fluids inlet/outlet temperatures and heat exchangers geometry are fixed as input for the algorithm.
2. The ambient temperature and the cooling load at the evaporator are fixed and obtained from the weather data file using the software TRNSYS [213]. Particularly, the cooling load for each operating hour is given by Eq.(5.41):

$$\dot{Q}_{user} = (UA)_{build} \cdot [T_{amb} - T_{user}] \quad (5.41)$$

Where the building global conductance $(UA)_{build}$ is evaluated in Eq.(5.42) at nominal load, considering the maximum ambient temperature and the desired user temperature (which is 26°C for domestic air conditioning):

$$\dot{Q}_{nom} = (UA)_{build} \cdot [T_{amb,max} - T_{user}] \quad (5.42)$$

3. Evaporation temperature is guessed and thus the temperature profiles and the overall heat transfer coefficient are calculated by means of the logarithmic mean temperature difference. Then, the overall heat transfer coefficient is evaluated also by means of the heat transfer correlations. The evaporator temperature is adjusted until the matching between the heat exchanger equation design and the heat transfer correlation is reached.
4. The undersized and the oversized multi-ejector configurations can be selected according to the control strategy previously shown.
5. Values of first attempt for the vapor generator and condenser saturation temperatures are fixed and the thermodynamic cycle is evaluated.
6. The ejector boundary conditions are known and the entrainment ratio is obtained by the ejector model. Consequently, the mass flow rates and the thermal powers can be evaluated.
7. The condenser is solved as described in the heat exchangers modelling section and the heat transfer surface is calculated and compared to the one obtained by the design process. The condenser saturation temperature is adjusted up to the numerical convergence by repeating steps 5, 6 and 7.
8. The vapor generator is integrated in order to evaluate its heat transfer surface. The vapor generator saturation temperature is then adjusted by repeating steps 5, 6, 7 and 8 up to the numerical convergence between heat transfer surfaces.
9. Steps from 5 to 8 are performed for each multi-ejector configuration according to step 4.
10. The thermodynamic cycle and the thermal and electrical powers are known: the oversized multi-ejector configuration operating time is evaluated, and the electric load required by the fans and the refrigerant pump are calculated. Finally, the seasonal performance indicator $SEER_{el}$ is evaluated, according to European regulation (EU) 2016/2281 [214], being the ratio between the

annual cooling demand and the annual energy consumption for cooling, by Eq. (5.43):

$$SEER_{el} = \frac{\Sigma Q_{ev}}{\Sigma(E_{el,pump,ref} + E_{el,fan})} \quad (5.43)$$

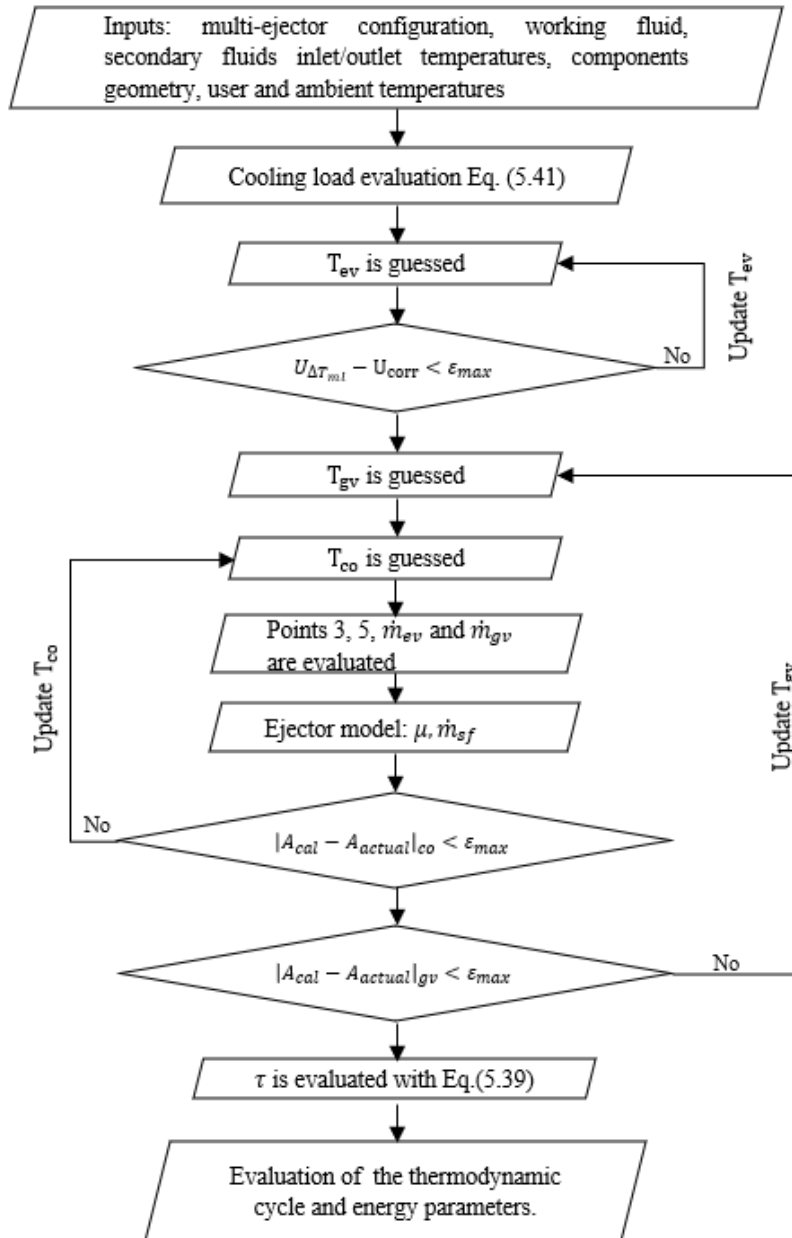


Figure 41 Resolution algorithm for the ejector cycle chiller simulations.

2. The condenser temperature is guessed. Points 5 (saturated liquid) and 3 (expansion device exit) are evaluated.
3. The evaporator mass flow rate is calculated:

$$\dot{m}_{ev} = \frac{\dot{Q}_{ev}}{i_4 - i_3} \quad (5.44)$$

4. Knowing the evaporator, condenser and generator pressure (which is an independent variable), the area ratio and the entrainment ratio are evaluated employing the ejector model.
5. With the solar collector model, given its surface and knowing the boundary conditions, the thermal power adsorbed by them is evaluated and thus the ejector primary flow rate is calculated. The secondary mass flow rate is then calculated, together with the total mass flow rate in the ejector.
6. If the secondary flow rate is lower than the mass flow rate at the evaporator, the difference is elaborated by the compressor. The condenser mass flow rate is then evaluated by summing the ejector and the compressor mass flow rates. Consequently, the ratio between the mass flow rate through the compressor and the total mass flow rate is given by:

$$\psi = \frac{\dot{m}_{comp}}{\dot{m}_{tot}} \quad (5.45)$$

7. The air temperature at the pinch point is calculated. If the value differs from the assigned one, the steps from 2 to 6 are reiterated until convergence.
8. The system COP is evaluated similarly to Eq.(5.46):

$$COP = \frac{\dot{Q}_{ev}}{\dot{W}_{pump,ref} + \dot{W}_{fan} + \dot{W}_{comp} + \dot{W}_{pump,cold}} \quad (5.46)$$

In this case there are two more terms compared to the previous case, namely \dot{W}_{comp} and $\dot{W}_{pump,cold}$, being the power required by the compressor and by the cold water pump, that was neglected in the previous case. The sizing procedure is shown also in Figure 43.

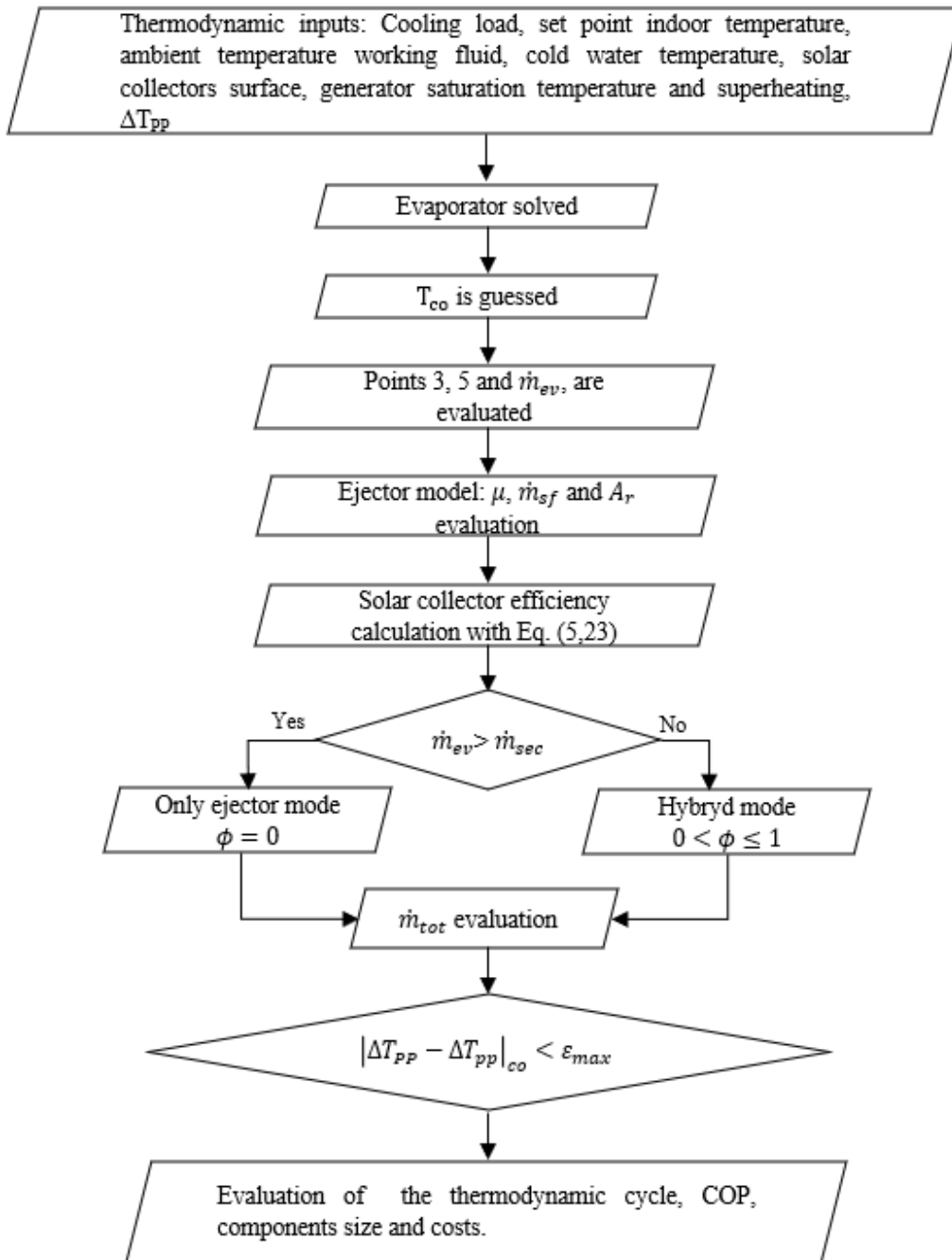


Figure 43 Algorithm to size a solar assisted chiller for domestic air conditioning.

Regarding the system dynamic simulation, the control strategy is similar to the one previously shown. In this case the total cross section of the ejector sized in the sizing phase has been divided on five ejectors, having the following proportion for the different

section's areas: 6.25%-6.25%-12.5%-25%-50%. The steps followed for the system dynamic simulations, reported also in *Figure 44*, are the following:

1. The multi-ejector configuration, the working fluid, the water temperatures, the refrigerant superheating in the generator and the components size are given as input.
2. Evaporation temperature is guessed and thus the primary and secondary fluid temperature profiles are calculated by means of the logarithmic mean temperature difference, allowing the evaluation of the overall heat transfer coefficient. The same calculation is then carried out by means of dedicated heat transfer correlations. Finally, the two values are compared, and the evaporation temperature is adjusted until the matching between the two methods is verified.
3. The vapor generator and the condenser saturation temperatures are assumed.
4. The collector's surface, the refrigerant saturation temperature and superheating in the generator are given as input and allow the evaluation of the collector efficiency. Thus, the thermal heat available from the generator is calculated. Consequently, the refrigerant mass flow rate in the solar collectors is obtained.
5. Through the ejector model, the ejector operating conditions and entrainment ratio is evaluated. Knowing the ejector primary mass flow rate and entrainment ratio, the secondary mass flow rate is calculated.
6. The evaporator mass flow rate (needed to provide the cooling load required by the user) and the percentage of it entrained by the ejector (being the secondary flow rate) are known from the previous steps, and thus compared. If $\dot{m}_{sf} < \dot{m}_{ev}$ the compressor is turned on and the corresponding mass flow rate is calculated.
7. The condenser is solved as shown before and the heat transfer surface is evaluated. The condenser temperature is adjusted, and steps 4, 5 and 6 are repeated, until the convergence is reached.

8. With the correct condenser temperature, the solar collectors and the ejector are solved again. The generator temperature is adjusted until the coupling between the vapor mass flow rate produced in the generator and the mass flow rate evolving in the ejector nozzle (namely primary flow rate) is reached. Steps 3, 4, 5, 6 and 7 are repeated until convergence.
9. Finally, the seasonal performances are evaluated by means of the electrical *SEER*:

$$SEER_{el} = \frac{\sum Q_{ev}}{\sum (E_{el,pump,ref} + E_{el,fan} + E_{comp} + E_{el,pump,cold})} \quad (5.47)$$

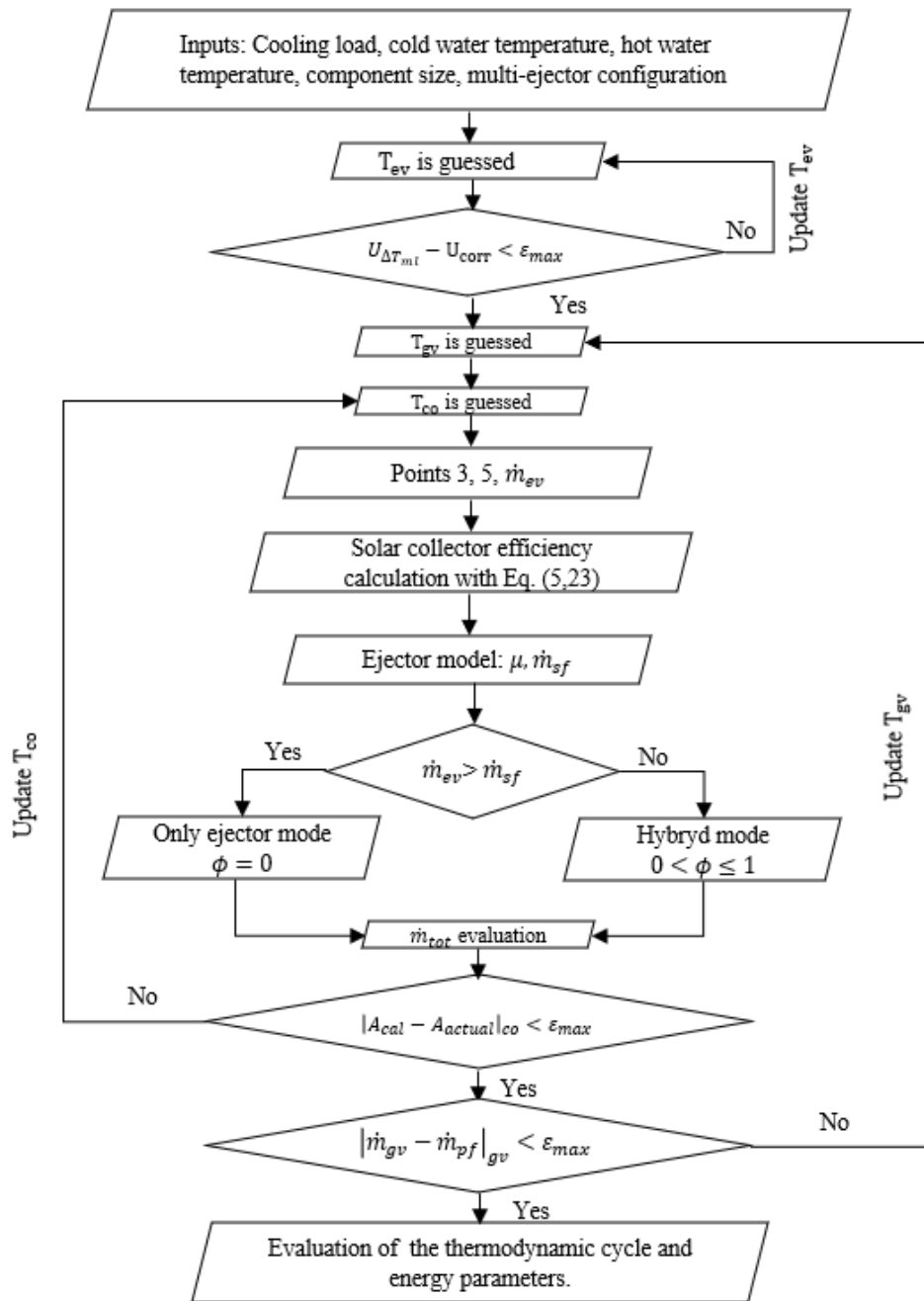


Figure 44 Algorithm for the dynamic simulations of a solar assisted ejector chiller for domestic air conditioning.

5.3.3 Resolution algorithms and control strategy for the waste heat drive multi-ejector compressor assisted chiller for cruise ships air conditioning

The system layout analysed in this case study is shown in Figure 45, together with the refrigerant thermodynamic cycle on the T-s diagram.

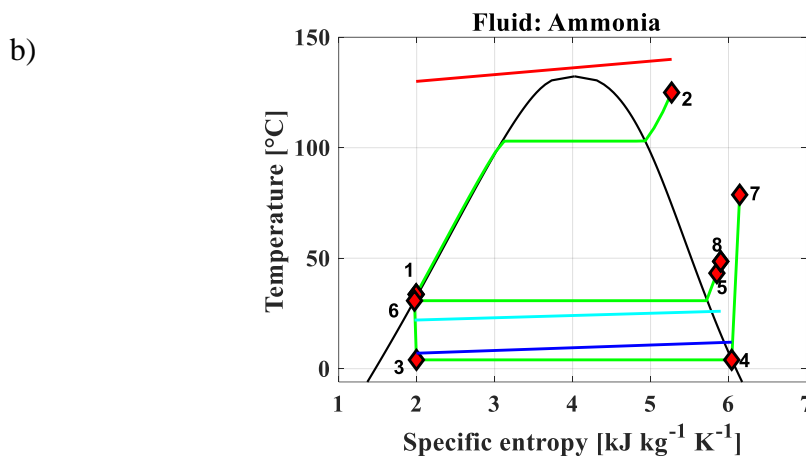
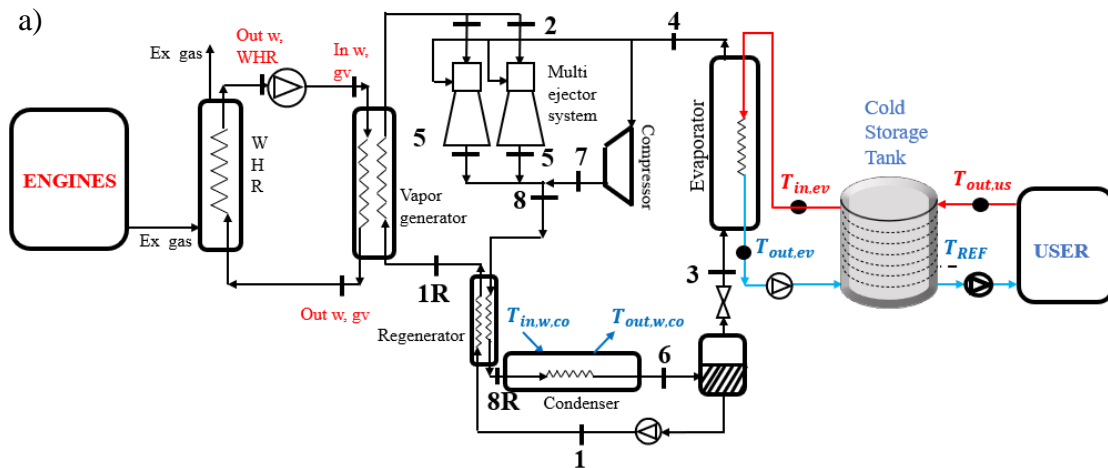


Figure 45 a) Schematic of the waste heat driven ejector cycle b) Thermodynamic cycle on the temperature-specific entropy for the refrigerant, in green, and the secondary fluids evolution (in red the water in the vapor generator, in cyan the sea water in the condenser and in blue the chilled water in the evaporator).

In this case the hybrid cycle is driven by means of the residual heat of the exhaust gas from the several engines of the ship, that enables the hot water production in the waste heat recovery heat exchanger (WHR). Then, in the vapor generator, the recovered heat is employed to produce the high-pressure refrigerant in superheated conditions, point 2. Also in this case, a booster compressor is included in the system. The remaining part of the system is similar to the previous cases. The only difference consists in the presence of a cold storage tank, included on the user side to decouple the cooling demand from the exhaust gas availability during the ship propulsion, aiming to guarantee a larger functioning time of the system without the intervention of the booster compressor.

The system is sized assuming the maximum cooling load required by the user and the maximum waste heat at disposal, according to the ship loading curves reported by Ancona et al. [215] and shown in Figure 46.

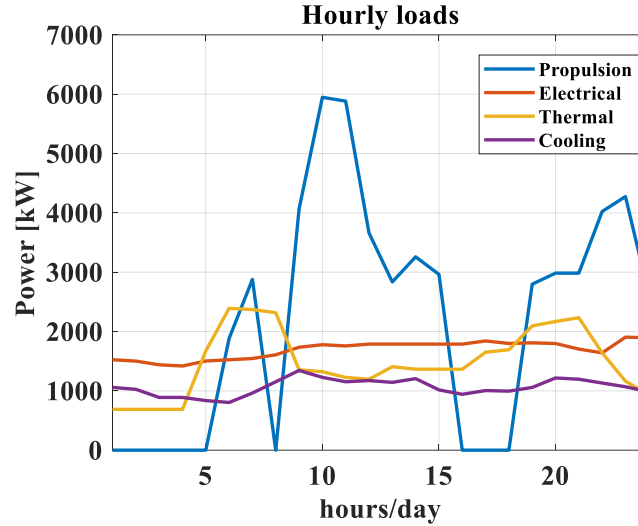


Figure 46 Loading curves of the ship for the warmest day of the cooling season.

The steps followed, schematically summarized in Figure 47, are the subsequent:

1. The waste heat at disposal and the cooling load are given as input, considering the maximum availability of waste heat and the higher cooling load required by the air conditioning system.
2. The evaporator saturation temperature is evaluated, knowing the chilled water in/out temperature and the minimum temperature difference in the evaporator.
3. The generator saturation pressure is assumed and the temperature at point 2 is evaluated.
4. The condenser temperature is guessed. Points 5 (saturated liquid), 3 (expansion device outlet) and the generator mass flow rate, \dot{m}_{gv} , are evaluated.
5. The evaporator mass flow rate is calculated:

$$\dot{m}_{ev} = \frac{\dot{Q}_{ev}}{i_4 - i_3} \quad (5.48)$$

6. Solving the ejector model, by the knowledge of the evaporator, condenser and generator pressure, the area ratio and the entrainment ratio are evaluated.
7. The ejector secondary mass flow rate and the evaporator one are compared. If the first one is lower than the latter, the difference goes into the compressor. The condenser mass flow rate is evaluated by summing the ejector and the compressor mass flow rates. Consequently, the ratio between the mass flow rate through the ejector and the total is defined according to Eq.(5.45), shown in the previous paragraph.
8. The cooling water temperature at the condenser pinch point is calculated. If the value differs from the chosen one, steps from 4 to 7 are reiterated until convergence.
9. The steam generator is solved. The temperature difference at the pinch point is evaluated and compared with the given one. Steps from 3 to 8 are repeated until convergence.
10. If the compressor is turned on and $\psi > 0$, the waste heat increases since a higher electric power to activate the compressor is required. Consequently, steps 1 to 9 are repeated with the new value of waste heat, until convergence.
11. The system COP is evaluated with Eq. (5.49):

$$COP = \frac{\dot{Q}_{ev}}{\dot{W}_{pump,ref} + \dot{W}_{comp} + \dot{W}_{sea,pump} + \dot{W}_{pump,cold} + \dot{W}_{pump,hot}} \quad (5.49)$$

where \dot{Q}_{ev} is the cooling load, $\dot{W}_{pump,ref}$, \dot{W}_{comp} , $\dot{W}_{sea,pump}$, $\dot{W}_{pump,cold}$, $\dot{W}_{pump,hot}$ are, respectively, the work required by the refrigerant pump, the compressor, the sea water pump (being the sea water the cooling media in the condenser), the chilled water pump at the user and the hot water pump.

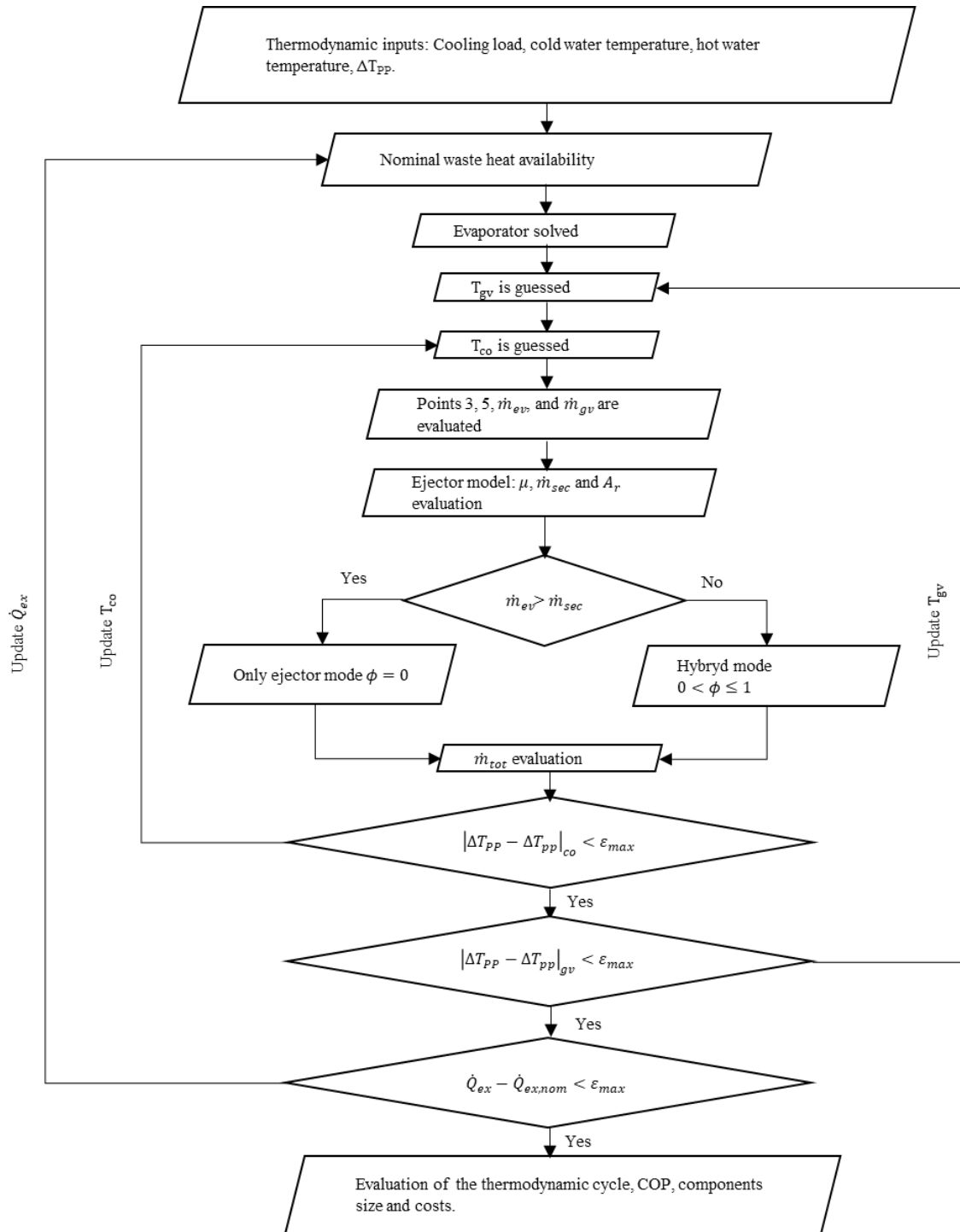


Figure 47 Resolution algorithm to size a waste heat driven hybrid ejector chiller for cruise ship air conditioning .

For the dynamic simulations, the total cross section of the ejector sized has been divided on five ejectors following the next proportion in terms of cross section areas: 6.25%-6.25%-12.5%-25%-50%. With this approach, each ejector, when activated, work at full

load and thus at its higher performance. The compressor has been sized to guarantee the satisfaction of the whole cooling load in case of waste heat lacks.

The system control strategy differs in the case with tank from the solution without it. In the first case, the control parameter is the cold-water temperature in the tank. Particularly, a control position is chosen inside the tank (assumed to be at $\frac{1}{4}$ of the total tank height) and its temperature is verified at each integration time step. According to the value assumed by the control temperature, the control strategy consists in the following options:

- $T_{\text{control}} < 5^{\circ}\text{C}$: the chiller is switched off to avoid the water freezing. The cooling effect is provided thanks to the cold water stored in the tank.
- $5^{\circ}\text{C} < T_{\text{control}} < T_{\text{set-point}} + \Delta T_{\text{deadband}}$: the chiller works only in ejector mode, using all the waste heat at disposal.
- $T_{\text{control}} > T_{\text{set-point}} + \Delta T_{\text{deadband}}$: the compressor is turned on, working at its nominal power in parallel with the multi-ejector system, which uses all the waste heat available. The system provides a cooling load higher than that required by the user and thus the storage temperature decreases. The compressor is switched off when the temperature becomes lower than $T_{\text{set-point}}$, to avoid continuous ON/OFF operations.

In the second case, without the cold storage tank, the system operates to provide the exact cooling demand by the user. As a matter of fact, given the waste heat availability, and solved the ejector model, the ejector secondary mass flow rate is evaluated, and the subsequent options can occur:

- $\dot{m}_{\text{sec}} > \dot{m}_{\text{ev}}$: in this case the secondary mass flow rate is higher than the evaporator one, thus the heat from the exhaust gas is not entirely recovered to reduce the secondary mass flow rate and to match the evaporator one.
- $\dot{m}_{\text{sec}} < \dot{m}_{\text{ev}}$: the multi-ejector system is not able to satisfy the required cooling demand, consequently the compressor is turned on and the evaporator mass flow rate is given by the sum of the ejector secondary one and the compressor one:

$$\dot{m}_{\text{ev}} = \dot{m}_{\text{ej}} + \dot{m}_{\text{comp}} \quad (5.50)$$

The dynamic simulations have been performed following the steps reported below:

1. The multi-ejector configuration, the working fluid, the hot water temperature, the refrigerant superheating in the generator, the chilled water temperature produced in the evaporator and the components size are given as input. The waste heat and the cooling load are obtained by the typical loading curves of the ship. However, the cooling load refers to the warmest day of the year, thus despite the daily cooling load is assumed to have the same trend, the actual load for each operating hour in summer season is updated as a function of the external temperature as follows:

$$\dot{Q}_{hour} = \dot{Q}_{hour,max} \cdot \frac{T_{amb} - T_{user}}{T_{amb,max} - T_{user}} \quad (5.51)$$

Where \dot{Q}_{hour} is the actual cooling load for the operating hour simulated; $\dot{Q}_{hour,max}$ and $T_{amb,max}$ are the cooling load and the ambient temperature in the same hour in the warmest day of the year; T_{amb} and T_{user} are, respectively, the external and the user temperatures in the simulated hour.

2. A first attempt value for the evaporation temperature is assumed and with this value the temperature profiles of both fluids and the overall heat transfer coefficient are evaluated by means of the logarithmic mean temperature difference. Then, using the heat transfer correlation shown in *Table 13*, the overall heat transfer coefficient is evaluated again. The evaporator saturation temperature is modified accordingly until the matching between the heat exchanger equation design and the heat transfer correlation is reached
3. The vapor generator and condenser saturation temperatures are guessed.
4. By the knowledge of the waste heat at disposal, being an input of the simulation, and solving the ejector model, the entrainment ratio, together with the primary and the secondary mass flow rate are evaluated.
5. If the secondary mass flow rate is lower than the evaporator one the compressor is turned on and its mass flow rate is evaluated. Then, the total mass flow rate, being the sum of the total ejector mass flow rate and the compressor one, is calculated.

6. The condenser is solved and the heat transfer surface is evaluated. The condenser temperature is adjusted and steps 2,3,4 and 5 are repeated until the calculated heat transfer surface is equal to the effective one.
7. With the correct condenser temperature, the steam generator and the ejector are solved again. The generator temperature is modified, repeating steps from 2 to 6, until the convergence on the steam generator is achieved.
8. If the compressor is turned on and $\psi > 0$, the higher electric demand to activate the compressor leads to a waste heat increase from the engine. Consequently, steps from 1 to 7 are repeated with the new value of waste heat, until convergence.
9. The tank, if present, is integrated to evaluate its temperature in the subsequent time step, fixed to 60 seconds.
10. Finally, the seasonal performances are evaluated by means of the electrical SEER, according to European regulation (EU) 2016/2281, being the ratio between the annual cooling demand and the annual energy consumption for cooling, as defined in Eq. (5.52):

$$\begin{aligned}
 & \text{SEER}_{\text{el}} \\
 &= \frac{\sum Q_{\text{ev}}}{\sum (E_{\text{el,pump,ref}} + E_{\text{el,sea,pump}} + E_{\text{comp}} + E_{\text{el,pump,cold,1}} + E_{\text{el,pump,cold,2}} + E_{\text{el,pump,hot}})}
 \end{aligned}
 \tag{5.52}$$

The algorithm described is schematized in Figure 48.

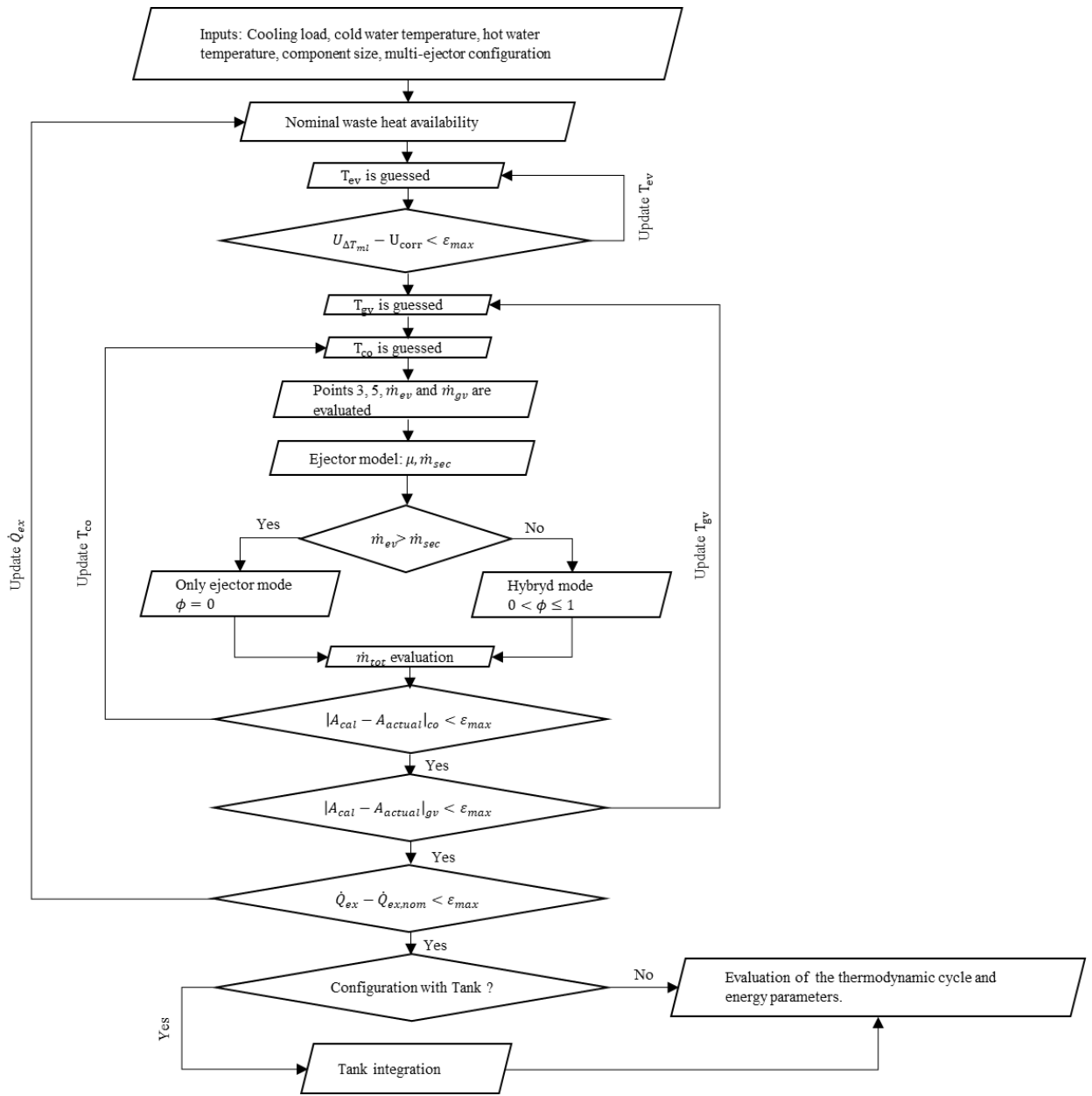


Figure 48 Resolution algorithm to simulate a waste heat driven hybrid ejector chiller for cruise ship air conditioning.

6. Optimization of design at partial load, seasonal performance and costs evaluation of a waste heat driven multi-ejector cooling system.

In this chapter, a seasonal performance analysis of a multi-ejector cooling system for domestic air conditioning, having a cooling power of 20 kW (see *Figure 38*), is carried out by means of the model developed in the previous chapter. Firstly, the system is optimized in order to find out the best configuration and the optimal ejector numbers. Then, the system is dynamically simulated considering different climate scenarios. Finally, the seasonal performance and the total costs of the proposed system are compared to the reference technologies, considering different costs of the electric energy. The analysis is carried out under the hypothesis of continuous and free availability of the heat source. All the details related to the model equations are reported in Section 5.3. These results are published in [216].

6.1 Objective of the study

The aim of this study is to compare different chiller technologies, both from the thermodynamic and the economic point of view, by means of a thermo-economic analysis, focusing on the seasonal performance of the proposed technology, namely the multi-ejector cooling system. The objective of the first part of the Chapter is to investigate the advantages to use of a multi-ejectors system instead of a single ejector and to find out the optimal ejectors number and geometrical features. After the optimization of the ejector cycle for each climate under investigation, different solutions have been dynamically simulated during the whole cooling season. The second objective of the chapter is to compare the chiller technologies now available on the market (namely electric and absorption chiller) with the proposed one, in term of seasonal performance and total costs, considering different values of the electric prices.

6.2 Operating conditions and climatic data

The system under investigation has a nominal cooling load of 20 kW and is driven by hot water, supplied at 120°C in the vapor generator. In the present analysis a continuous and free availability of the heat source is assumed. The boundary conditions of the system are listed in Table 15.

Table 15 Specification of the boundary conditions used for the sizing process.

Parameters	Value	Parameters	Value
Nominal cooling load [kW]	20	Water temperature at the 12/7 evaporator (inlet/outlet) [°C]	
Working fluid temperature at vapor generator outlet [°C]	110	Quality at evaporator outlet	1.0
Water temperature at the vapor generator (inlet/outlet) [°C]	120/80	Regenerative heat exchanger efficiency	0.90
Air temperature difference at the condenser [K]	5	Pinch points for the heat exchangers [K]	3
Quality at condenser outlet	0.0	Set point indoor temperature [°C]	26.0

To quantify the effects of different climate conditions on the ejector system performance, three different climatic zones (Milan, Madrid and Athens) are considered. The sizing of the components is carried-out by assuming the occurrence of the nominal cooling load when the external ambient temperature is equal to the maximum value, according to the weather data obtained by TRNSYS software libraries [213]. The set-point indoor temperature is set to 26.0°C. In Table 16 the maximum temperature values for each climatic zone considered in this analysis are shown.

Table 16 Maximum external ambient temperatures for each climatic zone.

Climatic zone	$T_{amb,max}$ [°C]
Milan	32.5
Madrid	36.7
Athens	37.4

6.3 Sizing results

In the first part of this analysis each component constituting the ejector cycle has been sized for the three aforementioned climate zones, assuming the same nominal cooling load. In this phase a single ejector with a fixed geometry is considered. The huge variations of the external temperature during the season cause a dramatic influence on the system performance, making the condenser design a sensitive issue, since it uses the external air as secondary fluid. Consequently, to evaluate and to choose its geometry, a careful analysis is carried out by varying different geometric parameters such as tube step, fin thickness, tube number and number of rows. For each climatic zone three different solutions have been selected on the Pareto front generated in the sizing process, as shown in Figure 49. Particularly, for each climate, solution A is the solution with lower investment costs, B is the solution having higher performance, and finally the optimal solution, C, is selected according to the utopian criterion, which is the Pareto solution having the lower distance from the utopia point, (maximum COP and the minimum set-up cost). Since the influence of the other heat exchangers is negligible, their optimization process is not described. Indeed, the plate heat exchanger (vapor generator) is characterized by low purchase costs with respect to the other devices, such as the fin and tube heat exchanger (condenser) and the flooded evaporator. Concerning the flooded evaporator, the refrigerant pressure drops are negligible, and the chosen geometry was already optimized by calculating the required number of tubes to get water Reynolds number at least equal to 2×10^4 , thus guaranteeing an optimized heat transfer performance. According to these considerations, only the optimization of the condenser is described and its influence on the total investment costs and system performance is commented in detail. Moreover, the operating costs related to the water loop circulating pump are not considered in this analysis.

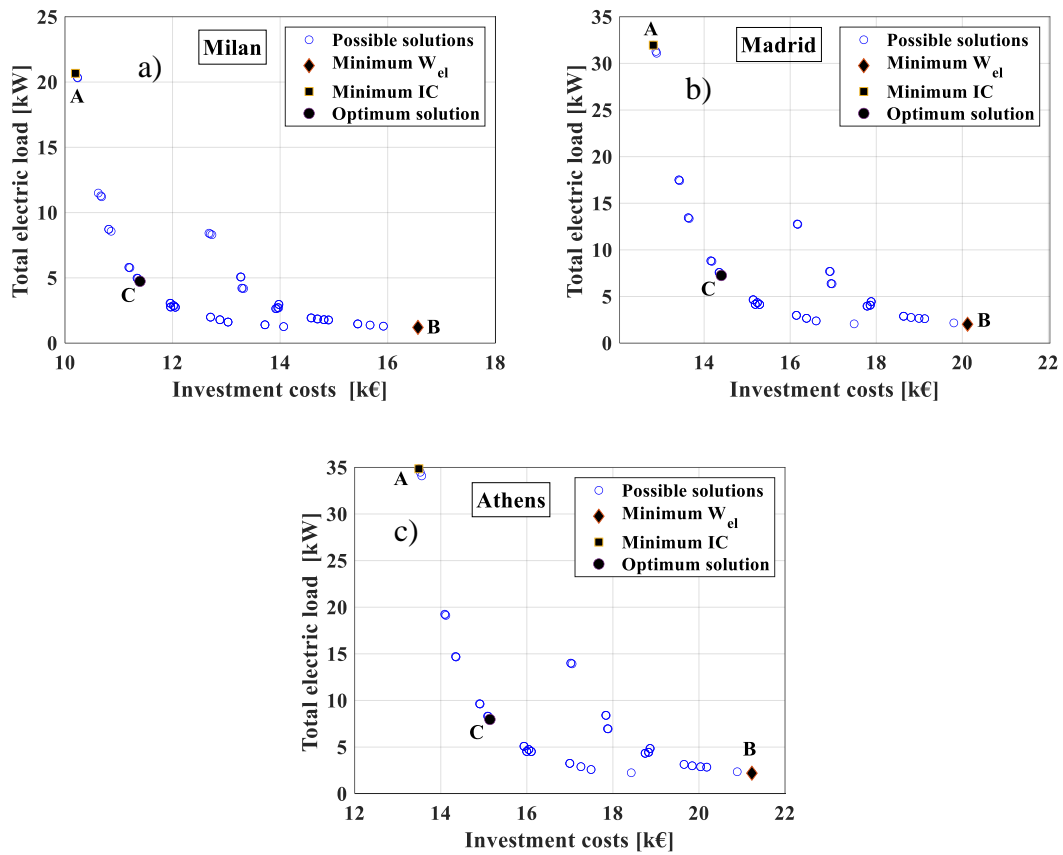


Figure 49 Total electric load of all feasible hybrid ejector configurations as a function of set-up costs for (a) Milan, (b) Madrid, (c) Athens. The distinctive points represent the arrangement characterized by the minimum costs A, the one with minimum electric load B, and the trade-off between costs and performance C.

The sizing results for each configuration and each climate are summarized in Table 17.

Table 17 Sizing results (D_t =motive nozzle throat section diameter; $D_{N,out}$ = motive nozzle outlet section diameter; D_m =mixing section diameter).

Climatic zone	Solution	T_{gv}	T_{co}	T_{ev}	D_t	$D_{N,out}$	D_m	A_{gv}	A_{co}	A_{ev}	A_{rhe}	μ	EER_{el}	IC
		[°C]	[°C]	[°C]	[mm]	[mm]	[mm]	[m ²]	[m ²]	[m ²]	[m ²]	[-]	[-]	[k€]
Milan	A	83.0	40.3	4.0	3.71	4.82	6.90	7.20	152.56	1.33	0.33	0.184	0.97	10.194
	B	83.0	40.3	4.0	3.71	4.82	6.90	7.20	407.29	1.33	0.33	0.184	16.61	16.563
	C	83.0	40.3	4.0	3.71	4.82	6.90	7.20	200.56	1.33	0.33	0.184	4.23	11.394
Madrid	A	82.2	44.4	4.0	4.55	5.91	7.78	10.48	202.11	1.33	0.47	0.127	0.63	12.819
	B	82.2	44.4	4.0	4.55	5.91	7.78	10.48	494.23	1.33	0.47	0.127	9.87	20.122
	C	82.2	44.4	4.0	4.55	5.91	7.78	10.48	265.32	1.33	0.47	0.127	2.76	14.399
Athens	A	82.0	45.2	4.0	4.75	6.17	8.00	11.30	215.25	1.33	0.50	0.118	0.57	13.491
	B	82.0	45.2	4.0	4.75	6.17	8.00	11.30	524.85	1.33	0.50	0.118	9.09	21.231
	C	82.0	45.2	4.0	4.75	6.17	8.00	11.30	281.31	1.33	0.50	0.118	2.51	15.142

6.4 Multi-ejector optimization

Before analysing the seasonal performance of the ejector cycle, the optimal ejectors number is investigated for each climatic zone. The effect of the ejectors number on the seasonal performance is shown in Figure 50. The ratio of each ejector cross section (nozzle throat, nozzle outlet, mixing section) between two subsequent ejectors assumes the following values: 0% (ejector with the same size), +20% (the cross section of the ejector 2 is 20% larger than that of the ejector 1), +40%, +80%. It is to note that the sum of the cross section of all the ejectors is always equal to the one of the nominal size ejector. The specifications of the investigated multi-ejector packs are listed in Table 18.

Table 18 Multi-ejector pack specifications.

Parameters	Value
Ejectors number [#]	1-9
Multi-ejector geometric scale ϕ_{ej}	0; 20; 40; 80

It appears evident that the use of multi-ejectors significantly increases the system performance. Indeed, by increasing the ejectors number from 1 to 2, with an area ratio, ϕ_{ej} (ratio between the cross section of the consecutive ejectors), of +80%, the electric SEER augments of 47.8%, 79.3% and 89.9% respectively for Milan, Madrid and Athens, as regards solution C. Moreover, the advantages in the adoption of multiple ejectors are more evident for warmer climates. Furthermore, a multi-ejector pack having 3 or 4 ejector allows to achieve the maximum in terms of SEER independently from the climatic zone and the multi-ejectors geometry (except for the solution having all the ejectors with the same size, namely $\phi_{ej} = 0\%$). Further increase of the ejectors number does not lead to substantial performance enhancement, but could cause technical issues in the system control. It is also noteworthy that the SEER tends to an asymptotic value for a higher ejectors number, for which there is no influence of the ejectors area ratio on the performance. These results underline the high advantages obtainable by means of a multi-ejector system instead of a single ejector with a fixed geometry, whose performance would be excessively penalized at partial load.

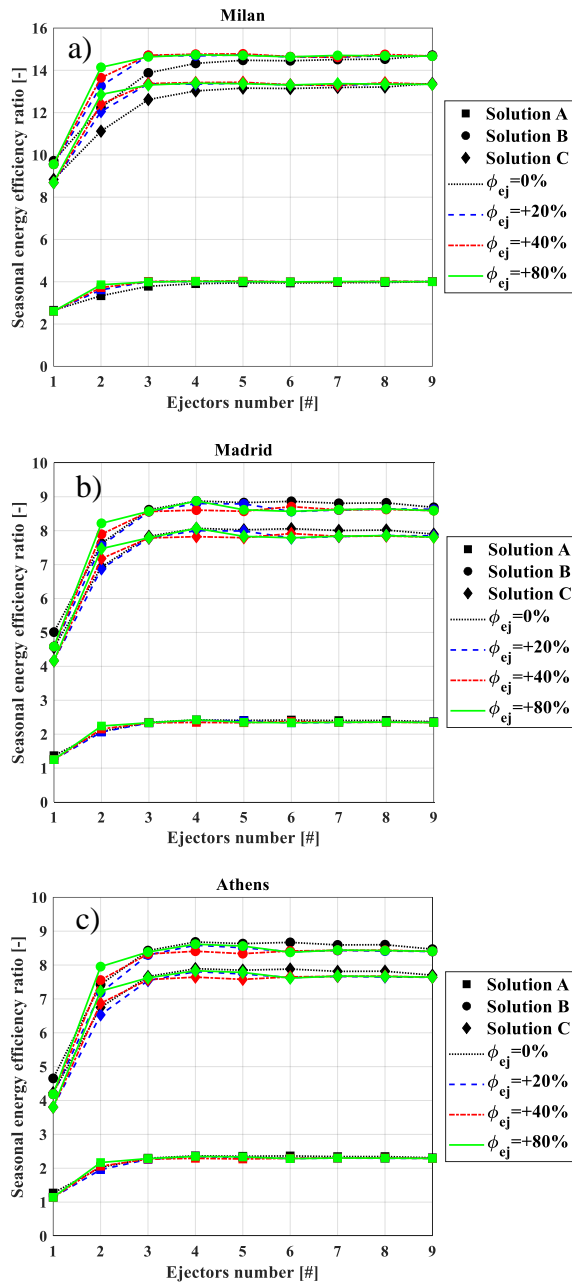


Figure 50 Seasonal performance as function of ejectors number for (a) Milan, (b) Madrid, (c) Athens and multi-ejector configuration.

6.5 Seasonal comparison

The seasonal performance of the multi-ejector chiller is compared with the conventional chiller technologies, namely electric and heat driven absorption chillers. Following the outcomes of the previous paragraphs, in terms of system design and multi-ejectors configuration optimization, this analysis is carried out for each climate condition considering the three aforesaid solution (namely A, B and C, being respectively the

solution with lower cost, higher performance and the optimal trade-off) and by considering 3 ejectors in the climate of Milan (with an area ratio of $\phi_{ej} = 20\%$) and 4 ejectors in case of Madrid and Athens ($\phi_{ej} = 80\%$). The typical seasonal performances of the electric chillers are reported in [217], while for an air-cooled absorption system the SEER is evaluated by considering electric load as energy input, and the typical performances are taken from [218]. Particularly, in Milan, the first can achieve an electric SEER of 4.0 while with the latter technology a SEER of 6.5 can be obtained. However, in the comparison a tolerance of $\pm 20\%$ is considered for these technologies to consider the market variety. The influence of the external temperature variation on the electric SEER of the electric and the absorption chiller is taken into account by considering constant the second law EER and by varying the reversible EER as a function of the external ambient temperature. The comparison among the different configurations sized and the reference technologies for the three climates under investigation is shown in Figure 51. Considering solutions B and C, the ejector cooling system is always characterized by higher performance than the reference technologies. This is more evident in moderate climate such as Milan, where solution B has an electric SEER of 14.8, respectively, 3.3 and 2.1 times higher than that of the electric and absorption chiller. On the other side, warmer the climate, lower is the performance of the ejector cycle. Indeed, in Madrid and Athens the maximum SEER achievable is, respectively, 8.1 and 7.8, considering solution B. This is mainly due to the high penalization on the ejector performance caused by the increase of the external ambient temperature (and thus condensation temperature). Solution A, the one having lower set-up costs, has always worse performance than the absorption chiller, for all the climates, while it has lower performance than the electric chiller in warmer climate, whereas their performances are comparable in the case of moderate climate (Milan).

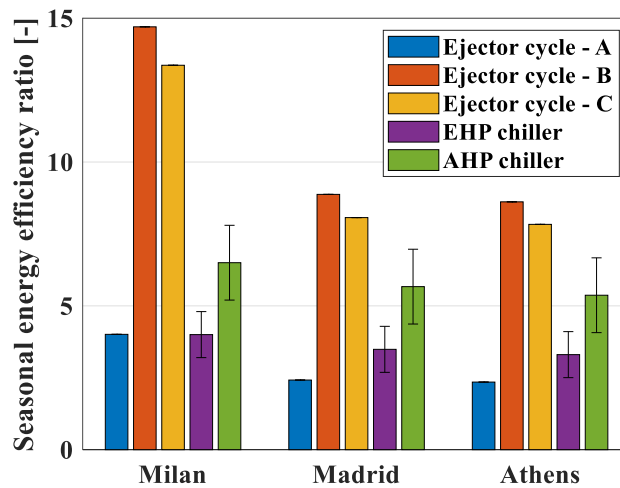


Figure 51 Seasonal performance comparison between hybrid ejector cycle and current technology (Electric chiller and absorption chiller).

6.6 Economic comparison

In this analysis, the total costs are evaluated as the sum of the investment and running cost. The purchase cost of the ejector cycle is obtained considering the sum of the cost of each component constituting the system, whereas the set-up costs of the electric and absorption chillers are obtained from a market analysis [106]. The investment costs for each system analysed and each climate are summarized in Table 19.

Table 19 Investment costs for the different solution analysed and the reference technology.

Climatic zone	Ejector cycle Solution A	Ejector cycle Solution B	Ejector cycle Solution C	EHP Chiller	AHP Chiller
Milan	10.2 k€	16.6 k€	11.4 k€	12.0 k€	19.2 k€
Madrid	12.8 k€	20.1 k€	14.4 k€	13.2 k€	21.1 k€
Athens	13.5 k€	21.2 k€	15.1 k€	14.4 k€	23.1 k€

The running costs are evaluated as reported in Eq.(6.1):

$$RC_{lifetime} = \frac{Q_{user}}{SEER_{el}} \cdot c_{el} \cdot \tau_{lifetime} \quad (6.1)$$

Where Q_{user} is the total energy demand during the whole cooling season for the analysed configuration, c_{el} is the electricity specific price and $\tau_{lifetime}$ is the system's lifetime, assumed to be 20 years. The analysis is carried out by considering three different electricity prices (0.10, 0.30 and 0.50 €·kWh⁻¹).

The total costs are evaluated by Eq.(6.2):

$$TC_{lifetime} = IC + RC_{lifetime} \quad (6.2)$$

The convenience lifetime of the ejector cycle with respect to the electric chiller for each configuration is reported in Table 20. Since absorption chillers are never economically convenient in the simulated conditions, they are not considered in Table 20.

It is evident that, due to the high set-up costs, considering the solutions that maximize the performance, namely B, the ejector cycle does not represent a practical solution, leading to a payback period equal to 15.3 and 18.1 years in Athens and Milan respectively, while the investment in Madrid does not reach the break-even point for a lifetime of 20 years. Solution A (characterized by lower investment cost, but lower performance) is always convenient in Milan, where the system performance is acceptable, due to the favourable ambient conditions, and the set-up costs are lower than other solutions. Differently, higher running costs occurring in warmer climates implicate an unfeasible lifetime convenience in the use of a multi-ejector cooling systems (up to 3.3 and 4.2 years in Madrid and Athens, respectively, when the electricity unit price of 0.10 €·kWh⁻¹ is considered). Higher electricity unit prices reduce the maximum lifetime convenience. As a matter of fact, as previously underlined, for warmer climate the ejector system with configuration A has worse performance than the electric chiller, making this solution not convenient at all.

The optimal solution C, being the trade-off between costs and performance, is always convenient in moderate climatic zone as Milan, whereas in warmer climates the hybrid ejector cooling systems are convenient with respect to EHP chillers after an acceptable lifetime (after 7.1 years in Madrid with 0.30 €·kWh⁻¹ electricity unit price and after 9.5

years in Athens with $0.10 \text{ €} \cdot \text{kWh}^{-1}$ electricity unit price). Of course, scenarios with higher electricity cost make ejector cooling systems more and more economical convenient with respect to electrical driven technologies reducing the lifetime convenience.

Table 20 Lifetime convenience of a hybrid ejector cycle with respect to an electric chiller.

Climatic zone Hybrid ejector solution	Convenience lifetime [years]		
	$c_{el}=0.10 \text{ €} \cdot \text{kWh}^{-1}$	$c_{el}=0.30 \text{ €} \cdot \text{kWh}^{-1}$	$c_{el}=0.50 \text{ €} \cdot \text{kWh}^{-1}$
Milan			
A – Minimum costs	always	always	always
B – Minimum electric load	never	never	>18.1
C - Optimum	always	always	always
Madrid			
A – Minimum costs	<3.3	<1.1	<0.7
B – Minimum electric load	never	never	never
C - Optimum	never	>7.1	>4.3
Athens			
A – Minimum costs	<4.2	<1.4	<0.8
B – Minimum electric load	never	never	>15.3
C - Optimum	>9.5	>3.2	>1.9

From Figure 52 to Figure 54 the total costs as a function of the lifetime are shown, by comparing the ejector cooling cycles with the references chillers technologies (electric and absorption) for three different values of the electricity unity prices. When the lifetime expected for the system is low, solution A represents the most convenient option due to its low set-up cost, regardless the climate conditions. An increase of the expected lifetime, instead, makes solution C the cheapest configuration.

Concerning a moderate climate as Milan, solution A is the most convenient during the whole lifetime with an electricity cost of $0.10 \text{ €}\cdot\text{kWh}^{-1}$, while for an increase in the electricity price (considering the case of $0.50 \text{ €}\cdot\text{kWh}^{-1}$), solution C becomes convenient after about 5 years. In Madrid, the lifetime value after which solution C is cheaper than solution A varies from 9.3 to 2 years when the electric energy unit price passes from 0.10 to $0.50 \text{ €}\cdot\text{kWh}^{-1}$. In Athens, lower lifetime threshold values are expected, passing from 5.7 to 1.2 years for an electricity price of 0.50 and $0.10 \text{ €}\cdot\text{kWh}^{-1}$, respectively.

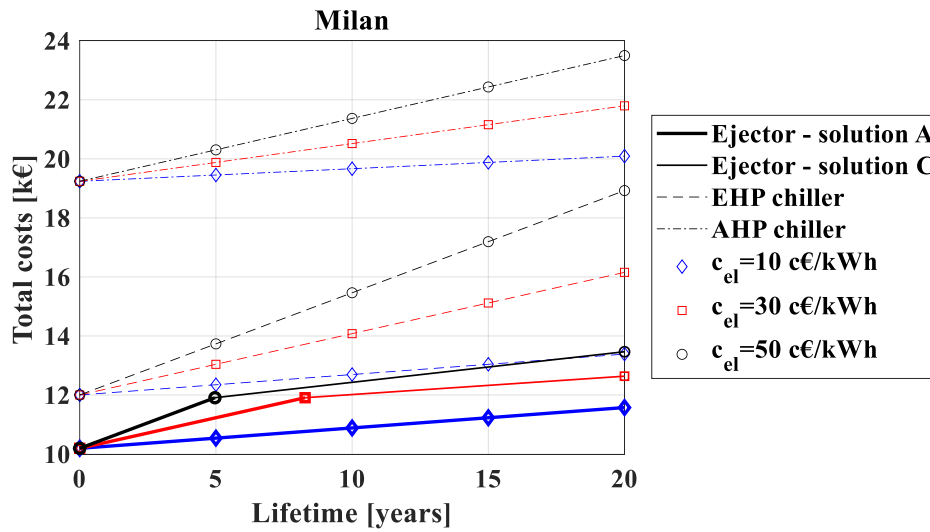


Figure 52 Total costs as function of lifetime and electric energy unit price for Milan climatic zone and comparison between hybrid ejector cycle and current technology.

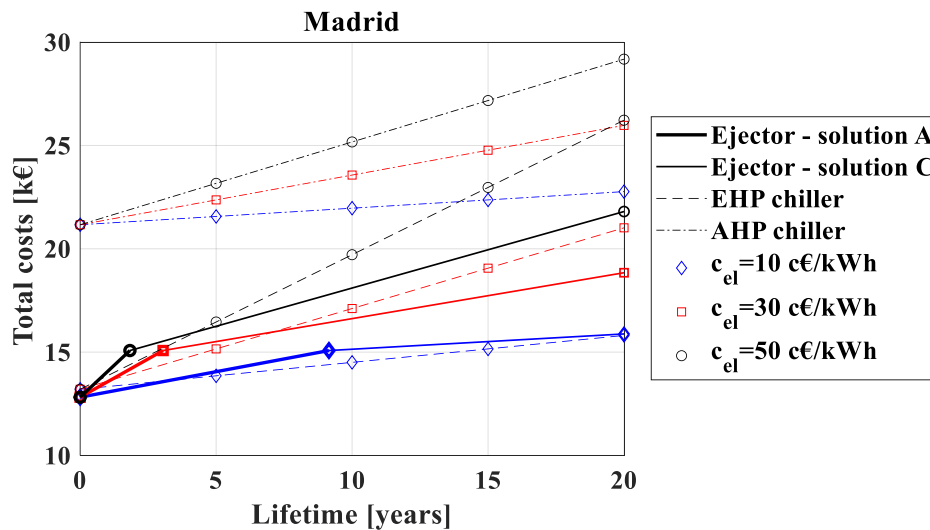


Figure 53 Total costs as function of lifetime and electric energy unit price for Madrid climatic zone and comparison between hybrid ejector cycle and current technology.

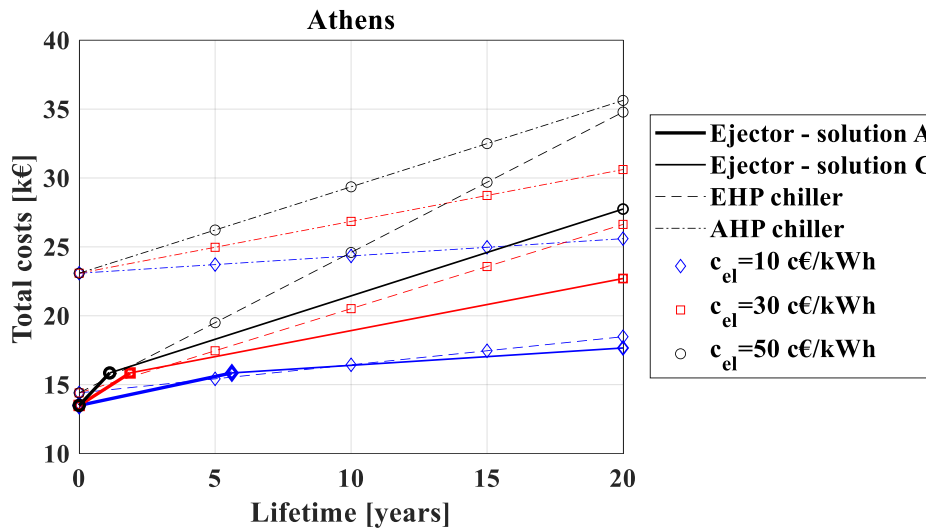


Figure 54 Total costs as function of lifetime and electric energy unit price for Athens climatic zone and comparison between hybrid ejector cycle and current technology.

6.7 Conclusions of the chapter

In this chapter, a thermo-economic analysis of a heat driven ejector chiller for domestic air conditioning is performed, assuming a free thermal source continuously available. The seasonal performance during the summer season and the total costs considering a system lifetime of 20 years are evaluated for three different climatic zones, namely Milan, Madrid and Athens, considering different electric energy specific prices with the purpose to make a comparison between the multi-ejectors cooling cycle and chillers technologies currently available on the market, namely the electric and the heat driven absorption chillers. The analysis was performed by considering different plant configurations of the ejector cycle: the solution that allows to minimize the investment costs (A); the configuration with the maximum system performance (B); the trade-off solution (C). The main outcomes of this study may be summarized as follows:

- The adoption of a multi-ejectors configuration instead of a single ejector having a fixed geometry allows the system to run at partial load without performance degradation. Warmer the climate higher are the performance improvements passing from 1 to 2 ejectors. Indeed, in Athens, the electric SEER increases of 89.9%.
- The maximization of the seasonal performance can be obtained with a multi-ejectors pack with 3 or 4 ejectors, respectively for moderate climate as Milan and

warmer climates, as Madrid and Athens. An asymptote in the seasonal performance is reached for a further increase in the ejectors number.

- The multi-ejectors cooling cycle can achieve seasonal performance significantly higher compared to the reference technology, especially in moderate climates, for which solution B reaches a SEER of 14.8, that is 3.3 and 2.1 times higher compared to the electrical and absorption chillers, respectively. For warmer climates, all the chiller technologies are characterized by a performance penalization, but the degradation due to the ambient temperature increase is stronger for the ejector cycle. As a matter of fact, the increase of the condenser temperature leads to a huge decrease of the ejector performance (leading to a lower ejector entrainment ratio). However, also in Madrid and Athens, solution B and C have a higher SEER than the traditional technologies.
- Among all the chiller technologies investigated, the hybrid ejector and the electrical system are the most economically convenient solutions, at least for low size applications. The solution C is always convenient in moderate climatic zone as Milan, whereas in case of high cooling loads the hybrid ejector cooling systems are convenient with respect to electrical chillers after an acceptable lifetime (after 7.1 years in Madrid with $0.30 \text{ €}\cdot\text{kWh}^{-1}$ electricity unit price and after 9.5 years in Athens with $0.10 \text{ €}\cdot\text{kWh}^{-1}$ electricity unit price). Scenarios with higher electricity cost make heat driven cooling systems as the ejector more and more economic convenient with respect to electrical driven technologies.

The proposed system is a brand-new technology, with no presence on the market and only few experimental prototypes, thus some hypotheses related to the components performance and costs may influence the analysis with respect to real cases. However, the convenience of the proposed optimized system when compared to conventional technologies is clearly shown and could not be affected by the uncertainty of the chosen assumptions.

7. Thermo-economic analysis and optimization strategy of a solar driven ejector cooling system employing natural refrigerants.

A thermodynamic and economic analysis of a low size (10 kW) solar driven hybrid multi-ejector compressor assisted cooling system for domestic air conditioning is presented in this Chapter. The system is firstly sized according to the procedure shown in Chapter 5, considering different scenarios in terms of solar collector size, three distinct climate conditions, to account the effects of different ambient temperatures and solar radiation, and two eco-friendly refrigerants, namely ammonia and propane. Finally, a thermo-economic comparison between the proposed technology and the reference electric chiller is carried out. The schematic of this study is presented in *Figure 42* and the complete set of equations and algorithm for the optimization and simulation processes are reported in Section 5.3.2. These outcomes are presented in [219].

7.1 Objective of the study

The purpose is to assess the effectiveness of the solar driven multi-ejector compressor assisted chiller for domestic air conditioning, both from the thermodynamic and the economic point of view with respect to the traditional cooling technologies. Particularly, given the discontinuity of the solar source, a booster compressor is embedded in the system allowing the system to work, in case of lacks the solar source, as a traditional vapor compression cycle, guaranteeing the non-stop operation. As a matter of fact, the matching between the solar radiation and the cooling demand is a critical aspect worthy of investigation to assess the performance of the proposed system. For these reasons, in the first part of the chapter the optimization of the system is carried out, considering propane and ammonia as refrigerant and Athens, Napoli and Strasbourg as climate zones. In the second part, each configuration is simulated and compared with the baseline technologies, in terms of seasonal performance and total costs.

7.2 Operating conditions and climatic data

The system analysed is a chiller for domestic air conditioning having a nominal power of 10 kW, for each climate condition considered, namely Athens, Naples and Strasbourg.

The set-point indoor temperature is set to 26.0°C. The nominal cooling load is the one corresponding to the maximum ambient temperature occurrence.

The maximum ambient temperature and the maximum solar radiation for each climate, according to weather data obtained by TRNSYS software libraries [213], are shown in Table 21.

Table 21 Maximum external ambient temperatures and solar radiation for each climatic zone.

Climatic zone	$T_{amb,max}$ [°C]	G_{max} [W·m ⁻²]
Athens	37.4	1043
Naples	34.2	1001
Strasbourg	31.9	927

All the boundary conditions assumed in this analysis are shown in Table 22.

Table 22 Boundary conditions for the system analysis.

Quantity	Value	Quantity	Value
Cooling load [kW]	10	Air temperature difference at the condenser [°C]	5
User temperature [°C]	26	Water temperature at the evaporator (inlet/outlet) [°C]	12/7
Ambient temperature [°C]	Maximum external temperature in the city considered	η nozzle	0.95
UA User [kW·K ⁻¹]	$UA_{ut} = \frac{Q_{ev}}{T_{amb,max} - T_{ut}}$	η mixing	0.85
Working fluid	Ammonia-Propane	η diffuser	0.95
Climatic zones	Strasbourg-Athens-Naples		

7.3 Sizing results

The design of the system components is obtained by varying all the parameters shown in Table 23. Particularly, for each configuration corresponding to a specific climate and working fluid, the optimum is chosen as a trade-off between costs and performance. It is worth mentioning that different scenarios in terms of solar collector size are considered, since this parameter is directly connected to the high pressure flow generated, that is strictly related to the ejector secondary flow and consequently to the share between the cooling load satisfied by the ejector and the compressor.

Table 23 Variables optimized in the sizing process.

Quantity	Value
Size solar collectors [m ²]	[25 50 75 100 125]
Pinch points for the heat exchangers [°C]	[3 6 10 15]
Condenser Fin step [mm]	[3 4 5]
Fin thickness [mm]	[0.1 0.2]
Tube diameter [mm]	6-9-12-15
Rank number [#]	1÷7
Form ratio [-]	2-3
Refrigerant mass flux [kg·m ⁻² ·s ⁻¹]	100-500
Saturation temperature in the vapor generator [°C]	[70 75 80 85 90 95 100 105 110]
ΔT superheating in the vapor generator [°C]	[10 20 30 40]

Figure 55 (a) shows all the solutions investigated during the sizing phase on the Investment costs/COP region with reference to the climate of Strasbourg and using ammonia as refrigerant, while Figure 55 (b) depicts only the Pareto front for all the other configurations (in terms of working fluid and climatic zone). Particularly, on each Pareto front four notable points are chosen: A, B and C are the solutions having the maximum nominal COP among all the points having, respectively, the lower, the intermediate and

the higher solar collector surface (25, 75 and 125 m²). Then, the optimal point, OPT, is chosen according to the Utopia criterion, considering all the solutions investigated.

It can be noticed that, by increasing the solar collector surface, the nominal performance of the hybrid ejector cycle is greatly enhanced, due to a major percentage of the cooling load satisfied by the ejector, avoiding the compressor operation. This is more evident for a cold climate, such as Strasbourg, where the COP enhancement reaches almost the 200% and the 44%, with respectively ammonia and propane, passing from solution A to C. Remarkable performance improvements are obtained also for the warmest climate of Athens, where the COP increases by 157% and 25% with, correspondingly, ammonia and propane. Nevertheless, the increase of the solar collector surface causes a dramatic increase in the investment costs. As a matter of fact, the set-up costs rise to 200% passing from solution A to C in Strasbourg. It is worth mentioning that all solutions A tends to a similar value since for smaller collector surfaces, a smaller cooling load is satisfied by the ejector and thus a higher power is required by the compressor. With no collectors, the system would be a traditional vapor compression cycle.

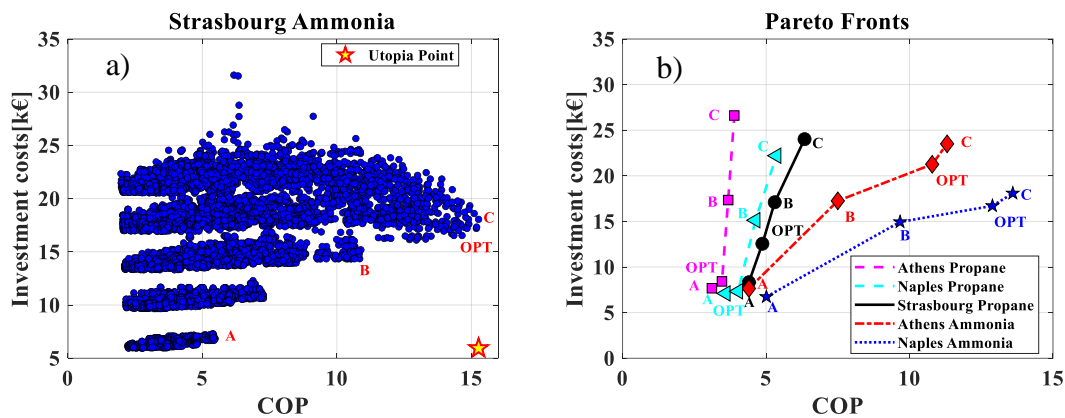


Figure 55 a) Plane investment costs/COP for Strasbourg using ammonia as refrigerant. b) Pareto front resulting by the sizing using ammonia and propane for Athens, Strasbourg and Naples.

7.4 Seasonal comparison

Figure 56 shows the electric seasonal energy efficiency ratio, for the two refrigerants under investigation and the three climates analysed. Beyond the four hybrid cycle solutions chosen in the sizing phase and described in the previous paragraph, also a traditional electric chiller has been sized and simulated for comparison purposes. All the hybrid cycle solutions are characterized by a higher SEER than the traditional electric

chiller, for both refrigerants and for all the climatic conditions. It is worth mentioning that, comparing the results obtained with the two refrigerants for the same climate, ammonia leads to better performance than propane thanks to a higher latent heat. Moreover, there is a remarkable effect of the external temperature, since there is a significant decrease in the hybrid cycle performance for warmer climates. As a matter of fact, the optimal solution with ammonia has a SEER of 9.2 in Strasbourg, 9.1 in Naples and 7.4 in Athens. It is also interesting to observe that, due to the discontinuity of the solar source, the system works as a traditional VCC for a not negligible number of hours. Consequently, considering the results for any of the climate and the working fluid, the differences between the four configurations analysed are limited. The solar load profile is the same in all configurations, as well as the weight of the operating hours having the same ambient temperature and solar radiation. On the other side, the scenarios with too large solar collectors make necessary their part load operation. Consequently, without a storage system, the adoption of a larger solar surface does not necessarily bring to a considerable increase of the seasonal performance.

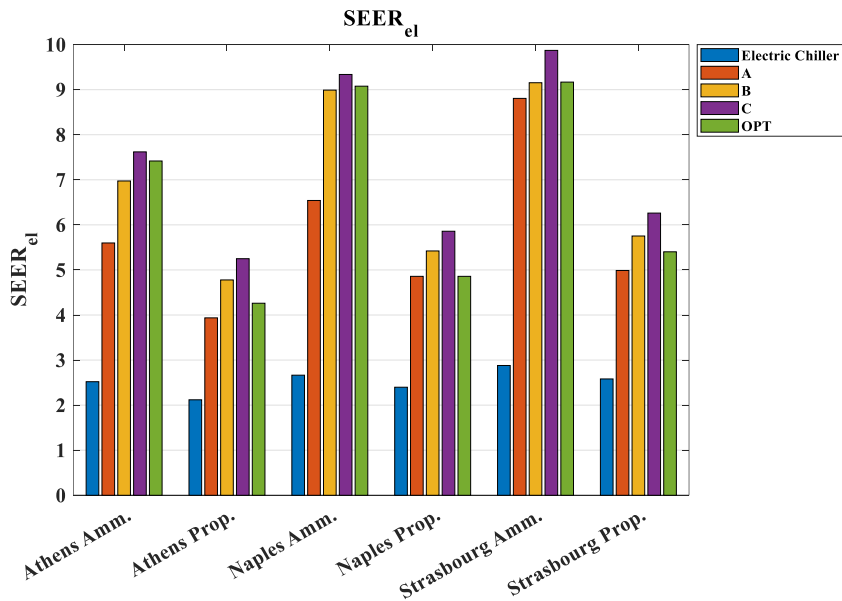


Figure 56 Seasonal efficiency ratio comparison among the several configurations investigated and the electric chiller.

7.5 Economic comparison

The convenience of all the solutions investigated with respect to the baseline technology, namely the electric chiller, is analysed assuming a lifetime of 20 years and an electric

energy price of $0.25 \text{ €} \cdot \text{kWh}_{el}^{-1}$. The results of the analysis, reported in Table 24, show that the convenience of the proposed system is dramatically penalized by the high cost of the solar collector. In Athens, for solution A, the one having the minimum surface of the solar collectors, the break-even point with respect to the traditional electric chiller is 13.5 years considering ammonia and 13 years considering propane as working fluid. With the latest fluid, also the optimal solution has a convenience only after a lifetime of 14 years in Athens. All the other solutions investigated do not have an economic convenience despite their higher electric SEER. This is ascribable to the fact that moderate and cold climates require lower running time of the chiller (643 hours/year in Naples and 130 hours/year in Strasbourg), thus limiting the convenience of a such expensive system.

Table 24 Total costs of a hybrid cycle and convenience lifetime compared to the electric chiller.

Climatic zone Hybrid ejector solution	Total costs [k€]		Convenience lifetime [years]	
	Ammonia	Propane	Ammonia	Propane
Athens				
Electric Chiller	13.7	14.9	/	/
Solution A	10.9	11.9	>13.5	>13
Solution B	19.9	21.1	never	never
Solution C	25.9	30.2	never	never
OPT Solution	23.4	12.1	never	>14
Napoli				
Electric Chiller	6.2	6.2	/	/
Solution A	8.4	9.4	never	never
Solution B	16.1	16.9	never	never
Solution C	19.2	23.9	never	never
OPT Solution	17.6	9.3	never	never
Strasbourg				
Electric Chiller	2.4	2.9	/	/
Solution A	7.8	8.6	never	never
Solution B	17.4	17.5	never	never
Solution C	25.4	26.8	never	never
OPT Solution	22.0	12.9	never	never

7.6 Conclusions of the chapter

In this chapter a solar driven multi-ejector compressor assisted chiller has been investigated for different climate zones: Athens, Naples and Strasbourg and using ammonia and propane as refrigerants. For each combination, in terms of climate and working fluid the systems have been sized by varying several design parameters and four

solutions have been chosen and then simulated during the whole cooling season. A, B and C are the solutions having the maximum COP for a solar collector surface of, respectively, 25, 75 and 125 m², while OPT is the optimal solution, among all the solution investigated for each climate and refrigerant, according to the utopia criterion. The main results are summarized below:

- The increase of the solar field surface, from 25 to 125 m² leads to an increase of the nominal COP up to 200% and 44% with, respectively, ammonia and propane. Similarly, also the purchase costs increase significantly, up to 200%, due to the high cost of the solar collectors.
- All the configurations investigated have a higher seasonal energy efficiency ratio than that of the conventional electric chiller, due to the benefits of using a free thermal energy source such as the solar one. Among the two refrigerants, the configurations using ammonia show a higher SEER.
- The hybrid cycle achieves a higher SEER in colder climates. As a matter of fact, the optimal solution with ammonia has a SEER of 9.2 in Strasbourg and 7.4 in Athens.
- The economic comparison highlights that the solar collector costs dramatically affect the convenience of the system. The solution proposed is convenient with respect to the electric chiller only if the system runs for a meaningful time (for instance 1203 hours/year in Athens) and with a solar field having a surface of 25 m² (solution A), due to the high cost of the solar collectors. In fact, due to the absence of a storage system, larger solar collectors do not allow a complete use of the solar energy, but conversely determine a dramatic increase in the investment costs. Therefore, in hot climates with high running hours/year and high solar radiation, the investigated system may be interesting compared to the traditional electric chiller solutions.

8. Thermo-economic analysis and optimization strategy of a waste heat driven cooling system employed for cruise ships air conditioning

A waste heat driven hybrid multi-ejector compressor assisted technology is operated as air conditioning system for a cruise ship in this Chapter, using the waste heat from the engine exhaust gas as thermal source, in order to assess its effectiveness in an application having a huge availability of waste heat. The schematic of the proposed system is shown in Figure 45, whereas the complete set of equations for the modelling procedure and the resolution algorithms are thoroughly described in Section 5.3.3.

8.1 Objective of the study

The aim of this study is to evaluate the adoption of the proposed heat driven chiller technology on a cruise ship, application with a considerable availability of waste heat from the several internal combustion engines employed for its propulsion and the electricity production. Particularly, the study is carried out considering the real loading curves of the ship, for a cruise ship operating continuously in the Baltic Sea and having a nominal cooling demand for air conditioning of 1350 kW. Since waste heat is neither unlimited nor continuous (i.e. during the port stay of the ship), the presence of a booster compressor is required for integration purposes. In the first part of the chapter a sensitivity analysis is carried out to quantify the influence of several design parameters on the system performance and costs. Then, the system design has been optimized by means of a genetic algorithm, to reduce the computational time. Afterwards, some notable points have been selected and simulated during the cooling season and the results are compared with those of a vapor compression chiller, in terms of performance, total costs (considering different price scenarios for the fuel) and pollutant emissions.

8.2 Case study description

The performance of the waste heat driven multi-ejector compressor assisted chiller are assessed for a cruise ship operating in the Baltic Sea. To take into account the real operating conditions of the ship, the real heating, electric and cooling demand, together with the effective propulsion load, are considered in the present analysis, as reported by [215] and shown in Figure 46. The cooling season lasts from the 1st of June till the 31st of

August and the same trends are assumed for the loading curves during the whole summer. However, the cooling demand varies according to the ambient temperature variation, as shown in Eq. (5.51). The ambient temperature is assumed to be the weighted average between Stockholm and Mariehamn, considering that the cruise ship operates continuously between these two cities. The boundary conditions and the fixed data for the simulation are summarized in Table 25.

Table 25 Boundary condition and data of the case study analyzed.

Quantity	Value	Quantity	Value
Nominal cooling load [kW]	1350	U_{WHR} [$Wm^{-2}K^{-1}$]	900
User temperature [$^{\circ}C$]	26	U_{Reg} [$Wm^{-2}K^{-1}$]	900
Climatic zone	Stockholm-Mannheim	η nozzle	0.95
Maximum ambient temperature [$^{\circ}C$]	29	η mixing	0.85
Water temperature at the evaporator (inlet/outlet) [$^{\circ}C$]	12/7	η diffuser	0.95
Exhaust gas temperature (inlet/outlet) [$^{\circ}C$]	350/130	η water pump	0.7
Working fluid	R1234yf/ammonia	Vapor quality at evaporator outlet	1.0
Vapor quality at condenser outlet	0.0		

8.3 Sensitivity analysis and system optimization

Given the high number of design and geometrical parameters considered during the sizing process, a sensitivity analysis is carried out to reduce the number of independent variables. The system design has been then performed through a multi-objective optimization approach, with the nominal COP and the investment costs as objective functions, to be, respectively, maximized and minimized.

8.3.1 Sensitivity analysis

The independent variables considered in the sensitivity analysis are reported, together with their range, in Table 26. The objective of the analysis is to quantify the influence of each parameter on nominal performance and cost. The analysis is performed employing a Latin hypercube sampling (LHS) [220] method to save simulation time.

The influence of the independent variables on the two objective functions (COP and investment costs) is quantified by means the Spearman coefficient, which formulation is given in chapter 2. The Spearman coefficient varies between -1, if the increase of the variable considered has a negative influence on the objective function, and 1 in the opposite case. As shown in Figure 57, some parameters cause both a COP increase and investment costs decrease, such as the condenser tube diameter. In such cases, their value is fixed, and they do not overcome the optimization process. Furthermore, the use of a regenerative heat exchanger, despite an increased set-up cost, does not substantially change the COP values and its presence has been neglected. In fact, the superheating of the ejector outlet is quite low due to the peculiar characteristic of the chosen refrigerant. Consequently, the parameters that will be considered in the multi-objective optimization are the working fluid, the refrigerant superheating in the vapor generator, the condenser shell diameter, the approach temperature in the condenser ($\Delta T_{PP,co}$), the approach temperature in the evaporator ($\Delta T_{PP,ev}$) and the Sea water temperature variation in the condenser ($\Delta T_{w,cond}$).

Table 26 Decisional variables considered in the sensitivity analysis and their range.

Quantity	Value	Quantity	Value
$T_{w,in,gv}$ [°C]	[100 105 110 115 120 125 130 135 140]	$\Delta T_{sh,gv}$	[10→40]
$\Delta T_{w,gv}$	[10→40]	$\Delta T_{PP,co}$	[3→15]
$\Delta T_{PP,gv}$	[3→15]	ϵ_{WHR}	[0.2→1]
$\Delta T_{PP,ev}$	[3→15]	$\Delta T_{w,co}$	[3→10]
ϵ_{REG}	[0→1]	Shell diameter evaporator [mm]	[1.5→5]
Shell diameter condenser [m]	[1.5→5]	Baffle spacing evaporator [mm]	[150→500]
Baffle spacing condenser [mm]	[100→500]	Tubes diameter evaporator [mm]	[20→60]
Tubes diameter condenser [mm]	[20→60]		

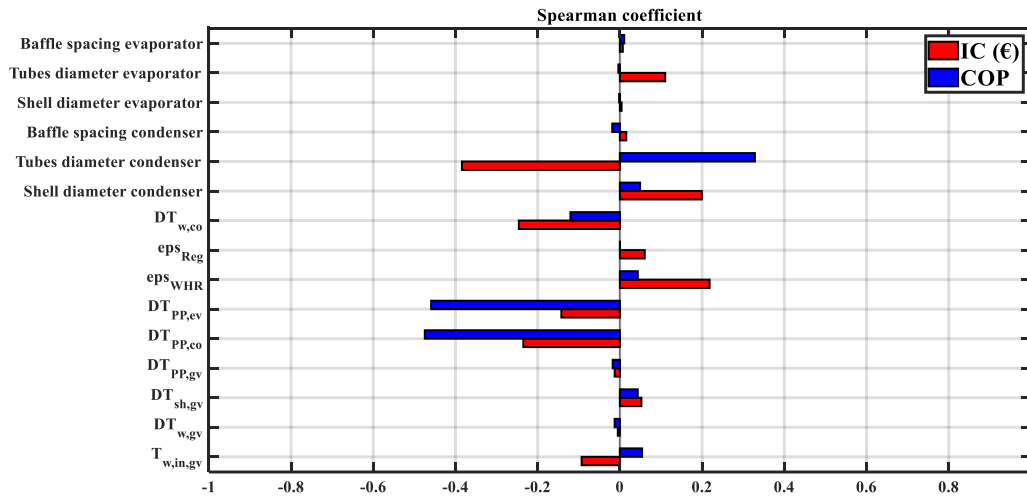


Figure 57 Results of the Sensitivity analysis in terms of Spearman coefficient for each decisional variables on the objective functions, investments costs and nominal COP.

8.3.2 System optimization

With the sensitivity analysis, six independent variables remain as influential ones. Their optimization is therefore fundamental to design the system properly, given the opposite effects they have on COP and costs. For this reason, an optimization of the system design

is performed in this section, by running a genetic algorithm (GA) [221], that allows to investigate a wide domain without performing an excessive number of simulations. Particularly, the GA tool of Matlab [52] is employed in this work, considering a population size of 50 and a crossover fraction of 0.7. The result of the GA is the Pareto front on the plane COP/investment costs reported in Figure 58. This front collects all the non-dominated solutions obtained in the GA, providing the best compromise between performance and costs. The optimal solution can be selected in several ways, according to the weight given to each objective function. In this case, to conduct an exhaustive analysis, three notable points are chosen: A is the solution having lower investment costs; B is the most efficient solution; the optimal solution is selected according to the utopian criterion.

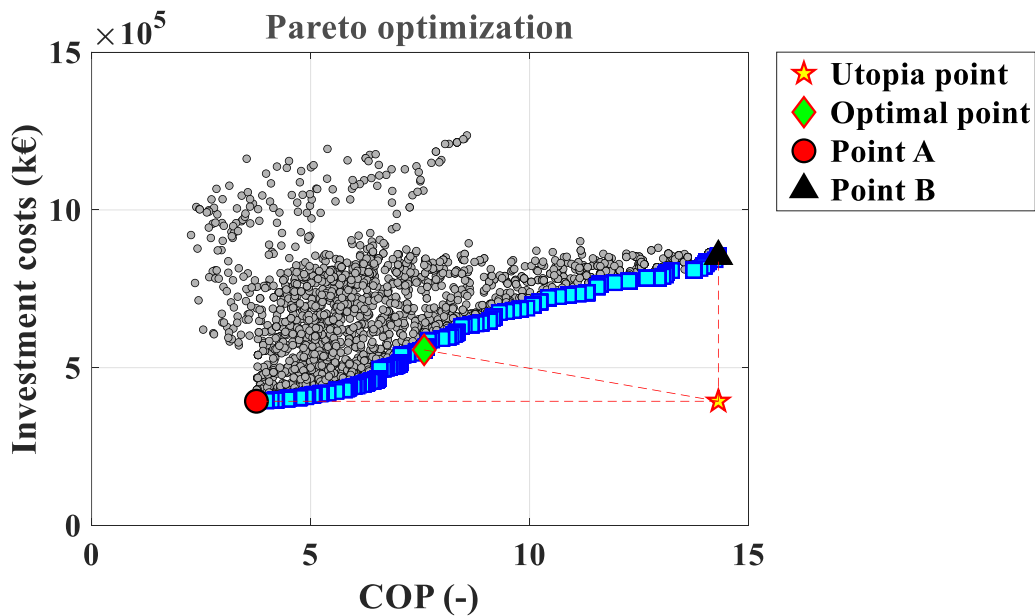


Figure 58 Investments costs vs. Nominal COP domain and Pareto fronts of the GA. Points A, B and OPT refer, respectively, to the solution with lower costs, higher nominal performance and the OPT is the optimum point according to utopian criterion.

Table 27 lists the values assumed for each design variable and the resulting objective functions for the three aforementioned points, namely A, B and OPT. In Figure are shown the refrigerant transformations for each thermodynamic cycle on the T-s diagram.

Table 27 Values of the decisional parameters, COP and investment costs for solution A, B and OPT of the Pareto Front.

Sim	Fluid	$\Delta T_{sh,gv}$	$\Delta T_{PP,ev}$	$\Delta T_{PP,co}$	ϵ_{WHR}	$\Delta T_{w,cond}$	COP	Investment cost [k€]
A	Ammonia	38	6	7	0.2	15	4.5	395
OPT	Ammonia	22	5	3	0.5	4	9.1	556
B	Ammonia	20	5	3	1	5	17.2	853

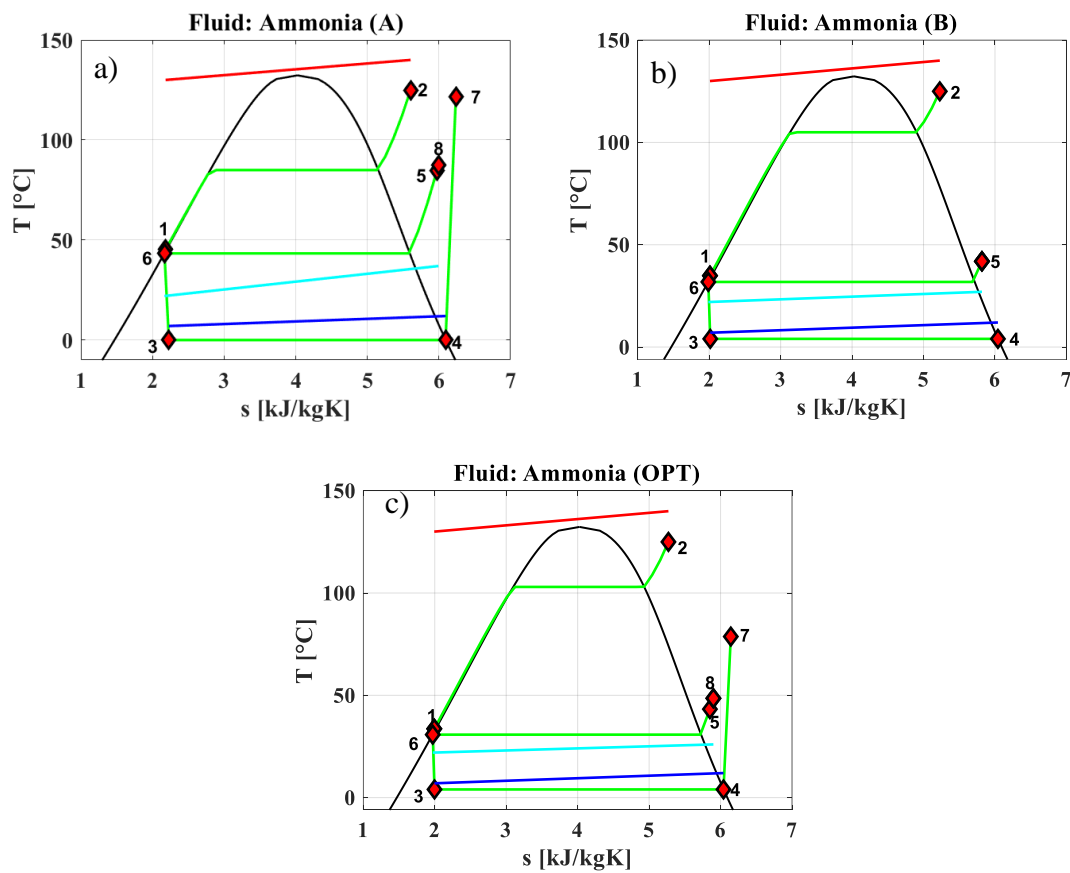


Figure 59 Thermodynamics cycle on the temperature-specific entropy diagram, in green, and the secondary fluids evolution (in red the hot water in the vapor generator, in cyan the sea water in the condenser and in blue the chilled water in the evaporator). a) Configuration A (minimum investments costs). b) Configuration B (maximum nominal COP). c) Optimal configuration (closest point to the utopian point).

The main results of the sizing procedure for the three chosen points are shown in Table 28.

Table 28 Results of the optimization procedure for the three points chosen.

Configuration	A	OPT	B
Vapor generator surface [m ²]	68.1	217.1	269.0
Plate height [mm]	19	24.5	25.5
Channel number [#]	35	88	105
Plate width [mm]	500	500	500
Plate spacing [mm]	25	25	25
Wavelength corrugation [mm]	1.0	1.0	1.0
Chevron angle [°]	80	80	80
Plate thickness [mm]	2	2	2
Condenser surface [m ²]	185.1	239.2	767.0
tube length [m]	15.3	16.0	17.7
tube number [#]	200	248	305
External tube diameter [mm]	20	20	20
Tube thickness [mm]	0.4	0.4	0.4
Baffle spacing [mm]	25	25	25
Shell diameter [m]	5	5	5
Evaporator surface [m ²]	142.4	307.4	443.0
Tube external diameter [mm]	20	20	20
tube length [m]	3.4	7.4	10.3
tube number [#]	691	691	454
Tube thickness [mm]	0.4	0.4	0.4

Baffle spacing [mm]	25	25	25
Shell diameter [m]	5	5	5
Ejector entrainment ratio	0.16	0.48	0.55
Ejector area ratio	3.66	8.76	8.69
Waste heat recovery heat Exchanger cost [k€]	155	208	286
Vapor generator cost [k€]	21	67	133
Condenser cost [k€]	97	119	320
Evaporator cost [k€]	49	82	102
Compressor cost [k€]	69	57	57
Refrigerant pump cost [k€]	1.7	2.5	2.9
Hot water pump [€]	2.23	3.5	4.8
Hot water pumps [€]	14	18	19

8.4 Seasonal analysis results

The three solutions chosen in the optimization phase are simulated during the whole cooling season to assess their seasonal performance. As specified in the system description in chapter 5, also in this case a multi-ejectors pack is considered to avoid performance degradation at partial load and to provide an optimal regulation. Furthermore, the chosen points on the Pareto front, A, B and the optimal one, are simulated, both with the configuration having the cold-water tank and without it. The tank considered has a volume of 750 m³, a set point temperature of 7°C, a dead-band of 1°C and the position for the control temperature is located at ¼ of the total tank height. For comparison purposes, a traditional electric chiller was sized and simulated, but it was not object of optimization, being a well-known technology. Only the solution with higher nominal COP is taken into account.

The seasonal performance of all the simulated configurations is reported in Figure 60 and Table 29. It appears evident that the hybrid cycle, with all the configurations analysed, can achieve a seasonal performance significantly higher than the traditional chiller. In

particular, configuration A without the storage tank is the hybrid cycle with lower SEER, equal to 7.6, while for solution B with the tank the seasonal performance remarkably increases, reaching an electric SEER of 23.1. Furthermore, it is evident that the storage tank provides better performance. Indeed, if the cooling demand is low, and the availability of the waste heat is higher than the needed to allow the multi-ejector system to satisfy all the required cooling load, the storage tank gives the opportunity to store the excess of the cool water produced. This aspect is, however, related to the specific application and for the loading curves considered. In fact, in the present case, the peak of the daily cooling demand is delayed from the peak of the waste heat at disposal (mainly depending on the ship propulsion).

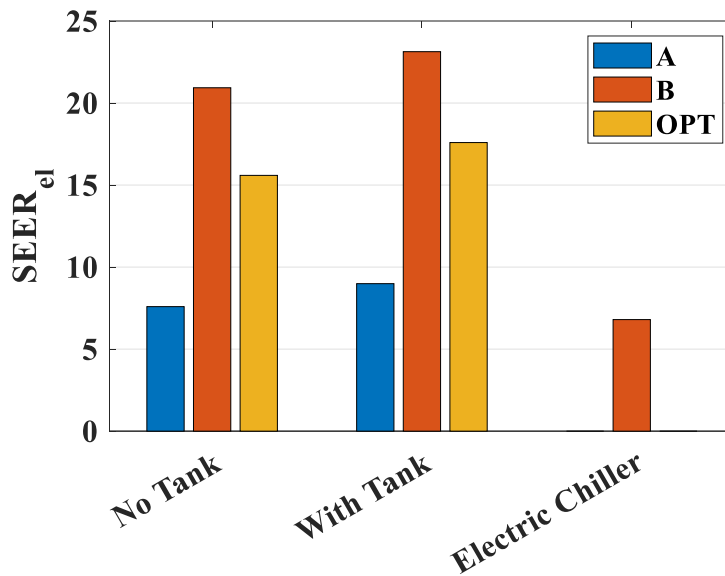


Figure 60 Seasonal performance comparison between the proposed solutions in the configuration with and without tank with respect to the electric chiller.

Table 29 Seasonal performance of the several configurations simulated.

Configuration	SEER _{el}
Hybrid cycle without tank	
Solution A	7.6
Solution B	20.9
Optimal solution	15.6
Hybrid cycle with tank	
Solution A	8.9
Solution B	23.1
Optimal solution	17.8
Electric chiller	
Optimal solution	6.8

8.5 Environmental comparison

In this section an environmental analysis is carried out aiming to compare the pollutant emissions related to the air conditioning system of the cruise ship with the traditional vapor compression chiller and those due to the hybrid ejector cycle analysed. The emissions factors of the main pollutants produced by a diesel marine engine are listed in Table 30, as reported by the Fourth IMO GHG study [222]. For simplicity purposes are considered average values of the emission factors, neglecting their variation during the engine start-up or at partial load. As shown in Figure 61, for all the three solutions analysed, considering only the configurations with tank (being those with higher SEER), the hybrid cycle allows to a remarkable reduction in pollutant emissions, up to 70%, for solution B.

Table 30 Average emission factors for a Diesel marine engine [222].

Pollutant	Emission factor [g/kg fuel]
CO	2.77
CO ₂	3.21 · 10 ³
NO _x	87.2
SO _x	2.64
PM _s	1.02
NMVOC	3.08

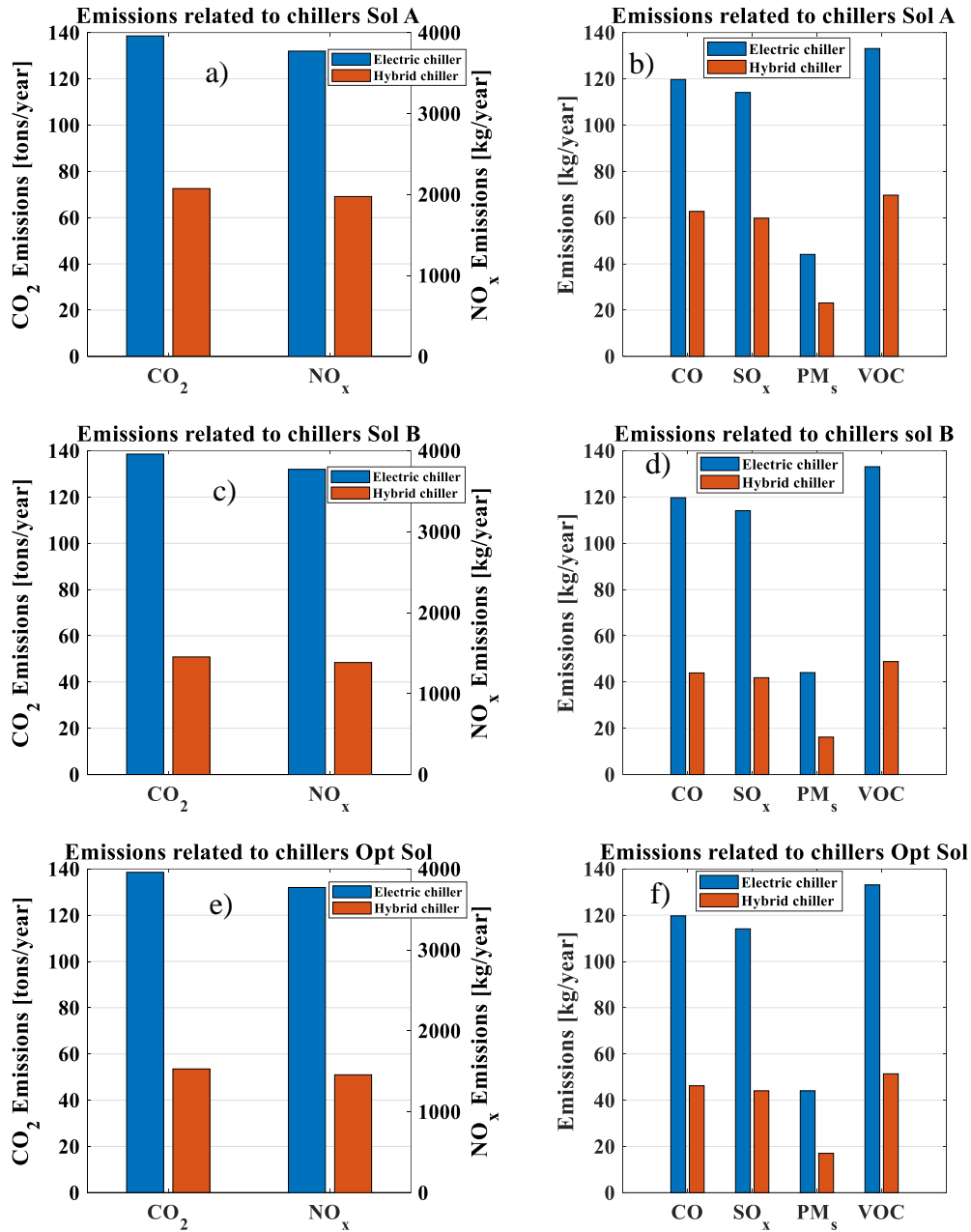


Figure 61 a) CO₂ and NO_x annual emissions for the electric chiller and the configuration A with tank. b) CO, SO_x, PM_s, VOC annual emissions for the electric chiller and the configuration A with tank. c) CO₂ and NO_x annual emissions for the electric chiller and the configuration B with tank. d) CO, SO_x, PM_s, VOC annual emissions for the electric chiller and the configuration B with tank. e) CO₂ and NO_x annual emissions for the electric chiller and the optimal configuration with tank. f) CO, SO_x, PM_s, VOC annual emissions for the electric chiller and the optimal configuration with tank.

8.6 Economic comparison

To assess the convenience of the system investigated with respect to a traditional vapor compression cycle the total costs (in terms of investment costs plus running costs) are

evaluated for the three hybrid cycle configurations with the tank and the baseline technology, considering four different fuel prices scenarios (1.5 €·kg⁻¹, 2.0 €·kg⁻¹, 2.5 €·kg⁻¹, 3.0 €·kg⁻¹). In this analysis, a total lifetime of 20 years is considered. The total costs against the lifetime are shown in Figure 62 for the different solution with tank, whereas Table 31 reports the minimum break-even point compared to the traditional chiller for each solution investigated, both, with and without the cold storage tank.

The running costs of the system are evaluated as follows:

$$RC_{lifetime} = \frac{Q_{user}}{SEER_{el}} \cdot \frac{1}{H_{Diesel}} \cdot \frac{1}{\eta_{eng} \cdot \eta_{el}} \cdot c_{fuel} \cdot \theta_{lifetime} \quad (8.1)$$

Q_{user} is the total energy demand during the whole cooling season for the analysed configuration, H_{Diesel} is the fuel low calorific power, η_{eng} and η_{el} are, respectively, the combustion and electrical engine efficiencies, c_{fuel} is the fuel cost and $\theta_{lifetime}$ is the lifetime. Then, the total costs are the sum of the investment cost and the running costs, evaluated as previously shown in Eq.(6.2).

It is evident that the convenience of the system is strongly influenced by the lifetime and the fuel cost scenario considered. However, the parameters having the stronger influence on the payback period is the system investment cost.

All the examined solutions have a break-even point within the maximum lifetime expected for the system. For a fuel price of 1.5 €·kg⁻¹ the optimal solution with a tank becomes convenient with respect to the traditional VCC chiller after approximately 8.25 years. Scenarios with higher fuel cost, instead, make the hybrid cycle more and more convenient. For a fuel cost of 3.0 €·kg⁻¹ the optimal solution with the tank is the configuration with the lower convenience lifetime (about 4 years), being the optimal trade-off between performance and costs.

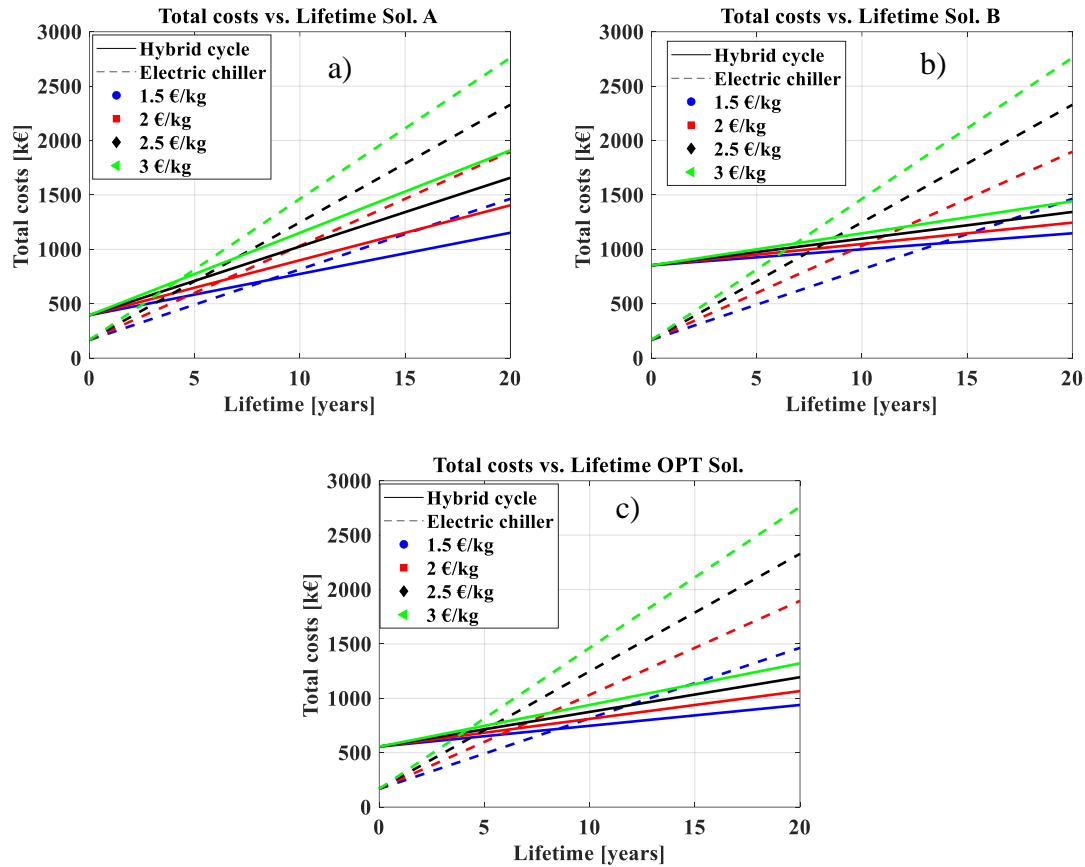


Figure 62 Comparison between total costs as a function of lifetime and fuel specific price for the hybrid cycle and the electric chiller, considering the configuration with the tank. a) Configuration A. b) Configuration B. c) Optimal configuration.

Table 31 Convenience lifetime of the hybrid cycle in the several configurations analysed with respect to an electric chiller.

Configuration	Convenience lifetime [years]			
Hybrid cycle without tank	$c_{\text{fuel}}=1.5 \text{ €}\cdot\text{kg}^{-1}$	$c_{\text{fuel}}=2 \text{ €}\cdot\text{kg}^{-1}$	$c_{\text{fuel}}=2.5 \text{ €}\cdot\text{kg}^{-1}$	$c_{\text{fuel}}=3 \text{ €}\cdot\text{kg}^{-1}$
Solution A	>13 years	>9.5 years	>7.75 years	>6.5 years
Solution B	>14 years	>10.5 years	>8.5 years	>7 years
Optimal solution	>9 years	>6.75 years	>5.5 years	>4.5 years
Hybrid cycle with tank	$c_{\text{fuel}}=1.5 \text{ €}\cdot\text{kg}^{-1}$	$c_{\text{fuel}}=1.5 \text{ €}\cdot\text{kg}^{-1}$	$c_{\text{fuel}}=2.5 \text{ €}\cdot\text{kg}^{-1}$	$c_{\text{fuel}}=3 \text{ €}\cdot\text{kg}^{-1}$
Solution A	>8.5 years	>6.25 years	>5 years	>4.25 years
Solution B	>13.75 years	>10.25 years	>8.25 years	>6.75 years
Optimal solution	>8.25 years	>6 years	>5 years	>4 years

8.7 Conclusions of the chapter

In this chapter a thermo-economic-environmental analysis of a waste heat driven multi-ejectors compressor assisted air conditioning system employed on a cruise ship operating in the Baltic Sea is performed. Firstly, the system design is conducted by means a multi-objective optimization, done by running a genetic algorithm, aiming to find the optimal compromise between nominal COP and investment costs. Subsequently, three noteworthy solutions (A minimum set-up costs, B highest nominal COP and the optimal solution according to the utopian criterion) were simulated for the whole cooling season, with and without a storage tank for chilled water. The main results are the following:

- Solution A with minimum set-up costs is characterized by a nominal COP of 5.1, with an investment cost of 395 k€; solution B, is the one with highest nominal COP (17.2), but a set-up cost of 853 k€; the chosen optimum, instead, has a nominal COP of 9.1 and a purchase cost of 556 k€.
- The comparison of the seasonal performance points out that the hybrid cycle allows to a remarkable improvement in the electric seasonal energy efficiency ratio with respect to the traditional chiller (whose SEER is 6.8). The better performance is reached for solution B in the configuration with the cold storage tank, achieving an electric SEER of 23.1.
- The presence of the cold storage tank leads to an improvement of the system performance, up to 20% compared to the corresponding configuration without the storage tank.
- The environmental analysis of the main pollutants released by a marine Diesel engine, considering only the contribution related to the air conditioning systems, points out that the hybrid cycle leads to a reduction in emission up to 70%, compared to the baseline solution employing an electric chiller.
- The economic comparison demonstrates that the convenience lifetime of the hybrid chiller is strongly related to the fuel price. When the fuel cost is low ($1.5 \text{ €}\cdot\text{kg}^{-1}$), the convenience lifetime is between 8 and 14 years. Considering scenarios with a higher fuel price ($3.0 \text{ €}\cdot\text{kg}^{-1}$), the hybrid system becomes more convenient,

having a payback period between 4 and 7 years, depending on the configuration considered.

9. Conclusions

In this thesis several innovations in the vapor compression cycles have been analysed, both at component and at system level, to define the efficiency, the economic feasibility, the competitiveness on the market and the performance with low-GWP refrigerants. A double approach has been followed, both experimental and modelling, to address the different issues affecting all the appliances operating with vapor compression cycle, for which the replacement of high-GWP refrigerants and the performance improvements must be achieved, according to the current regulation described initially. Particularly, the thesis has been divided into three sections, the first two dealing with research regarding the different components constituting the vapor compression cycle, namely compressors and heat exchangers, while the last one deals with innovations at system level. The main results are summarized below.

9.1 Summary of the numerical analysis on the linear compressor for domestic refrigeration

A detailed model of an oil-free linear compressor is developed for a domestic refrigerator having a nominal cooling capacity of 200 W. The main results are the following:

- The sensitivity analysis points out the influence of each parameter on the compressor design. Particularly, the compressor global efficiency is positively affected by the increase in piston diameter and suction valve diameter, while the global efficiency is strongly penalized increasing those parameters, bringing to higher friction losses, such as the dry friction coefficient, the stroke and the spring eccentricity. The volumetric efficiency benefits from a decrease of the piston diameter, dead volume and the clearance gap. The compressor costs are strongly influenced by the piston diameter and the stroke. Particularly, increasing the first results in a weight increase and thus higher cost, while the second has an opposite effect. All the other variables have a negligible effect on compressor efficiencies and cost.
- Following the outcomes of the sensitivity analysis, the linear compressor design has been optimized to carry out a thermo-economic comparison with the current technologies for domestic refrigerators. Firstly, the currently available

reciprocating compressors have lower cost and performances compared to both, the off-the-shelf linear compressor and the new sized solutions. However, the main result of the present analysis is the finding that there is a great of room for improvement in linear compressor technology, both in terms of higher performance and lower costs compared to the available linear compressor on the market. As a matter of fact, among all the solution analysed in this work, a compressor efficiency of 0.74 is reached, with a purchase cost of approximately 250 €.

Despite the satisfying results, which points out that linear compressor is a very interesting technology for household refrigeration, especially considering the high room for improvement, further analyses are suggested to deepen the coupling between the piston and the linear motor, to verify the applicability to a large-scale level.

9.2 Summary of the flow boiling experimental campaign on low-GWP mixtures R455A and R454C

Data regarding the flow boiling heat transfer coefficient and pressure drop of low-GWP mixtures R455A and R454C have been collected in order to optimize the heat exchangers design.

- For both refrigerants, the heat transfer coefficient is positively affected by the mass flux and heat flux increase. Particularly, the rise of the mass flux causes an enhancement of the convective contribution, while the heat flux augment leads to an increase of the nucleate boiling contribution, especially for heat fluxes higher than $20 \text{ kW}\cdot\text{m}^{-2}$. The bubble saturation temperature, instead, negatively affects the heat transfer coefficient, particularly when the mass flux is low. As a matter of fact, lower vapor density, and thus lower flow velocity, penalizes the convective contribution.
- The assessment of the experimental data with heat transfer coefficient predictive methods points out that several correlations provide a huge discrepancy with the present database, pointing out that these methods, calibrated on traditional high-GWP refrigerants, are not suitable for low-GWP mixtures. For this reason, some of these correlations are modified to consider the not-negligible temperature glide.

Consequently, using the Thome and Shakir [92] correction factor on nucleate boiling contribution, the agreement with the experimental data is remarkably improved. As a matter of fact, for R454C the modified version of the Kim-Mudawar [90] and Gungor-Winterton [91] correlations provide, respectively, a *MAPE* of 31.70% and 29.32%. Also for R455A a good agreement is provided by the modified Kim-Mudawar [90] correlation, with a *MAPE* and a *MRPE* of, respectively 23.5% and 3.67%. Finally, the Liu-Winterton [89] method gives good results for both refrigerants, having a *MAPE* of 30.04 % with respect to the experimental data collected for R454C, and a *MAPE* of 19.50 % with respect to the database of the mixture R455A.

- The adiabatic experiments highlight that pressure drop increases with the rise of the mass flux, while decreases with lower bubble saturation temperature. The separated flow method of Müller-Steinhagen and Heck [98] provides the best agreement providing a *MAPE* of 32.56% and 12.8%, respectively for R454C and R455A. With the latest also the Cicchitti [101] correlation provides a very good agreement, with a *MAPE* of 13.3% and the 98.6% of the points included in the interval $\pm 30\%$.

9.3 Summary of the hybrid ejector cycle investigation

The last part of the thesis deals with hybrid ejector cycles, representing an innovation in cold production systems, for which a thermodynamic model is developed. This system provides the cool production by means of solar energy or waste heat, allowing a reduction of the electricity consumption. Particularly, the model is employed to optimize the proposed system for several applications to assess its performance and the economic competitiveness with respect the traditional electric chiller, considering different scenarios of electricity and fuel specific costs.

- The analysis of a waste heat driven ejector chiller for domestic air conditioning, having a nominal cooling power of 20 kW, points out that the convenience of the proposed system is strongly influenced by the climates considered and the specific electricity cost. In moderate climates, such as Milan, considering the solution that maximizes the performance, the ejector chiller reaches a *SEER* of 14.8, that is 3.3 and 2.1 times higher compared with electrical and absorption chiller. Warmer

climates, such as Athens and Madrid, instead, cause a dramatic decrease of the ejector chiller performance, with a stronger penalization compared to other chiller technologies. However, also in these climates the ejector cycle can achieve higher performance than the traditional technologies. Moreover, to optimize the system performance, a multi-ejector configuration is preferable with respect to a single ejector with a fixed geometry, to maintain good performance also at partial load. The system, in case of unlimited heat source, is always economically convenient in Milan, due to the high performance, while its convenience with respect to the electric chiller depends on the lifetime in Madrid and Athens, with an increasing convenience in scenarios with high electricity costs.

- A solar driven hybrid ejector chiller for domestic air conditioning, having a nominal cooling load of 10 kW, has been investigated, taking into account also the real behavior of the solar collector, its cost and the discontinuity of the solar source, which make it necessary the presence of a booster compressor for integration purposes, in order to satisfy the cooling demand when the solar source is not available. Also in this case, the ejector chiller has higher performance in colder climates, reaching a maximum *SEER* of 9.2 in Strasbourg, 9.1 in Naples and 7.4 in Athens. The system has been simulated with ammonia and propane, pointing out that the first allows a higher performance. An increase of the solar collectors surface, from 25 to 125 m², despite a huge performance increase up to 200%, determines also a dramatic increase in the set-up costs, penalizing the economic convenience of the system, only relevant when it runs for a meaningful time (for instance 1203 hours/year in Athens) and with a solar field having the minimum surface (25 m²). Consequently, it emerges that, despite the performance improvement, the cost of the solar collectors is a critical aspect to consider in the economic assessment of this system.
- A waste heat driven hybrid ejector cycle has been assessed also for air conditioning of a cruise ship operating in the Baltic Sea, with a nominal cooling power of 1350 kW and considering the real loading curve of the ship, and thus the real availability of the waste heat at disposal. The hybrid cycle shows always better performance with respect to the conventional electric chiller (having a *SEER* of 6.8), with the highest *SEER* of 23.1, considering the solution that

maximizes the performance. Moreover, the inclusion of a cold storage tank, allowing to decouple the waste heat availability from the cooling demand, brings to a 20% increase in the performance compared to the configurations without the storage tank. Furthermore, also in this case scenarios with high fuel cost make the hybrid chiller very convenient with respect to the electric chiller. As a matter of fact, increasing the fuel cost from 1.5 €·kg⁻¹ to 3.0 €·kg⁻¹ the payback time decreases from a maximum of 14 years to 4 years. Finally, the pollutant emissions released by a marine Diesel engine, considering only the contribution related to the air conditioning system, are reduced up to 70% with the hybrid chiller.

Nomenclature

			$C_{springs}$	Springs cost	[€]
			C_{steel}	Steel cost	[€]
a_1	Effective panels heat transfer coefficient	$[W \cdot m^{-2} \cdot K^{-1}]$	c_v	Specific heat at constant volume	$[J \cdot kg^{-1} \cdot K^{-1}]$
a_2	Second-order panel efficiency coefficient	$[W \cdot m^{-4} \cdot K^{-2}]$	d	Inner diameter	[m]
A	Area	$[m^2]$	D	Outer diameter	[m]
A_m	ejector mixing section	$[m^2]$	D_h	Hydraulic diameter	[m]
A_r	ejector area ratio	$[m^2]$	E	Energy consumption	[kWh]
A_t	ejector motive nozzle throat section	$[m^2]$	f	Dry friction coefficient	[-]
C_{comp}	Compressor cost	[€]	F_g	Gas force	[N]
c_d	Drag coefficient for flow through the valves	[-]	G	mass flux	$[kg \cdot m^{-2} \cdot s^{-1}]$
c_{el}	electricity unit price	$[€ \cdot kWh_{el}^{-1}]$	g	Clearance gap	[m]
c_{fri}	Friction damping coefficient	$[N \cdot s \cdot m^{-1}]$	H	Fuel low calorific power	$[kJ \cdot kg^{-1}]$
C_{fuel}	Fuel unit price	$[€ \cdot kg^{-1}]$	h	Heat transfer coefficient	$[W \cdot m^{-2} \cdot K^{-1}]$
c_{gas}	Viscous damping coefficient	$[Ns \cdot m^{-1}]$	i	Specific enthalpy	$[kJ \cdot kg^{-1}]$
C_{motor}	Linear motor cost	[€]	I	Current	[A]
c_p	Specific heat at constant pressure	$[kJ \cdot kg^{-1} \cdot K^{-1}]$	IC	investment costs	[k€]
			J	Rotational moment of Inertia of the piston	$[kg \cdot m^2]$
			K	Stiffness	$[N \cdot m^{-1}]$
			k	Specific heat ratio	[-]

K_{gas}	Gas equivalent stiffness	$[N \cdot m^{-1}]$	\vec{u}	Fluid velocity	$[m \cdot s^{-1}]$
K_{mech}	Mechanical stiffness	$[N \cdot m^{-1}]$	u	Uncertainty	$[-]$
K_{valve}	Valve stiffness	$[N \cdot m^{-1}]$	\dot{V}	volumetric flow rate	$[m^3 \cdot s^{-1}]$
L	Length	$[m]$	V	Volume	$[m^3]$
m	Mass	$[kg]$	W	Work	$[J]$
\dot{m}	mass flow rate	$[kg \cdot s^{-1}]$	\dot{W}	Mechanical power	$[W]$
N	Normal force	$[N]$	x	Piston Position	$[m]$
$N_{springs}$	Number of springs	$[-]$	\dot{x}	Piston Velocity	$[m \cdot s^{-1}]$
P	Pressure	$[bar]$	\ddot{x}	Piston Acceleration	$[m \cdot s^{-2}]$
Q	Thermal energy	$[kWh]$	x_{tr}	Transition position	$[m]$
\dot{Q}	Thermal power	$[W]$	z	Position on the test section	$[m]$
q	Heat flux	$[W \cdot m^{-2}]$	Greek		
R	ideal gas constant	$[kJ \cdot kg^{-1} \cdot K^{-1}]$	Δ	variation	$[-]$
RC	running costs	$[k€]$	α	Motor factor	$[N \cdot A^{-1}]$
R_{conv}	Convective resistance	$[K \cdot kW^{-1}]$	β_L	liquid mass transfer coefficient	$[m \cdot s^{-1}]$
S	Piston stroke	$[m]$	δ	thickness	$[m]$
s	Specific entropy	$[kJ \cdot kg^{-1} \cdot K^{-1}]$	$\delta_{\pm 30\%}$	percentage of data points falling into a $\pm 30\%$ error band	$[\%]$
t	Time	$[s]$	γ	Heat capacity ratio	$[-]$
T	Temperature	$[^{\circ}C]$	ϵ	Eccentricity	$[m]$
TC	total costs	$[k€]$	ε	heat exchanger efficiency	$[-]$
U	overall heat transfer coefficient	$[W \cdot m^{-2} \cdot K^{-1}]$			

ψ	Ratio between compressor and total mass flow rate	[-]	ω_n	Natural pulsation	[s ⁻¹]
ϕ	multi-ejector geometric scale	[-]	ω_{res}	Resonant pulsation	[s ⁻¹]
ξ	Damping ratio	[-]	ν	Void fraction	[-]
λ	Thermal conductivity	[kW·m ⁻¹ ·K ⁻¹]	χ	Vapor quality	[-]
ζ	Viscosity	[Pa·s]	Dimensionless numbers		
ι	ι -th node	[-]	Fr	Froude number	
μ	entrainment ratio	[-]	M	Mach Number	
η	efficiency	[-]	M*	Critical Mach Number	
η_0	Zero-loss panels efficiency	[-]	Nu	Nusselt number	
η_{el}	Electric efficiency	[-]	Pr	Prandtl number	
η_g	Global efficiency	[-]	Re	Reynolds number	
η_v	Volumetric efficiency	[-]	Statistical Parameters		
θ	Piston rotation	[rad]	ER	Error in prediction	
$\dot{\theta}$	Piston angular velocity	[rad·s ⁻¹]	MAPE	Mean Absolute Percentage Error	
$\ddot{\theta}$	Piston angular acceleration	[rad·s ⁻²]	MRPE	Mean Relative Percentage Error	
Π	pressure lift	[-]	φ	Spearman Coefficient	
ρ	Density	[kg·m ⁻³]	τ	Mann-Kendall coefficient	
τ	time	[hr]	σ	Standard deviation	
			Subscripts		
			air	related to the air	
			amb	Ambient	

av	Available	f	Related to the secondary fluid
bot	related to the bottom side	fuel	Related to the fuel
build	related to the building	fan	Related to the fans
c	related to the C measuring point	flow	Flow through
calc	Calculated	fluid	Related to the fluid
cb	breakdown condition	fric	friction
cri	critical condition	glide	glide
cc	Compression chamber	gl	global
Co	Condenser	gv	vapor generator
cold	cold side	h	hydraulic
comp	compressor	high	High side
Conv	Convective	hot	hot side
cv	Control volume	hour	Related to the hour considered
Cyl	Cylinder	id	ideal
D	Diffuser	in	inlet
Dis	Discharge	ind	Indicated
ej	ejector	is	Isentropic
el	Electrical	l	liquid
eng	Related to the engine	leak	Leakage
ev	Evaporator	left	related to the left side
ex	Exhaust	LV	liquid to vapor
exp	experimental	low	Low side
		M	mixing chamber

m	mixing section	refe	reference
mat	material	res	Resonance
max	maximum value	reg	regenerative heat exchanger
mean	mean	right	related to the right side
mech	Mechanic	s	isentropic
ml	Logarithm mean	sat	saturation
mod	modified	sea	Sea water
mom	momentum	sf	secondary flow
N	motive nozzle	sh	Superheating
NB	nucleate boiling	sol	Solar
nom	nominal	Sub	Subcooling
opt	Optimal	Suc	Suction
out	Outlet	t	motive nozzle throat section
over	oversized conditions	th	thermal
p	Piston	th	related to the thermocouple measurement
pump	Related to the pump	theor	Theoretical
pf	primary flow	top	related to the top side
port	Valve port opening	tot	total
pp	Pinch point	TS	test section
pred	predicted	tube	related to the tube
preh	preheater	under	undersized conditions
R	rank		
ref	Refrigerant		

user	final user	VCC	Vapor compression cycle
v	vapor		
valve	Related to the valves	WHR	Waste heat recovery heat exchanger
vol	volumetric		
w	water		
wall	related to wall		

Abbreviations

AHP	absorption chiller
COP	coefficient of performance
EER	energy efficiency ratio
EHP	electrical chiller
GA	Genetic algorithm
GWP	Global warming potential
HFC	Hydrofluorocar bon
LHS	Latin Hypercube sampling
ORC	Organic Rankine cycle
SEER	seasonal energy efficiency ratio

List of Figures

Figure 1 Predicted growth of the cooling sector [6].....	12
Figure 2 Forecasted air conditioning stock increase [21].....	13
Figure 3 Expected electricity production distribution up to 2050 [21]	14
Figure 4 GWP values of several refrigerants [22].....	15
Figure 5 HFC emissions between 2005 and 2050 according to the business-as-usual scenario [24]	16
Figure 6 Label for refrigerating appliances according to [27].....	17
Figure 7 Comparison of HFC emissions trends with the Kigali Amendment and following the business-as-usual scenario [24]	18
Figure 8 HFCs phase-down schedule according to Kigali Amendment [9].....	19
Figure 9 GWP of several refrigerants as a function of the density.....	20
Figure 10 LG linear compressor	23
Figure 11 Schematic diagram of the linear compressor	24
Figure 12 Schematic representation of the piston as a two-degree of freedom vibration system.	28
Figure 13 Example of the simulated p-V diagram, for refrigerant R600a, suction temperature and pressure respectively equal to 8°C and 1.5 bar, and the discharge pressure set to 5.6 bar	35
Figure 14 Model validation. a) Calculated vs. experimental overall efficiency. b) Calculated vs. experimental mass flow rate	36
Figure 15 Sensitivity indices of the linear compressor efficiencies with respect to the independent design variables. a) Sensitivity indices of the linear compressor global efficiency. b) Sensitivity indices of the linear compressor volumetric efficiency	40
Figure 16 Sensitivity indexes of the linear compressor cost with respect to the independent design variables.	41

Figure 17 Diagram of the compressor cost and overall efficiency of the sized solutions compared with the prices and efficiencies ranges of the reciprocating and linear compressors now available on the market.....	44
Figure 18 GWP threshold value for refrigerated transports, commercial refrigeration and condensing units according to [10].....	49
Figure 19 Photography and piping layout of the test facility	53
Figure 20 Representation of the test section and its geometrical features.....	55
Figure 21 a) Adiabaticity tests performed for the test section. b) Experimental and predicted single-phase heat transfer coefficient against Reynolds number.....	62
Figure 22 Effect of the imposed heat flux on the R454C heat transfer coefficient for a bubble saturation temperature of 34.49°C. (a) Mass flux of 597.0 kg·m ⁻² ·s ⁻¹ . (b) Mass flux of 151.2 kg·m ⁻² ·s ⁻¹	64
Figure 23 Effect of the imposed heat flux on the R455A heat transfer coefficient, for a bubble saturation temperature of 19.0°C. (a) Mass flux of 498.4 kg·m ⁻² ·s ⁻¹ . (b) Mass flux of 300.1 kg·m ⁻² ·s ⁻¹	65
Figure 24 Effect of the mass flux on the R454C heat transfer coefficient at a bubble saturation temperature of 45.0°C and for an imposed heat flux of 9.9 kW·m ⁻² . (a) Average cross sectional heat transfer coefficient. (b) Heat transfer coefficient on the bottom side of tube.....	66
Figure 25 Effect of the mass flux on the R455A heat transfer coefficient, for a saturation bubble temperature of 19.0°C. (a) Imposed heat flux of 9.9 kW·m ⁻² . (b) Imposed heat flux of 20.0 kW·m ⁻²	67
Figure 26 Effect of the saturation pressure on the R454C heat transfer coefficient for a mass flux of 496.0 kg·m ⁻² ·s ⁻¹ and an imposed heat flux of 20.0 kW·m ⁻²	68
Figure 27 Effect of the bubble saturation temperature on the R455A heat transfer coefficient. (a) Mass flux of 49.05 kg·m ⁻² ·s ⁻¹ , heat flux of 10.1 kW·m ⁻² . (b) Mass flux of 301.0 kg·m ⁻² ·s ⁻¹ , heat flux of 20.0 kW·m ⁻²	69
Figure 28 Effect of the mass flux on the adiabatic frictional pressure gradient against local vapor quality. (a) Effect of the mass flux on pressure drop of R454C for a bubble	

saturation temperature of 35.0°C. (b) Effect of the mass flux on pressure drop of R455A for a bubble saturation temperature of 19.0°C.	70
Figure 29 Effect of the bubble saturation temperature on the adiabatic frictional pressure gradient against the local vapor quality. (a) Effect of the bubble saturation temperature on pressure drop of R454C for a mass flux of 301.0 kg·m ⁻² ·s ⁻¹ . (b) Effect of the bubble saturation temperature on pressure drop of R455A for a mass flux of 495.0 kg·m ⁻² ·s ⁻¹	71
Figure 30 Experimental vs. predicted heat transfer coefficients of R454C, by excluding stratified conditions and post-dryout heat transfer. a) Liu-Winterton [89]; b) original and modified version of Gungor-Winterton [91]; c) original and modified version of Kim-Mudawar [90] ; d) Cioncolini-Thome [95], filtered for only symmetric annular flow (vapor Froude numbers higher than 4.0).	73
Figure 31 Experimental vs. predicted heat transfer coefficients of R455A, by excluding stratified conditions and post-dryout heat transfer. a) Liu-Winterton [89]; b) Cioncolini-Thome [95] filtered for only symmetric annular flow (vapor Froude numbers higher than 4.0).; c) original and modified version of Gungor-Winterton [91]; d) original and modified version of Kim-Mudawar [90] ; e) Wojtan [96] [97].	75
Figure 32 Experimental vs. predicted frictional pressure drop of R454C, by excluding stratified conditions and post-dryout heat transfer. (a) Müller Steinhagen and Heck [98]. (b) Cicchitti [101], (c) Friedel [99], (d) Ciocolini-Thome [100], filtered for only symmetric annular flow (vapor Froude numbers higher than 4.0).	77
Figure 33 Experimental vs. predicted frictional pressure drop of R455A, by excluding stratified conditions and post-dryout heat transfer. (a) Müller Steinhagen and Heck [98]. (b) Cicchitti [101], (c) Friedel [99], (d) Ciocolini-Thome [100], filtered for only symmetric annular flow (vapor Froude numbers higher than 4.0).	78
Figure 34 (a) Schematic representation of the single-phase ejector. (b) Ejector internal transformation on T-s diagram.	106
Figure 35 Ejector entrainment ratio as a function of the condenser pressure.	107
Figure 36 Compressor global efficiency as a function of compression ratio	118
Figure 37 Pump global efficiency as function of pressure difference [205]	118

Figure 38 (a) Schematic lay-out of the hybrid ejector cycle proposed in this analysis. (b) Thermodynamic cycle of Ammonia on the Temperature-specific entropy diagram....	121
Figure 39 Sizing algorithm for an ejector cycle for domestic air conditioning.....	123
Figure 40 Example of multi-ejector control strategy by assuming four ejectors with the same size at (a) $T_{gv}=70^{\circ}\text{C}$, (b) $T_{gv}=80^{\circ}\text{C}$, (c) $T_{gv}=90^{\circ}\text{C}$	124
Figure 41 Resolution algorithm for the ejector cycle chiller simulations	127
Figure 42 a) Schematic of the solar assisted hybrid ejector cycle. b) Refrigerant transformation on the temperature- specific entropy diagram, in green, and the secondary fluids (in red the air in the condenser and in blue the chilled water)	128
Figure 43 Algorithm to size a solar assisted chiller for domestic air conditioning	130
Figure 44 Algorithm for the dynamic simulations of a solar assisted ejector chiller for domestic air conditioning	133
Figure 45 a) Schematic of the waste heat driven ejector cycle b) Thermodynamic cycle on the temperature-specific entropy for the refrigerant, in green, and the secondary fluids evolution (in red the water in the vapor generator, in cyan the sea water in the condenser and in blue the chilled water in the evaporator)	134
Figure 46 Loading curves of the ship for the warmest day of the cooling season	135
Figure 47 Resolution algorithm to size a waste heat driven hybrid ejector chiller for cruise ship air conditioning	137
Figure 48 Resolution algorithm to simulate a waste heat driven hybrid ejector chiller for cruise ship air conditioning	141
Figure 49 Total electric load of all feasible hybrid ejector configurations as a function of set-up costs for (a) Milan, (b) Madrid, (c) Athens. The distinctive points represent the arrangement characterized by the minimum costs A, the one with minimum electric load B, and the trade-off between costs and performance C	145
Figure 50 Seasonal performance as function of ejectors number for (a) Milan, (b) Madrid, (c) Athens and multi-ejector configuration.	148
Figure 51 Seasonal performance comparison between hybrid ejector cycle and current technology (Electric chiller and absorption chiller)	150

Figure 52 Total costs as function of lifetime and electric energy unit price for Milan climatic zone and comparison between hybrid ejector cycle and current technology.	153
Figure 53 Total costs as function of lifetime and electric energy unit price for Madrid climatic zone and comparison between hybrid ejector cycle and current technology.	153
Figure 54 Total costs as function of lifetime and electric energy unit price for Athens climatic zone and comparison between hybrid ejector cycle and current technology .	154
Figure 55 a) Plane investment costs/COP for Strasbourg using ammonia as refrigerant. b) Pareto front resulting by the sizing using ammonia and propane for Athens, Strasbourg and Naples.	159
Figure 56 Seasonal efficiency ratio comparison among the several configurations investigated and the electric chiller	160
Figure 57 Results of the Sensitivity analysis in terms of Spearman coefficient for each decisional variables on the objective functions, investments costs and nominal COP	167
Figure 58 Investments costs vs. Nominal COP domain and Pareto fronts of the GA. Points A, B and OPT refer, respectively, to the solution with lower costs, higher nominal performance and the OPT is the optimum point according to utopian criterion	168
Figure 59 Thermodynamics cycle on the temperature-specific entropy diagram, in green, and the secondary fluids evolution (in red the hot water in the vapor generator, in cyan the sea water in the condenser and in blue the chilled water in the evaporator). a) Configuration A (minimum investments costs). b) Configuration B (maximum nominal COP). c) Optimal configuration (closest point to the utopian point).	169
Figure 60 Seasonal performance comparison between the proposed solutions in the configuration with and without tank with respect to the electric chiller	172
Figure 61 a) CO ₂ and NO _x annual emissions for the electric chiller and the configuration A with tank. b) CO, SO _x ,PM _s , VOC annual emissions for the electric chiller and the configuration A with tank. c) CO ₂ and NO _x annual emissions for the electric chiller and the configuration B with tank. b) CO, SO _x ,PM _s , VOC annual emissions for the electric chiller and the configuration B with tank. e) CO ₂ and NO _x annual emissions for the electric chiller and the optimal configuration with tank. f) CO, SO _x ,PM _s , VOC annual emissions for the electric chiller and the optimal configuration with tank.	174

Figure 62 Comparison between total costs as a function of lifetime and fuel specific price for the hybrid cycle and the electric chiller, considering the configuration with the tank.

a) Configuration A. b) Configuration B. c) Optimal configuration..... 176

List of Tables

Table 1 Independent variables analysed and their variation range.....	36
Table 2 Boundary conditions and input parameter adopted in the simulations.....	37
Table 3 Spearman and Mann-Kendall coefficients for the three objective functions of interest	42
Table 4 Objective functions and input parameters values for the non-dominated points on the Pareto front. A: lower cost configuration. B higher efficiency configuration.....	43
Table 5 Properties comparison between mixtures R454C, R455A and R404A, at a bubble saturation temperature of 20°C.....	50
Table 6 Range and accuracy of the measurement instruments employed in the test rig	56
Table 7 Uncertainty equations for the derived parameters of interest.....	60
Table 8 Maximum uncertainty recorded for all the parameters of interest, both in stable boiling and for post-dryout conditions	61
Table 9 Operating condition investigated in the experimental campaign for the heat transfer coefficient measurement.....	63
Table 10 Assessment of all the chosen two-phase heat transfer coefficient predictive methods for the refrigerant R454C	74
Table 11 Assessment of all the chosen two-phase heat transfer coefficient predictive methods for the refrigerant R455A.....	76
Table 12 Assessment summary of all the chosen two-phase frictional pressure drop predictive methods.....	79

Table 13 Single-phase and two-phase heat transfer correlations for each heat exchanger considered.....	115
Table 14 Cost functions for each component of the system.....	120
Table 15 Specification of the boundary conditions used for the sizing process	143
Table 16 Maximum external ambient temperatures for each climatic zone.....	143
Table 17 Sizing results (D_t =motive nozzle throat section diameter; DN_{out} = motive nozzle outlet section diameter; D_m =mixing section diameter).	146
Table 18 Multi-ejector pack specifications	147
Table 19 Investment costs for the different solution analysed and the reference technology	150
Table 20 Lifetime convenience of a hybrid ejector cycle with respect to an electric chiller.	152
Table 21 Maximum external ambient temperatures and solar radiation for each climatic zone.....	157
Table 22 Boundary conditions for the system analysis	157
Table 23 Variables optimized in the sizing process	158
Table 24 Total costs of a hybrid cycle and convenience lifetime compared to the electric chiller	162
Table 25 Boundary condition and data of the case study analyzed.....	165
Table 26 Decisional variables considered in the sensitivity analysis and their range..	167

Table 27 Values of the decisional parameters, COP and investment costs for solution A, B and OPT of the Pareto Front.	169
Table 28 Results of the optimization procedure for the three points chosen.	170
Table 29 Seasonal performance of the several configurations simulated	173
Table 30 Average emission factors for a Diesel marine engine [222]	173
Table 31 Convenience lifetime of the hybrid cycle in the several configurations analysed with respect to an electric chiller	176

Bibliography

- [1] J. Rogelj, A. Popp, K.V. Calvin et al. Scenarios towards limiting global mean temperature increase below 1.5 °C. *Nature Clim Change* 8, 325–332 (2018).
- [2] R. James, R. Washington, Changes in African temperature and precipitation associated with degrees of global warming. *Climatic Change* 117 (2013) 859–872.
- [3] IEA (2020), *Energy Technology Perspectives 2020*, IEA, Paris.
- [4] IEA (2021), *Greenhouse Gas Emissions from Energy: Overview*, IEA, Paris.
- [5] The Paris Agreement. United Nations Climate Change.
- [6] University of Birmingham. *A Cool World: Defining the Energy Conundrum of Cooling for All* (2018).
- [7] IEA, Global air conditioner stock, 1990-2050, IEA, Paris <https://www.iea.org/data-and-statistics/charts/global-air-conditioner-stock-1990-2050>.
- [8] IEA (2022), Installation of about 600 million heat pumps covering 20% of buildings heating needs required by 2030, IEA, Paris <https://www.iea.org/reports/installation-of-about-600-million-heat-pumps-covering-20-of-buildings-heating-needs-required-by-2030>.
- [9] E. Heath, Amendment to the Montreal Protocol on Substances that Deplete the Ozone Layer (Kigali Amendment). *International Legal Materials*, 56(2017), 193-205., <https://doi.org/10.1017/ilm.2016.2..>
- [10] The European Parliament and the Council of the European Union, 2014. Regulation (EU) No 517/2014 of the European Parliament and the Council of 16 April 2014 on fluorinated greenhouse gases and repealing Regulation (EC) No 842/2006, *Off. J. Eur. Union* 150.

- [11] Commission Regulation (EU) 2016/2281 of 30 November 2016 implementing Directive 2009/125/EC of the European Parliament and of the Council establishing a framework for the setting of ecodesign requirements for energy-related products, with regard to, ecodesign requirements for air heating products, cooling products, high temperature process chillers and fan coil units (Text with EEA relevance)..
- [12] Sustainable Energy for All [SEforAll] (2018) Chilling Prospects: Providing Sustainable Cooling for All.
- [13] IIR, 2015. 29th Note: The Role of Refrigeration in the Global Economy.
- [14] FAO, International Fund for Agricultural Development, United Nations Children's Fund, World Food Programme, and WHO (2018). The State of Food Security and Nutrition in the World 2018. Building climate resilience for food security and nutrition, Rome..
- [15] Food and Agriculture Organization of the United Nations [FAO] (2013). Food Wastages Footprint: Impacts on natural resources, summary report. Food and Agriculture Organization of the United Nations.
- [16] International Institute of Refrigeration (2009) The Role of Refrigeration in Worldwide Nutrition..
- [17] Project Drawdown (2017) Reduced Food Waste, Technical Summary.
- [18] IEA (2018a). Future of Cooling: Opportunities for Energy Efficient Air conditioning..
- [19] C.Y. Yi, C. Peng, Correlating cooling energy use with urban microclimate data for projecting future peak cooling energy demands: Residential neighbourhoods in Seoul. Cities Soc. 35 (2017) 645-59.
- [20] IEA (2021), World Energy Outlook 2021, IEA, Paris <https://www.iea.org/reports/world-energy-outlook-2021..>

- [21] R.K. Pachauri, M.R. Allen, V.R. Barros, J. Broome, W. Cramer, R. Christ, et al. Climate change 2014: synthesis report. Contribution of Working Groups I, II and III to the fifth assessment report of the Intergovernmental Panel on Climate Change. Ipcc 2014..
- [22] DNV GL's Energy Transition Outlook..
- [23] UNEP (2019e). Handbook for the Montreal.
- [24] R.K. Pachauri, M.R. Allen, V.R. Barros, J. Broome, W. Cramer, R. Christ, et al. Climate change 2014: synthesis report. Contribution of Working Groups I, II and III to the fifth assessment report of the Intergovernmental Panel on Climate Change. Ipcc 2014.
- [25] P. Purohit, L. Höglund-Isaksson, Global emissions of fluorinated greenhouse gases 2005–2050 with abatement potentials and costs, *Atmos. Chem. Phys.*, 17 (2017) 2795–2816.
- [26] World Meteorological Organization [WMO], UNEP, National Oceanic and Atmospheric Administration [NOAA], National Aeronautics and Space Administration [NASA], & European Commission [EC] Scientific Assessment of Ozone Depletion: 2018, Scientific Assessment, of Ozone Depletion: 2018, Geneva. Global Ozone Research and Monitoring Project-Report No. 58..
- [27] Regulation (EU) 2017/1369.
- [28] Regulation (EU) 2021/340.
- [29] Montreal Protocol on Substances that Deplete the Ozone Layer Montreal, 16 September 1987.
- [30] ASHRAE. 2010a, Designation and Safety Classification of Refrigerants, ANSI/ASHRAE Standard 34-2010, American Society of Heating, Refrigerating and Air-Conditioning Engineers (ASHRAE), Atlanta, GA, USA.

- [31] P. Bansal, E. Vineyard, O. Abdelaziz, Advances in household appliances-A review. *Applied Thermal Engineering*. 31 (2011) 3748-3760.
- [32] M. Dongellini, G. Morini, On-off cycling losses of reversible air-to-water heat pump systems as a function of the unit power modulation capacity. *Energy Conversion and Management* 196 (2019) 966-978.
- [33] J. Gustavsson, C. Cederberg, U. Sonesson, R. Van Otterdijk, A. Meybeck, Global food losses and food waste-extent, causes and prevention (Rome: FAO). 2011.
- [34] R. Mastrullo, A.W. Mauro, G. Napoli, S. Strano, L. Viscito, Thermo-economical sensitivity analysis of a linear compressor. *International Journal of Refrigeration*. 142 (2022), 82-91.
- [35] K. Liang, A review of linear compressors for refrigeration. *Int J. of Refrig.* 84 (2017). 253-273.
- [36] K. Park, E. Hong, H.K. Lee, Linear motor for linear compressor. *International compressor engineering conference, Purdue*. C12-1 (2007).
- [37] A. Bijanzad, A. Hassan, I. Lazoglu, Analysis of solenoid based linear compressor for household refrigerator. *Int. J. of Refrig.* 74 (2017) 116-128..
- [38] M. Lamantia, A. Contarini. S. Giovanni, Numerical and experimental analysis of a linear compressor. *Proceedings of Internation compressors engineering conference. Purdue*, C23-2.
- [39] H. Chen, X. Liu, X. Zou, Z. Lv, W. Li, C. Chen, Study of the moving offset characteristic of multi-loop moving coil linear compressor. *Int. J. of Refrig.* 113 (2022). 289-301.
- [40] A. Jomde, A. Anderson, V. Bhojwani, S. Kedia, N. Jangale, K. Kolas, P. Khedkar, Modeling and measurement of a moving coil oil-free linear compressor

performance for refrigeration application using R134a, *Int. J. Refrig.* Volume 88 (2018) 182-194.

- [41] C. R. Bradshaw, E. A. Groll, S. V. Garimella, A comprehensive model of a miniature-scale linear compressor for electronics cooling. *Int. J. Refrig* 34 (2011) 63-73.
- [42] C.R. Bradshaw, E.A.Groll, S.V. Garimella, Linear compressors for electronics cooling: Energy recovery and its benefits. *Int. J. Refr.* 36 (2013) 2007-2013..
- [43] N.R. Van der Walt, R. Under, The simulation and design of a high efficiency lubricant free linear compressor for domestic refrigerator. In: *Proceedings of the international compressor engineering Purdue conference*, p. 787 (1992).
- [44] K. Liang, R. Stone, M. Dadd, P. Bailey, A novel linear electromagnetic-drive oil-free refrigeration compressor using R134a. *Int. J. Refrig.* 40 (2014) 450-459.
- [45] Z. Zhu, K. Liang, Z. Li, H. Jiang, Z. Meng, A numerical model of a linear compressor for household refrigerator. *Applied Thermal Engineering.* 198 (2021) 117467.
- [46] Z. Li, K. Liang, X. Chen, Z. Zhu, Z. Zhu, H. Jiang, A comprehensive numerical model of a vapour compression refrigeration system equipped with a variable displacement compressor. *Applied Thermal Engineering.* 204 (2022) 117967.
- [47] Z. Zhu, K. Liang, Z. Li, h. Jiang, Z. Meng, Thermal-economic-environmental analysis on household refrigerator using a variable displacement compressor and low-GWP refrigerants. *Int. J. Refrig.* 123 (2021) 189-197.
- [48] J. K. Kim, C. G. Roh, H. Kim, J.H. Jeong, An experimental and numerical study on an inherent capacity modulated linear compressor for home refrigerators. *Int. J. Refrig.* 34 (2011) 1415-1423...

- [49] J. K. Kim, J.B. Kim, Modulation characteristics of a linear compressor for evaporating and condensing temperature variations for household refrigerators. *Int. J. Refrig.* 40 (2014) 370-379..
- [50] X. Zhang, D. Ziviani, J.E. Braun, E. A. Groll, Theoretical analysis of dynamic characteristics in linear compressors. *Int. J. Refrig.* 109 (2020) 114-127.
- [51] X. You, L. Qiu, C. Duan, X. Jiang, C. Huang, X. Zhi, Study on the stroke amplitude of the linear compressor. *Applied Thermal Engineering.* 129 (2018) 1488-1495.
- [52] X. Li, H. Zou, M. Tang, Y. Wang, X. Tang, C. Tian, Optimization analysis of linear compressor using R290 for capacity-modulation performance improvement. *Int. J. of Refrig.* 127 (2021) 111-119.
- [53] MATLAB release. Natick, Massachussets, United States, The MathWorks, Inc.
- [54] E W Lemmon, Mc M.O. Linden, M.L. Huber, REFPROP NIST Standard Reference Database 23, Version 9.0; 2009.
- [55] X. Zhang, D. Ziviani, J.E. Braun, E.A. Groll, Experimental validation and sensitivity analysis of a dynamic, simulation model for linear compressors. *Int. J. of Refrig.* 117 (2020) 369-380.
- [56] R.P. Adair, E.B. Qvale, J.T. Pearson, Instantaneous heat transfer to the cylinder wall in reciprocating compressor. In: *Proceedings of the International Compressor Engineering Purdue Conference (1972)* (p. 86.
- [57] C.R. Bradshaw, A Miniature-Scale Linear Compressor for Electronics Cooling. Ph.D. thesis. Purdue University (2012).
- [58] Standard 23.1-2010, Methods of Testing for Rating the Performance of Positive Displacement Refrigerant Compressors and Condensing Units That Operate at Subcritical Temperatures..

- [59] S.M. Yeo, A.A. Polycarpou, Tribological performance of PTFE- and PEEK-based coatings under oil-less compressor conditions. *Wear* 296 (2012) 638-647.
- [60] <https://www.dim.molle.com/>.
- [61] J.H. Kim, E.A. Groll, Feasibility study of a bowtie compressor with novel capacity modulation. *International Journal of Refrigeration* 30 (2007) 1427-1438.
- [62] www.amazon.com.
- [63] A.W. Mauro, G. Napoli, F. Pelella, L. Viscito, Flow boiling heat transfer and pressure drop data of non-azeotropic mixture R455A in a horizontal 6.0 mm stainless-steel tube. *International Journal of refrigeration*. 119 (2020). 195-205.
- [64] A. Arcasi, A.W. Mauro, G. Napoli, L. Viscito, Heat transfer coefficient, pressure drop and dry-out vapor quality of R454C. Flow boiling experiments and assessment of methods. *International Journal of Heat and Mass Transfer*. 188 (2022), 122599.
- [65] A. Mota-Babiloni, J.R. Haro-Ortuño, J. Navarro-Esbrí, Á. Barragán Cervera, Experimental drop-in replacement of R404A for warm countries using the low GWP mixtures R454C and R455A. *International Journal of Refrigeration*. 91 (2018) 136-145.
- [66] P. Makhnatch, A. Mota-Babiloni, R. Khodabandeh, Characteristics of R454C and R455A as R404A alternatives in commercial refrigeration, *Refrigeration Science and Technology, International Institute of Refrigeration* (2018) 547-553.
- [67] M. Zgliczynski, J. Sedliak, Thermal Profile Of A Reciprocating Compressor Using Low GWP Refrigerants, *International Compressor Engineering Conference*, 2642. (2018).

- [68] A. Mota-Babiloni, J. Haro-Ortuño, J. Navarro-Esbría , A. Barragán-Cervera, Experimental drop-in replacement of R404A for warm countries using the low GWP mixtures R454C and R455A, *Int. J. of Refrigeration* 91 (2018) 136-145.
- [69] A. Sethi, G. Pottker, S.Yana-Motta, Experimental evaluation and field trial of low global warming potential R404A replacements for commercial refrigeration, *Science and Technology for the Built Environment* 22 (2016) 1175-1184.
- [70] V. Oruç, A.G. Devocioğlu, Experimental investigation on the low-GWP HFC/HFO blends R454A and R454C in a R404A refrigeration system, *International Journal of Refrigeration*, 128 (2021) 242-251.
- [71] B.Lee, N.H. Kim, Drop-In Tests of R-404A Alternative Refrigerants R-455A and R-454C in a Small Ice Maker, *International Journal of Air-Conditioning and Refrigeration*, Vol. 27, No. 2 (2019).
- [72] R. Llopis, D. Calleja-Anta, D. Sánchez, L. Nebot-Andrés, J. Catalán-Gil, R. Cabello, R-454C, R-459B, R-457A and R-455A as low-GWP replacements of R-404A: Experimental evaluation and optimization, *International Journal of Refrigeration*, Volume 106 (2019).
- [73] B.H. Minor, S. Shah, L. Simoni, "Testing of HFO Refrigerant with Less Than 150 GWP in a Commercial Freezer" . *International Refrigeration and Air Conditioning Conference*. Paper 1729. (2016).
- [74] M. Azzolin, A. Berto, S. Bortolin, L. Moro, D. Del Col, Condensation of ternary low GWP zeotropic mixtures inside channels. *International Journal of Refrigeration*. 103. 2019. 77-90.
- [75] A. Berto, M. Azzolin, S. Bortolin, C. Guzzardi, D. Del Col, Measurements and modelling of R455A and R452B flow boiling heat, transfer inside channels. *International Journal of refrigeration*. 120. 2020. 271-284.

- [76] A.T. Jacob, B.M. Fronk, In-Tube condensation of zeotropic refrigerant R454C from superheated vapor to subcooled liquid, *Science and Technology for the Built Environment*, 26 (9) (2020) 1177-1190.
- [77] B.M. Lee, H.H. Gook, S.B. Lee, Y.W. Lee, D.H. Park, N.H. Kim, Condensation heat transfer and pressure drop of low GWP R-404A alternative refrigerants (R-448A, R-449A, R-455A, R-454C) in a 5.6 mm inner diameter horizontal smooth tube, *IJR*, Volume 128, 2021.
- [78] C.H. Kim, N.H. Kim, Condensation heat transfer and pressure drop of low GWP R-404A-alternative refrigerants (R-448A, R-449A, R-455A, R-454C) in a 7.0-mm outer-diameter horizontal microfin tube, *IJR*, 126 (2021) 181-194.
- [79] D. Jige, S. Kikuchi, N. Mikajiri, N. Inoue, Flow boiling heat transfer of zeotropic mixture R1234yf/R32 inside a horizontal multiport tube, *International Journal of Refrigeration*, Volume 119, November 2020, Pages 390-400.
- [80] C.H. Kim, N.H. Kim, Evaporation heat transfer and pressure drop of the interim (R-448A, R-449A) and long term (R-455A, R-454C) low GWP R-404A alternative refrigerants in a smooth tube, *Int. J. Heat Mass Transfer* 181 (2021) 121903.
- [81] C.H. Kim, N.H. Kim, Evaporation heat transfer of the low GWP alternative refrigerants (R-448A, R-449A, R-455A, R-454C) for R-404A in a microfin tube, *International Journal of Refrigeration* 128 (2021) 118-128.
- [82] G. Lillo, R. Mastrullo, A. W. Mauro, L. Viscito, Flow boiling of R32 in a horizontal stainless steel tube with 6.00 mm ID. Experiments, assessment of correlations and comparison with refrigerant R410A, *Int. J. of Refrigeration* 97 (2019), 143-156.

- [83] G. Lillo, R. Mastrullo, A. W. Mauro, L. Viscito, Flow boiling of R1233zd(E) in a horizontal tube: Experiments, assessment and correlation for asymmetric annular flow, *Int. J of Heat and Mass Transfer* 129 (2019), 547-561.
- [84] R. Mastrullo, A.W. Mauro, L. Viscito, Flow boiling of R32 in a horizontal smooth tube of 6.0 mm internal diameter: Heat transfer coefficient and pressure drop, 35th Italian Union of Thermo-Fluid Dynamics Heat Transfer Conference, UIT 2017; Faculty of Engineering, Marche Polytechnic University Ancona; Italy.
- [85] Z. Rohuani, E. Axelsson, Calculation of volume void fraction in a subcooled and quality region, *Int. J. of Heat and Mass Transfer*, 17 (1970) 383-393.
- [86] D. Steiner, Heat transfer to boiling saturated liquids, in: Verein Deutscher Ingenieure (Ed.), *VDI-Wärmeatlas (VDI Heat Atlas)*. VDI-Gesellschaft Verfahrenstechnik und Chemieingenieurwesen (GCV), Düsseldorf, 1993.
- [87] R.J. Moffat, Using uncertainty analysis in the planning of an experiment, *Transac. ASME: J. Fluids Eng.* 107 (1985) 173–178.
- [88] G. Lillo, R. Mastrullo, A.W. Mauro, L. Viscito, Flow boiling heat transfer, dry-out vapor quality and pressure drop of propane (R290): experiments and assessment of predictive methods, *Int. J. Heat Mass Transf.* 126 (2018) 1236–1252.
- [89] F.W. Dittus, L.M.K. Boelter, Heat transfer in automobile radiators of the tubular type, *Univ. Calif. Publ. Eng.* 2 (1930) 443–461.
- [90] Z. Liu, R.H.S. Winterton, A general correlation for saturated and subcooled flow boiling in tubes and annuli, based on a nucleate pool boiling equation, *International Journal of Heat and Mass Transfer*, 34(11) (1991) 2759-2766.

- [91] S.M. Kim, I. Mudawar, Universal approach to predicting saturated flow boiling heat transfer in mini/micro-channels - Part II. Two-phase heat transfer coefficient, *Int. J. Heat Mass Transf.* 64 (2013) 1239–1256.
- [92] K. Gungor, R. Winterton, A general correlation for flow boiling in tubes and annuli, *Int. J. Heat Mass Transf.* 29 (1986) 351–358.
- [93] J.R. Thome, S. Shakir, A new correlation for nucleate pool boiling of aqueous mixtures, *AIChE Symp. Ser.* 83 (1987) 46–51.
- [94] R. Mastrullo, A.W. Mauro, L. Viscito, Flow boiling of R452A: Heat transfer data, dry-out characteristics and a correlation, *Experimental Thermal and fluid Science* 105 (2019) 247-260.
- [95] M. Cooper, Heat flow rates in saturated nucleate pool boiling - wide-ranging examination using reduced properties, *Adv. Heat Transf.* 16 (1984) 157–239.
- [96] A. Cioncolini, J.R. Thome, Algebraic turbulence modeling in adiabatic and evaporating annular two-phase flow, *Int. J. Heat Fluid Flow* 32 (2011) 805–817.
- [97] L. Wojtan, T. Ursenbacher, J.R. Thome, Investigation of flow boiling in horizontal tubes: Part II – development of a new heat transfer model for stratified-wavy, dryout and mist flow regimes, *Int. J. Heat Mass Transf.* 48 (2005) 2970–2985.
- [98] L. Wojtan, T. Ursenbacher, J.R. Thome, Investigation of flow boiling in horizontal tubes: part I – a new diabatic two-phase flow pattern map, *Int. J. Heat Mass Transf.* 48 (2005) 2955–2969.
- [99] H. Müller-Steinhagen, K. Heck, A simple friction pressure drop correlation for two-phase flow in pipes. *Chem. Eng. and Processing: Process Intensification* 20 (1986) 297-308.

- [100] L. Friedel, Improved friction pressure drop correlations for horizontal and vertical two-phase pipe flow. Paper E2, European Two Phase Flow Group Meeting. Ispra, Italia (1979).
- [101] A. Cioncolini, J.R. Thome, Pressure drop prediction in annular two-phase flow in macroscale tubes and channels, *Int J Multiphase Flow* 89 (2017) 321-330.
- [102] A. Cicchitti, C. Lombardi, M. Silvestri, G. Soldaini, R. Zavalluilli, Two-phase cooling experiments pressure drop, heat transfer and burnout measurements. *Energia Nucleare*, Vol. 7 (1960), 407-425.
- [103] H.M. Henning, Solar assisted air conditioning of buildings—an overview. *Applied thermal engineering*, 27(10) (2007) 1734-1749.
- [104] C.A. Balaras, G. Grossman, H.M. Henning, C.A. Infante Ferreira, E. Podesser, L. Wang, E. Wiemken, Solar air conditioning in Europe-an overview. *Renewable and Sustainable Energy Reviews*. 11 (2007) 299-314.
- [105] A.M. Baniyounes, Y.Y. Ghadi, M.G. Rasul, M.M.K. Khan, An overview of solar assisted air conditioning in Queensland's subtropical regions, Australia. *Renewable and Sustainable Energy Reviews*, 26, (2013) 781-804.
- [106] W.H. Güido, W. Lanser, S. Petersen, F. Ziegler, Performance of absorption chillers in field tests. *Applied Thermal Engineering*, 134 (2018) 353-359.
- [107] Summerheat Publishable Report. Meeting cooling demands in summer by applying heat from cogeneration. April 2009..
- [108] S. Rosiek, F.J. Batlles. Integration of the solar thermal energy in the construction: Analysis of the solar-assisted air-conditioning system installed in CIESOL building. 34 (2009) 1423-1431.

- [109] U. Desideri, S. Proietti, P. Sdringola. Solar-powered cooling systems: Technical and economic analysis on industrial refrigeration and air-conditioning applications. *Applied Energy* 86 (2009) 1376–1386.
- [110] E. Bellos, C. Tzivanidis, C. Symeou, K.A. Antonopoulos, Energetic, exergetic and financial evaluation of a solar driven absorption chiller – a dynamic approach. *Energy Conversion and Management*. 137 (2017) 34-48.
- [111] A. Shirazi, R. A. Taylor, S. D. White, G. L. Morrison. Transient simulation and parametric study of solar-assisted heating and cooling absorption systems: An energetic, economic and environmental (3E) assessment. *Renewable Energy*. 86. (2016) 955-971.
- [112] A. Shirazi, R. A. Taylor, G.L. Morrison, S.D. White. Solar-powered absorption chillers: A comprehensive and critical review. *Energy Conversion and Management*. 171. (2018) 59-81.
- [113] A. Al-Alili, M.D. Islam, I. Kubo, Y. Hwang, R. Radermacher, Modeling of a solar powered absorption cycle for Abu Dhabi. *Appl. Energy* 93. (2012) 160-167.
- [114] U. Eicker, A. Colmenar-Santos, L. Teran, M. Cotrado, D. Borge-Diez, Economic evaluation of solar thermal and photovoltaic cooling system through simulation in different climatic conditions: an analysis in three different cities in Europe, *Energy Build.* 70, (2014) 207-223.
- [115] F. Calise, Thermoeconomic analysis and optimization of high efficiency solar heating and cooling systems for different Italian school buildings and climates. *Energy and Buildings* 42 (2010) 992–1003.
- [116] A. Pongtornkulpanich, S. Thepa, M. Amornkitbamrung, C. Butcher, Experience with fully operational solar-driven 10.ton LiBr/H₂O single-effect absorption cooling system in Thailand. *Renewable Energy*. 33 (2008) 943-949.

- [117] A. Ghafoor, A. Munir. Worldwide overview of solar thermal cooling technologies. *Renewable and Sustainable Energy Reviews*. 43 (2015) 763-774.
- [118] J. Wang, J. Wu, Investigation of a mixed effect absorption chiller powered by jacket water and exhaust gas waste heat of internal combustion engine. *Int. J. of Refrig*. 50 (2015) 193-206.
- [119] C. Tao, L. Hoseong, H. Yunho, R. Radermacher, H.H. Chun. Performance investigation of engine waste heat powered absorption cycle cooling system for shipboard applications. *Applied Thermal Engineering*. 90 (2015) 820-830.
- [120] C. Ezgi. Design and thermodynamic analysis of an H₂O-LiBr AHP system for naval surface ship application. *International Journal of Refrigeration*. 48 (2014) 153-165.
- [121] Y. Shi, F. Li, Multi-objective optimization of series system for heat recovery: Technical and economic tradeoff. *Journal of Cleaner Production*. 367 (2022)133036.
- [122] S. Udomsri, A.R. Martin, V. Martin. Thermally driven cooling coupled with municipal solid waste-fired power plant: Application of combined heat, cooling and power in tropical urban areas. *Applied Energy* 88 (2011) 1532-1542.
- [123] C.Y. Hsu, T.Y. Lin, J.D. Liang, C.H. Lai. S.L. Chen, Optimization analysis of waste heat recovery district cooling system on a remote island: Case study Green Island. *Energy Conversion and Management*. 183 (2019) 660-670.
- [124] H.Z. Hassan, A.A. Mohamad, A review on solar-powered closed physisorption cooling systems. *Renewable and Sustainable Energy Reviews*, 16(5) (2012) 2516-2538.

- [125] C.I, Ferreira, D.S. Kim, Techno-economic review of solar cooling technologies based on location-specific data. *International Journal of Refrigeration*, 39 (2014) 23-37..
- [126] W. Wu, B. Wang, W. Shi, X. Li, An overview of ammonia-based absorption chillers and heat pumps. *Renewable and Sustainable Energy Reviews* 31 (2014) 681-707.
- [127] S. Aphornratana, T. Sriveerakul, Analysis of a combined Rankine–vapour–compression refrigeration cycle. *Energy Conversion and management*, 51(12), (2010) 2557-2564.
- [128] X.B. Bu, H.S. Li, L.B. Wang, Performance analysis and working fluids selection of solar powered organic Rankine-vapor compression ice maker. *Solar Energy*. 95 (2013) 271-278.
- [129] N. Zheng, J. Wei, L. Zhao. Analysis of a solar Rankine Cycle powered refrigerator with zeotropic mixture. *Solar Energy*. 162 (2018) 57-66.
- [130] M.T. Nasir, K.C. Kim, Working fluids selection and parametric optimization of an Organic Rankine Cycle coupled Vapor Compression Cycle (ORC-VCC) for air conditioning using low grade heat. *Energy and Buildings*, 129 (2016) 378-395.
- [131] K.H. Kim, H.Perez-Blanco. Performance analysis of a combined organic Rankine cycle and vapor compression cycle for power and refrigeration cogeneration. *Applied Thermal Engineering*. 91 (2015) 964-974.
- [132] H. Wang, R. Peterson, K. Harada, E. Miller, R. Ingram-Goble, L. Fisher, C. Ward, Performance of a combined organic Rankine cycle and vapor compression cycle for heat activated cooling. *Energy*, 36(1) (2011) 447-458.

- [133] H. Wang, R. Peterson, T. Herron, Design study of configurations on system COP for a combined ORC (organic Rankine cycle) and VCC (vapor compression cycle). *Energy*, 36(8) (2011) 4809-4820.
- [134] H. Li, X. Bu, L. Wang, Z. Long, Y. Lian, Hydrocarbon working fluids for a Rankine cycle powered vapor compression refrigeration system using low-grade thermal energy. *Energy and buildings*, 65 (2013) 167-172.
- [135] F. Molés, J. Navarro-Esbrí, B. Peris, A. Mota-Babiloni, K.K. Kontomaris, Thermodynamic analysis of a combined organic Rankine cycle and vapor compression cycle system activated with low temperature heat sources using low GWP fluids., *Applied Thermal Engineering*, 87 (2015) 444-453.
- [136] S. Karellas, K. Braimakis, Energy–exergy analysis and economic investigation of a cogeneration and trigeneration ORC–VCC hybrid system utilizing biomass fuel and solar power. *Energy Conversion and Management*. 107 (2016) 103-113.
- [137] J. Bao, L. Zhang, C. Song, N. Zhang, X. Zhang, G. He, Comparative study of combined organic Rankine cycle and vapor compression cycle for refrigeration: Single fluid or dual fluid?. *Sustainable Energy Technologies and Assessments*. 37 (2020) 100595.
- [138] N. Meng, T. Li, J. Wang, Y. Jia, Q. Liu. H. Qin, Synergetic cascade-evaporation mechanism of a novel building distributed energy supply system with cogeneration and temperature and humidity independent control characteristics. *Energy Conversion and, Management*. 209 (2020) 112620.
- [139] M.T. Nasir, M.A. Ali, T.S. Khan, E. Al-Hajri, M.B. Kadri, K.C. Kim, Performance assessment and multi objective optimization of an Organic Rankine Cycle driven cooling air conditioning system. *Energy & Buildings*. 191 (2019) 13-30.
- [140] G. Liao, L. Liu, F. Zhang, E. Jiaqiang, J. Chen, A novel combined cooling-heating and power (CCHP) system integrated organic Rankine cycle for waste heat

recovery of bottom slag in coal-fired plants. *Energy Conversion and Management*. 186 (2019) 380-392.

- [141] O. Bounefour, A. Ouadha, Y. Addad, An exergy analysis of various layouts of ORC-VCC systems for usage in waste heat recovery onboard ships. *Marine Systems & Ocean Technology*. 15 (2020) 26–44.
- [142] Y. Liang, A. Mckeown, Z. Yu, S.F.K. Alshammari, Experimental study on a heat driven refrigeration system based on combined organic Rankine and vapour compression cycles. *Energy Conversion and Management*. 234 (2021) 113953.
- [143] E. Bellos, C. Tzivanidis, Optimum design of a solar ejector refrigeration system for various operating scenarios. *Energy conversion and Management*. 154. 2017. 11-24.
- [144] M. Elakhdar, B.M. Tashtoush, E. Nehdi, L. Kairouani, Thermodynamic analysis of a novel Ejector Enhanced Vapor Compression Refrigeration (EEVCR) cycle. *Energy*. 163 (2018) 1217-1230.
- [145] M.T. Zegenhagen, F. Ziegler, Experimental investigation of the characteristics of a jet-ejector and a jet-ejector cooling system operating with R134a as a refrigerant. *International Journal of Refrigeration*. 56 (2015) 173-185.
- [146] D. Butrymowicz, J. Gagan, M. Łukaszuk, K. Smierciew, A. Pawluczuk, T. Zielinski, M. Kedzierski, Experimental validation of new approach for waste heat recovery from combustion engine for cooling and heating demands from, combustion engine for, maritime applications. *Journal of Cleaner Production*. 290 (2021) 125206.
- [147] M. Kędzierski, K. Smierciew, D. Butrymowicz, J. Gagan, "Application Of Waste Low Heat As A Motive Source For Ejection Air-Conditiong Systems For Motor Yachts". *International Refrigeration and Air Conditioning Conference*. (2018).

- [148] A. Hasan, B. Mugdadi, M. A. Al-Nimr, B. Tashtoush, Direct and indirect utilization of thermal energy for cooling, generation: A comparative analysis. *Energy* 238 (2022) 122046.
- [149] Lillo, G., Mastrullo, R., Mauro, A. W., Trinchieri, R., & Viscito, L. Thermo-economic analysis of a hybrid ejector refrigerating system based on a low grade heat source. *Energies*, 13(3) (2020) 562.
- [150] D. W. Sun, Comparative study of the performance of an ejector refrigeration cycle operating with various refrigerants. *Energy Conversion and Management*, 40(8) (1999) 873-884.
- [151] K. Cizungu, A. Mani, M. Groll, Performance comparison of vapour jet refrigeration system with environment friendly working fluids. *Applied Thermal Engineering*, 21(5) (2001) 585-598.
- [152] A. Selvaraju, A. Mani, Analysis of an ejector with environment friendly refrigerants. *Applied Thermal Engineering*, 24(5-6) (2004) 827-838.
- [153] J. Kasperski, B. Gil, Performance estimation of ejector cycles using heavier hydrocarbon refrigerants. *Applied Thermal Engineering*, 71(1) (2014) 197-203..
- [154] B.J. Huang, J.M. Chang, C.P. Wang, V.A. Petrenko, A 1-D analysis of ejector performance. *International journal of refrigeration*, 22(5) (1999) 354-364.
- [155] B. Gil, J. Kasperski, Efficiency analysis of alternative refrigerants for ejector cooling cycles. *Energy conversion and management*, 94 (2015) 12-18..
- [156] J. Chen, H. Havtun, B. Palm, Screening of working fluids for the ejector refrigeration system. *International Journal of Refrigeration*, 47 (2014) 1-14..
- [157] J. Chen, H. Havtun, B. Palm, Parametric analysis of ejector working characteristics in the refrigeration system. *Applied Thermal Engineering*, 69(1-2) (2014) 130-142.

- [158] K.O. Shestopalov, B.J. Huang, V.O. Petrenko, O.S. Volovyk, Investigation of an experimental ejector refrigeration machine operating with refrigerant R245fa at design and off-design working conditions. Part 1. Theoretical analysis., international journal of refrigeration, 55 (2015) 201-211.
- [159] K.O. Shestopalov, B.J. Huang, V.O. Petrenko, O.S. Volovyk, Investigation of an experimental ejector refrigeration machine operating with refrigerant R245fa at design and off-design working conditions. Part 2. Theoretical, and experimental results. international journal of refrigeration, 55 (2015) 212-223.
- [160] D.W. Sun, Variable geometry ejectors and their applications in ejector refrigeration systems. Energy, 21(10) (1996) 919-929.
- [161] P.R. Pereira, S. Varga, A.C. Oliveira, J. Soares, Development and performance of an advanced ejector cooling system for a sustainable built environment. Frontiers in Mechanical Engineering, 1 (2015) 7..
- [162] F. Mazzelli, A. Milazzo. Performance analysis of a supersonic ejector cycle working with R245fa. International Journal of refrigeration. 49 (2015) 79-92.
- [163] A.J. Meyer, T.M. Harms, R.T. Dobson, Steam jet ejector cooling powered by waste or solar heat. Renew. Energy, 34 (2009) 297-306.
- [164] S. Aphornratana, I.W. Eames, A small capacity steam-ejector refrigerator: experimental investigation of a system using ejector with movable primary nozzle. International Journal of Refrigeration, 20(5), (1997) 352-358.
- [165] S. Varga, A.C. Oliveira and B. Diaconu, Numerical assessment of steam ejector efficiencies using CFD. Int J Refrig, 32 (2009) 1203-1211.
- [166] J. Dong, M. Yu, W. Wang, H. Song, C. Li, X. Pan, Experimental investigation on low-temperature thermal energy driven steam ejector refrigeration system for cooling application. Applied Thermal Engineering. 123 (2017) 167-176.

- [167] A. Selvaraju, A. Mani, Experimental investigation on R134a vapour ejector refrigeration system. *Int J Refrig*, 29 (2006) 1160-1166.
- [168] R. Yapıcı, H.K. Ersoy, A. Aktoprakoğlu, H.S. Halkacı and O. Yiğit, Experimental determination of the optimum performance of ejector refrigeration system depending on ejector area ratio. *Int J Refrig*, 31 (2008) 1183-1189.
- [169] J. García del Valle, J.M. Saíz Jabardo, F. Castro Ruiz, J.F. San José Alonso, An experimental investigation of a R-134a ejector refrigeration system. *Int J Refrig*, 46 (2014), pp. 105-113.
- [170] Y. Jia and C. Wenjian, Area ratio effects to the performance of air-cooled ejector refrigeration cycle with R134a refrigerant *Energy Convers. Manage.*, 53 (2012) 240-246.
- [171] X. Ma, W. Zhang, S.A. Omer and S.B. Riffat, Experimental investigation of a novel steam ejector refrigerator suitable for solar energy applications. *Appl. Therm. Eng.*, 30 (2010) 1320-1325.
- [172] V. Van Nguyen, S. Varga, J. Soares, V. Dvorak, A.C. Oliveira, Applying a variable geometry ejector in a solar ejector refrigeration system. *International Journal of Refrigeration*, 113 (2020) 187-195.
- [173] Z. Aidoun, M. Ouzzane, The effect of operating conditions on the performance of a supersonic ejector for refrigeration. *International Journal of Refrigeration*, 27(8), (2004) 974-984.
- [174] S. Varga, A.C. Oliveira, A. Palmero-Marrero, J. Vrba, Preliminary experimental results with a solar driven ejector air conditioner in Portugal. *Renewable Energy*. 109 (2017) 83-92.

- [175] L. Boumaraf, A. Lallemand, Modeling of an ejector refrigerating system operating in dimensioning and off-dimensioning conditions with the working fluids R142b and R600a. *Applied Thermal Engineering*, 29(2-3) (2009) 265-274.
- [176] K. Chunnanond, S. Aphornratana, An experimental investigation of a steam ejector refrigerator: the analysis of the pressure profile along the ejector. *Applied Thermal Engineering*, 24(2-3) (2004) 311-322.
- [177] F. Li, R. Li, X. Li, Q. Tian, Experimental investigation on a R134a ejector refrigeration system under overall modes. *Applied Thermal Engineering*. 137 (2018) 784-791.
- [178] L. Boumaraf, R. Khadraoui, Investigation on the Performance of a Solar Hybrid Refrigeration System Using Environmentally Friendly Fluids, *International Journal of Heat and Technology*. Vol. 38, 4 (2020) 960-966.
- [179] R. Suresh, S.P. Datta, Drop-in Replacement of Conventional Automotive Refrigeration System to Hybrid-Ejector System with Environment-Friendly Refrigerants. *Energy Conversion and Management*. 266 (2022) 115819.
- [180] H. Wang, W. Cai, Y. Wang, J. Yan, L. Wang, Experimental study of the behavior of a hybrid ejector-based air-conditioning system with R134a. *Energy Conversion and Management*. 112 (2016) 31-40.
- [181] R. Dorantes, C.A. Estrada, I. Pilatowsky, Mathematical simulation of a solar ejector-compression refrigeration system. *Applied Thermal Engineering*. 16 (1996) 669-675.
- [182] H.R. Takleh, V. Zare, Performance improvement of ejector expansion refrigeration cycles employing a booster compressor using different refrigerants: Thermodynamic analysis and optimization. *Int. J. Refrig.* 101 (2019) 56–70.

- [183] Y. Zhu, P. Jiang, Hybrid vapor compression refrigeration system with an integrated ejector cooling cycle. *International Journal of Refrigeration*. 35 (2012) 68-78.
- [184] R.B. Mansour, M. Ouzzane, Z. Aidoun, Numerical evaluation of ejector-assisted mechanical compression systems for refrigeration applications. *International Journal of Refrigeration*. 43 (2014) 36-49.
- [185] S. Sanaye, M. Emadi, A. Refahi, Thermal and economic modeling and optimization of a novel combined ejector refrigeration cycle. *International Journal of Refrigeration* 98 (2019) 480-493.
- [186] V. Evely, Y. Alkand, Thermodynamic Performance Investigation of a Small-Scale Solar Compression-Assisted Multi-Ejector Indoor Air Conditioning System for Hot Climate Conditions. *Energies*. 14 (2021) 4325.
- [187] Y. Xu, N. Jiang, Q. Wang, N. Mao, G. Chen, Z. Gao, Refrigerant evaluation and performance comparison for a novel hybrid solar-assisted ejection-compression refrigeration cycle. *Solar Energy*. 160 (2018) 344-352.
- [188] Y. Xu, C. Wang, N. Jiang, M. Song, Q. Wang, G. Chen, A solar-heat-driven ejector-assisted combined compression cooling system for multistory building – Application potential and effects of floor numbers. *Energy Conversion and Management*. 195 (2019) 86-98.
- [189] N. Ruangtrakoon, T. Thongtip, S. Aphornratana, T. Sriveerakul, CFD simulation on the effect of primary nozzle geometries for a steam ejector in refrigeration cycle. *International Journal of Thermal Sciences*, 63 (2013) 133–145.
- [190] T. Sriveerakul, CFD and Experimental analysis of an R141b ejector used in a ejector refrigerator. Ph.D Thesis. Department of mechanical engineering, Sirindhorn International Institute of Technology, Thammasat University, Thailand. (2018).

- [191] J. Chen, H. Havtun, B. Palm, Investigation of ejectors in refrigeration system: Optimum performance evaluation and ejector area ratios perspectives. *Appl. Therm. Eng.* 64 (2014) 182–191.
- [192] H. El-Dessouky, H. Ettouney, I. Alatiqi, G. Al-Nuwaibit, Evaluation of steam jet ejectors. *Chemical Engineering and Processing: Process Intensification*, 41(6) (2002) 551-561.
- [193] D.W. Sun, I.W. Eames, Performance characteristics of HCFC-123 ejector refrigeration cycles. *International Journal of Energy Research*, 20(10) (1996) 871-885.
- [194] J. Yu, Y. Ren, H. Chen, Y. Li, Applying mechanical subcooling to ejector refrigeration cycle for improving the coefficient of performance. *Energy Conversion and Management*, 48(4) (2007) 1193-1199.
- [195] A. Mwesigye, S.B. Dworkin, Performance analysis and optimization of an ejector refrigeration system using alternative working fluids under critical and subcritical operation modes. *Energy conversion and management*, 176 (2018) 209-226.
- [196] M. Clause, K.C.A. Alam, F. Meunier, Residential air conditioning and heating by means of enhanced solar collectors coupled to an adsorption system, *Solar Energy* 82 (2008) 885–892.
- [197] S. Zhu, K. Zhang, K. Deng, A review of waste heat recovery from the marine engine with highly efficient bottoming power cycles. *Renewable and Sustainable Energy Reviews*, 120 (2020) 109611.
- [198] H. Martin, A. theoretical approach to predict the performance of chevron-type plate heat exchangers. *Chem. Eng. Process. Process Intensif.* 35 (1996) 301–310.

- [199] J.H. Park, Y.S. Kim, Evaporation heat transfer and pressure drop characteristics of R-134a in the oblong shell and plate heat exchanger. *KSME Int. J.* 18, (2014) 2284–2293.
- [200] W.H. McAdams, W.K. Wood, R.L. Bryan, Vaporization inside horizontal tubes II—benzene–oil mixtures. *Trans. ASME* 66 (1942) 671–684.
- [201] M. G. Cooper, Saturation nucleate pool boiling—a simple correlation. In *ICHEME Symp. Ser.* (1984) Vol. 86, p. 786..
- [202] F.W. Dittus, L.M.K. Boelter, Heat transfer in automobile radiators of the tubular type. *International Communications in Heat and Mass Transfer*, 12(1) (1985) 3–22.
- [203] K.J. Bell, Delaware method for shell side design, in S. Kakac, A.E., Bergles, F. and Mayinger, F. (eds). *Heat Exchangers: Thermal-Hydraulic Fundamentals and Design* (Hemisphere/McGraw-Hill, Washington, DC) (1981).
- [204] M.M. Shah, A general correlation for heat transfer during film condensation inside pipes. *International Journal of heat and mass transfer*, 22(4) (1979) 547–556.
- [205] C.C. Wang, K.Y. Chi, C.J. Chang, Heat transfer and friction characteristics of plain fin-and-tube heat exchangers, part II: Correlation. *Int. J. Heat Mass Transf.* 43(2000) 2693–2700.
- [206] S. Declaye, Improving the performance of μ -ORC systems, Phd thesis, Université de Liège, Liège, Belgium (2015).
- [207] M. Tamaro, A.W. Mauro, C. Montagud, J.M. Corberán, R. Mastrullo, Hot sanitary water production with CO₂ heat pumps: Effect of control strategy on system performance and stratification inside the storage tank, *App. Ter. Eng.* Volume 101 (2016) 730–740.

- [208] S. Quoilin, S. Declaye, B.F. Tchanche, V. Lemort, Thermo-economic optimization of waste heat recovery Organic Rankine Cycles. *Appl. Therm. Eng.* 31 (2011) 2885–2893.
- [209] P. Wildi-Tremblay, L. Gosselin, Minimizing shell-and-tube heat exchanger cost with genetic algorithms and considering maintenance. *International Journal of Energy Research*, 31(9) (2007) 867-885.
- [210] M. Taal, I. Bulatov, J. Klemes, P. Stehlik, Cost estimation and energy price forecasts for economic evaluation of retrofit projects, *Applied thermal engineering*, 23 (14) (2003) 1819–1835..
- [211] F. Botticella, F. De Rossi, A.W. Mauro, G.P. Vanoli, L. Viscito, Multi-criteria (thermodynamic, economic and environmental) analysis of possible design options for residential heating split systems working with low GWP refrigerants., *International Journal of Refrigeration*, 87 (2018) 131-153.
- [212] A.C. Ferreira, A. Silva, J.C. Teixeira, S. Teixeira, Multi-Objective Optimization of Solar Thermal Systems Applied to Portuguese Dwellings. *Energies*, 13 (2020) 6739.
- [213] G.N. Sakalis, Design and partial load operation optimization of integrated ship energy system based on supercritical CO₂ waste heat recovery cycle. *Sustainable Energy Technologies and Assessments*, 51 (2022) 101965.
- [214] TRNSYS 17, a TRaNsient System simulation program. Solar Energy Laboratory; University of Wisconsin-Madison; 2010.
- [215] Commission Regulation (EU) 2016/2281 implementing Directive 2009/125/EC of the European Parliament and of the Council establishing a framework for the setting of ecodesign requirements for energy-related product.

- [216] M.A. Ancona, F. Baldi, M. Bianchi, L. Branchini, F. Melino, A. Peretto, J. Rosati, Efficiency improvement on a cruise ship: Load allocation optimization. *Energy conversion and Management*. (2018) 164. 42-58.
- [217] L. Viscito, G. Lillo, G. Napoli, A.W. Mauro, Waste heat driven multi-ejector cooling systems: Optimization of design at partial load; season performance and cost evaluation. *Energies*. 14(18) (2021), 5663.
- [218] L. Cecchinato, M. Chiarello, M. Corradi, A simplified method to evaluate the seasonal energy performance of water chillers. *International journal of thermal sciences*, 49(9) (2010) 1776-1786.
- [219] Kühn, A. (Ed.). *Thermally driven heat pumps for heating and cooling*. Universitätsverlag der TU Berlin. (2013).
- [220] R. Mastrullo, A.W. Mauro, G. Napoli, R. Trinchieri, L. Viscito, Solar driven ejector cooling system employing natural refrigerants: thermo-economic analysis and optimization strategy. 15th IIR-Gustav Lorentzen conference on Natural Refrigerants June 13-, June 13-15 Trondheim, Norway. In press.
- [221] J.C. Helton, F.J. Davis, Latin hypercube sampling and the propagation of uncertainty in analyses of complex systems. *Reliability Engineering & System Safety*, 81(2003), Vol. 1, 23-69.
- [222] S. Forrest, Genetic algorithms. *ACM Computing Surveys (CSUR)*. 28(1) (1996) 77-80.
- [223] Fourth IMO GHG Study 2020..